Energy-loss Spectroscopy in Scanning Transmission Electron Microscopy

Adrian Paul Stephens

Selwyn College

Dissertation submitted for the degree of Ph. D.

Energy-Loss spectroscopy in Scanning-transmission Electron microscopy

Dissertation submitted for the degree of Ph.D. by
Adrian Paul Stephens, Selwyn College, Cambridge

Summary:

Chapters 1 to 3 are concerned with a discussion of the theory of energy-loss processes, the collection of energy-loss data and the numerical techniques used in the analysis of energy-loss data.

Chapter 1 contains a brief history of energy-loss spectroscopy (ELS) followed by a brief description of non-computer-based ELS on the Cambridge Scanning-transmission electron microscopy (STEM).

Chapter 2 contains a resume of energy-loss processes, concentrating on a presentation of the results pertainent to ELS. The reader is referred to the original papers for a more-exhaustive coverage.

Chapter 3 contains a description of the computer-based data-capture system, the computer-microscope interface and a development of the numerical techniques required for the numerical analysis of energy-loss data.

Chapters 4,5 and 6 contain an application of the techniques of chapters 2 and 3 to experimental energy-loss spectra.

Chapter 4 contains three demonstrations of quantitative micro-analysis (boron nitride, "boron" and "silicon carbide").

Chapter 5 compares the radial distribution function (RDF) of boron nitride obtained from extended energy-loss fine structure (EXELFS) data with the RDF predicted by the known crystal structure, and attempts to account for the discrepancy found.

Chapter 6 shows how the energy-loss spectra of Niobium and Vanadium -hydrides may be used to obtain a simple density of states diagram.

Adrian P. Stephens

12-Jun-81

Preface

This dissertation is the result of work performed between October 1977 and October 1980, under the supervision of Dr. L.M. Brown, at the Cavendish Laboratory, Cambridge.

This dissertation is not substantially the same as any submitted for a degree, diploma or any other qualification at any other university. Except for reviews of previous work, it is my own work and is not the result of work done in collaboration.

Parts of this work have been published in the following papers:

1) The plasmon shift correction and angular convolution correction: Ultramicroscopy 5 (1980) 343-349
2) The energy-loss spectra of vanadium and niobium hydride: Inst.Phys.Conf.Ser.No.52 (1980) 341-2 (with Brown, L.M.)
3) The EXELFS of boron nitride: (with L.M. Brown) to be published

I would like to thank Professor Pippard and the University of Cambridge for the research facilities.
I would also like to thank members of the Metal Physics group for their help, in particular Dr. S. Pennycook and Mr. L.P.G. Jones for their instruction at and repair of the HB5 microscope, and Mr. R. Brundish for his photographic work.

My particular thanks are due to Dr. L.M. Brown for the continuous help and enthusiasm he has shown as my supervisor.

A. P. Stephens.

A.P. Stephens

INDEX

Appendices

A. ENERGY-LOSS PROGRAMS AT CAMBRIDGE

Chapter 1 - Introduction to energy-loss spectroscopy on the Cambridge S.T.E.M.

Chapter 1 - Introduction to energy-loss spectroscopy on the Cambridge S.T.E.M.

1.1 A BRIEF HISTORY OF MICROANALYTICAL ENERGY-LOSS SPECTROSCOPY

The first observation of the possible utility of electron energy-loss spectroscopy (EELS) as a microanalytical technique was made by Rudberg (1930). He analysed the velocity distribution of electrons scattered from the surface of an incandescent metal specimen *in vacuo*. There was little control of the geometry of the scattering process, scattering angles and positions were not well defined. At that time, there was no clear understanding of the processes giving rise to the observed energy-loss spectrum (ELS), although it was thought that some of the structure of the ELS could be explained in terms of atomic photon emission spectra. Rudberg thought that this technique would be useful as an analytical tool.

There was little development in the study of EELS until the recently-developed transmission electron microscope (TEM) became commercially available in the 1950's. Then, home-made electron spectrometers were added to commercial machines and the first results because available (Marton & Leder 1954). The first spectrometers so added were of the Möllenstadt or Castaing-Henry type that used photographic emulsion as the recording medium. At the same time, low incident-energy, low spatial resolution instruments were developed. These generally offered superior energy resolution (Raether 1965), but they were not truly micro-analytical; and so their development is not described here. They did, however, contribute to the wealth of experimental energy-loss spectra, thus aiding the comparison of the developing energy-loss theory with experimental results.

The availability of EELS data, usually in the low- energy-loss range (0 to 100 eV loss) prompted the application of recently-developed theoretical techniques (Bohm & Pines 1951,2,3, Pines 1956, Ferrell 1956, Nozieres & Pines 1958a,b,c,1959) to the analysis and explanation of the data.

One of the first applications of EELS to quantitative microanalysis was the use of the plasmon frequency as a measure of the composition of binary alloys (Metherell 1965, Cundy 1967, Cook 1971).

When magnetic spectrometers and modern detectors were added to conventional TEMs (CTEMs), it became possible to obtain ELS at energy-losses as high as 2000 eV loss due to the good efficiency of the detector and the ability to scan the spectrometer current over a wide range of energy-losses.

The spatial resolution of microanalytical EELS was limited by the brightness of the conventional tungsten-filament electron gun. The availability of LaB_6 and, more recently, field emission guns (FEG) has meant that the spatial resolution that may be achieved has increased from several hundred angstrom units to several angstrom units (in the case of the FEG). One disadvantage of a field-emission electron source is the need for a very good vacuum near the emitter with the correspondingly increased hardware costs.

The energy resolution of the field-emission EM operating at the low currents employed in electron microscopy is governed solely by the quality of the electronics associated with the microscope and the design of the electron spectrometer. The energy-resolution of electron microscopes using a thermionic source may be limited by the energy spread of the emitted electrons.

One advantage of combining TEM and EELS is that it is possible to observe the image of a region of the specimen, and choose a small region of the specimen for analysis. Other microanalytical techniques are also available, such as X-ray microanalysis and microdiffraction (Lynch 1980). The region may be identified by its location on the specimen, and the techniques of conventional electron microscopy may also be applied (such as electron diffraction).

The recent development of the field-emission-gun scanning-transmission electron microscope (FEG STEM) which has a monochromatic electron source and both excellent energy and spatial resolution has opened up new possibilities in the application of ELS to the identification of small particles. Developments in computer-based data capture systems enable energy-loss data to be collected over long periods, thus improving the statistical quality of the recorded spectra (Batson 1978) .

The machines available commercially fall into two broad categories:
1) Conventional transmission electron microscopes with a manufacturer-supplied spectrometer, a LaB_6 electron source, computer-based data capture equipment. These machines have good energy resolution, a very good count-rate at the detector and a rather poor microanalytical spatial resolution of about 100 Å.
2) The FEG STEM which has a much higher spatial resolution than above (about 10 Å) at the cost of much reduced electron beam current and hence count-rate at the spectrometer. These machines are also very expensive and may be subject to long delivery times.

1.2 THE EQUIPMENT REQUIREMENTS OF MICROANALYTICAL ELS

In order to use the technique of quantitative EELS with a high spatial resolution, the following requirements should be satisfied:
1) In order to focus the electron probe to a very small (about 5 Å) spot, and still have sufficient beam current to form a useful electron energy-loss spectrum, it is neccessary to use a field-emission electron source with the consequent requirement of an ultra-high vacuum (UHV) gun chamber ($< 10^{-10}$ torr).
2) In order to be able to maintain a very high current density at the specimen, such as implied above, and not to suffer from a rapid build-up of contamination on the specimen caused by the breakdown of hydrocarbons present at the surface of the specimen, it is neccessary to maintain a good vacuum in the region near the specimen (the specimen chamber) (a pressure of $< 10^{-7}$torr) and ensure that the specimen is free of contaminants by baking the specimen in vacuo prior to its use in the microscope.
3) The specimen stage and cartridge should be mechanically stable so that vibration and drift do not affect the apparent position of the specimen whilst energy-loss data are being collected.
4) The lens, spectrometer, high-voltage and electron-beam-positioning electronics should all be stable enough to keep the position of the electron beam focus stationary in the plane of the specimen and to keep the observed energy of the unscattered electrons (the zero-loss peak) constant as measured by the spectrometer.

5) A lesser requirement is that the electron beam current should not fluctuate or drift quickly. This requirement has been somewhat relaxed by the use of digital data collection techniques in which successive spectra are summed, and beam current fluctuations tend to cancel out.

1.3 A BRIEF DESCRIPTION OF THE CAMBRIDGE HB5 STEM

The only commercially-available microscope, at the time of writing, that satisfied the requirements of section 1.2 was the HB5 (high brightness, 5Å probe size) microscope manufactured by Vacuum Generators Ltd. (East Grinstead, Sussex, England). The machine installed at the Cavendish Laboratories was their second production machine, and is still subject to continuing development.

A tungsten single-crystal, oriented so that the (310) crystal planes are normal to the optic axis of the microscope, is used as the field-emission source. The end of the crystal is sharpened to a very small radius of curvature (about 100 Å) and is approximately hemi-spherical, so the effective source size is smaller than the physical source size, in this case, about 20 Å.

An electrode, called the Wehnelt cap, is placed near the tip, and is charged to about +3000 Volts with respect to the tip. The very high electric field formed near the tip because of the very small radius of curvature is sufficient to cause electrons at the surface of the tungsten tip to leave the crystal surface. This is the phenomenon of field emission.

At the same time, gas molecules present in the gun chamber near the tip may be ionised by the very high electric field or by collisions with energetic electrons. Those which obtain a positive charge are accelerated towards the tip and coat the metal surface with a contamination layer that reduces the efficiency of the tip as a field-emission source. This contamination build-up occurs over a time-scale of about 10 minutes, and has to be removed by heating the field electrically by means of a special heating wire. This is called "tip flashing".

The gun chamber is kept at a very low pressure ($< 5.10^{-11}$ torr cold, and 10^{-10} torr operating), in order to minimise the contamination rate of the tip and the slow irreversible damage caused to the tip by erosion with fast ions. It is not possible to operate the specimen chamber at this low a pressure because of the time that would be required to outgas the specimen and because of the many vacuum joints in the specimen region which would make maintenance and the routine achievement of UHV in the specimen chamber difficult.
The specimen chamber is operated at a much higher pressure (about 10^{-8} torr) which may be achieved using an oil vapour diffusion pump, and, at which pressure, plastic "o-ring" vacuum seals may be used.

A small aperture connects the gun chamber and the specimen chamber. The flux of gas molecules through this aperture with the specimen chamber at its operating pressure of about 10^{-8} torr is not great enough to cause any significant increase in gun chamber pressure. The aperture may be stopped-off by means of a manually-controlled valve (the isolation valve), enabling the specimen chamber to be let up to atmospheric pressure without adversely affecting the vacuum or cleanliness of the gun chamber. The aperture is large enough to allow a beam of electrons to escape from the tip into the specimen chamber with a divergence angle of tens of milliradians. See figure 1.1.

The first lens consists of a magnetic lens and stigmator which form an image of the tip in the plane of the selected area diffraction aperture. This is the position of the first cross-over.
The second lens and associated stigmator (the objective lens) form a demagnified image of the tip in the plane of the specimen.

In order to understand how the microscope is aligned to perform energy-loss spectroscopy, it is necessary to consider the operation of the microscope in three modes (see fig 1.2), the details of which are given below.

1.3.1 Spot mode (or image mode)

A convergent beam of electrons forms a demagnified image of the tip at the specimen plane. The convergence angle is defined by the size of the objective aperture (situated in the back focal plane of the objective lens) and the focal length of the lens.

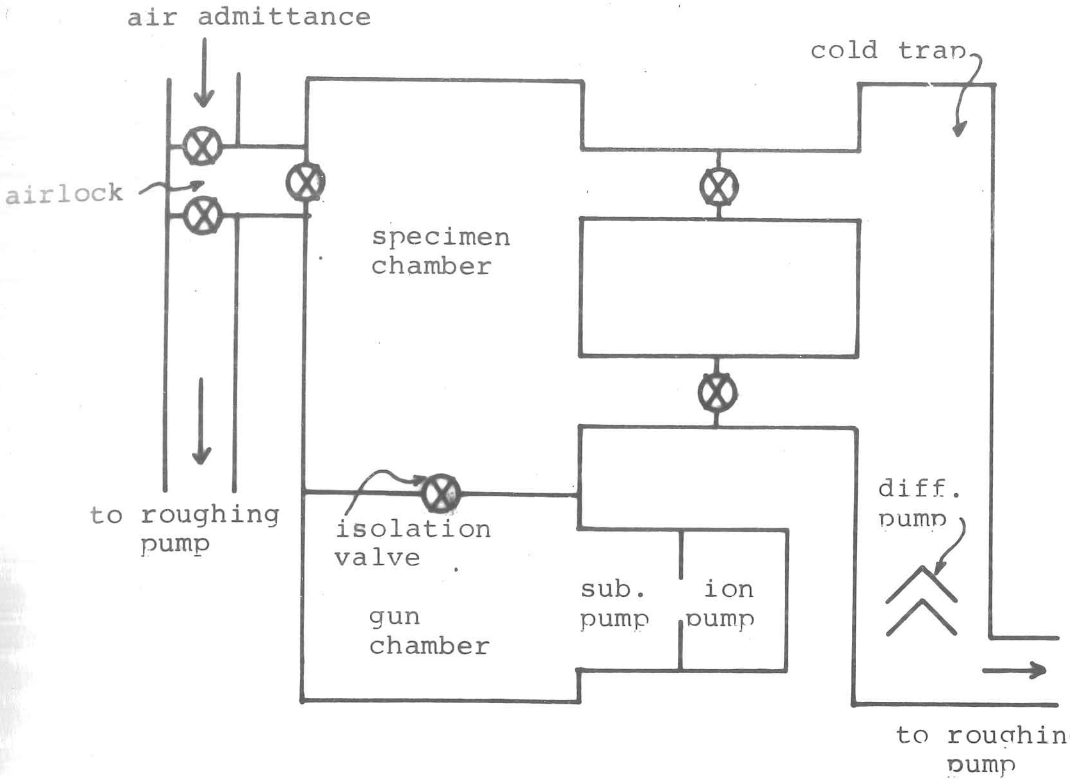

Figure 1.1 HB5 vacuum system (schematic)

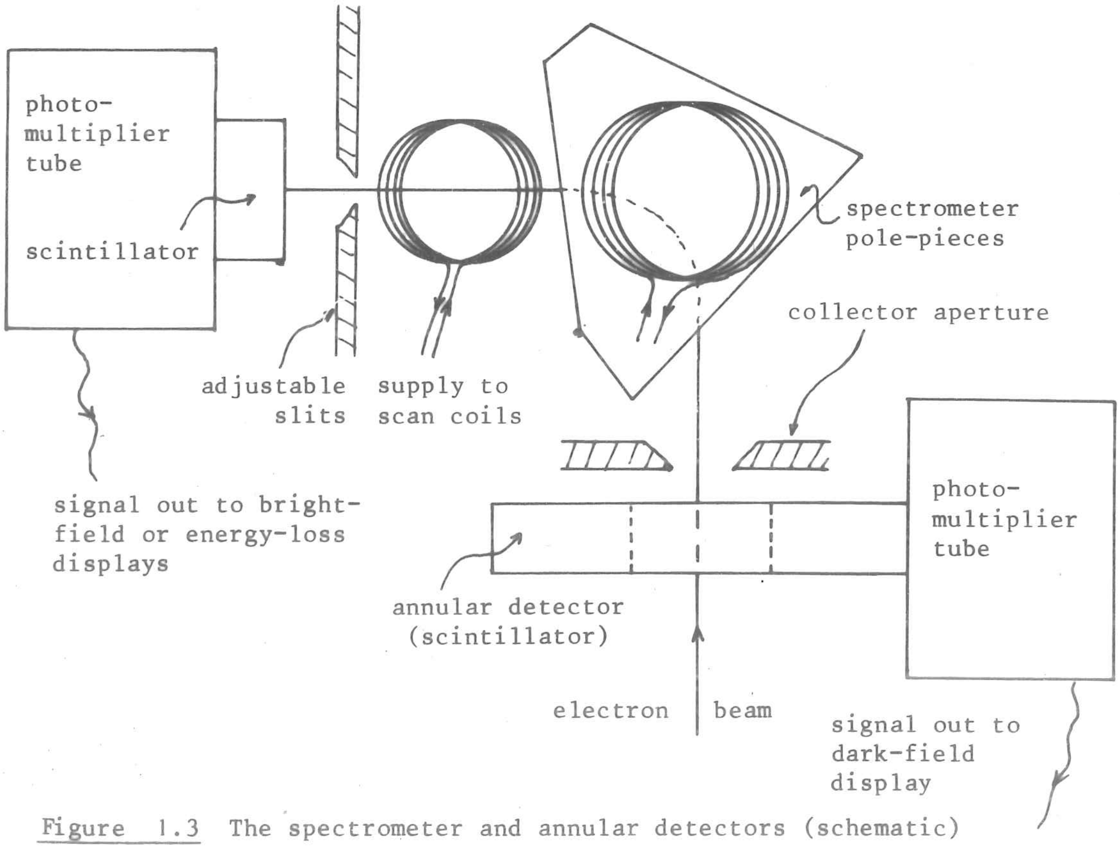

Figure 1.3 The spectrometer and annular detectors (schematic)

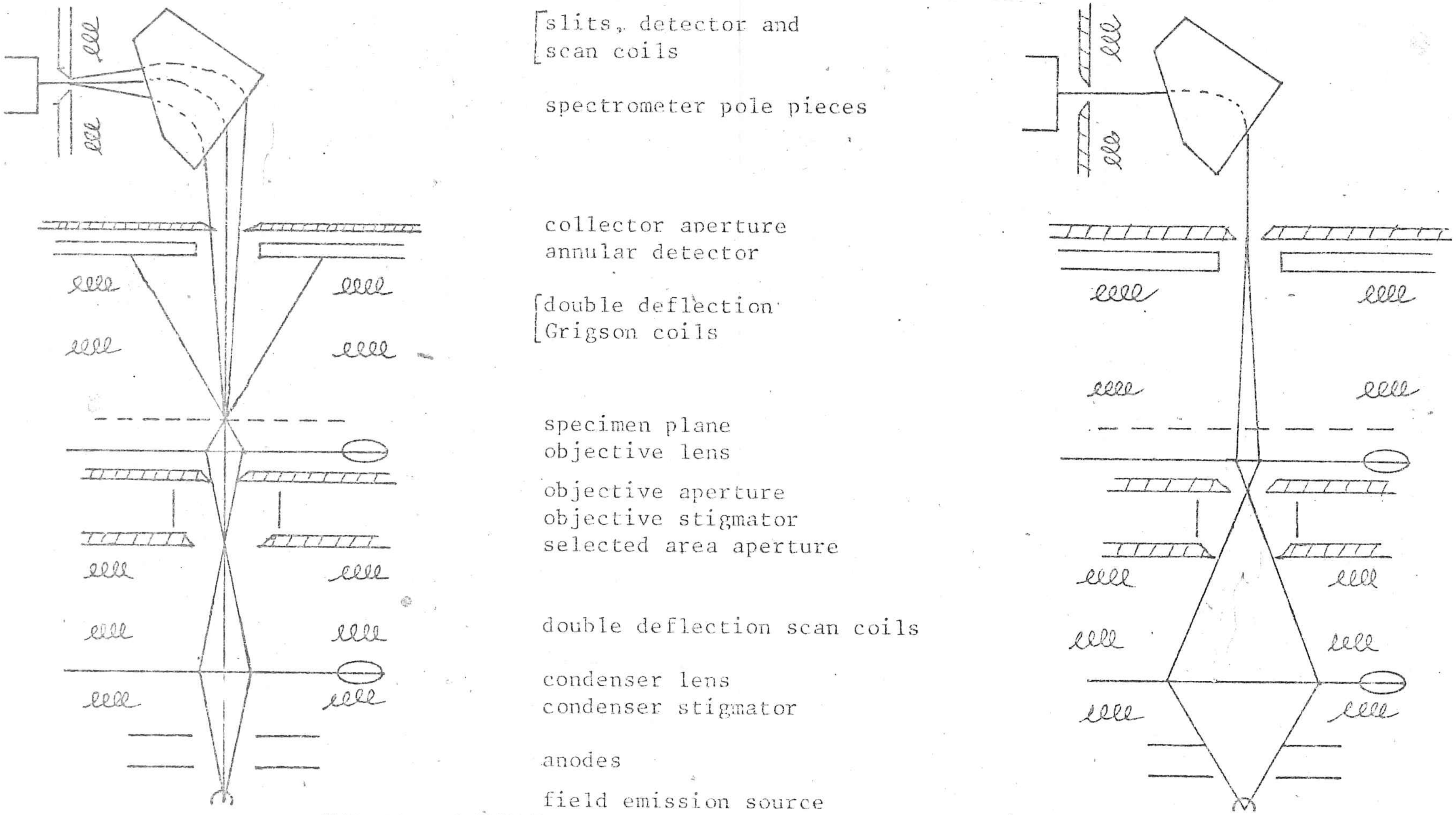

imaging mode

Selected area mode

Figure 1.2: the electron optical ray paths in the imaging and selected area microscope modes.

The spot size (> 5 Å) is determined by the beam convergence angle and the spherical aberration introduced by the objective lens. There are two conflicting desires: in order to reduce spherical aberration, the convergence angle should be made as small as possible; and in order to limit diffraction broadening of the beam, the convergence angle should be made as large as practicable. The reader is referred to Hirsch *et al* (1977) for a mathematical description of these effects.

The position of the beam on the specimen may be scanned in the form of a raster by using a set of coils which scan the position of the spot in the plane of the selected area diffraction aperture. The angle of the beam to the specimen is unchanged by scanning in position. See figure 1.2.

1.3.2 Selected area diffraction mode

The condenser lens current is weakened from the case of image mode so as to form an image of the tip in the plane of the collector aperture at the entrance to the electron spectrometer. This implies that the electron beam at the specimen plane is nearly parallel. The objective lens current is left unaltered, so the selected area diffraction aperture, being conjugate with the specimen plane, defines the portion of the specimen illuminated by the electron beam and therefore the beam convergence angle at the collector aperture. The objective aperture is conjugate to the plane of the collector aperture.

In order to obtain a selected area diffraction pattern electron beam is rocked about a point in the plane of the selected area aperture, and hence rocks in the specimen plane also, by means of the same double-deflection coils used for scanning in position. The collector aperture defines the angular resolution of the diffraction pattern, and the objective aperture defines an angular cut-off. See figure 1.2.

The procedure for the collection of energy-loss spectra differs slightly from the case of the two imaging modes, which is given in section 1.3.4. Energy-loss spectra are collected as follows:

1) The selected-area aperture is adjusted, whilst observing the specimen in image mode, to select the portion of the specimen from which energy-loss data are to be recorded.

2) Selected area diffraction (SAD) mode is selected, which alters the objective lens current to bring the probe into focus on the collector aperture. The apparent angular orientation of the collector aperture may be adjusted electrically (by means of the Grigson coils (see fig 1.2)) or manually to select the desired diffraction conditions for the collection of energy-loss data.

3) The scan generator is then disconnected from the angular scan of the beam about the specimen and is connected to the spectrometer scan coils. The double-deflection coils have no effect on the electron beam, except for a fixed shift which may be controlled from the microscope control panel. Thus an energy-loss spectrum is collected with a nearly-parallel illumination and with a collection angle defined by the size of the collector aperture.

1.3.3 Search mode

Search mode is entered by switching off the objective lens and adjusting the condenser lens to form an image of the tip at the specimen. One stage of demagnification of the image of the tip has thus been omitted, and the consequent tip image size at the specimen is thus much larger than in image mode (i.e. ≃ 200 Å). This defines the spatial resolution. The probe convergence angle is defined by the size of the selected area diffraction aperture.

The advantages of using this technique are twofold:

1) low values of convergence angle are combined with high beam current;

2) the scanning effect of the double-deflection scan coils at the specimen is much greater than in image mode, the observed magnification of the specimen is therefore much lower than in image mode thus enabling the whole of the 3mm specimen to be imaged at once. This facilitates the search for a desired feature (hence the name of the mode).

The disadvantages of search mode are:

1) the spatial resolution is very poor (about 200Å).

2) It is difficult to align the electron optics because the objective aperture may not be imaged in a scan in angle. Stigmation of the condenser lens is especially critical.

3) The electron beam convergence angle is limited, this is also the " collection angle " used in the evaluation of collection efficiency. Thus most of the beam intensity may be scattered outside the collector aperture by inelastic scattering at quite low energy-losses (this is also true for the SAD mode). See fig. 1.4 for a comparison of the three modes of operation.

Figure 1.4

Microscope mode	effective collection semi-angle	spatial resolution	qualitative count-rate
Image mode	high angle (1.5 mR to 8.5 mR)	very good (≃ 5 Å)	poor
Selected-area diffraction	incident beam nearly parallel, (1 μR to 4 μR), therefore defined by collector aperture (0.2 to 2 mR)	very poor defined by SAD aperture. (2μm to 8μm)	very high at low energy-loss (>50 eV). Collection efficiency drops rapidly with energy.
Search mode	0.2 to 2 mR defined by the larger of the probe convergence angle and the collector aperture angle	poor (≃ 300 Å)	very high due to increased beam current. efficiency drops rapidly (as above). **

** The electron optics are very difficult to align to achieve the full potential of the search mode of operation.

1.3.4 Image formation

Having passed through the specimen, the electron beam is deflected in both angle and position by a set of double-deflection coils (Grigson coils, see fig 1.2). The amount of shift in both angle and position is adjusted electrically in order to bring the collector aperture into the desired alignment with respect to the optic axis of the objective lens.

In general, an image is formed on a cathode-ray tube (CRT) by scanning the position of a spot on the CRT in synchronism with a scan of the first set of double-deflection coils which produce either a scan of the angle of the beam at the specimen (SAD mode) or a scan of the position of the electron probe at the specimen (image or search mode) and modulating the intensity of the spot on the CRT by some detected signal. As the data are displayed serially, it is possible to combine two detector outputs in some way (for instance by taking the ratio of two signals (Treacy 1980)) and then to display the processed signal on the CRT. If the scan rates are fast enough, the image displayed sequentially on the CRT may be interpreted visually as an image of the specimen. A camera attached to the CRT may be used to form a permanent record of the image, and this may be formed slowly, if required, which has some advantage when the detected signal is very noisy.

The two most-commonly used detectors are the annular detector and the electron spectrometer. The annular detector is able to detect electrons scattered within the range of angles 8 mR to 50 mRadians away from the optic axis of the collector system. The electron spectrometer focusses electrons which pass through a collector aperture on the optic axis of the collector system onto a pair of slits (see fig 1.3). The image of the collector aperture is dispersed in the spectrometer in a direction normal to the axis of the slits according to electron energy. Electrons which pass through the slits are detected by a scintillator and photomultiplier tube (PMT) assembly. For a more detailed description of these two detectors, see section 3.2.

Other detectors that have been used are:

1) Cathodoluminescense detector consisting of a light-pipe from the specimen to an external photomultiplier tube. (Pennycook 1979)

2) Very-high angle annular detector consisting of an annulus of scintillator material mounted in the specimen cartridge just after the specimen. Electrons which are scattered through large angles strike the scintillator. The light pulses produced are detected as in 1).

3) split detector consisting of two "D"-shaped scintillators mounted on the axis of the detector system, each "D" has a separate PMT. The two signals can be processed to display magnetic domain information directly on the CRT, (Chapman et al 1978)

4) X-ray detector consisting of a lithium-drifted semiconductor behind a thin beryllium window situated near to the specimen and biased so as to produce a pulse of current upon the arrival of an X-ray photon at the detector junction. The magnitude of the pulse can be converted to X-ray energy, and pulses wich fall within a chosen upper and lower energy window may be used to drive the CRT as before. This enables an X-ray energy-filtered image to be formed which can be used to provide an elemental map of the specimen.

1.3.5 The collection of energy-loss data

In order to obtain an energy-loss spectrum in image mode or search mode (the case of SAD mode has been discussed above in section 1.3.2), the specimen is first imaged normally. The point from which it is desired to collect energy-loss data is chosen by adjusting the position of an electronic cursor on the CRT so that it is above the desired point on the specimen. An energy-loss spectrum is then collected from the indicated point by disconnecting the scan generator outputs from the spot deflection coils, and connecting the cursor-controlled offset, so that the beam remains stationary at the chosen point. The scan generator is connected to the spectrometer scan coils, and the output of the spectrometer PMT may be used to drive the Y-axis of an X-Y chart recorder, the X- axis being driven in synchronism with the scan coil of the spectrometer. Alternatively, the spectrometer PMT output may be used to drive the vertical deflection of a CRT to provide a visual display of the energy-loss spectrum. A computer based data-capture system is described in chapter 3.

Although the process of going from an image to the collection of energy-loss data may seem complicated, these processes are realised, in practice, by the pressing of a few buttons which takes only a few seconds.

Chapter 2 - Summary of the theory of energy-loss processes

Chapter 2 - Summary of the theory of Energy-loss processes

Introduction:

The theory of energy-loss spectroscopy has received intense study since the 1950's. As early as 1930 (Rudberg 1930), energy-loss measurements had been made, and Hiller & Baker (1946) suggested the use of electron energy-loss spectroscopy (EELS) as a micro-analytical tool. Most of the early theoretical interest was devoted to the low-loss region of the energy-loss spectrum (i.e. the energy-loss range up to about 100 eV) because many of the problems under investigation could be solved analytically and most of the experimental energy-loss spectra (ELS) were from this region of the spectrum. As the energy-range of experimental data available was extended to higher energies, and with the advent of photo-multiplier tube detection systems, interest turned to the evaluation of atomic scattering cross-sections using fast computers and a good model for the atomic potential.

This chapter contains a summary of the important theoretical results on which the practical application of the energy-loss technique relies. It does not attempt to derive these results with any rigour; the reader is referred to the original papers for a more-complete description of the theory.

The energy-loss spectrum is divided into two regions:
1) the low-loss region (0 to 100 eV loss) in which the energy-loss spectrum is dominated by collective effects and;
2) the core-loss region where the excited electron behaves largely as a single-particle excitation, although the presence of other electrons or atoms has a modifying effect on the single-electron spectrum.

2.1 THE LOW-LOSS REGION

2.1.1 The classical plasma model

Following the method of Pines and Bohm (1952), the energy of interaction between two electrons i, j, interacting solely by means of a coulomb potential is given by:

$$\frac{e^2}{4\pi\varepsilon_0 |x_i - x_j|} = \frac{e^2}{\varepsilon_0} \sum_{K}{}' \frac{e^{i\underline{k}.(\underline{x}_i - x_j)}}{k^2} \qquad - \quad 2.1$$

where the electrons are at positions $\underline{x}_i$ and $\underline{x}_j$ and $\underline{k}$ is the wave-vector (which is the fourier inverse variable complementary to distance $\underline{x}$). The total potential of electron i is the sum of equation 2.1 over all electrons j . The force acting on this electron is the derivative of the total potential with respect to distance $\underline{x}_i$, which gives the acceleration $\ddot{\underline{x}}_i$ by Newton's third law. Thus:

$$\ddot{\underline{x}}_i = -(e^2 . i/\varepsilon_0 m) \sum_{\substack{j \neq i, \\ \underline{K}}} (\underline{K}/K^2) e^{i\underline{k}(\underline{x}_i - x_j)} \qquad - \quad 2.2$$

The gas of electrons may be represented by the electron density, per unit volume

$$\rho(\underline{x}) = \sum_i \delta(\underline{x} - \underline{x}_i) \qquad - \quad 2.3$$

Bohm and Pines introduce the idea of an electron density wave $\rho_{\underline{K}}$ characterised by its wave-vector, $\underline{K}$,

$$\rho_{\underline{k}} = \int d\underline{x} . \rho(\underline{x}) . e^{-i\underline{K}.\underline{x}} = \sum_i e^{-i\underline{k}.\underline{x}_i} \qquad - \quad 2.4$$

which is just the fourier transform of the space density $\rho(x)$.

The Equation of motion (equation 2.2) may be expressed in terms of the density wave, $\rho_{\underline{K}}$:

$$\ddot{\rho}_{\underline{K}} = -\sum_i (\underline{k} . \underline{v}_i)^2 . e^{i\underline{k}.\underline{x}_i} - \sum_{\substack{i,j, \\ \underline{K}' \neq 0}} \left(\frac{e^2}{\varepsilon_0 m K'^2}\right) \underline{K}.\underline{K}' . e^{i(\underline{K} - \underline{K}').\underline{x}_i} . e^{-i\underline{K}'.\underline{x}_j} \qquad - \quad 2.5$$

where: $\underline{v}_i = d\underline{x}_i/dt$

At this point, Bohm and Pines introduce the random-phase approximation (RPA) which assumes that two electron density waves with differing wavevector are not correlated, i.e.:

$$\sum_i e^{(i(\underline{K}' - \underline{k}).\underline{x}_i)} = 0 \quad \text{for } \underline{k}' \neq \underline{K} \qquad - \quad 2.6$$

Equation 2.5 may now be simplified, giving

$$\ddot{\rho}_{\underline{K}} = \sum_i (\underline{K}.\underline{v}_i)^2 . e^{-i\underline{k}.\underline{x}_i} - \frac{e^2 n}{\varepsilon_0 m} \sum_i e^{-i\underline{k}.\underline{x}_i} \qquad - \quad 2.7$$

where: n is the number density of electrons per unit volume, given by the sum over electrons i .

The first term is independent of the coulomb interaction, and arises from a random (thermal) motion of the electrons. This term is second order in k and for k sufficiently small, this term may be ignored.

The second term represents the coulomb interaction, and, provided that the first term may be ignored, results in a simple-harmonic solution of equation 2.7 :

$$\ddot{\rho}_{\underline{k}} = \frac{-e^2 n}{\varepsilon_0 m}\sum_i e^{-i\underline{k}.\underline{x}_i} = \frac{-e^2 n}{\varepsilon_0 m}.\rho_{\underline{k}} \qquad - \quad 2.8$$

The angular frequency of oscillation, ω_p, is given by:

$$\omega_p = \left(\frac{ne^2}{\varepsilon_0 m}\right)^{1/2} \qquad - \quad 2.9$$

For the thermal motion term in equation 2.7 to be less important than the coulomb term requires

$$\frac{ne^2}{\varepsilon_0 m} \gg \langle(\underline{k}.\underline{v}_i)^2\rangle_{av} \qquad - \quad 2.10$$

where $\langle(\underline{k}.\underline{v}_i)^2\rangle_{av}$ is an average over all the electrons, i. An estimate of this average may be obtained by using the Maxwell distribution for the velocity of a gas of particles at a given temperature, T. Thus inequality 2.10 becomes:

$$k^2 \ll k_c^2 = \frac{3n.e^2}{\varepsilon_0 m\langle v_i^2\rangle_{av}} = \frac{ne^2}{\varepsilon_0 K_B T} = \lambda_D^{-2} \qquad - \quad 2.11$$

where K_B is Boltzmann's constant, and λ_D is the Debye wavelength. For a typical metal, at room temperature, $\lambda_D \simeq 0{\cdot}4\,\mathring{A}$. For values of wavevector in excess of k_c, the random term in equation 2.7 dominates the motion of the particles, and the density wave $\rho_{\underline{k}}$ is not harmonic. For very small values of $\underline{k}$, the coulomb interaction dominates equation 2.7, and the $\rho_{\underline{k}}$ are harmonic. In between these two extremes the harmonic solution is coupled into the single-particle solution of $\rho_{\underline{k}}$. Pines & Bohm introduce a new variable:

$$q_{\underline{k}} = \sum_i \frac{1}{\omega^2-(\underline{k}.\underline{v}_i)^2}.\,e^{i\underline{k}.\underline{x}_i} \qquad - \quad 2.12$$

which may be shown to obey the equation of motion

$$\ddot{q}_{\underline{k}} + \omega^2 q_{\underline{k}} = 0 \qquad - \quad 2.13$$

provided that

$$1 = \frac{e^2}{\varepsilon_0 m}.\sum_i(\omega - \underline{k}.\underline{v}_i)^{-2} \qquad - \quad 2.14$$

Thus, a solution of the equation of motion (2.2) can be found that, unlike a simple charge density wave, $\rho_{\underline{k}}$, is exact for non-zero wavevector. It has the disadvantage that it cannot be directly interpreted in terms which can be understood in terms of the original physical model (i.e. the positions of electrons).

Provided that $\underline{k}$ is small enough, equation 2.14 may be re-arranged to give:

$$\omega^2 = \omega_p^2 + k^2\langle v^2\rangle_{av} \qquad 2.13$$

Thus, the motion of a gas of free-electrons may be represented by the $q_{\underline{k}}$ "density waves" with a known dispersion relation for small $\underline{k}$.

Pines and Bohm calculate the energy-loss per unit length travelled of an incident fast electron, moving with velocity $\underline{v}_0$ by evaluating the response of the gas of electrons in terms of the normal modes of oscillation (the $q_{\underline{k}}$) to an electron density perturbation given by $\delta(\underline{x} - \underline{v}t)$. They show that the motion of the is now that of a forced oscillation

$$\ddot{q}_{\underline{k}} + \omega^2 . q_{\underline{k}} = -\omega_p^2 . e^{-i\underline{k}.\underline{v}_0 t} \qquad - \quad 2.14$$

This equation may be solved to obtain the $q_{\underline{k}}$, from which the electron density $\rho(\underline{x})$ and hence the electric field at the position of the incident electron may be determined. Thus, a force, exerted on the incident fast electron, may be calculated:

$$F = \frac{e^2\omega_p^2}{2v_0^2 . 4\pi\varepsilon_0} . \ln\left(1 + \frac{2v_0^2}{\langle v^2\rangle_{av}}\right) \qquad - \quad 2.15$$

Therefore, the energy-loss per unit length is equal to this force:

$$\partial E/\partial z = \frac{\pi . ne^4}{E_0 . (4\pi\varepsilon_0)^2} . \ln\left(1 + \frac{2v_0^2}{\langle v^2\rangle_{av}}\right) \qquad - \quad 2.16$$

where E_0 is the kinetic energy of the incident fast electron. For small values of $\underline{k}$, the normal modes of the system, $q_{\underline{k}}$, approximate to the simple charge density waves, the $\rho_{\underline{k}}$, which may be interpreted as a purely collective excitation. For values of $\underline{k}$ greatly exceeding $\underline{k}_c$, the normal modes $q_{\underline{k}}$ do not correspond to a simple collective oscillation, but correspond to a single particle excitation. For values of wavevector between these two extremes the nature of the perturbation produced by the incident fast electron cannot be described as purely collective or purely single-particle, but as a mixture of the two.

To summarise: Pines & Bohm (1952) show that a purely classical description of the interactions between electrons in a free-electron gas results in a description of the perturbation of the electron gas by a fast electron producing plasma oscillations at low values of wavevector transfer, and single-particle excitations at large values of $\underline{k}$. The frequency of plasma oscillations and the dispersion relation have been described.

2.1.2 The Quantum-mechanical plasma model

In this section, the response of a gas of electrons is defined by its hamiltonian, H , from which the eigenfunctions (wavefunctions) may be derived. These describe the normal modes of the system from which the response to an incident fast electron may be derived.

Following the method of Pines (1956) in his review paper, the hamiltonian, H , is given by:

$$H = \sum_i \frac{p_i^2}{2m} +$$

kinetic energy term - 2.17a

$$\sum_i V(\underline{r}_i) +$$

potential of ion cores - 2.17b

$$\frac{e^2}{2\varepsilon_0} \sum_{\substack{\underline{k},j,\\ i \neq j}} \frac{e^{i\underline{k}(\underline{x}_i - x_j)}}{k^2} +$$

coulomb interaction between electrons and - 2.17c

$$\frac{p_0^2}{2m} +$$

kinetic energy of incident electron - 2.17d

$$\sum_{i,\underline{k}} \frac{e^2}{\varepsilon_0 k^2} \cdot e^{i\underline{k}.(\underline{R}_0 - \underline{x}_i)}$$

- 2.17e.

The last term is the coulomb interation between the incident fast electron and all other electrons, where the sum over i is taken over all electrons in the gas. The last two terms arise from the presence of a fast incident electron, and are collectively referred to as H_{ext} .

The density waves $\rho_{\underline{k}}$ are defined as for the classical gas:

$$\rho_{\underline{k}} = \int d\underline{x}\, \rho(\underline{x}) \cdot e^{-i\underline{k}\cdot\underline{x}} = \sum_i e^{-i\underline{k}\cdot\underline{x}_i} \qquad - \quad 2.18$$

Bohm and Pines (1953) shown that the $\rho_{\underline{k}}$ obey the operator equation of motion

$$\frac{\partial^2 \rho_{\underline{k}}}{\partial t^2} + \omega_p^2 \cdot \rho_{\underline{k}} = \sum_i \left(\frac{\underline{k}\cdot\underline{p}_i}{m} - \frac{\hbar^2 k^2}{2m} \right)^2 \cdot e^{-i\underline{k}\cdot\underline{x}_i} + \frac{e^2}{\varepsilon_0 m} \sum_{k' \neq k} \frac{\underline{k}\cdot\underline{k}'}{(\underline{k}')^2} \cdot \rho_{\underline{k}'-\underline{k}} \cdot \rho_{\underline{k}} \qquad - \quad 2.19$$

For a simple-harmonic solution to exist the terms on the right-hand side of equation 2.19 should be much smaller than those on the left. The first term on the RHS represents the effects of individual electron kinetic energy on the response of the gas. Pines and Bohm obtain an estimate of its value by averaging over electron momenta, giving:

$$\sum_i \left(\frac{\underline{k}\cdot\underline{p}_i}{m} - \frac{\hbar^2 k^2}{2m} \right)^2 \cdot e^{-i(\underline{k}\cdot\underline{x}_i)} \approx \left\{ \frac{k^2 \langle p^2 \rangle_{av}}{m^2} + \frac{\hbar^2 k^4}{4m^2} \right\} \rho_{\underline{k}} \qquad - \quad 2.20$$

This term becomes comparable with the coulomb term $(\omega_p^2 \rho_k)$ for values of $\underline{k}$ such that

$$k^2 \gtrsim k_c^2 \simeq \frac{\omega_p^2}{\langle v^2 \rangle_{av}} \approx \omega_p^2 / V_F^2 \qquad - \quad 2.21$$

where V_F is the fermi velocity.

For values of $\underline{k}$ much smaller than $\underline{k}_c$, the gas responds as a plasma (i.e. a collective excitation). For values of $\underline{k}$ greater than $\underline{k}_c$, single-particle excitations become important. In a typical metal, $\underline{k}_c^{-1}$ is of the order of the inter-electron spacing.

The second term on the RHS of equation 2.19 represents the effects of non-linear interactions between the density fluctuations $\rho_{\underline{k}}$. Bohm and Pines (1953) have examined the behaviour of this term, and provided that $\underline{k} < \underline{k}_c$, this term is always much smaller than the term which preceedes it.

The response of the gas is given by the matrix elements of the operators $\rho_{\underline{k}}$ between different states of the valence electrons. The valence electrons are represented by eigenstates of the non-interacting-electron hamiltonian, H_0 :

$$H_0 = \sum_i \left(\frac{p_i^2}{2m} + V(\underline{x}i)\right) \qquad - \quad 2.22$$

Thus

$$\left[\ddot{\rho}_K + \omega_p^2 \cdot \rho_{\underline{K}}\right]_{no} = -\omega_{no}^2 (\rho_{\underline{K}})_{no} \qquad - \quad 2.23$$

+ non-linear terms

where the wavefunctions of the non-interacting electron gas, $|n\rangle$ and $|o\rangle$, are separated by an energy ω_{no}. As before, in order for the $(\rho_K)_{no}$ to have an harmonic solution, the perturbing term on the RHS of equation 2.23 must be much smaller than the harmonic term on the left-hand side, thus

$$\omega_{no}^2 \ll \omega_p^2 \qquad - \quad 2.24$$

In the same way as in the case of purely classical plasma theory, Bohm and Pines transform from the operator $\rho_{\underline{K}}$ to a new, related, operator $q_{\underline{K}}$ which obtains an harmonic solution of equation 2.23 without restriction on ω_{no}, $q_{\underline{K}}$ being given by:

$$q_{\underline{K}} = \sum_i \frac{\omega_p^2}{\omega^2 - (\underline{K}\cdot\underline{p}i/m - \hbar K^2/2m)^2} \cdot e^{-i\underline{K}\cdot\underline{x}i} \qquad - \quad 2.25$$

Pines & Bohm show that this obeys the operator equation of motion, (equation 2.19) provided that ω and $\underline{K}$ satisfy the dispersion relation:

$$1 = \frac{e^2}{\varepsilon_0 m} \cdot \sum_i \left((\omega - \underline{K}\cdot\underline{p}i/m)^2 - \hbar K^4/4m^2\right)^{-1} \qquad - \quad 2.26$$

In the long-wavelength limit ($k \rightarrow 0$), this simplifies to

$$\omega^2 = \omega_p^2 + k^2 \langle v^2 \rangle_{av} + \hbar^2 K^4/4m^2 \qquad - \quad 2.27$$

For non-vanishing $\underline{K}$, the matrix elements of the operators are given by

$$(q_K)_{no} = \frac{\omega_p^2}{\omega^2 - \omega_{no}^2} \cdot (\rho_K)_{no} \qquad - \quad 2.28$$

The dispersion relation now becomes:

$$1 = \frac{e^2}{\varepsilon_0 \hbar K^2} \cdot \sum_n \frac{2\omega_{no}\,|(\rho_{\underline{K}})|_{no}^2}{\omega^2 - \omega_{no}^2} \qquad - \quad 2.29$$

which may be written in the form

$$\left.\begin{aligned} 1 &= \frac{e^2}{\varepsilon_0 m} \cdot \sum_n \frac{f_{no}}{\omega^2 - \omega_{no}^2} \\ \text{where} \quad f_{no} &= \frac{2m}{\hbar K^2} \cdot \omega_{no} \cdot |(\rho_{\underline{K}})|_{no}^2 \end{aligned}\right\} \qquad - \quad 2.30$$

The f_{no} is called the general oscillator strength, and represents the coupling between two states $|n\rangle$ and $|0\rangle$ introduced by the existence of the density fluctuations, $q_{\underline{K}}$.

To summarise: Pines and Bohm show that the response of an electron gas, interacting by means of a coulomb potential, may be described by the operators $q_{\underline{K}}$, and obtain a dispersion relation between ω and $\underline{K}$ from the matrix elements of these operators with the wave-functions of the non-interacting electron hamiltonian.
The nature of the excitation is purely collective at low values of $\underline{K}$, but cannot be described by a purely collective excitation $\rho_{\underline{K}}$ at large $\underline{K}$, which means that the excitation is partly collective and partly single-particle for these values of $\underline{K}$.

2.1.2.1 Plasmon scattering cross-section

For values of $\underline{K} < \underline{K}_c$, the response of a gas of electrons is mainly collective in nature. It is this cross-section that is sought here. Following the method of Pines (1956) and the previous section, the response of the gas of electrons is given by the operators $q_{\underline{K}}$ (equation 2.25). The long-wavelength interaction between an incident fast electron and the valence electrons, given by a coulomb interaction is

$$\sum_{K<K_c} \frac{e^2}{\varepsilon_0 K^2} \cdot \rho_{\underline{K}} \cdot e^{i\underline{K}\cdot\underline{R}_0} = \sum_{\underline{K}<\underline{K}_c} \cdot\, i\left(\frac{e^2}{\varepsilon_0 K^2}\right)^{1/2} \cdot P_{\underline{K}} \cdot e^{i\underline{K}\cdot\underline{R}_0} \qquad - \quad 2.31$$

where $P_{\underline{K}}$ is the plasmon momentum. The probability , per unit time, that a plasmon is generated, W , may be obtained by an application of first-order perturbation theory, giving

$$W = \frac{d\Omega}{2\pi a_0} \cdot \frac{\omega P_0}{\hbar K^2} \qquad - \quad 2.32$$

where P_0 is the momentum of the incident electron, a_0 is the Bohr radius, and $d\Omega$ is solid angle into which the incident electron is scattered.
The conservation of momentum requires that (see figure 2.1):

$$\hbar^2 \underline{K}^2 = (\Delta P)^2 + P_0^2 . \theta^2 = P_0^2 (\theta^2 + \theta_E^2) \qquad - \quad 2.33$$

where $$\theta_E = \Delta P / P_0 = \hbar\omega / 2E_0 \ll 1 \qquad - \quad 2.34$$

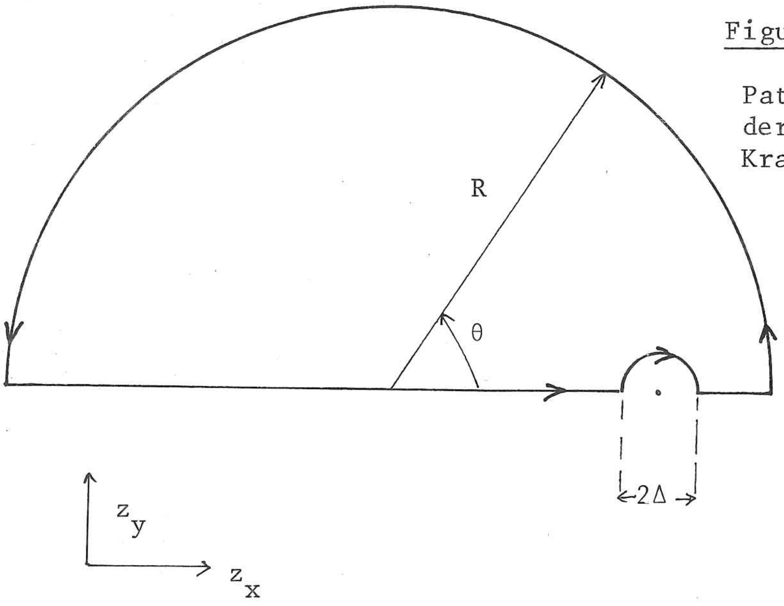

Figure 2.2:

Path Γ used in the derivation of the Kramers-Kronig transform

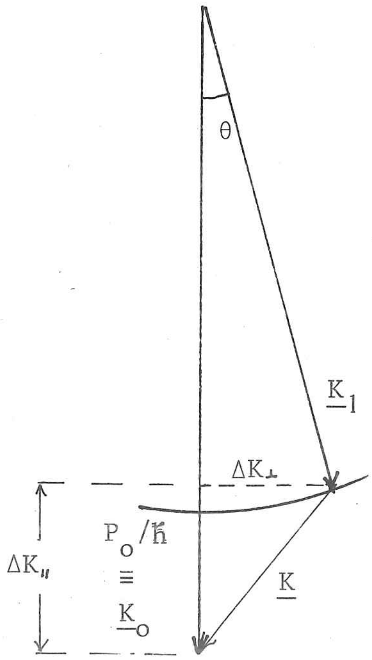

Figure 2.1:

for small $\Delta E/E_o$,

$K^2 \propto E$, therefore

$$\frac{\Delta K_{min}}{K} = \frac{1}{2} \cdot \frac{\Delta E}{E_o} = \theta_E .$$

Therefore:

$$\Delta K_{min} = K . \theta_E .,$$

$$K^2 = \Delta K_\parallel^2 + \Delta K_\perp^2$$
$$= K_o^2 . \theta_E^2 + K_o^2 . \theta^2$$

(for small θ).

Therefore:

$$\hbar^2 . K^2 = P_o^2 . (\theta_E^2 + \theta^2)$$

The scattering cross-section for plasmon generation, per unit solid angle, is given by:

$$\frac{\partial\sigma(\theta)}{\partial\Omega} = \frac{1}{2\pi a_0}\cdot\frac{\theta_E}{\theta^2 + \theta_E^2} \qquad - \qquad 2.35$$

Integration of equation 2.35 over solid angle Ω yields a value for the inelastic scattering cross-section, per unit volume:

$$\sigma = \frac{\theta_E}{a_0}\cdot \ln\left(\theta_c/\theta_E\right) \qquad \text{for } \theta_c \gg \theta_E \qquad - \qquad 2.36$$

where $\theta_c = (\hbar\omega/E_0)^{1/2}$ is the angle corresponding to $\underline{k}_c$. Equation 2.35 includes only interactions between the incident electron and plasmon excitations for $\underline{k} < \underline{k}_c$. When $\underline{k}$ becomes large, the non-linear terms in equation 2.19 require that the interaction between the incident electron and single-particle excitations be treated separately. For further discussion of this point, the reader is referred to Nozieres & Pines (1958a,b,c, 1959).

2.1.3 The dielectric function of a plasma

2.1.3.1 The classical plasma

For the purposes of ELS, it is often convenient to consider the specimen to be homogenous and to express the effect of the specimen on an incident electron in terms of a dielectric function, ε, which describes the response of the specimen as a function of wavevector and frequency, but independent of position. It is shown, later, how this enables the direct comparison of energy-loss results with those obtained by other techniques (e.g. optical measurements of reflectivity).

Following the method of Ritchie (1957), the electric potential, ϕ, due to a point charge, $-e$, at position $\underline{R}$, moving with uniform volocity $\underline{v}$ in an infinite homogenous plasma is written:

$$\varepsilon_0\, \varepsilon_r(\underline{k},\omega)\,.\,\nabla^2\phi(\underline{r},t) = e\,\delta(\underline{r} - \underline{v}t) \qquad - \qquad 2.37$$

which defines $\varepsilon_r(\underline{k},\omega)$, the relative dielectric function. The fourier transform of equation 2.37 gives:

$$\phi(\underline{k},\omega) = \frac{-2\pi e}{\varepsilon_0.\varepsilon_r(\underline{k},\omega)}\cdot\frac{\delta(\underline{k}\cdot\underline{v} + \omega)}{k^2} \qquad - \qquad 2.38$$

where $\phi(\underline{k},\omega)$ is the fourier transform of $\phi(\underline{r},t)$ given by:

$$\phi(\underline{r},t) = (2\pi)^{-4}\int d\underline{k}\int d\omega .\ \exp(i(\underline{k}\cdot\underline{r}+\omega t)).\ \phi(\underline{k},\omega) \qquad - \quad 2.39$$

The energy-loss, per unit path length, in the medium is:

$$W = e.E_x\Big|_{\underline{r}=\underline{v}t} = \left(\frac{e}{v}\right).\underline{v}.\underline{E}\Big|_{\underline{r}=\underline{v}t} \qquad - \quad 2.40$$

where $\underline{E} = -\nabla_r\phi$ and E_x is the electric field in the direction of $\underline{v}$. The probability of exciting a plasmon, per unit path length is given by:

$$P(\underline{k},\omega) = \frac{1}{\hbar\omega}.\ W(\underline{k},\omega) \qquad - \quad 2.41$$

The application of equations 2.37 and 2.39 to 2.41 gives

$$P(\underline{k},\omega) = \frac{e^2}{4\pi^3.\varepsilon_0\hbar v}.\mathrm{Im}\left(\frac{-1}{\varepsilon_r}\right).\frac{\delta(\underline{k}.\underline{v}+\omega)}{k^2} \qquad - \quad 2.42$$

The energy-loss per unit path length, integrated over wave-vector and frequency, W_{TOTAL} is given by:

$$W_{TOTAL} = \frac{e^2}{4\pi^3.\varepsilon_0 v^2}\int d\underline{k}_\perp\int d\underline{k}_\parallel\int_0^\infty \omega.d\omega.\ \mathrm{Im}\left(\frac{-1}{\varepsilon_r}\right).\frac{\delta(\underline{k}.\underline{v}+\omega)}{k^2} \qquad - \quad 2.43$$

where the integral over wavevector has been separated into integrals over $\underline{k}_\perp$ perpendicular to $\underline{v}$ $(\underline{k}_\perp)$ and k parallel to $\underline{v}$ $(\underline{k}_\parallel)$. Performing the integral over $\underline{k}_\parallel$ gives:

$$W_{TOTAL} = \frac{e^2}{4\pi^3.\varepsilon_0 v^2}\int dk_\perp\int_0^\infty \omega d\omega\ \mathrm{Im}(-1/\varepsilon_r)\cdot\frac{1}{k_\perp^2+\omega^2/v^2} \qquad - \quad 2.44$$

The energy-loss per unit path length may also be expressed in terms of the differential scattering cross-section per unit volume,

$$W_{TOTAL} = \int d\Omega\int E.dE.\ \frac{\partial^2\sigma}{\partial E\partial\Omega} \qquad - \quad 2.45$$

Transforming from ω to E and from $\underline{k}_\perp$ to θ in equation 2.47 gives:

$$\begin{aligned} W_{TOTAL} &= \frac{e^2}{4\pi^3.\varepsilon_0 v^2}.\int 2\pi\theta.d\theta\left(\frac{p}{\hbar}\right)^2.\int_0^\infty\frac{E.dE}{\hbar^2}.\mathrm{Im}(-1/\varepsilon).\frac{\hbar^2/p^2}{\frac{\hbar^2 k_\perp^2}{p^2}+\theta_E^2} \qquad - \quad 2.46 \\ &= \frac{e^2}{4\pi^3.\varepsilon_0 v^2}\int d\Omega\int E.dE.\ \mathrm{Im}(-1/\varepsilon)\cdot\frac{1}{\theta^2+\theta_E^2} \end{aligned}$$

Equating the integrands of equations 2.45 and 2.46 gives an expression for the scattering cross-section as a function of the dielectric response:

$$\begin{aligned}\frac{\partial^2\sigma}{\partial E\partial\Omega} &= \frac{e^2}{4\pi^3.\varepsilon_0 v^2}\cdot \mathrm{Im}\left(-1/\varepsilon\right)\cdot\frac{1}{\theta^2+\theta_E^2} \\ &= \frac{1}{2\pi^2 a_0\cdot E_0}\cdot \mathrm{Im}\left(-1/\varepsilon\right)\cdot\frac{1}{\theta^2+\theta_E^2}\end{aligned} \qquad - \quad 2.47$$

where a_0 is the bohr radius, given by:

$$a_0 = 4\pi\varepsilon_0\hbar^2/me^2 \qquad (= 0.529\ \mathring{A}) \qquad - \quad 2.48$$

Therefore, given the dielectric response of a homogenous medium, it is possible to evaluate the inelastic scattering cross-section as a function of energy-loss and scattering angle.

2.1.3.2 The quantum-mechanical dielectric function and oscillator strength

This section summarises the work of Nozieres & Pines (1959) which obtains the dielectric function $\varepsilon_r(\underline{k},\omega)$ in the context of their quantum-mechanical description of an electron gas.

A test charge, of density

$$e.\ r_{\underline{k}}\ .\ e^{i(\underline{k}\cdot\underline{r}\ -\ \Omega t)} \qquad - \quad 2.49$$

is introduced, where $r_{\underline{k}}$ are the fourier components of the charge density $r(\underline{x})$.

The interactions introduced by this term are represented by adding the term

$$H_1 = \frac{e^2}{\varepsilon_0 k^2}\cdot\rho_{-\underline{k}}\cdot r_{\underline{k}}\cdot e^{-i\Omega t}.e^{\eta t} \qquad - \quad 2.50$$

to the system hamiltonian (equation 2.17), this term being the coulomb interaction between the test charge and the density fluctuations $\rho_{\underline{k}}$ defined by equation 2.18. The presence of η ensures that the interaction can be turned on adiabatically.

The dielectric constant is defined by analogy to Maxwell's equations:

$$\underline{\nabla}.\underline{D} = \rho_{free} \qquad - \quad 2.51$$

$$\varepsilon_0.\underline{\nabla}.\underline{E} = \text{(relaxed charge density)} \qquad - \quad 2.52$$

where $\underline{D} = \varepsilon_0.\varepsilon_r.\underline{E}$.

Therefore, taking the fourier transform of equation 2.51 gives

$$\varepsilon_0 . ik . \varepsilon(\underline{k},\Omega) . E_{\underline{k}} = e r_{\underline{k}} . e^{-i\Omega t} \qquad - \qquad 2.53$$

and equation 2.52 gives:

$$\varepsilon_0 . ik E_{\underline{k}} = e\left[r_{\underline{k}} . e^{-i\Omega t} + \langle \rho_{\underline{k}} \rangle \right] \qquad - \qquad 2.54$$

where $\langle \rho_k \rangle$ is the response of the gas of electrons to the perturbing test charge. This is evaluated using first-order perturbation theory. Equations 2.53 and 2.54 give that:

$$\frac{1}{\varepsilon_r(\underline{k},\Omega)} = 1 + \frac{\langle \rho_k \rangle}{r_{\underline{k}} . e^{-i\Omega t}} \qquad - \qquad 2.55$$

which becomes Nozieres & Pines's definition of the dielectric function ε_r . A straight-forward application of perturbation theory yields the result

$$\frac{1}{\varepsilon_r} = 1 - \frac{e^2}{\varepsilon_0 \hbar k^2} \sum_n |(\rho_k)_{no}|^2 \left\{ (\omega_{no} - \Omega - i\eta)^{-1} + (\omega_{no} + \Omega + i\eta)^{-1} \right\} \qquad - \qquad 2.56$$

where the sum is taken over all excited states in the electron gas. Therefore, as $\eta \rightarrow 0$, the energy-loss function $Im(-1/\varepsilon)$ may be evaluated:

$$Im(-1/\varepsilon_r) = \frac{e^2}{\varepsilon_0 \hbar k^2} \sum_n |(\rho_k)_{no}|^2 \left\{ \delta(\omega_{no} - \Omega) - \delta(\omega_{no} + \Omega) \right\} \qquad - \qquad 2.57$$

Nozieres & Pines re-introduce the oscillator strength, $f_{on}(k,\Omega)$, already defined in equation 2.30:

$$f_{on} = \frac{2m}{\hbar k^2} . \omega_{no} . |(\rho_k)|^2_{on} \qquad - \qquad (2.30)$$

The energy-loss function may now be written as:

$$Im(-1/\varepsilon) = \frac{e^2}{2\varepsilon_0 m} . \sum_n \frac{f_{on}}{\omega_{on}} . \left\{ \delta(\omega_{no} - \Omega) + \delta(\omega_{no} + \Omega) \right\} \qquad - \qquad 2.58$$

The dielectric function, as $\eta \rightarrow 0$, may be written (Pines 1956)

$$\varepsilon_r(\underline{k},\omega) = 1 - \frac{e^2}{\varepsilon_0 m} . \sum_n \frac{f_{on}}{\omega^2 - \omega_{on}^2} \qquad - \qquad 2.59$$

The existence of undamped plasmons requires that an oscillating electric field be sustained without any driving perturbation.

Therefore $\underline{\nabla} . \underline{D}$ = driving charge fluctuation = 0 - 2.60

and $\underline{E} \neq 0$ for plasmons to exist - 2.61

These two conditions require that $\varepsilon_r(\underline{k},\omega) = 0$.

This result, together with equation 2.59 gives a dispersion relation between ω and $\underline{k}$ which must be satisfied if a self-sustaining plasmon is to exist.

$$1 = \frac{e^2}{\varepsilon_0 m} \cdot \sum_n \cdot \frac{f_{on}}{\omega^2 - \omega_{on}^2} \qquad - \qquad 2.62$$

So far, the test charge has only been considered to interact with a free-electron gas. In a real metal, the loosely-bound valence electrons and the unbound conduction electrons both contribute to the plasma gas. The deeper-lying core-electrons are not able to contribute to a plasma excitation, but do relax in the presence of the oscillating electric field of a plasmon, tending to depolarise the plasmon excitation. This may be represented by introducing a core-polarisability, α, given by

$$\alpha = \frac{-e^2}{4\pi\varepsilon_0 m} \cdot \sum_i \frac{f_i}{\omega^2 - \omega_i^2} \qquad - \qquad 2.63$$

where f_i is the oscillator strength between core state i and all unfilled (conduction) states, ω_i is the frequency of the core-state to fermi-level transition, and the sum is taken over all core states.

The modified expression for ε becomes

$$\varepsilon(\omega) = 1 - \frac{e^2}{\varepsilon_0 m} \sum_n \frac{f_{on}}{\omega^2 - \omega_{on}^2} - \frac{e^2}{\varepsilon_0 m} \sum_i \frac{f_i}{\omega^2 - \omega_i^2} \qquad - \qquad 2.64$$

Raether (1965) shows how the effect of an extra oscillator (bound state) on the dielectric constant may be represented by the addition of $\delta\varepsilon_1^b(\omega)$, the contribution to the real part of ε due to the bound state, giving

$$\varepsilon_1(\omega) = 1 - \frac{\omega_p^2}{\omega^2} - \delta\varepsilon_1^b(\omega) = \varepsilon_1(\omega)_{plas} - \delta\varepsilon_1^b(\omega) \qquad - \qquad 2.65$$

where $\omega_p = (ne^2/\varepsilon_0 m)^{1/2}$ is the free-electron plasma frequency (a result of the f-sum rule, see Fano & Cooper 1968, Raether 1965). The condition for plasma resonance, $\varepsilon_1(\omega) = 0$ is now modified to:

$$\delta\varepsilon_1^b(\omega) = \varepsilon_1(\omega)_{plas} \qquad 2.66$$

The resonance is now at the frequency given by the intersection of the two curves $\delta\varepsilon_1^b(\omega)$ and $\varepsilon_1(\omega)_{plas}$ (see Raether 1965). Therefore, in the case of an oscillator with $\omega_i < \omega_p$ (an interband transition), the modified plasma frequency will be raised. The converse is true for a core-loss oscillator ($\omega_i > \omega_p$). Although there is no rigid delineation between an inter-band and a core-loss transition, it is helpful, in practise, to use this partition. The reader is referred to papers by Raether (1965) and Daniels <u>et al</u> (1970) for more detail of the effects of core polarisability, and chapter 6 for the case of an oscillator of frequency just below the plasmon frequency. In the latter case, a slightly-different formalism is employed (the twoband model, see section 6.7).

2.1.3.3 Plasmon lifetime, broadening and peak position shift

Up to this point, plasma excitations have been considered to be undamped. The effect of this on the energy-loss function is to produce poles at the frequencies corresponding to the excitation of the normal modes of the free-electron gas (the ω_{10} of equation 2.58).

At non-zero wavevector the normal modes of an electron gas are not purely free-electron-like. This has been recognised by replacing the collective electron-density fluctuations $\rho_{\underline{K}}$ by $q_{\underline{K}}$, which are no longer purely collections (sections 2.1.1 and 2.1.2). This implies that a collective oscillation is coupled to a single-particle excitation and may therefore decay into a single-particle excitation. Nozieres & Pines (1958a,b,c, 1959) calculate the probability of such an excitation, exciting an electron from the fermi level, and calculate the probability that a plasmon, with wavevector $\underline{K}$ will decay per unit time, $W_{\underline{K}}$,

$$W_{\underline{K}} = \frac{1}{2}\pi\omega_p^2 \cdot \frac{1}{N} \cdot \sum_n f_{on}(\underline{K},\omega) . \delta(\omega - w_{on}) \qquad - \quad 2.67$$

where the sum is taken over all excited states of the electron gas. The lifetime of the plasmon is therefore:

$$\tau_c = 1/W_{\underline{K}} \qquad - \quad 2.68$$

A finite lifetime modifies the expression for the dielectric function (Raether 1965) and replaces the poles in $1/\varepsilon_r$ by peaks. The modified dielectric function is:

$$\varepsilon_r(\omega) = 1 - \frac{\omega_p^2}{\omega^2} \cdot \frac{1}{1 - 1/i\omega\tau_c} \qquad - \quad 2.69$$

Therefore

$$\varepsilon_1 = 1 - \frac{\omega_p^2}{\omega^2} \cdot \frac{1}{1 + 1/\omega^2\tau_c^2} \qquad - \quad 2.70a$$

and

$$\varepsilon_2 = \frac{1}{\omega\tau_c} \cdot \frac{\omega_p^2}{\omega^2} \cdot \frac{1}{1 + 1/\omega^2\tau_c^2} \qquad - \quad 2.70b$$

It can be shown, from equation 2.69, that the width (FWHM) of a plasmon in the energy-loss function ($Im(-1/\varepsilon_r)$) is given by $1/\tau_c$. Similarly, the position of the plasmon frequency defined by $\varepsilon_1(\omega) = 0$ is modified to

$$\Omega_{\varepsilon 1}^2 = (\omega_p^2 - 1/\tau^2)^{1/2} \qquad - \quad 2.71$$

The position of the plasmon peak in the energy-loss spectrum defined as the maximum of $Im(-1/\varepsilon)$ is given by

$$\Omega_{els}^2 = (2\omega_p^2 - 1/\tau^2).\left[1 + \left(1 + \frac{12\omega_p^4}{2\omega_p^2 - 1/\tau^2}\right)^{1/2}\right] \qquad - \quad 2.72$$

In the case of a typical plasmon peak, $\hbar\omega_p$ = 20 eV, and $\hbar/\tau_c$ = 10 eV. Application of equations 2.71 and 2.72 gives

$\hbar\Omega_{\varepsilon 1}$ = 17.3 eV

$\hbar\Omega_{els}$ = 19.3 eV.

Thus damping has a significant effect on the position of the zero of $\varepsilon_1(\omega)$, but has a much-smaller effect on the position of the plasmon peak observed in the energy-loss spectrum.

2.1.3.4 Surface effects and surface plasmon excitation

The existence of a surface has two effects on the energy-loss process. Firstly, plasmon volume excitations have been assumed to be excited from an infinite electron gas. The surface acts so as to depolarise volume plasmons. This effect is discussed by Ritchie (1957) and is not considered further.

The second effect is that a solution of Maxwell's equations exists for the case of an excitation which decays exponentially with penetration depth, and satisfies the boundary condition $\underline{\nabla} . \underline{D} = 0$ at the surface.
More generally, a surface plasmon may be excited at any surface which separates volumes with differing dielectric functions.

Given a boundary at $z = 0$ between two homogenous media with dielectric functions $\varepsilon^{(1)}$ and $\varepsilon^{(2)}$, the charge density wave given by

$$\rho_0 \exp(i(K_x.x + K_y.Y) - i\omega_s t).\delta(z)$$

satisfies the boundary condition $\underline{\nabla}.\underline{D} = 0$, provided that (Ræther 1965)

$$\varepsilon^{(1)} = -\varepsilon^{(2)} \qquad - \quad 2.73$$

If the medium (2) has dielectric function ε_r, then

$$\omega_s = \omega_p^{(1)} / (1 + \varepsilon_r(\omega_s))^{1/2} \qquad - \quad 2.74$$

alternatively, if both media are free-electron plasmas

$$\omega_s = \left[\frac{1}{2}\left((\omega_p^{(1)})^2 + (\omega_p^{(2)})^2\right)\right]^{1/2} \qquad - \quad 2.75$$

If the specimen is very thin, then the two surface plasmons may couple, and the frequency of the surface plasmon becomes split in two:

$$\omega_s^{\pm} = \frac{\omega_p}{\sqrt{2}} \cdot \sqrt{1 \pm e^{-KD}} \qquad - \quad 2.76$$

in the case of both boundaries between a specimen and vacuum, where D is the thickness of the foil. This effect should not be important in foils > 10 Å thick under normal experimental circumstances.

These results ignore the finite velociy of propagation of the electric field. A corrected treatment is given by Ritchie (1957).

The differential probability for the excitation of a surface plasmon on a semi-infinite medium is given by (Stern & Ferrell 1960)

$$\frac{\partial P}{\partial \Omega} = \frac{1}{4\pi\varepsilon_0} \cdot \frac{e^2}{\pi\hbar v_0} \cdot \frac{2}{1+\varepsilon_r} \, \frac{\theta . \theta_E}{(\theta^2 + \theta_E^2)^2} \cdot f \qquad - \quad 2.77$$

where f is a geometric factor (≃ 1). The integration of equation 2.77 over all scattering angles gives:

$$P = \frac{1}{4\pi\varepsilon_0} \cdot \frac{1}{1+\varepsilon_r} \cdot \frac{\pi e^2}{\hbar v_0} \qquad - \quad 2.78$$

2.1.3.5 Kramers-Kronig analysis

Kramers-Kronig analysis is a powerful technique that enables the real part of an analytic function to be calculated, given the imaginary part of that function, and vice versa. Electron energy-loss spectroscopy enables the determination of $Im(-1/\varepsilon)$ to be made, and by the use of Kramers-Kronig analysis (KKA), $Re(-1/\varepsilon)$ and thence $Re(\varepsilon)$ and $Im(\varepsilon)$ may be calculated.

Suppose that a function $\eta(\zeta)$ is analytic in the upper half of the complex plane Ⓩ, then the contour integral around path Γ (see figure 2.2), which does not include any poles, is zero (Cauchey's theorum - Riley (1974)). The contour integral is given by:

$$I_0 = \int_\Gamma \frac{\eta(\zeta).d\zeta}{\zeta-\omega} = 0 \qquad - \quad 2.79$$

The only pole on the complex plane is at $\zeta = \omega$, provided that η is analytic. The integral is divided into three parts:

$$I_1 = \int_0^{-\pi} \frac{\eta . Re^{i\theta}.id\theta}{Re^{i\theta}}$$ taken over the outer semi-circle - 2.80

$$I_2 = P\int_{-\infty}^{\infty} \frac{\eta\, d\Omega}{\Omega-\omega}$$ where $P \equiv$ Cauchey principle part (= limit as $r \rightarrow 0$ of integral from $-\infty$ to $(\omega - r)$ - +integral from $\omega + r$ to ∞) 2.81

$$I_3 = \int_{-\pi}^{0} \frac{\eta . i.\Delta e^{i\theta}.d\theta}{\Delta e^{i\theta}}$$ taken over the small semi-circle - 2.82

The technique of KKA requires that the analytic function, η, to be transformed tends to zero at large R, i.e. $\eta(\zeta) \rightarrow 0$ as $|\zeta| \rightarrow 0$
In this case, $I_1 \rightarrow 0$.
The total integral $I_0 = I_1 + I_2 + I_3 = 0$ gives that

$$P\int_{-\infty}^{\infty} \frac{\eta(\Omega).d\Omega}{\Omega-\omega} = -i\pi\eta(\omega) \qquad - \quad 2.83$$

Taking the imaginary part gives:

$$Re(\eta(\omega)) = \frac{1}{\pi} P\int_{-\infty}^{\infty} \frac{Im(\eta(\Omega))d\Omega}{\Omega-\omega} \qquad - \quad 2.84$$

Two points should be noted:

1) the function $\eta(\zeta)$ must tend to zero at large $|\zeta|$;

2) $\eta(\omega)$ must be specified for ω in the range $-\infty$ to ∞.

The modulus of $\varepsilon(\omega)$ tends to 1 at large ω, so a change of origin is required, and the transform of $\eta(\omega) = (1/\varepsilon(\omega) - 1)$

is taken. To evaluate $1/\varepsilon(\omega)$ at negative frequencies, one uses $\varepsilon(\omega) = \varepsilon^*(-\omega)$. With these two substitutions, equation 2.84 becomes:

$$Re\left(1/\varepsilon(\omega)\right) = 1 - \frac{2}{\pi} P\int_0^\infty \frac{Im\left(-1/\varepsilon(\Omega)\right).\Omega.d\Omega}{\Omega^2 - \omega^2} \quad - \quad 2.85$$

which is the form used in the chapter on numerical techniques (section 3.3.4) .

2.2 THE HIGH ENERGY-LOSS REGION

The energy-loss spectrum is considered to be split into two energy regions: the low-loss region and the high-loss (core-loss or edge) region. This is not an arbitrary partition because the detail of independent electron excitations in the low-loss region is considerably modified by the presence of the plasma formed by conduction electrons and loosely-bound valence electrons. The plasma gas can relax at the frequency of a low-loss excitation ($\omega \leqslant \omega_p$) producing a significant electrostatic screening effect (Pines 1956). For a single-particle excitation with frequency much higher than the plasmon frequency, there is little relaxation of the valence/ conduction electrons, and the edges are largely independent of any plasma effects. This does not hold true in the case of multiple-scattering after an edge, see section 3.3.3.2.
A convenient division between the two partitions is at 100 eV.

2.2.1 Classical cross-section calculations

Gryzinski (1965) has calculated the classical inelastic scattering cross-section of a fast electron incident upon a system of orbital electrons in motion. The orbital kinetic energy and the probability of finding an electron at a given radial distance are given by simple quantum theory. The interaction between the incident electron and the orbital electrons is considered to be purely two-body, this is the classical nature of the approximation employed.

It is the existence of orbital kinetic energy that enables the incident electron to be scattered at angles other than the classical "hard spheres" scattering angle

$$\theta_c = (\Delta E/E_0)^{1/2} \qquad - \quad 2.86$$

where ΔE is the energy lost by the incident electron and
E_0 is its initial kinetic energy.

The result of Gryzinski for the total cross-section is

$$\sigma_{nl} \cdot E_{nl}^2 = (6.51 \times 10^{-18}) . z_{nl} \cdot g(U_{nl}) \quad m^2 (eV)^2 \qquad - \quad 2.87$$

where: $g(u) = 1/u \cdot (u-1)^{1.5} \cdot (u+1)^{-1.5} \cdot \left(1 + \frac{2}{3}\left(1 - \frac{1}{2u}\right) \cdot \ln\left(2.7 + (u-1)^{0.5}\right)\right)$

$U_{nl} = E_0/E_{nl}$

z_{nl} is the number of electrons in state nl labelled by radial quantum number n and angular-momentum quantum number l ;

E_{nl} is the depth of state nl below the Fermi level (in eV).

Powell (1976) has compared this expression against other quantum-mechanical and classical expressions and experimental results. The various formulae tend to differ in detail near threshold ($U = 1$), but he finds good agreement in the region of large u ($U > 10$), which is precisely the region that is relevent in the study of energy-loss spectroscopy.

The Gryzinski formula has the great advantage over other expressions of having no free parameters. In the other formulae examined by Powell, discretion needs to be exercised in the choice of suitable parameters.

2.2.2 The Born approximation and the Bethe cross-section

The Gryzinski method is successful in obtaining the integrated cross-section. In order to obtain a differential cross-section as a function of energy and solid angle, a quantum-mechanical description of the inelastic scattering process is required.

Following the method of Inokuti (1971): a fast electron with velocity $\underline{v}$ is incident on a stationary atom, of atomic number z in the groundstate $|0\rangle$, which is then excited to state $|n\rangle$ of energy E_n measured with respect to the groundstate. The incident electron is inelastically scattered into solid angle element $d\Omega$.

The differential form of the scattering cross-section is given by perturbation theory (first order perturbation is the Born approximation):

$$d\sigma_n = (2\pi)^{-2} . M^2 . \hbar^{-4} . (k'/k) \quad \times \qquad - \quad 2.88$$

$$\left| \int e^{i\underline{K}.\underline{r}} u_n^*(\underline{r}_1, \underline{r}_2, \ldots \underline{r}_Z) . V . u_0(\underline{r}_1, \underline{r}_2, \ldots \underline{r}_Z) \right|^2 . d\Omega$$

where $M = m . M_0/(M_0 + m)$ is the reduced electronic mass and V is the interaction potential. The u 's are the eigenfunctions of the atomic electrons expressed in terms of the coordinates of the atomic electrons. $\hbar\underline{k}$ is the momentum of the incident electron before collision and $\hbar\underline{k}'$ is its momentum after collision. $\hbar\underline{K}$ is the momentum transfer.

The interaction between the incident electron and the atom is coulombic. Thus

$$V = \sum_{j=1}^{Z} \frac{e^2}{4\pi\varepsilon_0 |\underline{r} - \underline{r}_j|} + \frac{Z_{nuclear} . e^2}{4\pi\varepsilon_0 . r} \qquad - \quad 2.89$$

where $\underline{r}$ is the position of the incident electron measured with respect to the position of the nucleus. Performing the integration of equation 2.88 over $\underline{r}$ using the result

$$\int |\underline{r} - \underline{r}_j|^{-1} . \exp(i\underline{K}.\underline{r}) \, d\underline{r} = 4\pi K^{-2} . \exp(i\underline{K}.\underline{r}_j) \qquad - \quad 2.90$$

gives

$$d\sigma_n = 4\left(\frac{Me^2}{4\pi\varepsilon_0\hbar^2}\right)^2 . (k'/k) . K^{-4} . |\mathcal{E}_n(\underline{K})|^2 . d\Omega \qquad - \quad 2.91$$

where $\mathcal{E}_n(\underline{K})$ is the atomic matrix element:

$$\mathcal{E}_n(\underline{K}) = \langle n | \sum_{j=1}^{Z} e^{i\underline{K}.\underline{r}_j} | 0 \rangle \qquad - \quad 2.92$$

Note that the nuclear potential cannot contribute to $\mathcal{E}_n$ because states $|n\rangle$ and $|0\rangle$ are orthogonal.

The matrix element is usually considered to be independent of the azimuthal scattering angle, ϕ : this is equivalent to writing $\mathcal{E}_n$ as a function of the scalar variable K . The integration over ϕ is then implied.

$d\sigma_n$ may be written:

$$d\sigma_n = \frac{2\pi e^4}{(4\pi\varepsilon_0)^2} \cdot (Mv^2)^{-1} \cdot Q^{-1} \cdot |\mathcal{E}_n(K)|^2 \cdot d(\ln(Q)) \qquad - \quad 2.93$$

where $Q = \hbar K^2/2m$.

The oscillator strength is defined as:

$$f_n(K) = \left(\frac{E_n}{Q}\right) \cdot |\mathcal{E}_n(K)|^2 \qquad - \quad 2.94$$

Note that this is equivalent to the definition used in connection with plasmon excitation (equation 2.30). The oscillator strength may be written:

$$f_n(K) = (E_n/R) . (Ka_0)^{-2} . |\mathcal{E}_n(K)|^2 \qquad - \quad 2.95$$

where $R = Me^4/2\hbar^2 . (4\pi\varepsilon_0)^2$ = 13.6 eV (the Rydberg), and
$a_0 = (4\pi\varepsilon_0).\hbar^2/me^2$ = 0.529 Å (the Bohr radius).

The kinetic energy of the incident electron is given by:
$T = \frac{1}{2} Mv^2$ which enables the scattering cross-section to be written:

$$d\sigma_n = \frac{4\pi a_0^2}{T/R} \cdot \frac{f_n(K)}{E_n/R} . d[\ln(Ka_0)^2] \qquad - \quad 2.96$$

Conservation of energy requires that

$$(\hbar k)^2 = (\hbar k')^2 + 2ME_n \qquad - \quad 2.97$$

Note that the oscillator strength $f_n(K)$ depends only on the atom and not on the incident particle.

In the case of excitation to a continuum of states (as is normal in the energy-loss spectrum above a core-loss edge), the discrete oscillator strength $f_n(K)$ is replaced by a density of oscillator strength per unit energy:

$$\partial f(K,E)/\partial E = \left(\frac{E}{R}\right) . (Ka_0)^{-2} \sum_{\Omega} |\mathcal{E}_{E\Omega}(K)|^2 \qquad - \quad 2.98$$

where $$\mathcal{E}_{E\Omega}(K) = \langle E, \Omega | \sum_j e^{i\underline{K}\cdot\underline{r_j}} | 0 \rangle \qquad - \quad 2.99$$

The final state is specified by E and a set Ω of all other quantum numbers. An equivalent definition is

$$\partial f(K,E)/\partial E = \sum_{\substack{n,\\ \text{all states}}} (E_n/R).[|\mathcal{E}_n(K)|^2 (Ka_0)^{-2}] . \delta(E_n - E) \qquad - \quad 2.100$$

The relativistic inelastic-scattering cross-section has been calculated by Bethe (1930). It may differ from the non-relativistic treatment, the results of which have been outlined above, by as much as ten percent at T = 100 keV and typical core-loss voltages. Instead of using the absolute values of cross-sections, typical micro-analytical applications require the ratios of cross-sections, in which case the relativistic corrections tend to cancel out.

It has been shown that, given a fast electron incident on an atom, the inelastic-scattering cross-section can be factored into the oscillator strength, which describes the response of the atom at a given energy and wave-vector transfer, and remaining terms which depend on the energy of the incident electron, the energy-loss and the wave-vector transfer in a simple way.

2.2.3 The oscillator strength

The inelastic response of an atom to a fast incident electron is defined by the oscillator strength of that atom as a function of energy and wave-vector transfer.

The evaluation of the oscillator strength requires an expression for the electronic wave-functions of that atom. The only atom for which a complete analytic description of the atomic wave-functions exists is hydrogen. The oscillator strength has been calculated for hydrogen (Inokuti 1971, see also Leapman 1978) as a function of normalised coordinates (E/R) and $\ln(Ka_0)^2$. The following points should be noted from the form of the oscillator strength (Inokuti 1971):

1) at low energy, the distribution of angles ($\underline{K}$) is peaked around zero scattering angle. This is termed forward scattering.

2) At E/R = 1 (corresponding to the core-loss voltage), the shape of the scattered intensity as a function of K is fairly square, exhibiting a cutoff near $K = a_0^{-1}$, which corresponds to a scattering angle $\theta_c = (\Delta E/E_0)^{1/2}$. The angular dependence of the oscillator strength is often taken to be a step function which switches off at scattering angle θ_c.

3) At larger values of E/R, the oscillator strength does not peak at $\theta = 0$, but near the angle θ_c. This is the classical hard-spheres scattering angle.

4) Viewed as a function of $\ln(Ka_0)$ the peak around θ_c becomes narrower with increasing energy-loss. The width of the peak in $\ln(Ka_0)$ space is proportional to $1/\Delta E$ at large $\Delta E/R$.

The oscillator strength possesses several useful sum rules: (Inokuti 1971, Fano & Cooper 1968), the most important of which is the Bethe (or f-) sum rule:

$$\sum_n f_n(K) = Z \qquad - \quad 2.101$$

That is: the sum of the oscillator strength from the groundstate to all excited states is equal to the number of electrons in that atom. This may also be expressed as the sum over all excited states for the excitation of an electron from a given band (ℓ), in which case the sum is equal to the number of electrons in that band.

The asymptotic behaviour of $\partial f/\partial E$ for fixed finite $\underline{K}$ and $E \to \infty$ is given by (Rau & Fano 1967):

$$\partial f/\partial E \sim E^{-3.5} \qquad - \quad 2.102$$

For transitions to states of high angular momentum, the so-called centrifugal potential,

$$\ell(\ell+1).\hbar^2/2mr^2$$

becomes important, especially when it is sufficient to form a subsidiary maximum in the total atomic potential:

$$V_{TOT} = \frac{Ze^2}{4\pi\varepsilon_0 r} + \frac{\ell(\ell+1)\hbar^2}{2mr^2} \qquad - \quad 2.103$$

The reader is referred to Fano & Cooper (1968) for a discussion of this effect together with calculations on certain transition metals. The effect of the centrifugal potential is to produce a delayed edge, the delay depending on the angular momentum and the number of electrons in the shells taking part. The delay may be as much as 100 eV (for example the Krypton $3p \rightarrow \varepsilon d$ transition, Fano & Cooper 1968).

The asymptotic form of $\partial f/\partial E$ as $E \to \infty$, including the centrifugal potential effect is (Fano & Cooper 1968):

$$\partial f/\partial E \quad \sim \quad E^{-(3\cdot 5+\ell)} \qquad - \quad 2.104$$

The details of the calculations involved and the nature of the approximations employed are not relevant here. The inelastic-scattering cross-section is given by:

$$\partial \sigma/\partial E \quad \sim \quad \frac{1}{E}\cdot \partial f/\partial E \qquad - \quad 2.105$$

when the incident-particle and angular terms are removed. Thus, $\partial\sigma/\partial E$ should behave as a power law as $E \to \infty$:

$$\partial \sigma/\partial E \quad \sim \quad E^{-(4\cdot 5+\ell)} \qquad - \quad 2.106$$

For a careful survey of this topic, the reader is referred to Fano & Cooper (1968).

2.2.4 The integrated scattering cross-section

The differential inelastic-scattering cross-section given by equ. 2.96 may be integrated over all kinematically-allowed wavevector, giving:

$$\sigma_n = \frac{4\pi a_0^2}{T/R}\cdot\left[M_n^2 .\ \ln\left(\frac{4C_n.T}{R}\right) + O\left(\frac{E_n}{T}\right)\right] \qquad - \quad 2.107$$

where: $M_n^2 = |\langle n| \sum_j x_j |0\rangle|^2 / a_0^2$ – 2.108a

is the optical coupling matrix element and

$$\ln C_n = \ln(\bar{K}a_0)^2 .\ (R/E_n)^2 \qquad - \quad 2.108b$$

where: $\bar{K}$ is an average wave-vector transfer, as a function of n defined by:

$$\ln(\bar{K}a_0)^2 = \int_0^\infty \frac{f_n(K)}{f_n(0)}.\,d[\ln(Ka_0)^2] - \int_{-\infty}^{0} \frac{1-f_n(K)}{f_n(0)}.\,d[\ln(Ka_0)^2] \qquad - \quad 2.109$$

The integrated cross-section is usually expressed in the form:

$$\sigma_{n\ell} = \frac{\pi e^4}{E_0.E_{n\ell}}\cdot\frac{b_{n\ell}}{(4\pi\varepsilon_0)^2}\cdot\ln\left[\frac{c_{n\ell}.E_0}{E_{n\ell}}\right] \qquad - \quad 2.110$$

where: $b_{n\ell}$ and $c_{n\ell}$ are parameters which may be determined theoretically for hydrogen, or measured from a Fano plot of experimental results (Inokuti 1971). The Fano plot consists of a graph of $\sigma_{n\ell}.E_{n\ell}^2.U_{n\ell}$ versus $\ln(U_{n\ell})$ where $U_{n\ell} = E_0/E_{n\ell}$.

2.2.5 Chemical environment and bandstructure effects

The discussion to this point has assumed that the atom involved in inelastically-scattering the fast electron is not affected by its environment. When this atom is in a solid, it is affected by neighboring atoms. In the case of a crystalline specimen, the loosely-bound electron states of different atoms couple together, and the electron state with a fixed energy attached to a particular atom becomes a band of states covering a finite energy-span, and may no longer be localised at a particular atom (in the case of a metal). The atomic wavefunctions $U_n(\underline{r}_1, \underline{r}_2, \ldots \underline{r}_z)$ are replaced by Bloch wavefunctions which have the symmetry properties of the arrangement of atoms in the specimen.

The effect of neighboring atoms on the more-deeply lying atomic states (> 50 eV below the Fermi level) is to shift the energy-origin of the core-state due to the finite average potential of the neighboring atom at the position of this atom. This is the chemical shift effect, so called because it is sensitive to the local chemical environment and manifests itself as a shift in the observed energy-loss at an edge. (An example of the effect, seen in X-ray absorption spectra is given in Salem et al 1978).

The probability of inelastic scattering from a specimen at energy-loss E, may be expressed, using first-order perturbation theory as:

$$W_{no} \propto \rho_{bs}(E) \left| \langle n | H_{int} | 0 \rangle \right|^2 \qquad - \quad 2.111$$

where $\rho_{bs}(E)$ is the joint density of states for the scattered incident electron and crystal electron; and the final state $|n\rangle$ and initial state $|0\rangle$ are Bloch wavefunctions. The function ρ_{bs} differs significantly from the atomic joint density of states only in the first 20 eV (approx) after the onset of a transition. This corresponds to the excitation of a core electron into the conduction bands of the crystal. At higher energy-losses, the core-electron is promoted to unbound states which are only very weakly affected by the presence of crystal structure.

2.2.6 Extended energy-loss fine structure

The inelastic-scattering cross-section for a crystalline solid, from first order perturbation theory may be written (Platzman & Wolff 1973):

$$\frac{\partial^2\sigma}{\partial\Omega\partial\omega} = \frac{1}{K^4}\cdot\sum_f |\langle f|e^{i\underline{K}\cdot\underline{r}}|i\rangle|^2\cdot\delta(\omega-\omega_f-\omega_i) \quad - \quad 2.112$$

where: $\hbar\omega$ is the energy lost,

K is the change in wavevector of the incident electron,

$|i\rangle$ and $|f\rangle$ are the initial and final states, which are orthogonal.

Therefore, in the case of small K ($\underline{K}\cdot\underline{r} \ll 1$), equation 2.112 simplifies to:

$$\frac{\partial^2\sigma}{\partial\Omega\partial\omega} \propto K^{-2}\cdot\sum_f |\langle f|\underline{u}\cdot\underline{r}|i\rangle|^2\cdot\delta(\omega-\omega_f-\omega_i) \quad - \quad 2.113$$

where $\underline{u}$ is the unit vector parallel to $\underline{K}$.

In the case of a crystalline solid, $|i\rangle$ and $|f\rangle$ are Bloch wavefunctions. For core-losses ($\hbar\omega > 50$ eV), $|i\rangle$ is relatively unaffected by the neighboring atoms, whereas $|f\rangle$ is modified to include back-scattering from neighboring atoms. $|f\rangle$ thus contains an admixture of a spherical outgoing wave centred on the origin atom plus incoming spherical waves centred on neighboring atoms. The modification of $|f\rangle$ by neighboring atoms has been shown (Stern 1974, Lee & Pendry 1975) to introduce a modulation term $\chi(K)$ into the observed inelastic-scattering cross-section, where:

$$\chi(K) \simeq \frac{A(K)}{K}\sum_j \frac{N_j}{R_j^2}\, e^{-R_j/\lambda(K)}\cdot e^{-\sigma_j^2K^2/2}\cdot \sin(2KR_j+\phi(K)) \quad - \quad 2.114$$

where N_j is the number of atoms in shell j around the origin atom,

R_j is the radius of shell ,

$A(K)$ is the backscattering amplitude of the outgoing crystal electron upon encountering a neighboring atom,

$\phi(K)$ is the total phase shift of the outgoing crystal electron in leaving the origin atom, being backscattered by a neighboring atom and rejoining the origin atom,

$\lambda(K)$ is the mean-free-path of the outgoing crystal electron with wavevector K,

σ_j^2 is the mean-square radial fluctuation of shell j due to disorder or thermal motion.

The experimentally-observed cross-section is then given by:

$$\left.\frac{\partial^2\sigma}{\partial\Omega\,\partial\omega}\right|_{expt} = (\chi(K)+1)\cdot\left.\frac{\partial^2\sigma}{\partial\Omega\,\partial\omega}\right|_{single-atom} \qquad - \quad 2.115$$

The main effect of $\chi(K)$ is to introduce modulations caused by the interference of the outgoing and incoming waves at the position of the origin atom. The observed radial position of peaks in the fourier transform of $\chi(K)$ would be at the values of the shell radii (R_j) were it not for the effect of the phase-shift and back-scattering amplitude $A(K)$. This effect is discussed in more detail in chapter 5.

The $e^{-R_j/\lambda(K)}$ term in equation 2.114 ensures that the effect samples local order ($\lambda(K) < 100$ Å for K corresponding to a secondary electron kinetic energy in the range normally employed in EXELFS (20 to 200 eV)).

The effect of disorder is to reduce the amplitude of the oscillations at large values of wavevector. This is not important in extended energy-loss fine structure (EXELFS) (due to the restricted wavevector range used), but must be considered in extended X-ray absorption fine-structure (EXAFS) because of the much-larger range of wavevector usually employed.

Equation 2.114 does not include any multiple-scattering effects, which may become important for elements in which the mean-free-path at about 100 eV is more than several atomic spacings. In such materials (e.g. Copper (Stern 1974)), multiple-elastic-scattering effects may become important and may cloud the interpretation of experimental data (see chapter 5).

The phase-shifts may be calculated, given a good model of the atomic wavefunctions (Lee & Pendry 1971) or, because of the transferability of phase-shift data from one chemical environment to another (Citrin et al 1976), they may be measured on one standardised system, parameterised (Lee et al 1974) and the parameterised forms used to determine the structure of a specimen under examination.
The numerical evaluation of the radial distribution function is discussed in chapter 3.

2.3 SUMMARY OF USEFUL FORMULAE:

1) The differential inelastic cross-section for plasmon excitation, calculated by Pines & Bohm is

$$\frac{\partial\sigma(\theta)}{\partial\Omega} = \frac{1}{2\pi a_0}\cdot\frac{\theta_E}{\theta^2+\theta_E^2}\quad,\quad d\Omega = 2\pi\theta d\theta \qquad - \quad 2.116$$

2) The probability of surface plasmon excitation is

$$P = \frac{1}{4\pi\varepsilon_0}\cdot\frac{1}{1+\varepsilon_r}\cdot\frac{e^2}{\hbar v_0} \qquad \text{per surface} \qquad - \quad 2.117$$

3) The Gryzinski classical total cross-section is given by

$$\sigma_{nl}\cdot E_{nl}^2 = (6{\cdot}51\times10^{-18}).z_{nl}.g(U_{nl}) \quad m^2(eV)^2 \qquad - \quad 2.118$$

where: $g(u) = \frac{1}{u}\cdot(u-1)^{1\cdot5}\cdot(u+1)^{-1\cdot5}\cdot\left[1+\frac{2}{3}\left(1-\frac{1}{2u}\right)\ln\left(2{\cdot}7+(u-1)^{1/2}\right)\right]$

and: $U_{nl} = E_0/E_{nl}$

4) Bethe theory for the cross-section of a core-loss gives

$$\frac{\partial\sigma}{\partial E} = \frac{4\pi a_0^2}{T/R}\cdot\frac{\partial f(K)/\partial E}{E/R}\cdot d(\ln(Ka_0)^2) \qquad - \quad 2.119$$

or, in terms of scattering angle, θ,

$$\frac{\partial\sigma}{\partial E} = \frac{4\pi a_0^2}{T/R}\cdot\frac{\partial f(K)/\partial E}{E/R}\cdot\frac{2\theta.d\theta}{\theta^2+\theta_E^2} \qquad - \quad 2.120$$

where: $\theta_E = \Delta E/2E_0$.

5) It is possible to integrate equation 2.120 over angle θ, by first approximating the dependence of the oscillator strength by a step function

$$G(E,\theta) = 1,\ \theta \leqslant \theta_c$$
$$= 0,\ \theta > \theta_c$$

Therefore $\partial f(K)/\partial E = \partial f'/\partial E\ .\ G(E,\theta)$

where $\partial f'/\partial E$ has no dependence on scattering angle, θ.

The upper bound of the integration is given by the acceptance angle of the spectrometer or the convergence angle of the electron probe (whichever is the larger). Thus the dependence on angle, β, of the integral is given by

$$I_\beta(E) = \int_0^\beta \frac{\theta.d\theta}{\theta^2+\theta_E^2}\cdot G(\theta) \qquad - \quad 2.121$$

The efficiency of collection of the probe geometry is given by:

$$\eta_\beta(E) = I_\beta(E)/I_{\theta_c}(E)$$
$$= \ln(1+\beta^2/\theta_E^2)/\ln(1+\theta_c^2/\theta_E^2)\ ,\quad \beta \leqslant \theta_c$$
$$= 1 \qquad\qquad ,\quad \beta > \theta_c \qquad - \quad 2.122$$

6) Energy window efficiency:

The energy-dependence of the inelastic-scattering cross-section may be approximated by:

$$\partial\sigma/\partial E \sim E^{-s} \quad \text{where} \quad s = 4{\cdot}5 \qquad - \quad 2.123$$

The collection efficiency of an energy-window of width Δ above an edge at E_t is given by

$$\xi(\Delta) = \int_{E_t}^{E_t+\Delta} . \, E^{-s}.dE \Big/ \int_{E_t}^{\infty} E^{-s}.dE \qquad - \quad 2.124$$

$$\therefore \quad \xi(\Delta) = 1 - \left(\frac{E+\Delta}{E}\right)^{-s+1}$$

7) Kramers-Kronig analysis:

Given the energy-loss function $Im(-1/\varepsilon)$, it is possible to evaluate the real part $Re(1/\varepsilon)$ by Kramers-Kronig analysis:

$$Re\left(1/\varepsilon(\omega)\right) = 1 - \frac{2}{\pi}\int_0^{\infty} \frac{Im\left(-1/\varepsilon(\Omega)\right).\Omega\, d\Omega}{\Omega^2 - \omega^2} \qquad - \quad 2.125$$

It is then possible to obtain $Re(\varepsilon)$ and $Im(\varepsilon)$ given by

$$\varepsilon(\omega) = \left(Re\left(1/\varepsilon(\omega)\right) - i\, Im\left(-1/\varepsilon(\omega)\right)\right)^{-1} \qquad - \quad 2.126$$

Chapter 3 - Numerical techniques of electron energy-loss spectroscopy

Chapter 3 - Numerical techniques of electron energy-loss spectroscopy

Chapter 3 - Numerical techniques of electron energy-loss spectroscopy

3.1 THE NEED FOR COMPUTER-CONTROLLED DATA CAPTURE

The electron energy-loss spectrum (ELS) is recorded serially. The current in the spectrometer scan coils is increased slowly, and the output of a photo-multiplier tube (PMT) detector provides the intensity of the energy-loss spectrum. A detailed description of the spectrometer is deferred to section 3.2. See also figure 3.1. The maximum scan time, and hence the data collection time, is limited by the stability of the field emission tip current and the microscope electronics to, at best, a collection time of several minutes. Over this period, the tip emission current fluctuates and, more seriously, decays as the active region of the tip becomes coated with contaminants. The tip has to be heated every ten minutes to drive off these contaminants (called tip flashing). Over a period of minutes, fluctuations and drift in the spectrometer drive electronics and high-voltage supply cause the apparent position of the energy-zero to wander. This may indroduce a non-linear distortion of the energy scale of the collected spectrum.

The advantages which accrue from the use of a digital data collection system are three-fold:

1) data may be collected for as long as is desired. The limitations of supply drift and tip contamination on a single scan are no longer important when the scan period is several seconds. Moreover, fluctuations in the position of the energy-zero or tip current are averaged out over many scans, causing only a slight loss of energy-resolution which may be estimated from the increase in width of the zero-loss peak of a spectrum collected over many scans from the width of the zero-loss peak of a single-scan spectrum. The process of data capture may be interrupted at the end of a scan to reset the microscope conditions (zero-loss position, tip emission) or adjust for specimen drift.

2) The spectrum may be displayed on a cathode-ray tube (CRT) display during data capture, and much time may be saved by aborting unwanted spectra after little time has elapsed.

3) A completed spectrum may be stored in a digital form on any of

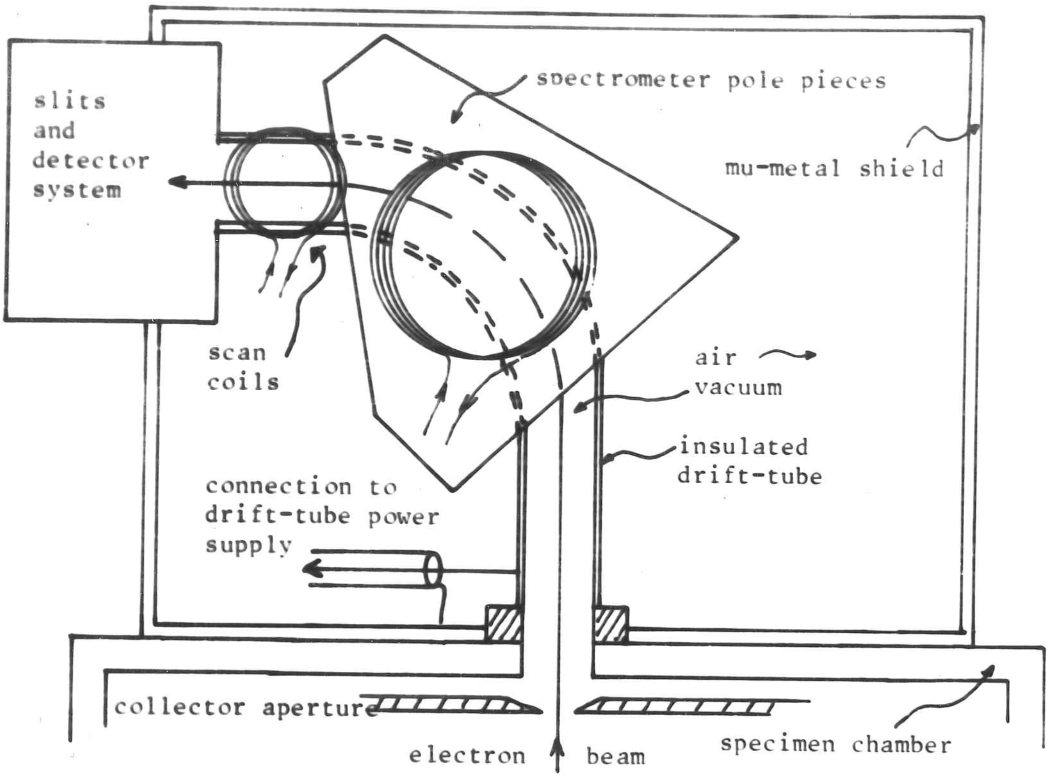

<u>Figure 3.1</u> The HB5 electon spectrometer (schematic)

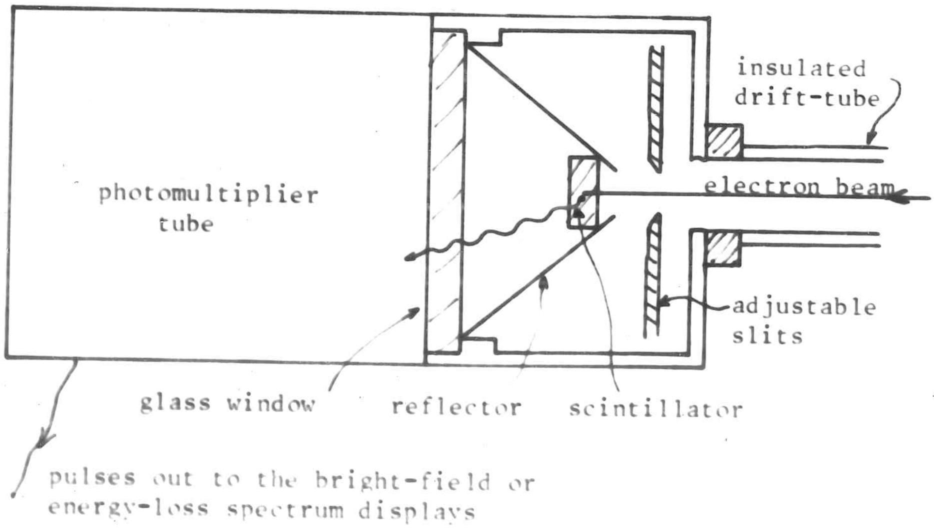

<u>Figure 3.2</u> The spectrometer detector system

several media (e.g. magnetic disc or paper tape) whence it may be recalled for comparison with a different spectrum. In a digital form, the spectrum is readily transferable to a central computer.

A LINK SYSTEMS EDX data-collection system, modified to collect energy-loss data was used to collect energy-loss data on the Cambridge HB5 STEM (Batson & Craven 1979, Batson et al 1978, Batson 1978a,b). The digital data could be plotted onto paper using and X-Y plotter, punched onto paper tape in ASCII code (i.e. as a table of channel electron counts) or punched onto paper-tape in binary code. Once punched onto paper-tape, there is a permanent record of the data which may then be entered into the IBM 370/165 computer which forms the Cambridge University central computing facility.

Once a spectrum is in the IBM 370, it may be stored on a magnetic disc (with a retrieval time of milli-seconds), or when no longer of immediate interest, it may be stored on magnetic tape (with a retrieval time of minutes).

The availability of powerful data-processing capabilities on the IBM 370 makes it possible to perform manipulations that would not be possible on a smaller computer (such as the NOVA computer, which forms the heart of the LINK system) such as the fourier transformation of large numbers of data points, which is essential in the techniques of deconvolution (see section 3.3.3). It should be noted that this last point is unlikely to remain a predominant reason for the use of a central computing facility. At the time of writing, the development of powerful microprocessor-based computers which will place the ability to perform all the numerical processing required in this chapter in the hands of the average research group is likely to take place over the next few years (1980- 1985).

3.2 THE MICROSCOPE - COMPUTER INTERFACE

3.2.1 The conventional spectrometer system

In a conventional spectrometer system, a single ramp signal-generator controls all timing. The scan signal is fed to the spectrometer scan coils (see fig 3.1) which scan the position of a dispersed spectrum across a slit assembley (see fig 3.2) and the ramp signal is fed to the X input of an X-Y plotter, or the timebase of a CRT display. The HB5 spectrometer contains two sets of coils: one providing the sector magnet fields which provides the dispersion and defines the position of the energy zero of the dispersed spectrum; and a smaller set of air-cored coils which scan the dispersed spectrum past a set of slits. Being air-cored, these latter coils can be operated a much higher frequencies than the sector magnet coils without exhibiting hysteresis effects.

The energy resolution of s symmetrical double-focussing spectrometer is given by Crewe et al (1971):

$$\delta E/E = \frac{2 + E/m^*c^2}{1 + E/m^*c^2} \cdot \frac{\delta y}{4\rho} \qquad - \quad 3.1$$

where: E is the incident electron's kinetic energy,
m^* is the rest mass of the incident electron,
δy is the separation of the slits at the detector,
ρ is the radius of curvature of the electron trajectory in the field of the sector magnet.

The minimum value of δy is given by the flatness to which the two opposing slits are manufactured, a typical value is $\delta y = 2$ µm. The radius of curvature is contrained by the physical size of the sector magnets: it is difficult to make large sector magnets with a suitably homogenous magnetic field because of the presence of defects in the pole-pieces. A typical value of ρ is $\rho = 10$ cm (used on the HB5). For 100 keV electrons, $E/m^*c^2 \simeq 0.2$, thus equation 3.1 simplifies to:

$$\delta E/E \simeq \frac{\delta y}{2\rho} \; . \qquad - \quad 3.2$$

Thus the energy resolution of the spectrometer under typical HB5 experimental conditions is:

$\delta E_S = 0.8$ eV. (The subscript denotes spectrometer resolution)

The presence of electrical noise in the EHT and spectrometer supply electrons worsens the energy-resolution of the spectrometer. These two sources introduce an effective electrical noise, δE_E . If δE_E were large (i.e. $\delta E_E >> \delta E_S$), the electrical noise would be responsible for a very marked degradation in the observed energy resolution of the spectrometer (as measured from the width of the zero-loss peak on a collected spectrum). In practice, the electronics are designed so that δE_E is of the same order as δE_S. In the case of the HB5, this requires 10 ppm stability in the electronics, which can be achieved using present technology.

Spectrometer aberrations also reduce the effective energy-resolution. An electron entering the spectrometer at an angle to the optic axis of the microscope or entering at a position not on the optic axis of the spectrometer is detected as though it has a different kinetic energy as compared with the same electron entering the spectrometer on axis. There are two conflicting aims: in order to increase the count-rate at the detector, the aperture which limits entrance angle (the collector aperture) should be made as large as possible; but, in order to minimise loss of energy resolution, the collector aperture should be made as small as possible. In practice, the collector aperture size selected represents a compromise which depends on the detail of the experiment. The collector aperture is usually chosen so that the effective aperture aberration, δE_A is roughly the same as the spectrometer resolution δE_S.

The lowest (best) value that has been reported for the slit separations is, to the author's knowledge, $\delta y = 0.25$ m (Crewe <u>et al</u> 1971). This would result in about 0.1 eV spectrometer resolution in the case of the HB5. The spectrometer angle and position aberations may be made very small be decreasing the size of the collector aperture as is required. It is not, however, possible to obtain 0.1 eV stability of the electical supplies using present techniques. A radical re-design of the spectrometer system using retarding-field techniques would be necessary to achieve 0.1 volt effective electrical stability and this would required an extensive re-design of the microscope hardware.

The best energy-resolution thatis available on the HB5 at Cambridge, which is a combination of δE_S and δE_E is approximately 1.5 eV. The working resolution is usually slightly worse than this to allow for a reasonably-large collector aperture (2 eV at 0.5 mR collector semi-angle).

<u>3.2.2 The detector system</u>

The dispersed energy-loss spectrum is formed in the focal plane of the spectrometer. The aperture formed by the slits lies on the same focal plane. The dispersed spectrum is then scanned electrically across the detector slits, which remain stationary, using the air-cored scan coils (see figure 3.1). Electrons which pass through the aperture formed by the slits pass on to a glass scintillator (i.e. doped YAG which is bakeable (Pennycook 1980)). The electrons are slowed down, generating electron-hole pairs, some of which recombine with the emission of visible light. Each incident primary electron may generate hundreds of photons. An efficient optical coupling ensures that most of these end up at the photo-cathode of a PMT (see fig 3.2). Each photon has a chance (a few percent) of causing a photo-electron to be emitted from the photo-cathode. The photo-electron is amplified by a conventional dynode structure and results in a current pulse being detected at the anode.

Due to the large number of photons generated per incident primary electron; each primary electron has a low probability of not being detected. In the conventional detector system, the PMT output is in the form of a current which is used to drive the Y-amplifier of and X-Y plotter or used to control the intensity modulation of a CRT (to form an energy-filtered image) or the vertical displacement of a CRT (to display the energy-loss spectrum). The pulses due to individual electron events are not normally resolved due to the slow response of the amplifiers used.

3.2.3 The computer - microscope interface

The computer interface is provided by the microscope electronics and the LINK SYSTEMS computer-controlled EDX system, both of which have been substantially modified to collect digital energy-loss data (Batson 1978a,b, Batson & Craven 1979), see figure 3.3.

The existing microscope display scan generator has been modified to produce two sets of pulses to the computer electronics, one at 'line' frequency, and one at 'frame' frequency, synchronised together. The ramp output from the scan generator at 'frame' frequency is used as before, to drive the spectrometer scan coils. The line-blanking pulses, at a multiple of the frame scan frequency, are used to

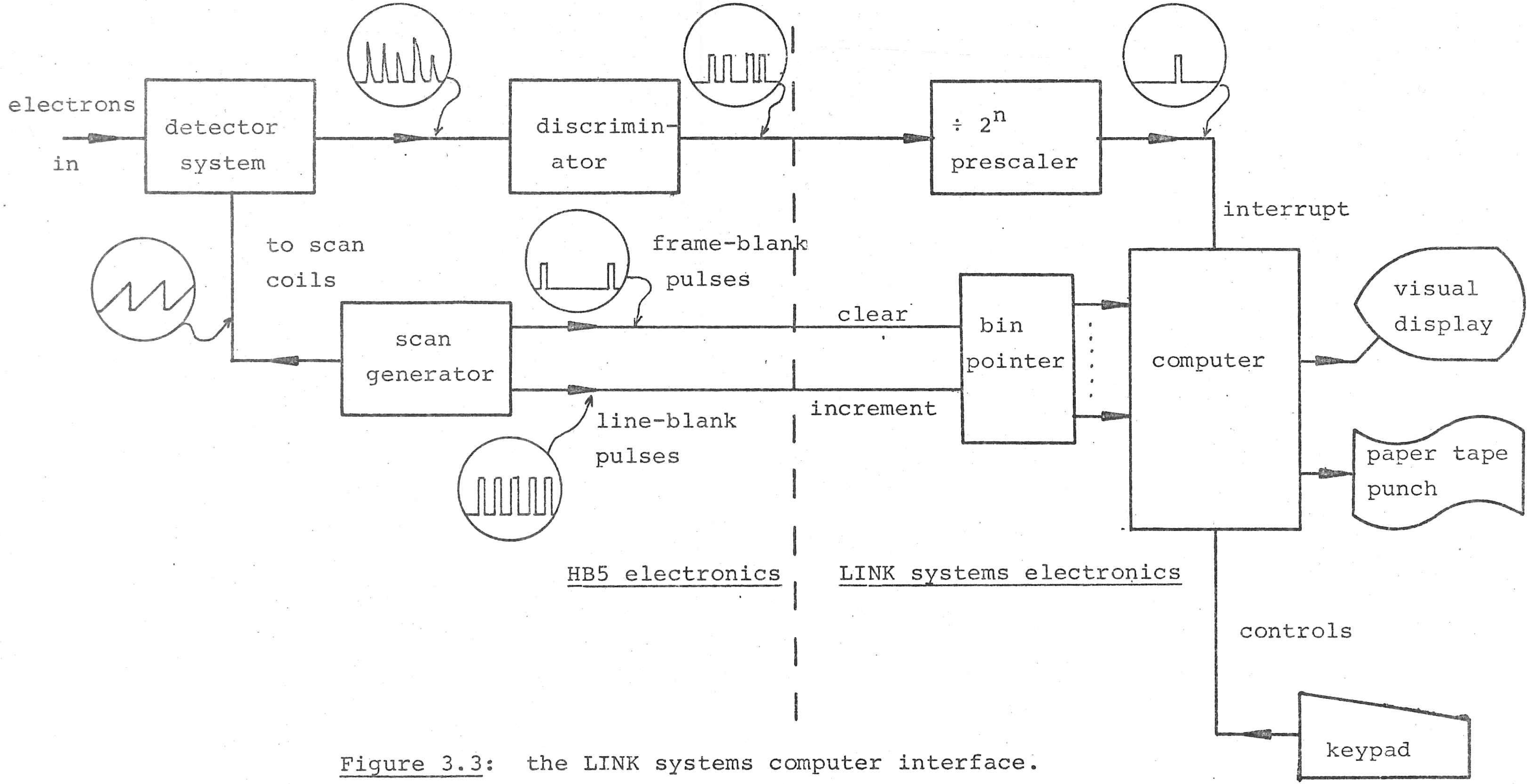

Figure 3.3: the LINK systems computer interface.

delineate successive time slots, each of which corresponds to a storage channel (or bin) in the computer. The energy-loss spectrum is represented by the electron counts in successive channels.

Individual electron arrivals at the scintillator generate current pulses in the anode circuit which are discriminated and shaped to produce acceptable logic levels. Thus, primary electrons are detected and result in a digital pulse, but secondary or other spurious electrons present in the detector system and dark-current pulses in the PMT do not cause a digital pulse to be generated, provided that the discriminator level is properly adjusted.

The frame-blank pulses are generated at the end of a scan, and they are used to reset a counter, called the bin (or channel) pointer which points to the channel which is to be incremented by the arrival of prescaled electron pulses.

The line-blank pulses increment the bin pointer.
The logic-level electron event pulses are prescaled (that is, the input pulse frequence is divided by 2^n where $n = 0,1,2 ..10$). The factor by which they are prescaled is set by means of a switch on the computer system. The resulting pulses (call pre-scaled pulses) generate an interrupt which instructs the computer to increment the number stored in the channed currently being updated (as determined by the bin pointer). Whilst the computer is servicing this interrupt, it is insensitive to further interrupts, and hence further prescaled electron events. Thus, prescaled electron pulses arriving separated by less than the interrupt service time (or dead time) are not all counted. The design of a data-collection system that can operate at much higher frequencies is discussed briefly in appendix B.

While the computer is not servicing the data-generated interrupt, it runs the visual display, polls the keypad (the device on which instructions to the computer are entered by the operator) and services any other active peripherals (X-Y plotter, teletype or floppy discs).

Two regions of memory are used to store energy-loss data: one is usually reserved for the collection of data, whilst the other may simultaneously be used to communicate with the other peripherals. Keypad commands are available to manipulate the two stored spectra.

Energy-loss data can be punched onto paper-tape, for transfer to the University computer, using a keypad command, in one of two formats:
1) as a table of numbers giving electron counts in each channel in a form that allows the channel contents to be read directly from the teletype output (ASCII format);
2) as a list of numbers giving successive channel contents in binary code.

The second form produces a shorter punched tape and therefore punches more quickly than the first form, but the channel contents cannot be read from the teletype printout. The advantage of using binary punched tape lies in this reduction of punching time: a typical 500-channel spectrum may take 15 minutes to punch using format 1), but would take only one quarter of this time to punch using format 2). The binary tape, however, is not directly readable by the University computer, and has to be converted to format 1) using a separate PDP-8 computer with fast paper-tape peripherals.

A floppy disc unit was added to the LINK SYSTEMS computer in the last year of this work (1980), and spectra may be stored on a floppy (magnetic) disc. It is still necessary, however, to use paper-tape as a medium of communication between the LINK system and the University computer.

3.3 A DESCRIPTION OF THE DATA PROCESSING AND NUMERICAL TECHNIQUES EMPLOYED IN ENERGY-LOSS SPECTROSCOPY

In order to process energy-loss data, a package of computer programs was written by the author and made available on the University IBM 370/165 computer. Details of the program package are given in appendix A. This section is concerned with the theory of numerical processing necessary to write such a program package, using the theory of energy-loss spectroscopy given in chapter 2.

3.3.1 Count-rate error correction

The LINK SYSTEMS computer has a deadtime of approximately 50 μs in its response to a pre-scaled electron pulse. Thus the pre-scaled count-rate should be kept substantially below 20 kHz if dead-time corrections are to remain unimportant. The recommended maximum pre-scaled count-rate is 7 kHz resulting in a maximum count-rate error of about 5 % (Papoulis 1965). The effect of count-rate errors is to depress the indicated energy-loss signal in regions of the spectrum where the count-rate is highest. It is usually possible to arrange experimental conditions such that the count-rate error is minimal at the plasmon energy-loss, whilst the count-rate at the zero-loss peak may be much greater than 20 kHz. The count-rate error correction seeks to replace a distorted zero-loss peak with an estimate of what the undistorted peak should have been.

In addition to the distorted energy-loss spectrum, the correct ratio of zero-loss peak height to plasmon-loss peak height is required. This ratio is measured off an analogue scan, under experimental conditions identical to those used for the digital scan, from either an X-Y plot or the CRT display of the analogue spectrum.

The portion of the zero-loss peak that is deemed to be distorted (i.e. the channel counts are greater than the plasmon peak count) is replaced by a gaussian of the estimated correct height (see figure 3.4), the width and position of the gaussian being determined by requiring that the generated zero-loss peak should fit the highest undistorted points of the experimental zero-loss peak.

The program call APCOR (see appendix A) was written to perform these operations. A correct zero-loss peak is essential if the spectrum is to be used by the deconvolution programs.

3.3.2 Finite aperture-size correction

The energy-loss spectrum from electrons which have been scattered into an axial aperture of size α ($\alpha > \theta_c$) is given by integration of equation 2.120:

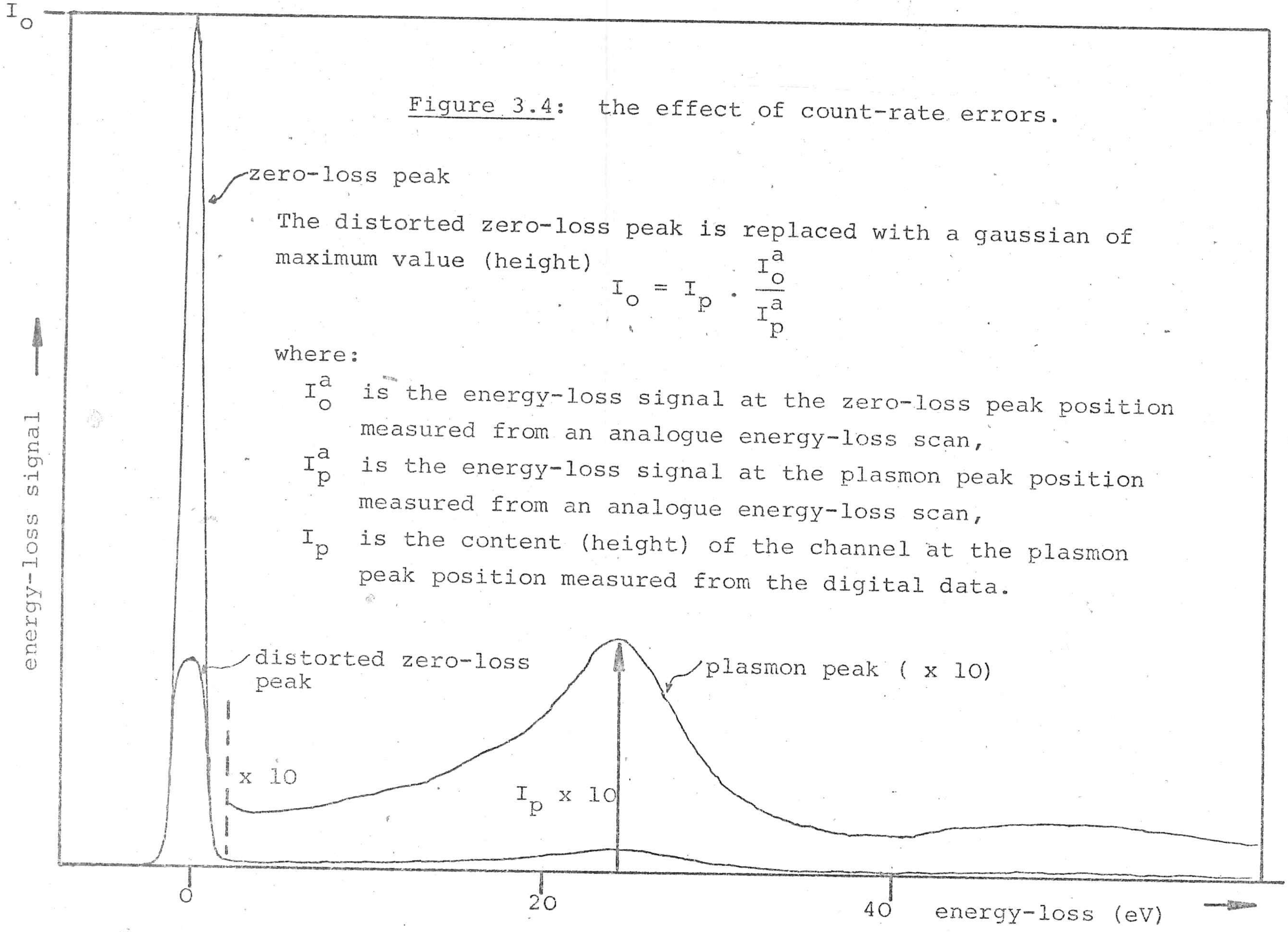

Figure 3.4: the effect of count-rate errors.

The distorted zero-loss peak is replaced with a gaussian of maximum value (height)

$$I_o = I_p \cdot \frac{I_o^a}{I_p^a}$$

where:

I_o^a is the energy-loss signal at the zero-loss peak position measured from an analogue energy-loss scan,

I_p^a is the energy-loss signal at the plasmon peak position measured from an analogue energy-loss scan,

I_p is the content (height) of the channel at the plasmon peak position measured from the digital data.

$$\left[\frac{\partial\sigma}{\partial E}\right]_0^{\theta_c} = \frac{B(E)}{2}\,\ell n(1 + \theta_E^2/\,\theta_c^2) \qquad - \qquad 3.3$$

where: B(E) is a function of energy alone. The spectrum recorded from electrons that are scattered into a small axial aperture ($\alpha < \theta_c$) is given by:

$$\left[\frac{\partial\sigma}{\partial E}\right]_0^{\alpha} = \frac{B(E)}{2}\,\ell n(1 + \alpha^2/\theta_E^2). \qquad - \qquad 3.4$$

Energy-loss results recorded using an aperture of semi-angle α (see figure 3.5 for a definition of α) may be normalised so that they appear to have been collected using a large aperture by dividing the experimental spectrum by the collection efficiency, η, where

$$\begin{aligned} \eta(E,\alpha) &= \ell n(1 + \alpha^2/\theta_E^2) \;/\; \ell n(1 + \theta_c^2/\theta_E^2\,), \alpha < \theta_c \\ &= 1 \qquad\qquad\qquad\qquad\qquad\qquad\qquad\;\;, \alpha > \theta_c \end{aligned} \qquad - \qquad 3.5$$

This correction may be in error for multiple inelastic scattering into very small apertures (see section 3.3.3.4.2).

3.3.3 Deconvolution

An energy-loss spectrum obtained from a specimen which is not very thin (< 50 Å) contains a significant contribution from incident electrons that have been inelastically scattered more than once. It is desired to be able to remove the effects of multiple scattering from experimental spectra, from specimens of thickness $t < \lambda_p$, (i.e. t < 700 Å), which would otherwise introduce error into the evaluation of atomic concentrations and into the dielectric function, ε, determined by the technique of Kramers-Kronig analysis.

Consider a specimen to be composed of slices Δ thick. The single-scattering spectrum, per unit thickness is written R(E). The single-scattering spectrum for a slice is then $R(E).\Delta$. Electrons having traversedone slice, pass through a second slice. The resulting spectrum, MR(E), is a convolution:

$$MR(E) = \int_0^E (\delta(E') + R(E').\Delta).(\delta(E-E') + R(E - E').\Delta)\,dE' \qquad 3.6$$

where: $\delta(E)$ represents the incident monochromatic electrons . The convolution theorum enables this result to be expressed as:

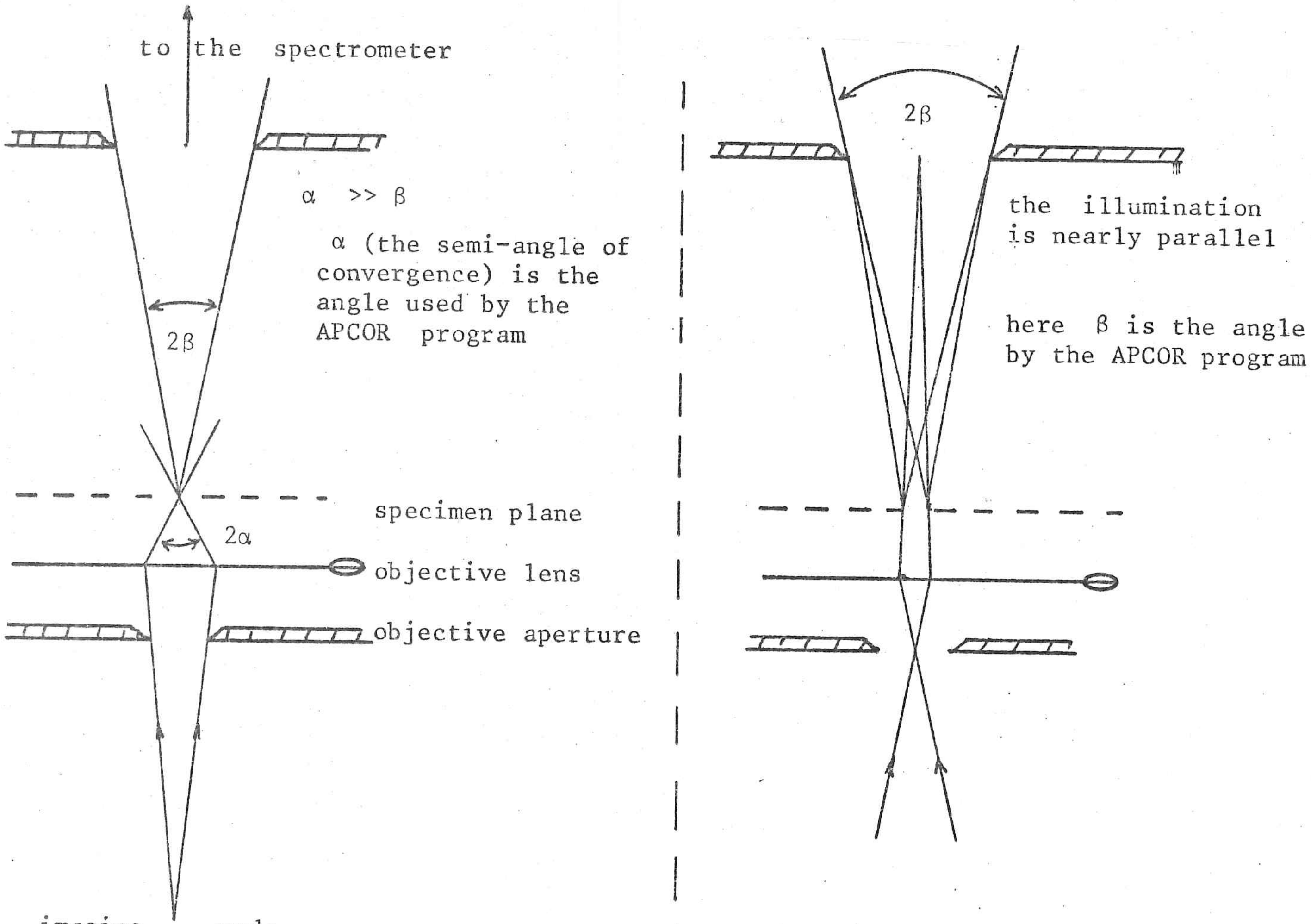

α (the semi-angle of convergence) is the angle used by the APCOR program

the illumination is nearly parallel

here β is the angle by the APCOR program

imaging mode

selected area diffraction mode

Figure 3.5: the angles relevant to the APCOR program for microscope imaging and selected area diffraction modes.

$$mr = (1 + r.\Delta)^2 \qquad - \quad 3.7$$

where: mr is the fourier transform of MR(E),
r " R(E).

Throughout this chapter, functions of energy, such as R(E) have their fourier transforms denoted by a transformation to lower case, e.g. R(E) → r.

After passage through a foil of thickness t, the multiple-scattering spectrum, MS(E), is given by:

$$ms = (1 + r.\Delta)^{t/\Delta}. \qquad - \quad 3.8$$

In the limit as $\Delta \to 0$,

$$ms = \exp(t.r) \qquad - \quad 3.9$$

thus:

$$ms = 1 + t.r + \frac{1}{2!}(t.r)^2 + \ldots \qquad - \quad 3.10$$

The contribution to the multiply-scattered spectrum from single-scattering, through the specimen of thickness t, is given by t.r, which is called the single-scattering spectrum SS(E). Thus:

$$ms = \exp(ss). \qquad - \quad 3.11$$

Under experimental conditions, the finite spectrometer resolution and electrical noise combine to produce an experimental zero-loss peak of finite width. The finite width of the zero-loss peak, so far represented by a δ-function, degrades the experimental resolution, and may be represented in the experimental spectrum, ES(E), by a convolution of the multiple-scattering spectrum with a zero-loss function, Z(E), which may be represented by:

$$es = z.\ \exp(ss). \qquad - \quad 3.12$$

Therefore, given an experimental spectrum whence Z(E) may be measured directly, it is possilbe, in theory, to calculate the single-scattering spectrum, given by:

$$ss = \ell n(es/z). \qquad - \quad 3.13$$

The presence of noise in the data complicates the numerical extraction of the single-scattering spectrum and places a limit on the energy resolution that may be achieved (Cooper 1967, Wertheim 1975).

3.3.3.1 Multiple deconvolution

It is possible, in theory, to obtain the single-scattering spectrum, SS(E), given the experimental energy-loss spectrum, ES(E). The presence of noise in the data limits the accuracy and resolution that may be achieved by deconvolution. Straight-forward evaluation of the logarithm in equation 3.13 involves a positive power series expansion of (es/z). An alternative technique is to attempt to remove multiple-scattering only up to a given order of multiple-scattering using a power series expansion of (es/z). Because a complete deconvolution is not attempted, the result is not so susceptible to noise as the evaluation of the logarithm (equation 3.13) would be. Equation 3.11 gives that:

$$ms = 1 + ss + \frac{ss^2}{2!} + \frac{ss^3}{3!} + \ldots = \exp(ss) \qquad - \quad 3.14$$

and

$$ms^{(1/m)} = 1 + \frac{ss}{m} + \left(\frac{ss}{m}\right)^2 \cdot \frac{1}{2!} + \ldots = \exp(ss/m) \qquad - \quad 3.15$$

In order to remove N orders of multiple scattering, the sum, Q is formed:

$$Q = ms + \sum_{m=1}^{N} \frac{C_m}{(m+1)^{(n+1)}} \,. \qquad - \quad 3.16$$

Setting the coefficients of $(ss)^{n+1}$, n = 1,2, ... N to zero results in N simultaneous equations:

$$1 + \sum_{m=1}^{N} \frac{C_m}{(m+1)^{(n+1)}} = 0, \qquad - \quad 3.17$$

for n = 1,2, ... N,

which may be solved, giving the coefficients C_m.

Thus:

$$Q = \left(\xi + \sigma.ss + o\left(\frac{ss^{N+2}}{(N+2)!}\right) + \ldots \right) \qquad - \quad 3.18$$

where: $\xi = 1 + \sum_{m=1}^{N} C_m$,

$$\sigma = 1 + \sum_{m=1}^{N} \frac{C_m}{m+1} \,.$$

The single-scattering spectrum with multiple-scattering up to order N + 1 removed is then given by:

$$\frac{Q - \xi}{\sigma} = ss + o\left(\frac{ss^{N+2}}{(N+2)!}\right) \cdot \frac{1}{\sigma} + \ldots \qquad - \quad 3.19$$

As an example, the solution of equation 3.17 for N = 2 yields:

$C_1 = -8.8,$

$C_2 = 10.8.$

The coefficent of the first residual multiple-scattering term ($ss^4/4!$) is then 2.92.

An alternative method is to used a positive power-law expansion in equations 3.15 to 3.19 (i.e. (1/m) replaced by m). This results in a closer approximation to the evaluation of the logarithm in equation 3.13 by a positive power-law expansion than the inverse power-law expansion used so far. The details of the mathematics are not reproduced here. The coefficient of the first residual, using a power-law expansion with integer coefficients in the case of N = 2 was found to be 6.0; more than twice the value calculated for the inverse power-law expansion method. On the basis of this evidence, the inverse power-law expansion method was adopted for use in the multiple deconvolution program MULDEC (see appendix A).

The author did not attempt to prove that the inverse power-law expansion produced optimum convergence (lowest residual multiple-scattering). The MULDEC program is usually used to remove 5 orders of multiple scattering. As will be shown later, the single-scattering spectrum contains an arbitrary "high frequency" (i.e. fine energy scale) noise content which may be suppressed by reconvoluting the single-scattering spectrum with the zero-loss peak. This is done automatically by the MULDEC program.

Figure 3.6 shows the results of applying the MULDEC program to the energy-loss spectrum of a thick diamond specimen (about 1000 Å thick). Multiple scattering up to order 4 (i.e. 4 plasmon losses) can be seen in the untreated data. The multiply-deconvoluted results show that most of the multiply-scattered intensity has been removed, although a little structure is still evident near 60 eV.

3.3.3.2 Deconvolution of edge spectra

Spectra from thick specimens (i.e. thickness about one plasmon mean-free-path (MFP) ≃ 800 Å) will show the effects of multiple inelastic scattering which modify the energy-loss spectrum in the region of the spectrum up to several plasmon excitation energies

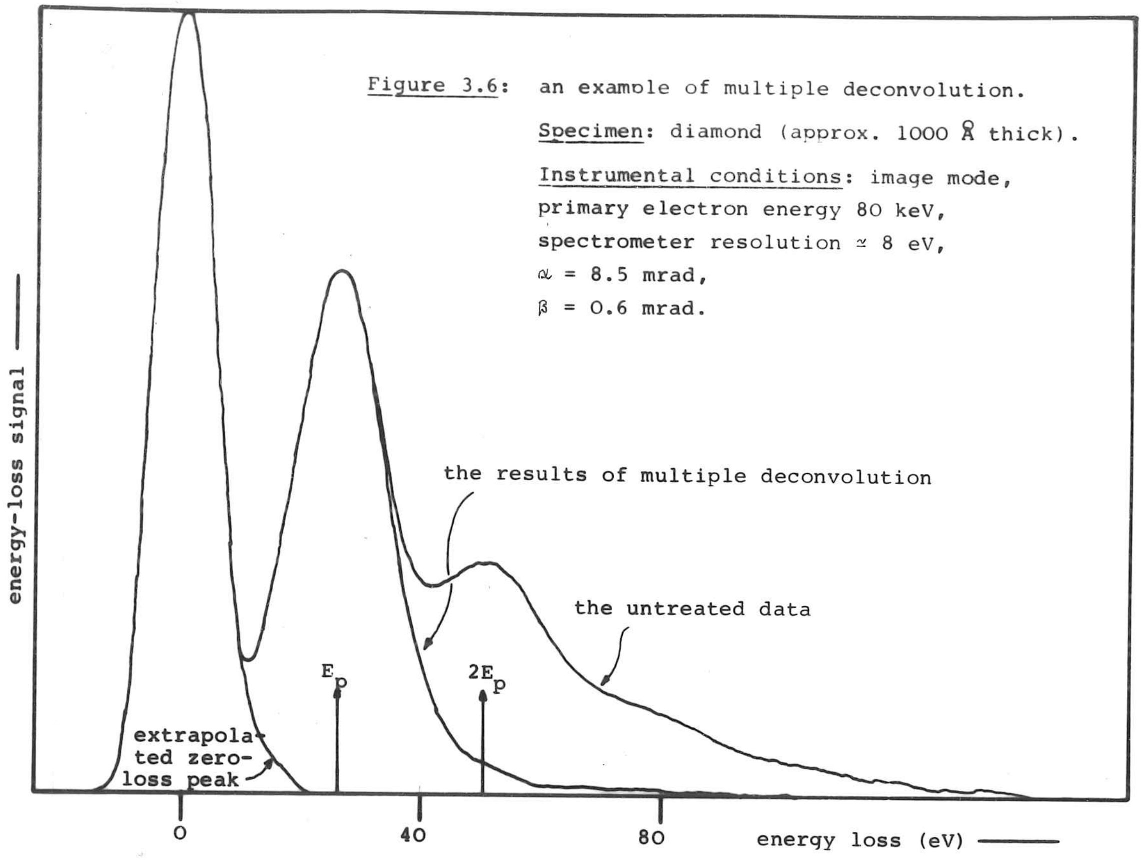

Figure 3.6: an example of multiple deconvolution.
Specimen: diamond (approx. 1000 Å thick).
Instrumental conditions: image mode, primary electron energy 80 keV, spectrometer resolution ≃ 8 eV, α = 8.5 mrad, β = 0.6 mrad.

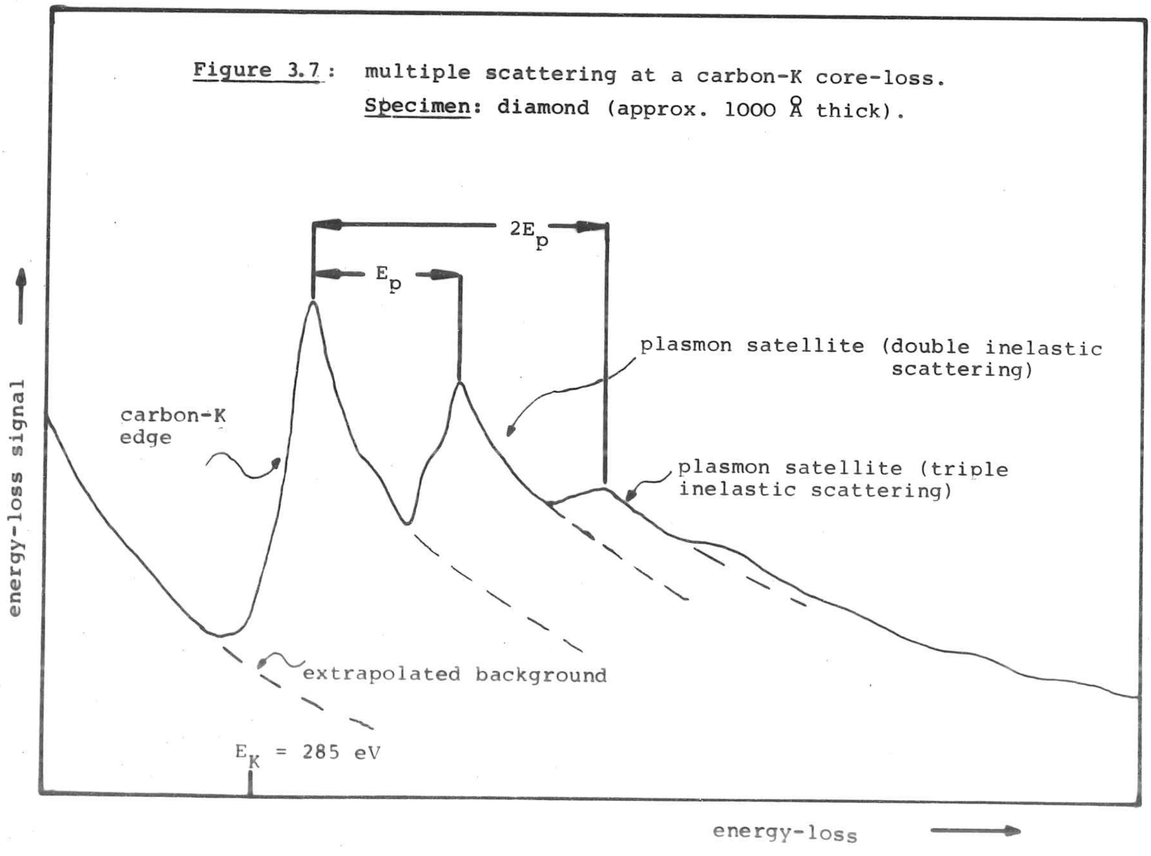

Figure 3.7: multiple scattering at a carbon-K core-loss.
Specimen: diamond (approx. 1000 Å thick).

above a core-loss edge. For an example, see figure 3.7. It is shown below that, given the low-loss region (0 to 100 eV) and the core-loss region of the energy-loss spectrum, it is possible to remove the effects of multiple-scattering in the core-loss spectrum. The two regions of the spectrum do not have to overlap on the energy axis.

It is necessary to remove multiple-scattering effects from a core-loss signal before extracting EXELFS information, although it is preferable to use a spectrum from a thin specimen rather than perform numerical deconvolution, as illustrated in section 5.3.1.1. It is also necessary, to a lesser extent, to remove multiple-scattering before processing an edge spectrum to extract quantitative microanalytical information.

The single-scattering spectrum SS(E) can be extressed as the sum of a core-loss signal CS(E) and a background signal BS(E) due to other single-particle excitations (for example, other lower-energy core losses or calence electron excitations) or collective excitations (the plasmon loss). Thus:

$$SS(E) = CS(E) + BS(E) \quad . \qquad - \quad 3.20$$

The experimental spectrum, ES(E), given by equation 3.12 may be expressed:

$$es = z(1 + (cs + bs) + (cs + bs)^2 . \frac{1}{2!} + \ldots) \qquad - \quad 3.21$$

In a typical spectrum, the core-loss signal CS(E) is very much weaker than the background signal at the respective maxima, and multiple-scattering of CS(E) with itself may be ignored. Equation 3.21 then simplifies to:

$$es = z(1 + cs)(1 + bs + bs^2/2! + \ldots). \qquad - \quad 3.22$$

The low-loss spectrum LS(E) is just the experimental spectrum without the core-loss contribution:

$$ls = z(1 + bs + bs^2/2! + \ldots). \qquad - \quad 3.23$$

Removal of the background from an experimental edge spectrum is equivalent to the removal of the multiply-scattered background spectrum given by equation 3.23. This is precisely the same as the high-energy region of the low-loss spectrum. The experimental edge spectrum with background removed is:

$$\begin{aligned} es - ls &= z(1 + cs)(\exp(bs)) - z(\exp(bs)) \qquad - \quad 3.24 \\ &= z.cs.\exp(bs). \end{aligned}$$

Therefore:

$$\frac{es - ls}{ls} = \frac{z.cs.\exp(bs)}{z.\exp(bs)} = cs. \qquad - \qquad 3.25$$

Thus, given the experimental edge spectrum, it is possible, in theory, to remove the background contribution and deconvolute with the experimental low-loss spectrum to yield the single-scattering core-loss spectrum CS(E). It is not necessary for the complete spectrum to be collected. In practise, most of the low-loss intensity is below 100 eV. The low-loss spectrum may be collected for a different length of time than the core-loss spectrum. All that this does is to introduce a scale factor into equation 3.25.

The presence of noise in the experimental data requires that the core-loss spectrum CS(E) evaluated from equation 3.25 be convoluted by a gaussian to limit the noise amplitude at fine energy scale, and this degrades the energy-resolution of the deconvoluted core-spectrum. It is convenient to reconvolute the core-spectrum with the zero-loss peak extracted from the low-loss spectrum.
The program DECONV (see appendix A) was written to perform these operations.

3.3.3.3 Other deconvolution techniques

1) van Cittert's method (Wertheim 1975, Cooper 1977):
Given two spectra A and B, this method is used to evaluate an approximation to the deconvolute C (where c = a/b) thus:

a) an initial guess, C_o, is made of the deconvolute (it is customary to choose $C_o = A$);

b) the current approximation, C_n, is convoluted with B thus giving $B*C_n$;

c) an error term $\varepsilon_n = A - B*C_n$ is formed, and this is used to correct C_n, yielding C_{n+1}.

Steps b) and c) are repeated until the error term is arbitrarily small. Provided that this technique converges, $|C_{n+1}| - |C_n| \rightarrow 0$, and it may be shown that $C_n * B \rightarrow A$. Thus C is the required deconvolute of A with B. In practise, the iterative procedure is continued until the error term is sufficiently small.

Therefore:

$$\frac{es - ls}{ls} = \frac{z.cs.\exp(bs)}{z.\exp(bs)} = cs. \qquad - \qquad 3.25$$

Thus, given the experimental edge spectrum, it is possible, in theory, to remove the background contribution and deconvolute with the experimental low-loss spectrum to yield the single-scattering core-loss spectrum CS(E). It is not necessary for the complete spectrum to be collected. In practise, most of the low-loss intensity is below 100 eV. The low-loss spectrum may be collected for a different length of time than the core-loss spectrum. All that this does is to introduce a scale factor into equation 3.25.

The presence of noise in the experimental data requires that the core-loss spectrum CS(E) evaluated from equation 3.25 be convoluted by a gaussian to limit the noise amplitude at fine energy scale, and this degrades the energy-resolution of the deconvoluted core-spectrum. It is convenient to reconvolute the core-spectrum with the zero-loss peak extracted from the low-loss spectrum.
The program DECONV (see appendix A) was written to perform these operations.

3.3.3.3 Other deconvolution techniques

1) van Cittert's method (Wertheim 1975, Cooper 1977):
Given two spectra A and B, this method is used to evaluate an approximation to the deconvolute C (where c = a/b) thus:

a) an initial guess, C_o, is made of the deconvolute (it is customary to choose $C_o = A$);

b) the current approximation, C_n, is convoluted with B thus giving $B*C_n$;

c) an error term $\varepsilon_n = A - B*C_n$ is formed, and this is used to correct C_n, yielding C_{n+1}.

Steps b) and c) are repeated until the error term is arbitrarily small. Provided that this technique converges, $|C_{n+1}| - |C_n| \to 0$, and it may be shown that $C_n * B \to A$. Thus C is the required deconvolute of A with B. In practise, the iterative procedure is continued until the error term is sufficiently small.

2) approximate partial multiple deconvolution:

Colliex *et al* (1976) use a simplified deconvolution scheme as follows:

The experimental spectrum is written

$$es = z(1 + ss + ss^2/2! + \dots). \qquad - \qquad 3.26$$

Note that z is required to be normalised to unit area in the following discussion. An estimate of the double-scattering is formed

$$ds = \frac{1}{2!}(es - z)^2 = z^2.ss^2/2! + o(ss^3) + \dots \qquad - \qquad 3.27$$

which is subtracted from the experimental spectrum, ES(E), yielding a partially-corrected spectrum

$$ps = z(\ 1 + ss + (1-z)ss^2/2! + \dots)\ . \qquad - \qquad 3.28$$

Second-order scattering is only completely removed when the resolution function of the spectrometer (Z(E)) is a delta function; otherwise an amount of residual second-order scattering is left which may vary across the spectrum. Having "removed" double-scattering, it is then possible to go on to higher orders of inelastic scattering, "removing" as many as is required. The accuracy of this technique may be estimated as follows:

Suppose that an overall accuracy of 5 % is required for the correction of second order scattering, then

$$|(1 - z)| < 0.05\ . \qquad - \qquad 3.29$$

As z is usually symmetric about zero, z is real. Thus

$$z > 0.95\ . \qquad - \qquad 3.30$$

The zero-loss peak is assumed to take the form of a gaussian σ wide. The fourier transform of Z(E) is z(U), where U is the independent variable in the fourier transform space (U). Thus the fourier transform of Z(E) is a gaussian $2\pi/\sigma$ wide

$$z(U) = \exp(-\sigma^2U^2/(2\pi)^2.2).a \qquad - \qquad 3.31$$

where: a is a normalisation factor. The inequality 3.30 gives

$$0.95 < \exp(-\sigma^2U^2/8\pi^2)/\exp(0) \qquad - \qquad 3.32$$

therefore

$$\frac{\sigma}{2\pi} < \frac{0.32}{U}\ . \qquad - \qquad 3.35$$

The maximum value of U for which the inequality should hold true is the maximum value of U at which ss(U) has appreciable amplitude. Considering SS(E) to be a gaussian of width Γ, ss(U) becomes a gaussian envelope of width $2\pi/\Gamma$, which may be taken for a convenient maximum value of U to be used in inequality 3.35. Therefore

$$\sigma < 0.32.\Gamma \qquad - \quad 3.36$$

Therefore, provided that the width of the zero-loss peak is less than one third the width of the plasmon peak, the removal of the double-plasmon scattering contribution will be accurate to better than 5 %.

A comment on these two techniques:

Van Cittert's method and the approximate partial deconvolution method have the advantage that they do not required fourier transforms to be taken of large data arrays and thus are not precluded from being used on small computer systems. They are not recommended for use on large scientific computers which have fast fourier transforms available because of the approximate nature of the second technique and problems associated with determining when the solution has converged sufficiently in the first technique. As the author has access to and IBM 370, these two techniques were not used.

3) Maximum entropy technique:

The deconvolution techniques mentioned thus far, except the partial multiple deconvolution technique, all exacerbate the unwanted effect of noise in the experimental data. Maximum entropy deconvolutions is a technique that yields a deconvolute with the same signal to noise ratio as the data, and , furthermore, the result is unique and may be produced from incomplete data. The technique will not be described in detail here, the reader is referred to Gull & Daniells (1978). The disadvantage of this technique is that, although it produces a unique deconvolute which satisfies the constrain of maximising entropy (a somewhat arbitrary measure of the data), the deconvolute is not necessarily the best deconvolute (Fiddy & Greenaway 1978). In the case of energy-loss deconvolution, given a power-law background curve with no features, the deconvolution of this curve with a low-loss curve corresponding to a foil about 1 mean free path thick should leave the power-law background relatively unchanged in the edge-loss region. If can be seen from figure 3.8 that the maximum entropy deconvolute does not follow the slope of the original power-law. This is called the 'tilt' error,

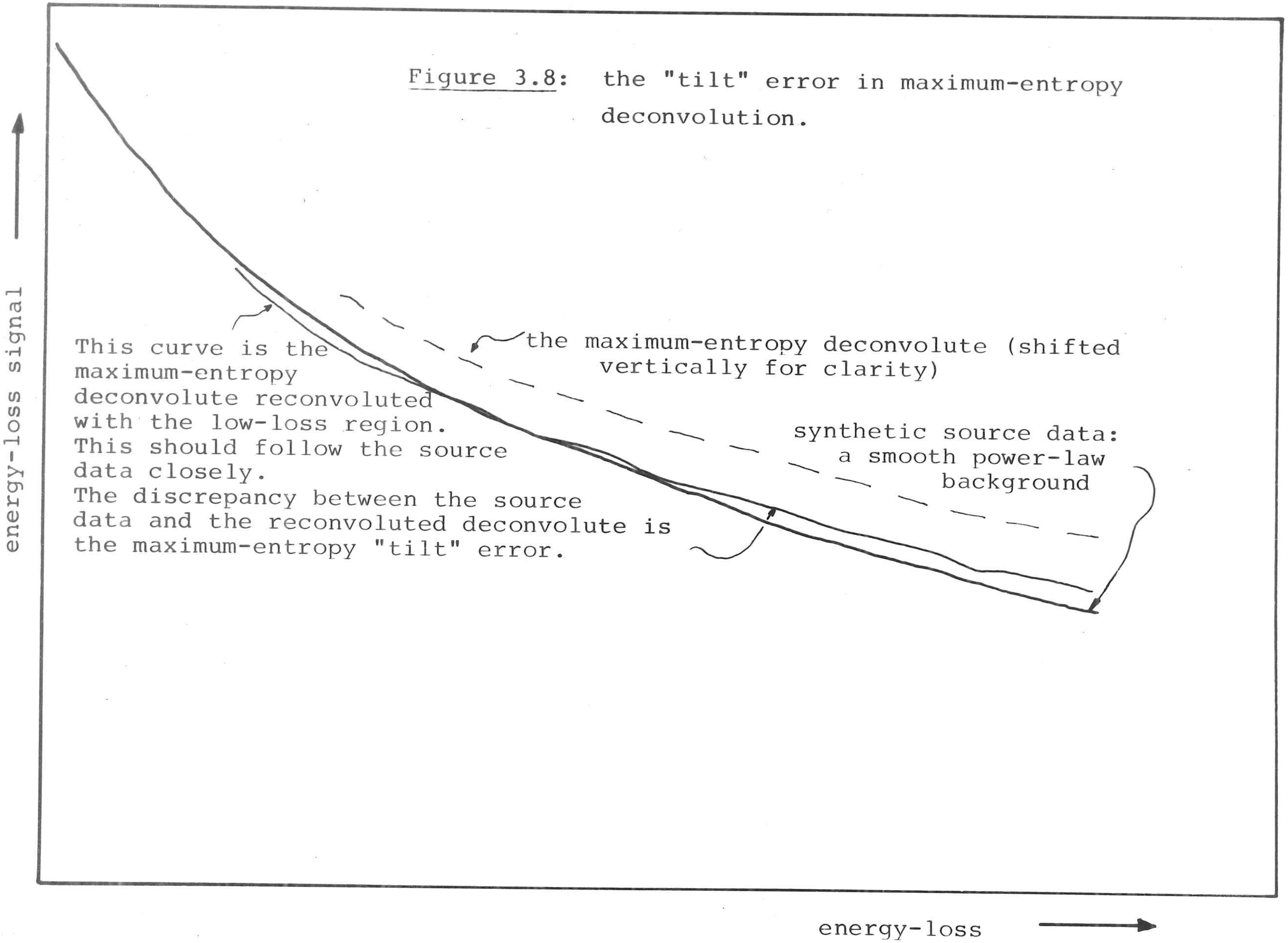

Figure 3.8: the "tilt" error in maximum-entropy deconvolution.

the maximum-entropy deconvolute (shifted vertically for clarity)

This curve is the maximum-entropy deconvolute reconvoluted with the low-loss region. This should follow the source data closely. The discrepancy between the source data and the reconvoluted deconvolute is the maximum-entropy "tilt" error.

synthetic source data: a smooth power-law background and would be disastrous in quantitative EELS, and therefore this technique was abandoned. Moreover, there were problems in defining the action to be taken at the ends of the spectra to minimise termination effects.

3.3.3.4 Errors in deconvolution

This section discusses two error that can effect the deconvolution techniques discussed above:

1) noise:

The experimental sepctrum, being the accumulated number of electrons measured within a paricular energy range in each channel, must display statistical variations on these accumulated electron counts. The probability of having recorded n electrons in a particular channel where m is the expected value may be expressed as a poisson distribution (Papoulis, 1965)

$$P(n) = \exp(-m).\frac{m^n}{n!} \quad . \qquad - \quad 3.37$$

The variance of this distribution, for large n ($n > 100$) is

$$\sigma = \sqrt{n}. \qquad - \quad 3.38$$

The variance may be regarded as an average statistical noise signal added to the noise-free signal representing the "true" spectrum. The signal to noise ratio is:

$$S/N = 1/\sqrt{n}. \qquad - \quad 3.39$$

Statistical noise in an energy-loss spectrum introduces a noise component in the fourier-transformed spectrum which is of uniform average power density. Consider two experimental spectra S1 and S2 which may be expressed as the sum of the noise-free components ($S1_c$ and $S2_c$) and the statistical noise components (N1 and N2):

$$S1 = S1_c + N1,$$
$$S2 = S2_c + N2. \qquad - \quad 3.40$$

In general, $S1_c$ and $S2_c$ are smoother than N1 and N2 (which requires that the channel energy width be finer than the spectrometer resolution). Thus $s1_c$ and $s2_c$ (the fourier transformed correct spectra) approach zero at the limit of high inverse energy (inverse energy being the inverse fourier variable to energy) whereas n1 and n2 have a uniform power density (i.e. the locally averaged value of the modulus of n1 and n2 is constant over the whole range of inverse energies used), even out to the highest inverse energy. Thus while $s1_c$ and $s2_c$ approach zero at high inverse energy, the results of deconvolution of the experimental spectra:

$$s3 = \frac{s1_c + n1}{s2_c + n2} \qquad - \quad 3.41$$

need not approach zero at high inverse energy. Indeed, is is entirely likely that there may be a zero (or very low value) of the denominator at an inverse energy at which n1 is finite. This introduces an arbitrarily-large noise component into the experimental deconvolute at that value of the inverse energy.

The noise component in the experimental deconvolute is:

$$n3 = \frac{s1_c + n1}{s2_c + n2} - \frac{s1_c}{s2_c} \simeq \frac{n1}{n2} \text{ at large inverse energy} \qquad - \quad 3.42$$

This noise component is only likely to become very large when:

$$|s1_c| < |n1| \qquad \text{and} \qquad |s2_c| < |n2|,$$

i.e. at high inverse energies. The noise component may be suppressed by multiplication of s3 with a gaussian of maximum width σ where σ is the lowest inverse energy at which:

$$|s1_c| < |n1| \qquad \text{or} \qquad |s2_c| < |n2|.$$

In practise, this may be satisfied by re-convoluting the deconvoluted spectrum with the zero-loss peak of the same experimental low-loss spectrum, although this will not be sufficient if the foil is very thick. An increase of energy resolution may only be achieved at the cost of a decreased signal-to-noise ratio (S/N). Deconvolution may be used to remove spurious structure from noisy data, provided that the overall energy resolution remains roughly constant (Cooper 1977).

2) angular convolution correction:

The energy-loss spectra considered thus far have been taken to be as a function of energy alone. The removal of multiple scattering has ignored the possibly-different angular distribution of multiple inelastic scattering compared to the angular distribution of the single-scattering contribution. In this section, the error introduced by ignoring the angular distributions is examined and a table is presented that may be used to determine then conventional deconvolution is seriously in error.

The single-scattering spectrum has been extressed in section 2.3, equation 2.120 which approximates the weak angular dependence of the oscillator strength on scattering angle (α) by introducing a step function

$$G(\theta,E) = 1,\ \theta < \theta_c \qquad - \quad 3.43$$
$$= 0,\ \theta > \theta_c$$

where: $\theta_c = \sqrt{E/E_o}$,

E = energy loss

E_o = primary electron energy.

Single scattering into an axial aperture of semi-angle α is given by

$$\left[\frac{\partial(SS)}{\partial E}\right]_{E,\theta} = B(E).\int_0^{\alpha} \frac{\theta.d\theta.G(\theta,E)}{\theta^2 + \theta_E^2} \qquad - \quad 3.44$$

where: $B(E)$ is a function of energy alone.

Double scattering to a final energy-loss E by two events of energy-loss E1 and E2 (= E - E1) results in a convolution in both energy and angle:

$$\left[\frac{\partial(DS)}{\partial E}\right] = \int_{E1=0}^{E} dE1.B(E1).B(E - E1).\ \int_0^{\theta_{c1}} d\theta 1.\ \int_0^{2\pi} \frac{d\phi}{2\pi} \times$$

$$\times \int_0^{\theta_{c2}} \frac{\theta 1.\theta 2.d\theta 2}{(\theta 1^2 + \theta_{E1}^2).(\theta 2^2 + \theta_{E2}^2)} \times$$

$$\times \quad H(\theta 1,\theta 2,\alpha,\phi).G(\theta 1,E1).G(\theta 2,E2) \qquad - \quad 3.45$$

where:

$$H(\theta 1,\theta 2,\alpha,\phi) = 1,\ \theta 1^2 + \theta 2^2 - 2\theta 1.\theta 2.\cos(\phi) < \alpha^2$$
$$= 0, \qquad \text{otherwise.}$$

Conventional deconvolution in energy alone would correct for a double-scattering contribution of:

$$\left[\frac{\partial(DS)}{\partial E}\right]_E = \int_0^E dE1.B(E1).B(E - E1) \qquad \times - \quad 3.46$$

$$\times \int_0^{\alpha} \frac{d\theta 1.\theta 1.G(\theta 1,E1)}{(\theta 1^2 + \theta_{E1}{}^2)} \int_0^{\alpha} \frac{d\theta 2.\theta 2.G(\theta 2,E2)}{(\theta 2 + \theta_{E2}{}^2)}$$

The ratio between equations 3.45 and 3.46 may be formed to find a correction factor μ.

$$\mu(E1,E2) = \int_0^{\theta_{c1}} d\theta 1 . \int_0^{2\pi} \frac{d\phi}{2\pi} . \int_0^{\theta_{c2}} \frac{d\theta 2.\theta 2}{\theta 2^2 + \theta_{E2}^2} . \frac{\theta 1}{\theta 1^2 + \theta_{E1}^2} \times$$

$$\times \quad H(\theta 1,\theta 2,\alpha,\phi).G(\theta 1,E1).G(\theta 2,E2) \quad \times$$

$$\times \quad \left[\int_0^{\alpha} \frac{d\theta 1.\theta 1.G(\theta 1,E1)}{\theta 1^2 + \theta_{E1}^2} . \int_0^{\alpha} \frac{d\theta 2.\theta 2.G(\theta 2,E2)}{\theta 2^2 + \theta_{E2}^2} \right]^{-1} \qquad - \quad 3.47$$

Any deviation of μ from unity indicates that conventional deconvolution in energy alone will not correctly remove double-scattering events.

The correction factor, μ, has been colculated by a Monte-Carlo method for several values of α, E1 and E2; and is presented as a table in figure 3.9. Note that values of $\mu > 1$ imply that conventional deconvolution will underestimate the amount of double-scattering present. It can be see from figure 3.9 that the double-scattering angular correction only becomes important for small values of collection aperture. $\mu - 1$ is less than 10 % for collection semi-angles (α) greater than 10 milli-radians. For typical plasmon plus core-loss double-scattering, with very small collection angles ($\alpha < 1$ mR), $\mu - 1$ may be of the order of unity.

The main use of these results is as an indication of when conventional deconvolution is likely to fail. It does not seem possible to calculate the angular correction for more than second-order inelastic scattering because of the prohibitive amount of computer time required. It is, however, possible to use the angular correction, μ, in numerical deconvolution as long as the foil is thin enough ($t/\lambda_{\text{plasmon}} < 0.1$) for the three-scattering events not to effect the results at the current accuracies achieved ($\simeq 5\%$). The double-scattering contribution in the region of the core-loss can now be approximated by:

$$DS(E) = \mu(E_p,E_c) \int_0^E SS(E1).SS(E - E1).dE1 \qquad - \quad 3.48$$

and the data can be corrected for double-scattering by removing this term using a modification of the approximate deconvolution

α (mRad)	E_1 (eV)	E_2 (eV)	μ	±
5	20	100	1.00	0.02
		200		
		400		
		800	1.07	
		1600	1.15	
	30	100	1.00	
		200		
		400		
		800	1.09	
		1600	1.25	
2	20	100	1.00	
		200	1.05	
		400	1.12	
		800	1.30	0.03
		1600	1.65	0.07
	30	100	1.00	0.02
		200	1.07	
		400	1.16	
		800	1.43	0.03
		1600	1.57	0.07
1	20	100	1.10	0.02
		200	1.24	0.03
		400	1.44	
		800	1.67	0.1
		1600	2.5	0.2
	30	100	1.07	0.02
		200	1.31	0.03
		400	1.47	
		800	1.9	0.1
		1600	2.6	0.2
0.5	20	100	1.36	0.03
		200	1.7	0.1
		400	2.2	0.2
		800	2.3	0.2
		1600	3.0	0.3
	30	100	1.40	0.03
		200	1.9	0.1
		400	2.2	0.1
		800	3.2	0.3
		1600	3.6	

Figure 3.9: computed values of the angular convolution correction. E_o = 80 keV.

procedure of section 3.3.3.3.2.

3.3.4 Kramers-Kronig analysis

The single-scattering energy-loss spectrum may be written (Raether 1965):

$$SS(E,\theta) = \frac{A.\theta d\theta}{\theta^2 + \theta_E^2} . \operatorname{Im}(-1/\varepsilon) \qquad - \quad 3.49$$

where: A in a constant.

The dependence of Im(-1/ε) on scattering angle is weak and may be modelled by a step funtion (Inokuti 1971)

$$\begin{aligned} G(E,\theta) &= 1, \ \theta < \theta_c \\ &= 0, \ \theta > \theta_c \end{aligned} \qquad - \quad 3.50$$

where: $\theta_c = \sqrt{E/E_o}$.

The energy-loss data represent an integration of equation 3.49 over angle (as defined by the collector angle or probe convergence angle). The angular dependence may be removed from the energy-loss data by diving by the integral ν(E) where

$$\nu(E) = \int_0^\alpha \frac{d\theta.\theta}{\theta^2 + \theta_E^2} . G(E,\theta) \qquad - \quad 3.51$$

leaving

$$SS'(E) = B.\operatorname{Im}(-1/\varepsilon) \qquad - \quad 3.52$$

where: B is a constant. Thus, given an energy-loss spectrum, it is possible to obtain a function proportional to Im(-1/ε). The technique of Kramers-Kronig analysis enables Re(ε) to be obtained from a knowledge of Im(ε), provided that the function ε is analytic (see section 2.1.3.5). Thus, given Im(-1/ε), it is possible to obtain Re(-1/ε) and hence Re(ε) and Im(ε). The theory of section 2.1.3.5 gives that:

$$\operatorname{Re}(1/\varepsilon(\omega)) = 1 - \frac{2}{\pi} P \int_0^\alpha \frac{\operatorname{Im}(-1/\varepsilon(\Omega)).\Omega d\Omega}{\Omega^2 - \omega^2} \qquad - \quad 3.53$$

where: P implies the Cauchey principle part (defined in section 2.1.3.5).

It is possible to obtain an absolute value of the energy-loss function Im(-1/ε) given that the real part of the dielectric constant at zero frequency is known ($\varepsilon_1(0)$). In the case of metals, $\varepsilon_1(0)$ is infinite, and for non-conductors, $\varepsilon_1(0)$ may be large (about 10). Thus 1/ε(0) is known for the specimen under examination. Equation

3.53 may be re-written

$$1 - \mathrm{Re}(1/\varepsilon(0)) = \frac{2}{\pi}.\frac{1}{B}.P\int_0^{\alpha}\frac{SS(E).dE}{E} \quad . \qquad - \quad 3.54$$

Hence, given SS(E), the scale-factor B may be determined. Note that, for a 10 % accuracy in the scale factor, $1 - \mathrm{Re}(1/\varepsilon(0))$ may be approximated by the value of unity, even for insulators (Raether 1965).

The programs DENSITY was written (see appendix A) to perform Kramers-Kronig analysis of energy-loss data. Given SS(E), it evaluates the scale factor B and then performs the Kramers-Kronig transformation to obtain $\mathrm{Re}(1/\varepsilon(E))$ and thence $\mathrm{Re}(\varepsilon(E))$ and $\mathrm{Im}(\varepsilon(E))$. $\mathrm{Im}(-1/\varepsilon)$, $\mathrm{Re}(\varepsilon)$ and $\mathrm{Im}(\varepsilon)$ are displayed graphically.

It is seen that energy-loss spectroscopy is a powerful tool by which the complete dielectric response of a specimen may be obtained (Raether 1965, Daniels et al 1970, Taft & Philipp 1965, Wehenkel & Gauthe 1974a,b) with a resolution of approximately 1.5 eV in the case of the HB5 STEM. One advantage of this technique is that data may readily be collected from energies which correspond to the unltraviolet region of the photon spectrum, where optical techniques for determining the dielectric function are subject to experimental difficulties. The outstanding disadvantage of this technique is that the energy - resolution of EELS is usually far surpassed by that of optical techniques.

The reader is referred to papers by Raether (1965) and Daniels et al (1970) for an excellent discussion of this technique.

It was desired to investigate the effect of noisy data on the Kramers-Kronig transformation. A theoretical investigation proved intractable. To this end, the program GENERATE (see appendix A) was used to synthesise noisy energy-loss spectra. The spectrum was generated using the following procedure:

1) the dielectric function $\varepsilon(E)$ was calculated for given values of plasmon energy and the width of the plasmon energy-loss peak (which equals 1/scattering-time, τ) using a free-electron model (equation 2.69);

2) the energy-loss function Im(-1/ε) was obtained from ε and scaled corresponding to a thin specimen (≃ 50 Å) so that multiple-scattering would not be introduced by multiple convolution;

3) the spectrum thus obtained was multiply convoluted and then convoluted with a zero-loss peak which represents the loss of energy resolution due to the spectrometer. The zero-loss peak was chosen to be 1.5 eV wide (FWHM);

4) Poisson noise was then added to the spectrum and the spectrum was digitised (rounded to the nearest integer) to simulate electron detection statistics.

Figure 3.10a shows the dielectric funtion generated in step 1) above for a 20 eV plasmon peak 10 eV wide (FWHM). Steps 2) and 3) were performed and the DENSITY program was applied to this spectrum. Figure 3.10b shows the recovered energy-loss function which peaks at 19.3 eV and is 10 eV wide. The calculated peak position is 19.3 eV also (using equation 2.72), and Re(ε) should pass through zero as 17.3 eV (using equation 2.71).
Figure 3.10c shows the dielectric function recovered from the noise-free spectrum. It can be seen that, apart from the region near 0 eV (0 to 3 eV), agreement between the synthesised dielectric function and the recovered dielectric function is excellent.
The recovered dielectric function Re(ε) passed through zero at 17.2 eV, 0.1 eV below the predicted value (the discrepancy being due to digitisation and rounding errors). It can be seen that Kramers-Kronig analysis of the synthesised noise-free spectrum is able to recover the dielectric function without significant error.

This procedure was repeated, but step 4) (above) was included, prior to which, the plasmon peak had been scaled to simulate a peak channel count of 30 electrons/channel, which is far below that which is considered to be a useable low-loss spectrum. The Kramers-Kronig analysis was performed, as before, and the recovered energy-loss function is shown in figure 3.10d. It can be seen to be extremely noisy, and shows digitisation error near 42 eV. The peak position, height and width agree with the values of figure 3.10b. Thus, the presence of noise has not adversely affected the normalisation process. The dielectric funtion is presented in figure 3.10e.

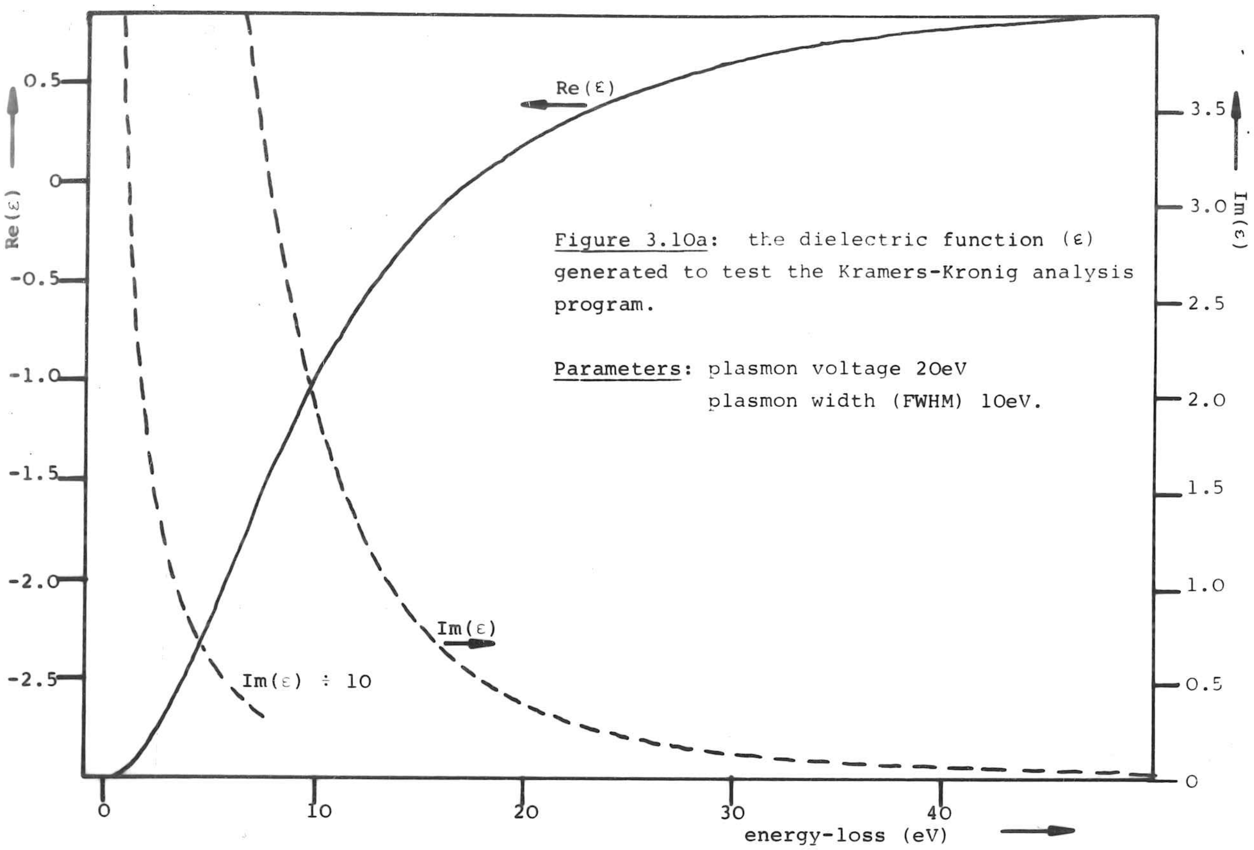

Figure 3.10a: the dielectric function (ε) generated to test the Kramers-Kronig analysis program.

Parameters: plasmon voltage 20eV
plasmon width (FWHM) 10eV.

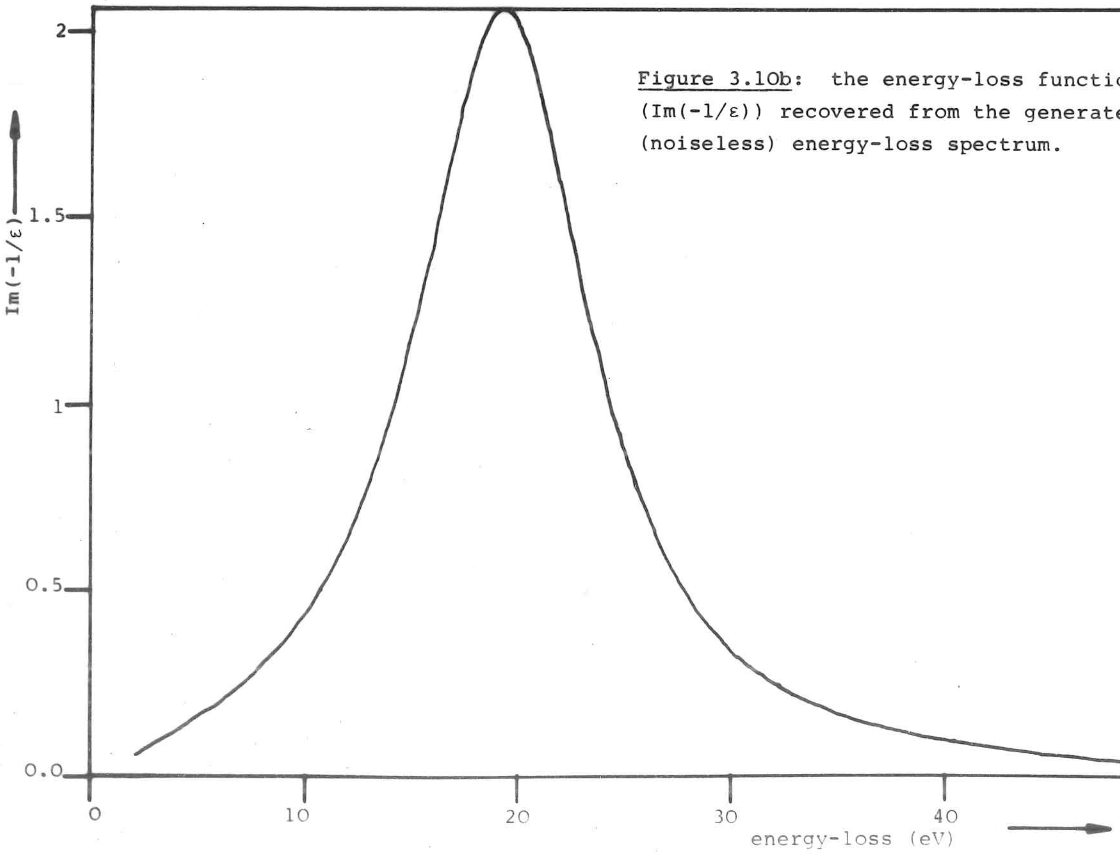

Figure 3.10b: the energy-loss function (Im(-1/ε)) recovered from the generated (noiseless) energy-loss spectrum.

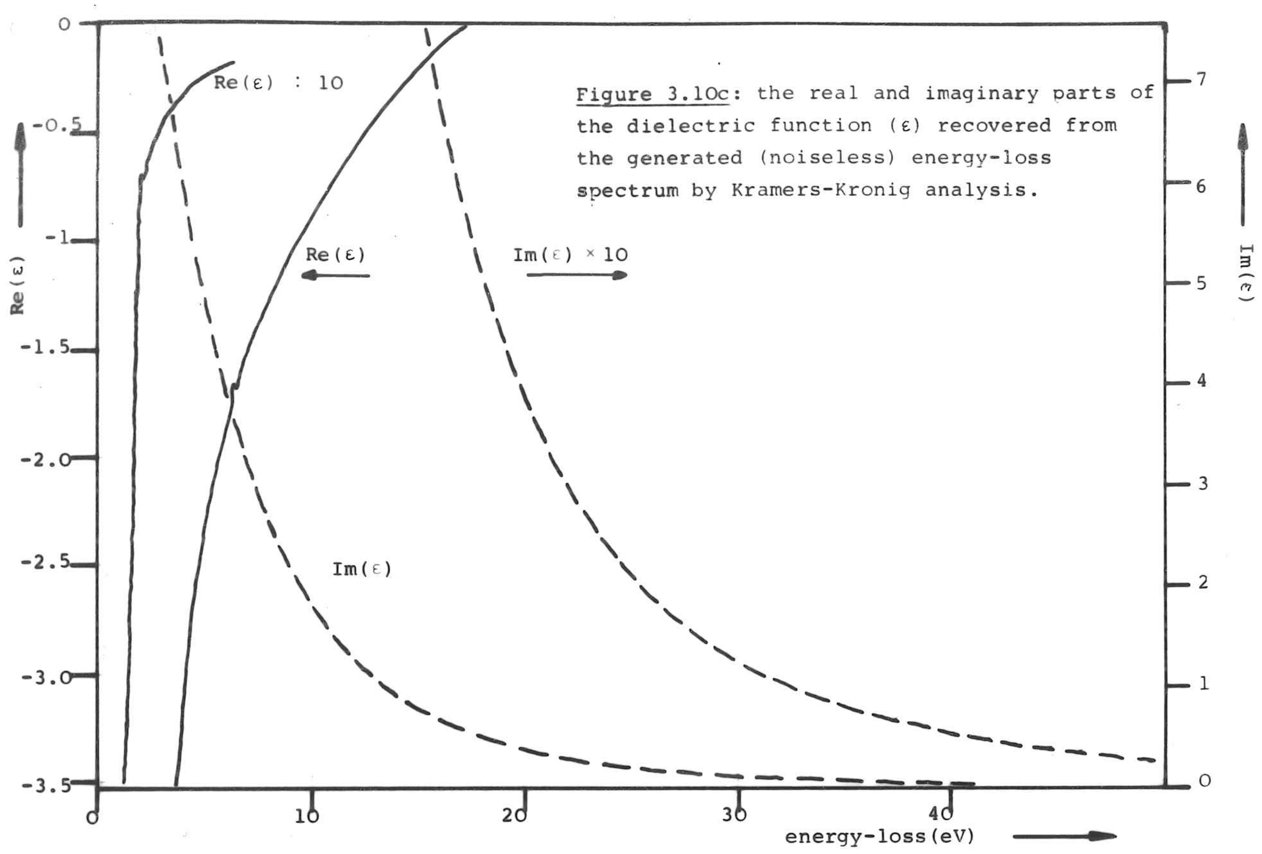

Figure 3.10c: the real and imaginary parts of the dielectric function (ε) recovered from the generated (noiseless) energy-loss spectrum by Kramers-Kronig analysis.

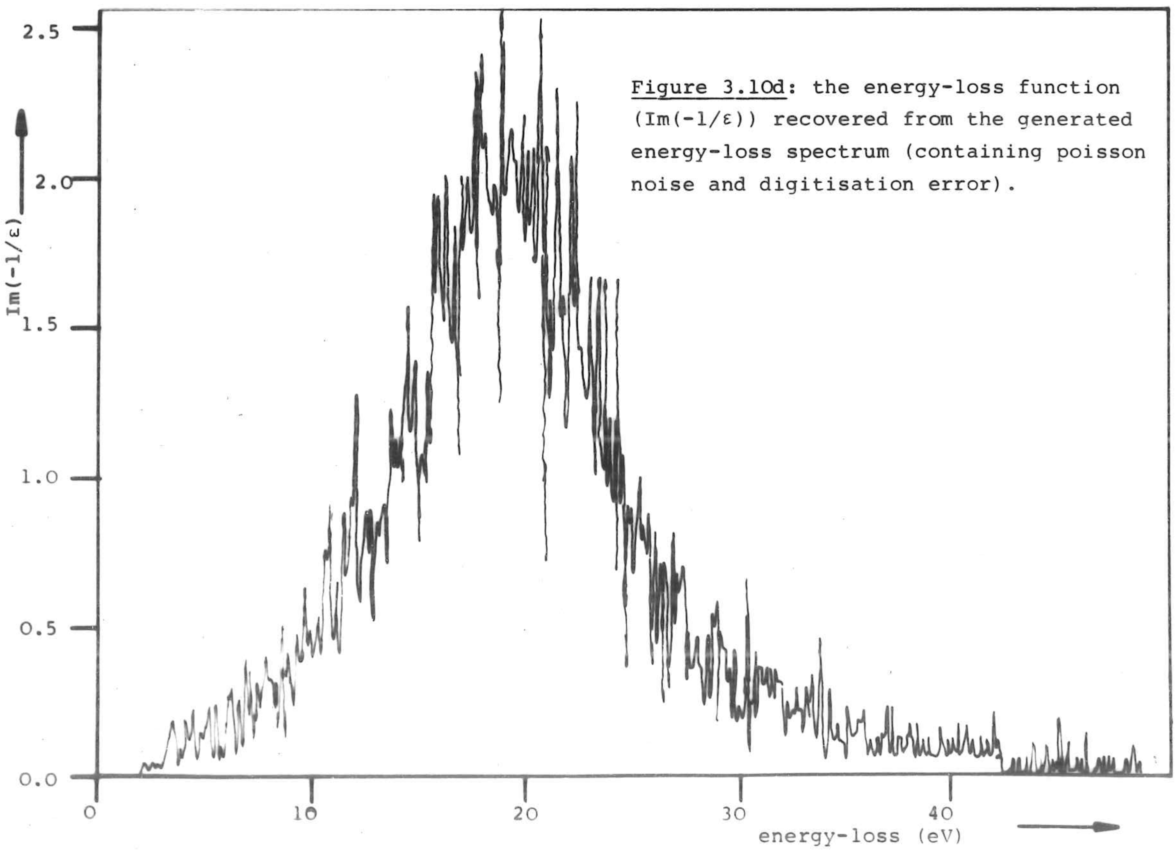

Figure 3.10d: the energy-loss function (Im(-1/ε)) recovered from the generated energy-loss spectrum (containing poisson noise and digitisation error).

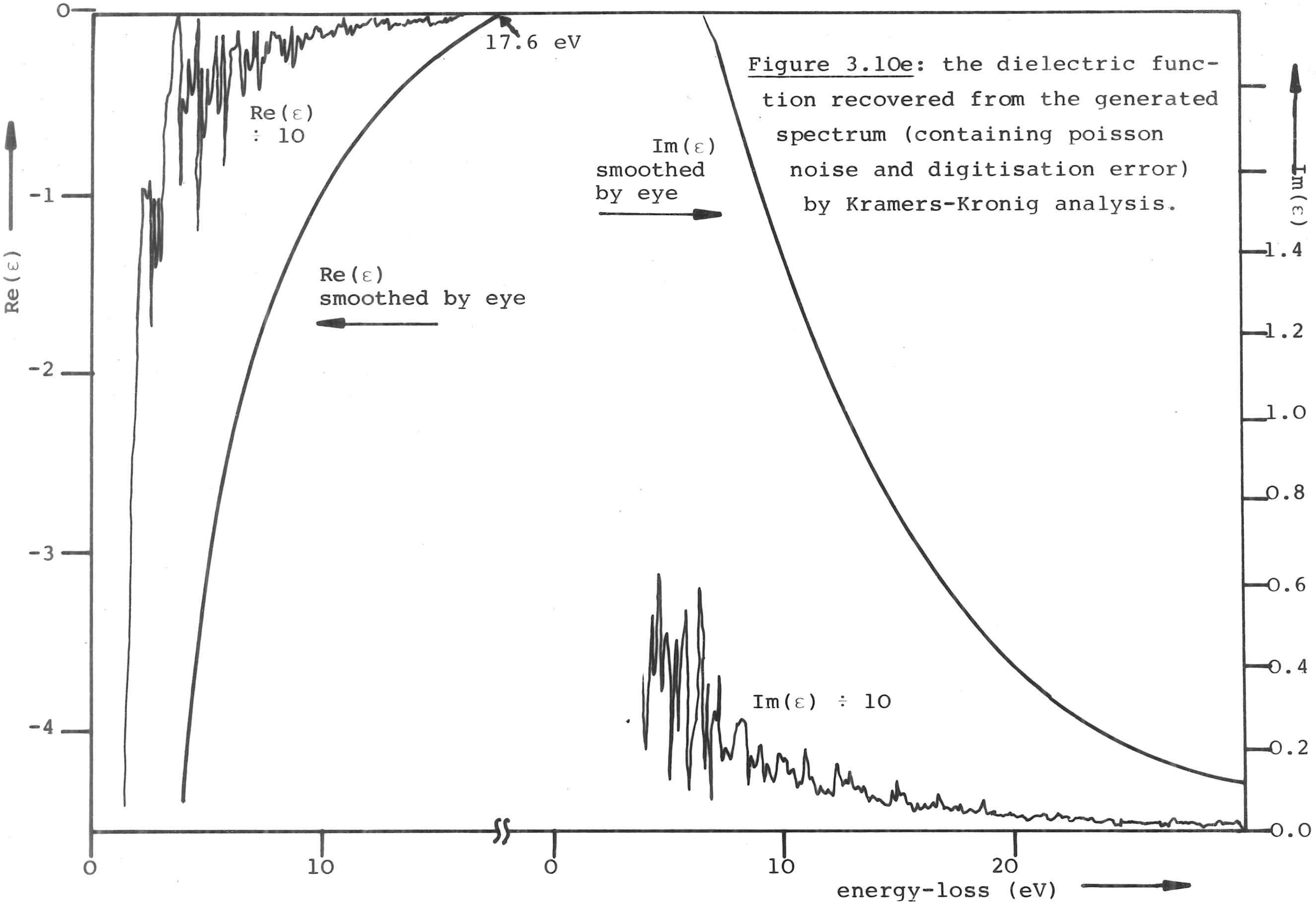

Figure 3.10e: the dielectric function recovered from the generated spectrum (containing poisson noise and digitisation error) by Kramers-Kronig analysis.

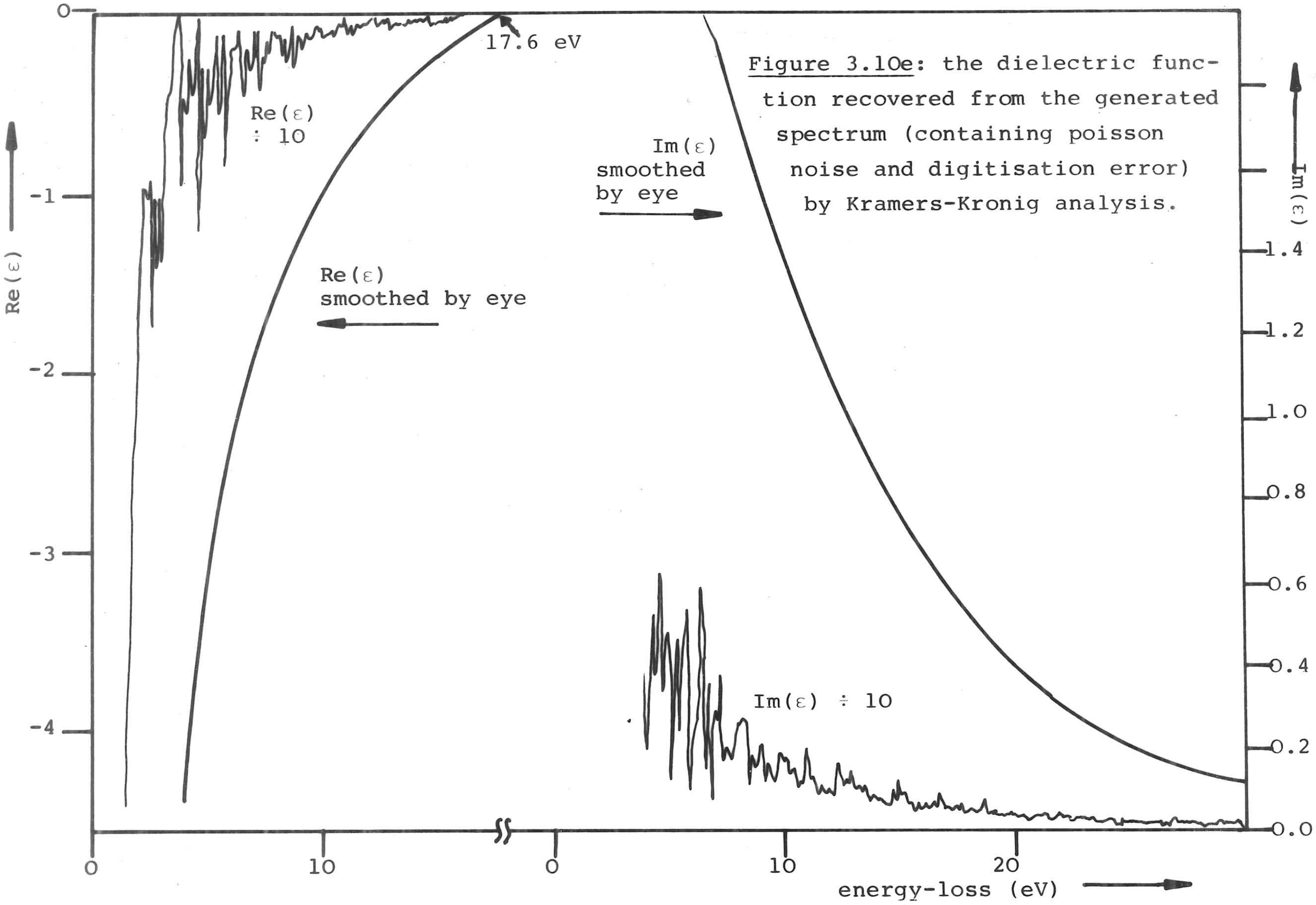

Figure 3.10e: the dielectric function recovered from the generated spectrum (containing poisson noise and digitisation error) by Kramers-Kronig analysis.

The signal to noise ratio for both curves is similar to an average signal to noise ratio in the energy-loss data (≃ 4:1). The two curves in figure 3.10e at higher magnification have been smoothed by eye, the eye being an excellent instrument by which means to extract an averaged signal or smooth trend from extremely noisy data. Re(ε) passes through zero near 17.5(±0.5) eV, in excellent agreement with the noise-free figure. Spot comparisons of values of Re(ε) and Im(ε) measured from figures 3.10e and 3.10c show that the effect of noise in the energy-loss spectrum is to introduce noise in the recovered spectrum, but not to cause any observable gross error in scale or position of either of the two curves.

3.3.4.1 Sum rules - $n_{effective}$

It can be shown, from the sum rules of the oscillator strength (Nozieres & Pines 1958,1959, Raether 1965, Fano & Cooper 1968, Colliex et al 1976) that a sum-rule may be expressed for the energy-loss function, Im(-1/ε), viz:

$$\int_0^\infty \omega \mathrm{Im}(-1/\varepsilon)\, d\omega \quad = \quad \frac{\pi}{2}\omega_p^2 \quad . \qquad - \quad 3.55$$

It is possible to define an effective number density of electrons taking part in the energy-loss spectrum up to a frequency ω, $n_{eff}(\omega)$

$$n_{eff}(\omega) \quad = \frac{n}{\omega_p^2}.\frac{2}{\pi}.\int_0^\omega \omega' \mathrm{Im}(-1/\varepsilon)\, d\omega' \qquad - \quad 3.56$$

where: n is the number density of electrons/units volume,

ω_p is the plasmon frequency

$$\omega_p^2 \quad = \quad \frac{ne^2}{\varepsilon_o m} \qquad - \quad 3.57$$

Therefore equation 3.56 may be expressed:

$$n_{eff}(\omega) \quad = \quad \frac{2\varepsilon_o m}{\pi e^2}.\int_0^\omega \omega' \mathrm{Im}(-1/\varepsilon(\omega'))\, d\omega' . \qquad - \quad 3.58$$

A similar expression may be used to calculate the effective number of electrons taking part in transverse oscillations up to a frequency ω , which is relevent to optical studies of the dielectric function,

$$n_{\perp eff}(\omega) \quad = \quad \frac{2\varepsilon_o m}{\pi e^2}.\int_0^\omega \omega' \mathrm{Im}(\varepsilon)\, d\omega' . \qquad - \quad 3.58$$

The program DENSITY (see appendix A) calculates both n_{eff} and $n_{\perp eff}$, given an energy-loss spectrum, including the low-loss region, and presents the results graphically. For an example of the use of n_{eff}, the reader is referred to the work of Colliex et al (1976).

3.3.5 Numerical extraction of EXELFS

The experimental energy-loss signal in the tail of a core-loss may show fine-structure that may extend over hundreds of electron volts. The theory of chapter 2 (section 2.2.6) results in an expression for the experimental cross-section:

$$\left.\frac{\partial^2\sigma}{\partial\Omega\partial\omega}\right|_{expt} = (\chi(k) + 1).\left.\frac{\partial^2\sigma}{\partial\Omega\partial\omega}\right|_{atomic} \qquad - \quad 3.59$$

where: $\left.\frac{\partial^2\sigma}{\partial\Omega\partial\omega}\right|_{atomic}$ represents the atomic inelastic-scattering cross-section for the core-loss under investigation. It is required to be able to extract the modulations term $\chi(k)$ from the experimental data in order to compare the observed and theoretical radial distribution functions (RDF's) for a specimen (see chapter 5). Figure 3.11a shows the boron-K core-loss region of the energy-loss spectrum of graphitic boron nitride about 80 Å thick.

The energy-loss spectrum consists of the following components:

1) a background which is a straight line in log-log space, and hence is a power-law in linear space (i.e. of the form AE^{-r} where A and r are constants). This is in agreement with theory (Fano & Cooper 1968).

2) a core-loss signal due to the boron-K core-loss;

3) a contribution due to multiple inelastic scattering after the core-loss which is negligible for a very thin specimen;

4) a contribution due to other core-losses, in this case, the nitrogen -K core-loss at 400 eV. The practical implication of this term is to limit the range of energy over which EXELFS may be extracted from preceeding edges.

The background contribution is extrapolated beyond the boron-K edge by fitting a power-law curve AE^{-r} to the background before the edge. The background contribution is then removed by subtracting the extrapolated background. At this point, multiple-scattering can be removed by using a deconvolution procedure (see section 3.3 and appendix A). The contribution due to other following edges can only be removed by windowing the spectrum such that any following edges are excluded. The presence of bandstructure near the core-loss edges is not taken into account in the simple EXELFS formulation, hence data within ≃30 eV of the edge should be excluded by introducing a low-energy window (see chapter 5). This low-energy limit and the previous high-energy limit define a window within which the data should be adequately described by the simple EXLEFS theory (equations 2.114 or 3.59).

The atomic cross-section is assumed to vary smoothly with no structure in K-space coarser than a chosen value of Δk. The value of Δk is chosen so that the nearest neighbor spacing introduces structure finer than Δk in $\chi(k)$ (in practise, $\Delta k \simeq 3\ \text{Å}^{-1} \equiv R = 1\text{Å}$).

Each point within the energy window defined above is processed as follows to obtain a smoothed version of the energy-loss spectrum ($SS_{smoothed}$):

1) for the chosen window in K-space, Δk, the corresponding upper and lower bounds in Energy-space are calculated. A power law, AE^{-r}, is fitted to the data within this window;

2) the value of the power-law fit at the point being processed is evaluated and defines the value of the smoothed spectrum at this point.

The modulations $\chi(E)$ may then be evaluated using (see fig 3.11b):

$$\chi(E) = \frac{SS_{expt} - SS_{smoothed}}{SS_{smoothed}} . \qquad - \quad 3.60$$

The modulations $\chi(E)$ are then transformed from energy to wave-vector space. The origin of K-space is chosen to be at the point in the energy-loss spectrum halfway up the edge, although this may be varied, if necessary (see appendix A: RAMP). The transformation of the independent variable is given by:

$$k = \frac{2m}{\hbar} (E - E_{edge})^{0.5} . \qquad - \quad 3.61$$

The modulations $\chi(k)$ are then multiplied by k^2 partially to compensate for the term $A(k)/k$ in equation 2.114, and then multiplied by a gaussian centred at zero wave-vector of standard deviation $16\ \text{Å}^{-1}$. These two processes reduce the effect of statistical noise at high

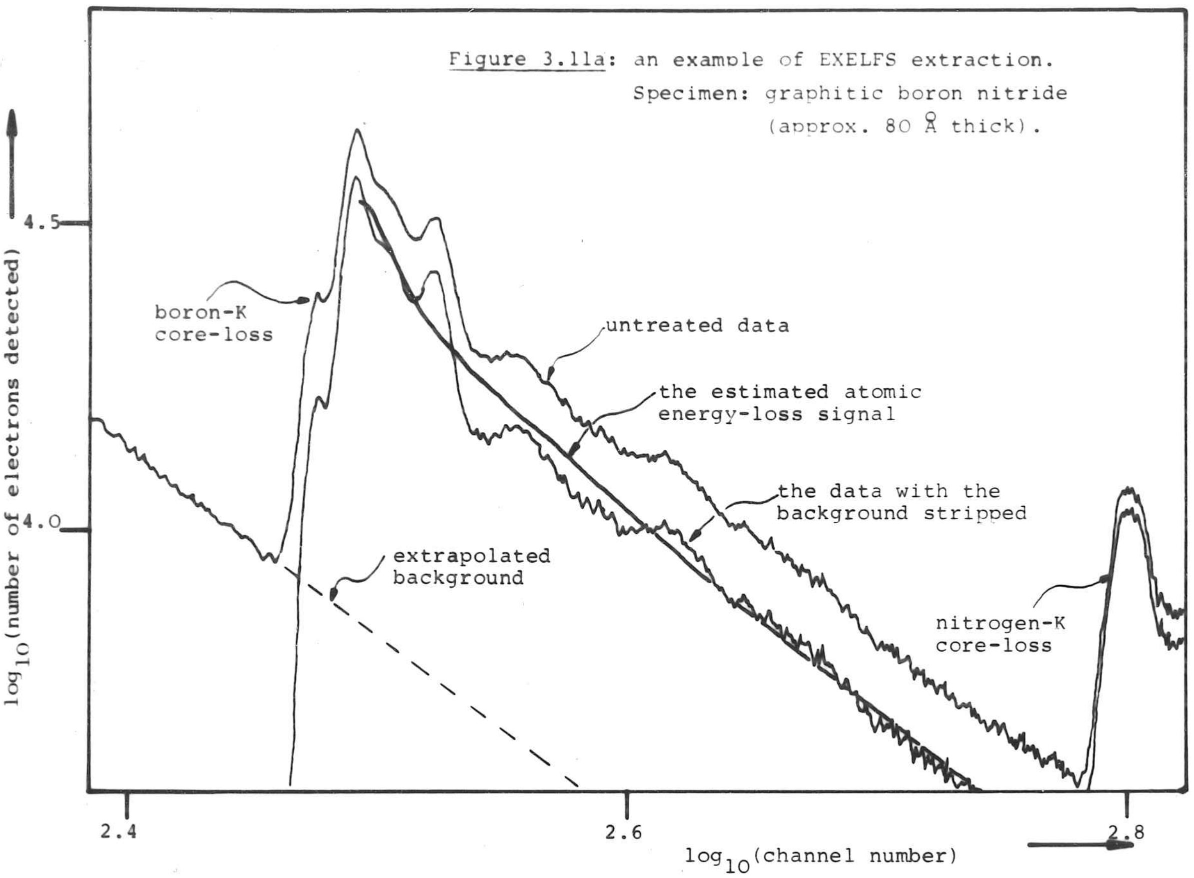

Figure 3.11a: an example of EXELFS extraction. Specimen: graphitic boron nitride (approx. 80 Å thick).

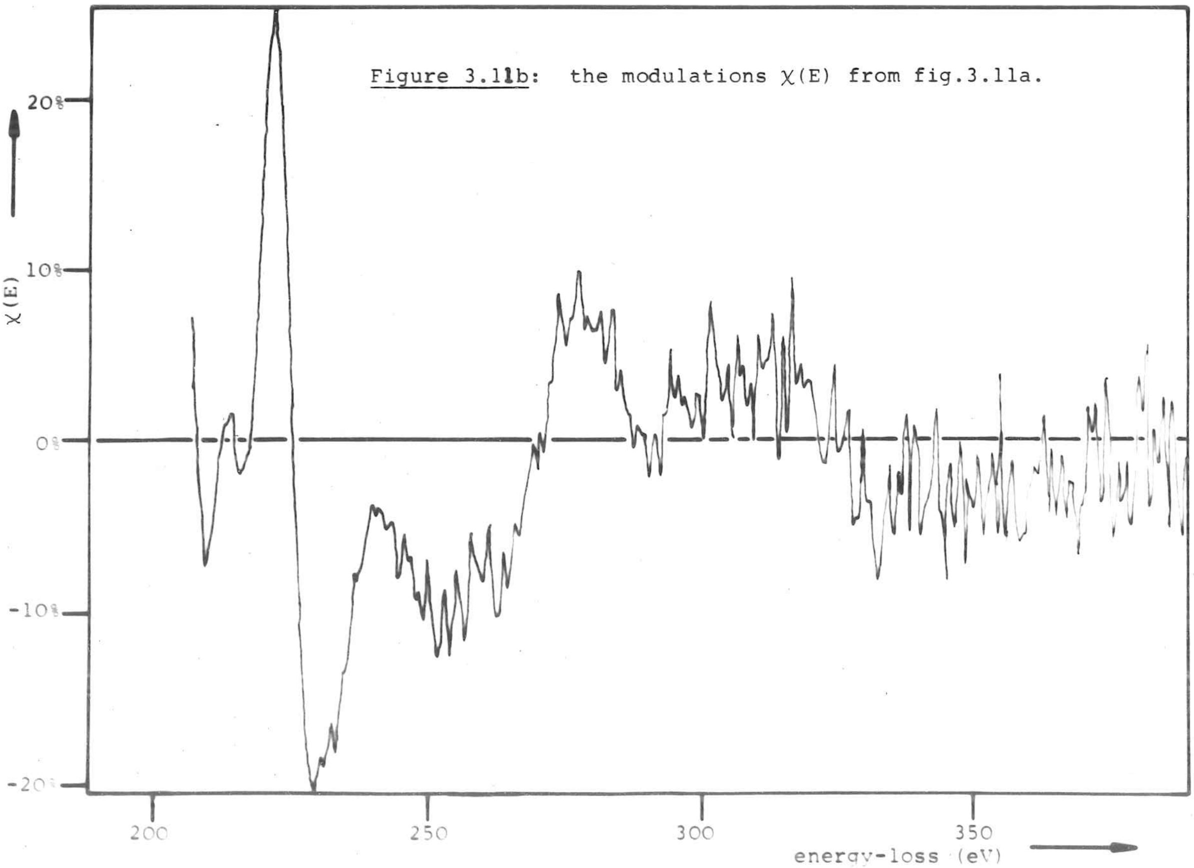

Figure 3.11b: the modulations $\chi(E)$ from fig.3.11a.

values of wave-vector compared with a more-correct treatment which approximates A(k)/k by k^{-3}. The effects of these operations are demonstrated in section 5.3.1.3.

The modulations are the multiplied by a window function which eliminates termination effects by turning off and on smoothly, over a 2 $Å^{-1}$ wave-vector range, at the extrema of the energy window defined above. The fourier transform of the modulations is evaluated and the modulus of the fourier transform is displayed graphically. The RDF, thus displayed, is an approximation of the radial distribution function given by:

$$\sum_j \frac{N_j}{R_j^2}.\delta(R - R_j) \qquad - \quad 3.62$$

where: N_j is the number of atoms in shell j situated a distance R_j away from the origin atom.

In practise, the experimentally-determined RDF will not be a series of δ-functions, but will represent the loss of resolution introduced by the finite data range (the effect of the window function) and, to a lesser extent, the effect of disorder in the specimen.

The effects of the total phase-shift $\phi(k)$ have, so far, been ignored. $\phi(k)$ may be represented in a parameterised form (Lee et al 1974):

$$\phi(k) = a + b.k + c.k^2 + d/k^3. \qquad - \quad 3.63$$

It is possible to remove the effect of the linear term by a shift in the origin of R in the final RDF. This requires that the non-linear terms are not significant at the values of k used. The reader is referred to chapter 5 for an illustrated discussion of the numerical treatment of EXELFS data.

The program RAMP was written to perform the steps required to obtain $\chi(E)$, and the program TRANS was written to obtain the radial distribution function from $\chi(E)$.

3.3.6 Quantitative microanalysis

Energy-dispersive X-ray rechniques have been in use for may years, values of wave-vector compared with a more-correct treatment which approximates $A(k)/k$ by k^{-3}. The effects of these operations are demonstrated in section 5.3.1.3.

The modulations are the multiplied by a window function which eliminates termination effects by turning off and on smoothly, over a 2 Å^{-1} wave-vector range, at the extrema of the energy window defined above. The fourier transform of the modulations is evaluated and the modulus of the fourier transform is displayed graphically. The RDF, thus displayed, is an approximation of the radial distribution function given by:

$$\sum_j \frac{N_j}{R_j^2}.\delta(R - R_j) \qquad - \quad 3.62$$

where: N_j is the number of atoms in shell j situated a distance R_j away from the origin atom.

In practise, the experimentally-determined RDF will not be a series of δ-functions, but will represent the loss of resolution introduced by the finite data range (the effect of the window function) and, to a lesser extent, the effect of disorder in the specimen.

The effects of the total phase-shift $\phi(k)$ have, so far, been ignored. $\phi(k)$ may be represented in a parameterised form (Lee _et al_ 1974):

$$\phi(k) = a + b.k + c.k^2 + d/k^3. \qquad - \quad 3.63$$

It is possible to remove the effect of the linear term by a shift in the origin of R in the final RDF. This requires that the non-linear terms are not significant at the values of k used. The reader is referred to chapter 5 for an illustrated discussion of the numerical treatment of EXELFS data.

The program RAMP was written to perform the steps required to obtain $\chi(E)$, and the program TRANS was written to obtain the radial distribution function from $\chi(E)$.

3.3.6 Quantitative microanalysis

Energy-dispersive X-ray rechniques have been in use for may years, (Reed 1975), and it is now possible to buy a small computer system that is supplied with the programs necessary to obtain quantitative microanalytical results with a good level of accuracy (<1 %). EELS is a far less developed technique; the experimental data are more difficult to understand, theoretically and more difficult to process numerically to give quantitative microanalytical results.

3.3.6.1 Egerton's method

Quantitative microanalytical information may be extracted from EELS by a method due to Egerton & Whelan (1974).
Suppose the electron spectrometer has an acceptance angle α. An estimate is made of the numer of electron counts into an energy-window up to an energy Δ above the zero-loss peak, $I_o(\Delta,\alpha)$ (see figure 3.12). Similarly, an estimate is made of the total electron count into each core-loss edge, after the background contribution for that edge has been removed, $I_c^n(\Delta,\alpha)$ (for the $n^{\underline{th}}$ core-loss on the spectrum). The number of atoms in the beam corresponding to the $n^{\underline{th}}$ core-loss is then given by:

$$N_c^n = \frac{I_c^n(\Delta,\alpha).B}{I_o(\Delta,\alpha).\sigma_c^n(\Delta,\alpha)} \qquad - \quad 3.64$$

where: B is the effective beam area and
$\sigma_c^n(\Delta,\alpha)$ is the appropriate inelastic scattering cross-section, which may be determined in one of three ways:

1) first-principle calculations involving the evaluation of atomic wave-functions for a particular atomic species and perturbation-theoretic calculations of the relevent cross-section as a function of both energy and angle. The integrated cross-section $\sigma_c^n(\Delta,\alpha)$ may then be evaluated (Egerton 1979);

2) calculations using a simplified representation of the cross-section as a function of energy and angle. It is customary to have a table of total cross-sections as a function of the core-loss voltage (obtained either by direct measurement or one of the theoretical expressions for the total cross-section (section 2.2.4) and apply two efficiency terms: one for the efficiency of an energy window of width Δ (see equation 2.124), given the expected form of the cross-section as a function of energy; and one for the efficiency

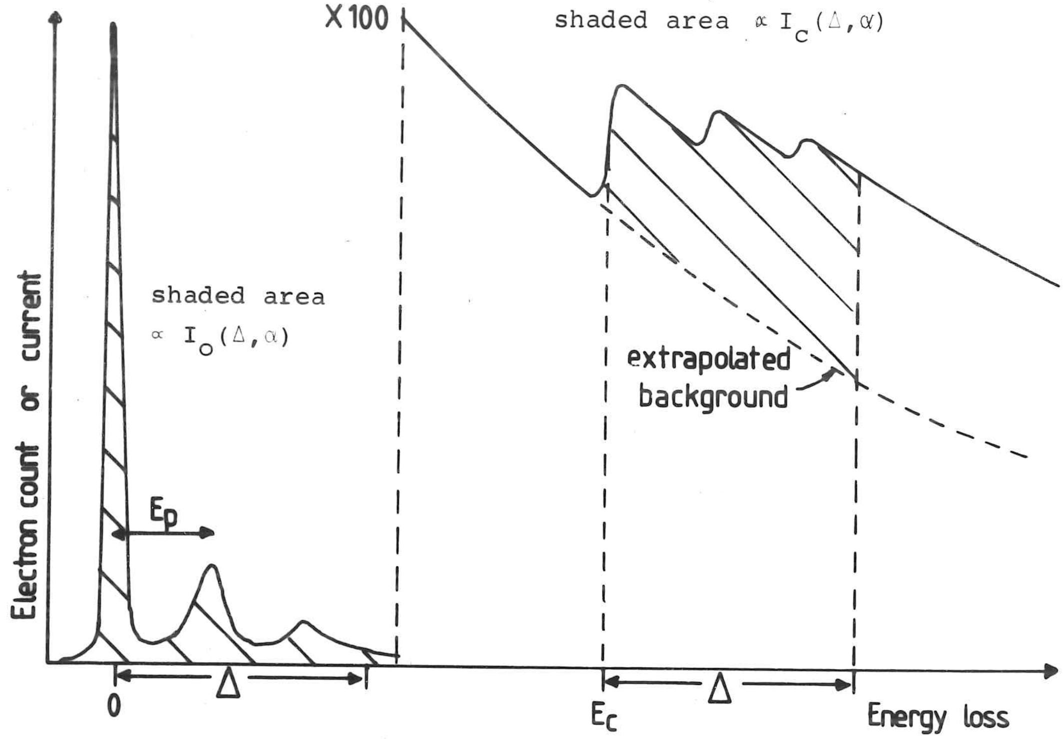

Figure 3.12: a typical energy-loss spectrum. $I_o(\Delta,\alpha)$ and $I_c(\Delta,\alpha)$ are proportional to the shaded areas in the low-loss and core-loss regions respectively.

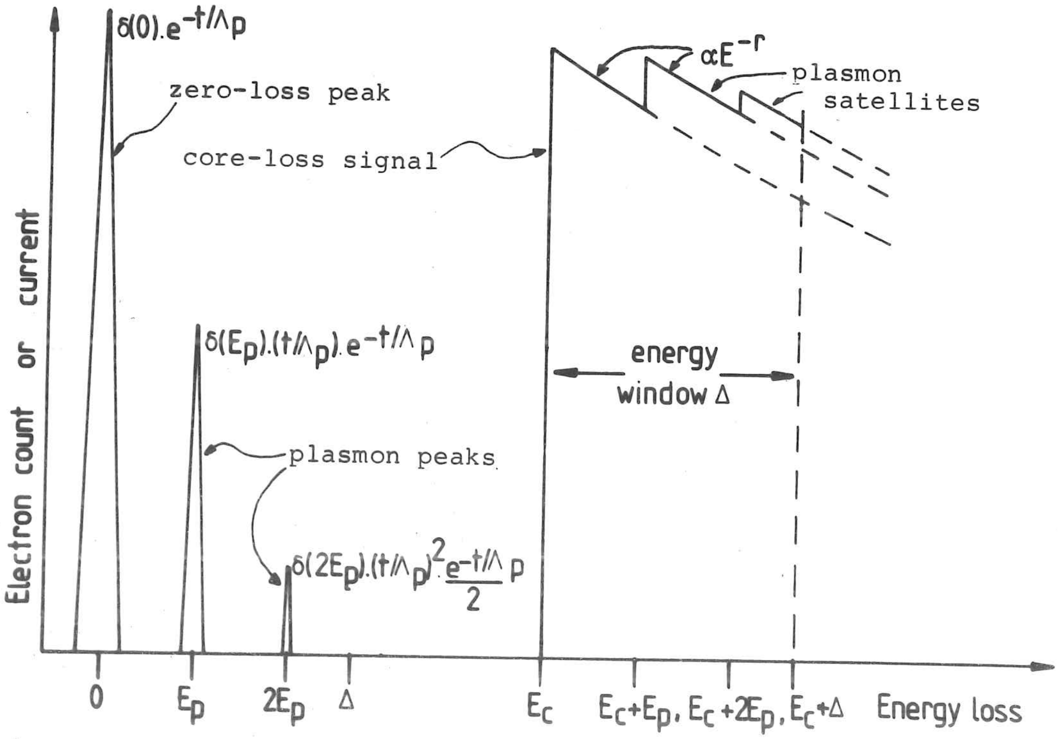

Figure 3.13 The model for the energy-loss spectrum used in the calculation of the plasmon-shift correction.

of angular collection for the convergence/collection semi-angle (α) employed;

3) the use of a standard of known composition or mass thickness (Menzies et al 1980, Pennycook 1978).

First-principle calculations have been performed by Leapman et al (1978), Maher et al (1978), Egerton (1979), and, for the first time, appear to give a good agreement between theory and practise. Note that they do not calculate an absolute value for the atomic scattering cross-section, but scale their results arbitrarily to fit the experimental data. Whatever the theoretical method employed, the results of model calculations must be tested against experimental results in order to validate the calculations of cross-sections. This has been done, so far, for only a few elements (Maher et al (1978), Boyce & Embling 1980).

The method of step 2) (above) is that most often used. It has the advantage of being very easy to use, and could certainly be made part of a program package on a small computer energy-loss system. Either the Bethe formula for the total cross-section (see section 2.2.2 and 2.2.4) (Bethe 1930) which has two free parameters, or the semi-classical Gryzinski formula (see section 2.2.4) (Gryzinski 1965) which has no free parameters may be used. A paper by Powell (1976) compares the various expressions for the total inelastic scattering cross-section. It is seen that, for the values of incident electron energy usually encountered in EELS, the Gryzinski cross-section compares favourably with the more-exact quantum-mechanical calculations. Because of the simplicity of this formulation, and because there are no free parameters, the Gryzinski cross-section is to be preferred.

Straightforward application of equation 3.64, given that the beam area B is well defined, results in an absolute measure of the number of atoms of chemical species with core-loss n in the beam, subject only to the approximation that there is no multiple-scattering. In practise, the beam is rather poorly defined, unless a careful calibration is performed. The chief use of equation 3.64 is likely to be in estimating ratios of atomic concentrations,

$$\frac{N_c^1}{N_c^2} = \frac{I_c^1(\Delta,\alpha).\sigma_c^2(\Delta,\alpha)}{I_c^2(\Delta,\alpha).\sigma_c^1(\Delta,\alpha)} \qquad - \quad 3.65$$

and, if allowance can be made for multiple-scattering, it should be possible to estimate such a ratio with a high degree of accuracy, depending only on the accuracy with thich the background contributions may be removed and the accuracy to which the inelastic-scattering cross-sections are known.

3.3.6.2 The plasmon-shift correction

Equation 3.64 only holds true in the case of no multiple-scattering. When there is appreciable double-scattering at an edge (i.e. a pronounced plasmon satellite), there is a low of collection efficiency at the edge for the double-scattered electrons because of the apparently reduced energy collection window (which appears reduced by approximately a plasmon energy). The correction for multiple-scattering is usually small, so a relatively crude model can be used to derive it.

Consider a low-loss region enclosing a zero-loss peak and n plasmons, represented by (n + 1) δ-functions (see figure 3.13). The area under the zero-loss peak may be taken to be

$$I_o = \exp(-t/\Lambda_p) \qquad - \quad 3.66$$

and under the n^{th} plasmon loss:

$$I_{pn} = \frac{1}{n!}.(t/\Lambda_p)^n.\exp(-t/\Lambda_p) \qquad - \quad 3.67$$

where: t is the thickness of the foil, and

Λ_p is the mean free path for plasmon excitation.

The technique of quantitative EELS is only viable is the foils is less than about Λ_p in thickness.

The core-loss region may be modelled as follows (see fig 3.13):

1) a background falling rapidly with energy;

2) a core-loss signal, per unit energy, resulting from single-scattering:

$$\begin{aligned} I_{co} &= A.(t/\Lambda_c).E^{-r}.\exp(-t/\Lambda_p), \quad E > E_c \\ &= 0 \qquad\qquad\qquad\qquad\qquad\quad , \quad E < E_c \end{aligned} \qquad - \quad 3.68$$

where: A and r are constants,

Λ_c is the mean-free-path for core-loss excitation,

E is the energy-loss and

E_c is the core-loss edge energy.

3) A core-loss signal, resulting from multiple-scattering with the $n^{\underline{th}}$ plasmon:

$$I_{cn} = A.(t/\Lambda_c).(E - n.E_p)^{-r}.\frac{1}{n!}.(t/\Lambda_p)^n.\exp(-t/\Lambda_p), \quad E > E_c + n.E_p$$
$$= 0 \quad , E < E_c + n.E_p \qquad - \quad 3.69$$

Using equations 3.66 to 3.69, it is possible to evaluate equation 3.64. Therefore, provided that the energy-window includes just N plasmons:

$$I_o(\Delta,\alpha) \quad = \quad \exp(-t/\Lambda_p).(1 + \sum_{n=1}^{N}\frac{1}{n!}.(t/\Lambda_p)^n) \qquad - \quad 3.70$$

and:

$$I_c(\Delta,\alpha) \quad = \quad \int_{E_c}^{E_c+\Delta} (I_{co} + \sum_{n=1}^{N} I_{cn}).dE \qquad - \quad 3.71$$

giving, for the number of atoms associated with the core-loss,

$$N_c \quad \propto \quad \frac{I_c(\Delta,\alpha)}{I_o(\Delta,\alpha)} \quad = \quad \text{constant}.\frac{t}{\Lambda_p}.\gamma \qquad - \quad 3.72$$

In equations 3.66 to 3.72, the question of any angular correction has been deferred; the parameter γ measures the departure from linearity in thickness dependence which results from multiple-scattering. This correction arises essentially because multiple-scattering produces extra intensity in the core-loss at energies $n.E_p$ above the edge. In the Egerton formula (equation 3.64), this scattering is assumed to occur with the same partial cross-sections as the single-scattering core-loss, but this is not the case, because the collection efficiency of the energy window for multiple-scattering events is less than the collection efficiency for single-scattering. Due to the strong energy-dependence of $\sigma(\Delta,\alpha)$, which includes a window efficiency term, a significant correction can result.

The factor γ thus represents the correction which must be applied where: A and r are constants,

Λ_c is the mean-free-path for core-loss excitation,

E is the energy-loss and

E_c is the core-loss edge energy.

3) A core-loss signal, resulting from multiple-scattering with the n^{th} plasmon:

$$I_{cn} = A.(t/\Lambda_c).(E - n.E_p)^{-r}.\frac{1}{n!}.(t/\Lambda_p)^n.\exp(-t/\Lambda_p), \quad E > E_c + n.E_p$$
$$= 0 \quad , E < E_c + n.E_p \qquad - \quad 3.69$$

Using equations 3.66 to 3.69, it is possible to evaluate equation 3.64. Therefore, provided that the energy-window includes just N plasmons:

$$I_o(\Delta,\alpha) = \exp(-t/\Lambda_p).(1 + \sum_{n=1}^{N}\frac{1}{n!}.(t/\Lambda_p)^n) \qquad - \quad 3.70$$

and:

$$I_c(\Delta,\alpha) = \int_{E_c}^{E_c+\Delta} (I_{co} + \sum_{n=1}^{N} I_{cn}).dE \qquad - \quad 3.71$$

giving, for the number of atoms associated with the core-loss,

$$N_c \propto \frac{I_c(\Delta,\alpha)}{I_o(\Delta,\alpha)} = \text{constant}.\frac{t}{\Lambda_p}.\gamma \qquad - \quad 3.72$$

In equations 3.66 to 3.72, the question of any angular correction has been deferred; the parameter γ measures the departure from linearity in thickness dependence which results from multiple-scattering. This correction arises essentially because multiple-scattering produces extra intensity in the core-loss at energies $n.E_p$ above the edge. In the Egerton formula (equation 3.64), this scattering is assumed to occur with the same partial cross-sections as the single-scattering core-loss, but this is not the case, because the collection efficiency of the energy window for multiple-scattering events is less than the collection efficiency for single-scattering. Due to the strong energy-dependence of $\sigma(\Delta,\alpha)$, which includes a window efficiency term, a significant correction can result.

The factor γ thus represents the correction which must be applied to the Egerton formula to correct for multiple-scattering. The true number of atoms in the beam differs from the number calculated from equation 3.64 by the factor

$$\gamma = \frac{1 + \left(\sum_{n=1}^{N} \frac{\beta^n}{n!} . (1 - (\eta - n\xi)^s) \right) / (1 - \eta^s)}{1 + \sum_{n=1}^{N} \frac{\beta^n}{n!}} = 1 - \varepsilon \qquad - \qquad 3.73$$

where:
$s = 1 - r$,
$\eta = (E_c + \Delta)/E_c$,
$\xi = E_p/E_c$ and
$\beta = t/\Lambda_p$.

In the limit of small correction, i.e. $\gamma \simeq 1$ or $\varepsilon \simeq 0$, that is, when the foil is very thin ($\beta << 1$) and both E_p and Δ are much less than E_c, we find

$$\varepsilon \simeq \frac{\beta}{1 + \beta} . \frac{E_p}{\Delta} \qquad - \qquad 3.74$$

independent of the power-law coefficient r. The error term, ε, has been calculated for $\beta = 1, \frac{1}{2}, \frac{1}{4}, \frac{1}{8}$ and for $s = -3.5$ (corresponding to $r = 4.5$, the expected value (Inokuti 1971)). The results, parameterised in terms of ξ and Δ/E_p are displayed in figure 3.14, which can be used to calculate the error term for any value of foil thickness between $\beta = 1$ and $\beta = 0.125$ by linear interpolation. For foils thinner than $\beta = 0.125$, the correction may be obtained by multiplying the result of fig 3.14a by $9\beta/(1 + \beta)$; however, in this limit, the correction is usually negligible.

In a typical example, consider a foil of thickness $\beta = 1$, containing Fe and C, displaying a low-energy-loss peak at 20 eV and core-losses at approximately 750 and 280 volts respectively: a convenient energy window is 100 eV. The factor γ_{Fe} is found to be 0.81, and γ_C is 0.85. Thus the ratio of Fe:C calculated from the single-scattering formula is in error by about 5 %, the amount of iron relative to the amount of carbon being underestimated by the uncorrected Egerton formula (equation 3.64).

The model by which these corrections are deduced is admittedly crude, but the resulting correction is only just significant at the level of accuracy currently being obtained by quantitative EELS, and

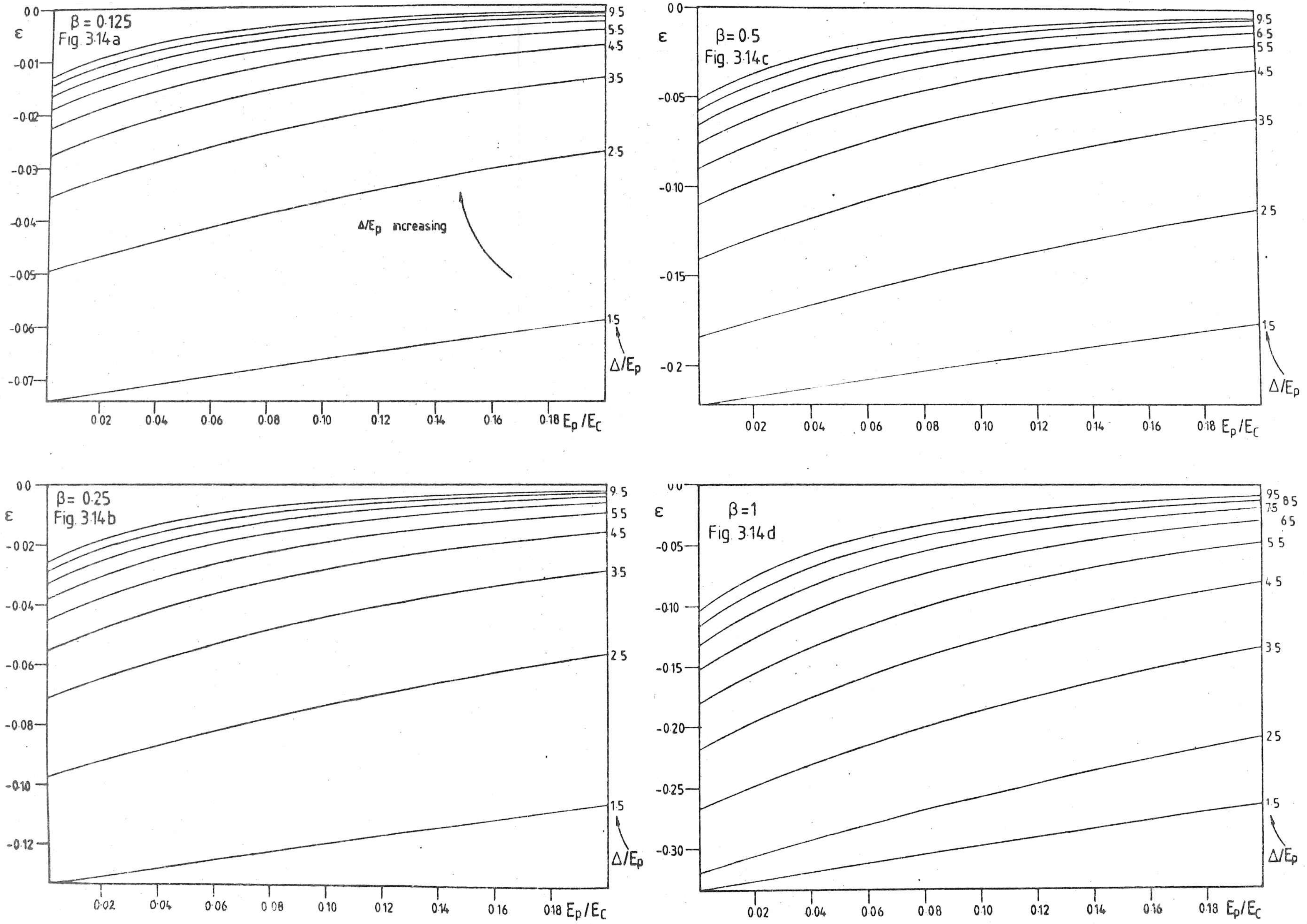

Figure 3.14: computed values of the plasmon shift correction ($\varepsilon = \gamma - 1$) for four values of foil thickness, parameterised in terms of E_p/E_c and Δ/E_p ; s= -3.5.

an increase in the complexity of the model (for example, by introducing a plasmon whose shape is given by the free-electron gas model and a core-loss shape that shows the effects of centrifugal potential) greatly complicates the calculation of the correction factor.

The plasmon-shift correction is usually important ($\varepsilon \simeq 10\ \%$) in thick films (i.e. $t \simeq 1000$ Å). Figure 3.15 indicates that only for very large core-loss energies and very wide energy windows can the correction be neglected.

3.3.6.3 Combined angular and plasmon-shift corrections

It is possible to apply both the angular correction of section 3.3.3.3.2 and the plasmon-shift correction (above) to obtain a combined correction:

$$\gamma_{TOTAL} = (1 + \beta.\mu(E_p,E_c)).(1 - (\frac{E_c + \Delta - E_p}{E_c})^s) \times$$
$$\times (1 - (\frac{E_c + \Delta}{E_c})^s)^{-1}.(1 + \beta)^{-1} \qquad - \quad 3.75$$

subject to the following considerations:

1) that the angular correction $\mu(E_p,E_c)$ as a function of E_c does not vary appreciably ($\simeq 10\ \%$) over the window chosen;

2) that the foil is thin enough for three- and higher-order-scattering events to be unimportant ($\beta < 0.1$).

3.3.6.4 Step-height analysis

A K-shell core-loss may be approximated by a power-law function (Inokuti 1971):

$$\frac{\partial\sigma_K}{\partial E} = \begin{cases} A.E^{-r}, & E > E_K \\ 0, & E < E_K \end{cases} \qquad - \quad 3.76$$

This may be integrated over all energy-losses to give:

$$I_K = \frac{A}{r}.E^{-r+1} \qquad - \quad 3.78$$

The signal at the edge due to the K-loss is given by the difference between the signals just before the edge and the signal just after the edge. This is called the step-height of the edge.

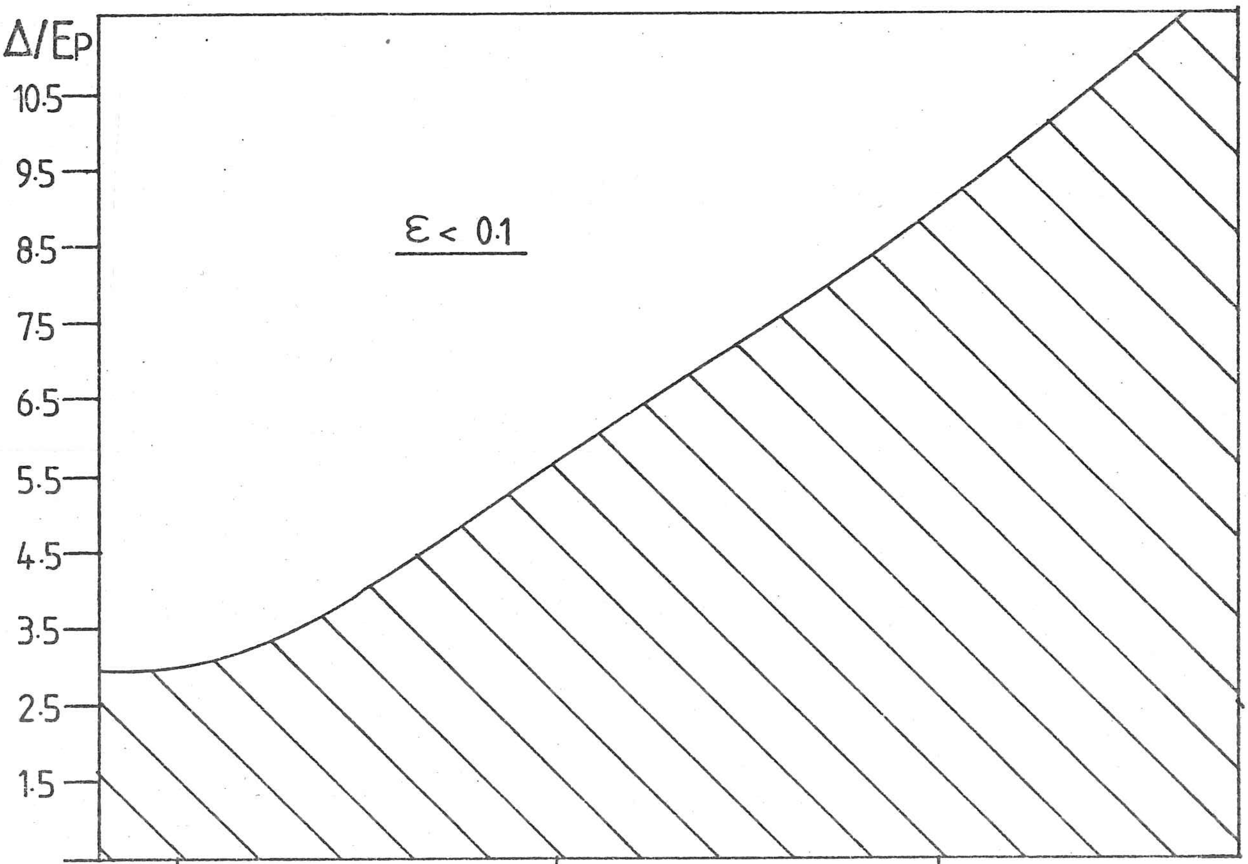

Figure 3.15 The plasmon shift correction for thick foils ($\beta=1$). The correction ($\varepsilon = \gamma-1$) is significant ($\varepsilon \simeq 10\%$) in the shaded area.

$$V_K = A.E_K^{-r} \qquad - \quad 3.78$$

Therefore, the integral I_K may be evaluated provided that V_K, E_K and r are known:

$$I_K = \frac{V_K}{r} . E_K \qquad - \quad 3.79$$

The program STEP was written which evaluated the integral by fitting two power-law curves to the data, one before the edge and one after the edge. This enables the value of V_K at the edge to be calculated, and the power-law coefficient, r, is also given by the fit after the edge. Thus the integral I_K may be evaluated.

The program is most useful in obtaining the ratio of integrated cross-sections of two K-edges on the same spectrum as then neither vertical nor horizontal scales need be calibrated.

3.3.7 The command package

The numerical techniques discussed in this chapter have been implemented on the University's IBM 370/165 computer, and are available to users of that system. A detailed list of commands available, command syntax and default parameters used is contained in appendix A. The complete numerical package source, written in FORTRAN is about 8000 lines long, and the run-time support and command environment program source, written in PHOENIX (a local command language) is about 3000 lines long. For further information on the system, please contact the Metal Physics Computing Services Representative at the Cavendish Laboratories.

Chapter 4 - Examples of quantitative microanalysis using energy-loss spectroscopy

4.1 Boron nitride
  4.1.1 Numerical processing of the energy-loss data
  4.1.2 Analysis of the energy-loss spectra of boron nitride
4.2 Aℓ - Mg - Be alloy
4.3 Thin "boron" films
  4.3.1 The energy-loss results from thicker regions
  4.3.2 Summary of results from "boron" films
4.4 Silicon carbide

Chapter 4 - Examples of quantitative microanalysis using energy-loss spectroscopy

4.1 BORON NITRIDE

A specimen of graphitic boron nitride was prepared by scratching a hole in the centre of a 3 mm disc cut from polycrystalline boron nitride rod.

This allotrope of boron nitride has a graphite-like structure (Wycoff 1960) shown in fig 5.2, and, like graphite, cleaves easily into platelets of uniform thickness (typically 500 Å across and 50 Å thick). Conventional transmission electron microscopy (CTEM) investigations confirm the graphitic structure of figure 5.2 (see section 5.1 and figure 5.1).

Graphitic boron nitride has a covalently-bonded (III- V) structure, is stoichiometric BN and has two K-shell core-losses well within the working range of electron energy-loss spectroscopy (K_{boron} = 188 eV, $K_{nitrogen}$ = 399 eV (Bearden & Burr 1967)). It is therefore an excellent specimen with which to investigate the accuracy of quantitative electron energy-loss spectroscopy (EELS).

4.1.1 Numerical processing of the energy-loss data

The energy-loss spectra are first treated by the APCOR program (a detailed description of how to use the energy-loss programs at Cambride is to be found in appendix A) to correct for the finite probe convergence angle. The results then approximate to the energy-loss spectrum that would be collected using either a very large probe convergence angle or a very large collector aperture. This spectrum is then analysed using either the INTEGRATE or STEP programs.

The action of the INTEGRATE program is as follows:

1) a power-law function (of the form AE^{-r}) is fitted to the background before the edge specified in the terminal input to the program.

2) The background, approximated by the power-law, is subtracted from the spectrum, yielding a remnant spectrum.

3) The area under the remnant is determined for several energy-windows, the lower bound in energy being the edge energy, the upper

bound being given by the sum of the lower bound and the required window width.

4) Steps 1) to 3) are repeated for each successive edge given in the input to the INTEGRATE program.

The results are evaluated for several energy windows. The choice of a suitable energy window is contrained by:

1) If the window is too narrow, the value of the integral is strongly influenced by structure at the edge, but is not very sensitive to the accuracy of the background fit. However, the estimated value of the total integral is dependent on the estimated energy collection efficiency (see section 2.1.2.4) which is sensitive to inaccuracies in the background fit.

2) If the window is very wide, the energy collection efficiency is close to unity, and errors in the estimated total integral due to errors in the energy-collection efficiency are negligible. However, the integral is sensitive to the backtround fit which may need to be extrapolated over a wide energy range.

In practise, one seeks a compromise between these two extremes dependent on the details of the system under examination.

The action of the STEP program is as follows:

1) for each edge specified in the input to the STEP program, two power-law curves are fitted, one above and one below the edge.

2) The estimated total integral is evaluated from these power-laws using the technique of step-height analysis (see section 3.3.6.4).

The STEP program offers the following advantages compared to the INTEGRATE program:

1) no integration window need be chosen;

2) very noisy data, data with a curved background (as seen on a log-log plot) and data with very many closely-spaced edges can be accommodated.

The main advantage of the INTEGRATE program over the STEP program is that is makes no assumption as to the shape of the edge, and will therefore evaluate the integrals under L amd M edges more accurately than will the STEP program.

The number ratio of boron to nitrogen atoms is given by:
(see section 3.3.6.1)

$$\frac{n_B}{n_N} = \frac{\sigma_N}{\sigma_B} \cdot \frac{I_B^T}{I_N^T} \qquad - \quad 4.1$$

where: σ_N is the total inelastic scattering cross-section for the nitrogen-K core-loss;
I_N^T is the total scattered intensity under the nitrogen K-shell core-loss;
+ similar terms for boron.

An estimate of I_N^T is given by:

$$I_N^T \simeq I_N(\Delta) \;/\; \eta_N(\Delta) \qquad - \quad 4.2$$

where: $I_N(\Delta)$ is the intensity under the nitrogen core-loss up to an energy Δ above the edge energy;
$\eta_N(\Delta)$ is the estimated energy collection efficiency given by equation 2.124.

An approximation of the value of the inelastic scattering cross-section is given by the Gryzinski formula for the cross-section (discussed in section 2.2.1). It is expected that the estimated value of the cross-section given by the gryzinski formula will be accurate to within experimental accuracies, more importantly, the ratio of the cross-sections of nitrogen and boron given by the Gryzinski formula should be correct to much better than experimental accuracy.
The evaluation of equation 2.87 for nitrogen and boron K-losses gives:

$\sigma_N = 0.577 \;.\; 10^{-24}$ m^2 electron^{-1} atom^{-1}
$\sigma_B = 1.32 \;.\; 10^{-24}$ "

4.1.2 Analysis of the energy-loss spectra of boron nitride

Energy-loss spectra are presented which have been recorded from two different portions of the specimen on different days.
The low-loss region of one of these spectra is shown in fig 4.1, from which the following points should be noted:

1) the zero-loss peak indicates an instrumental resolution of approximately 2.5 eV (full width at half maximum (FWHM)) .

2) There are two plasmon peaks at about 8 eV and 25 eV corresponding

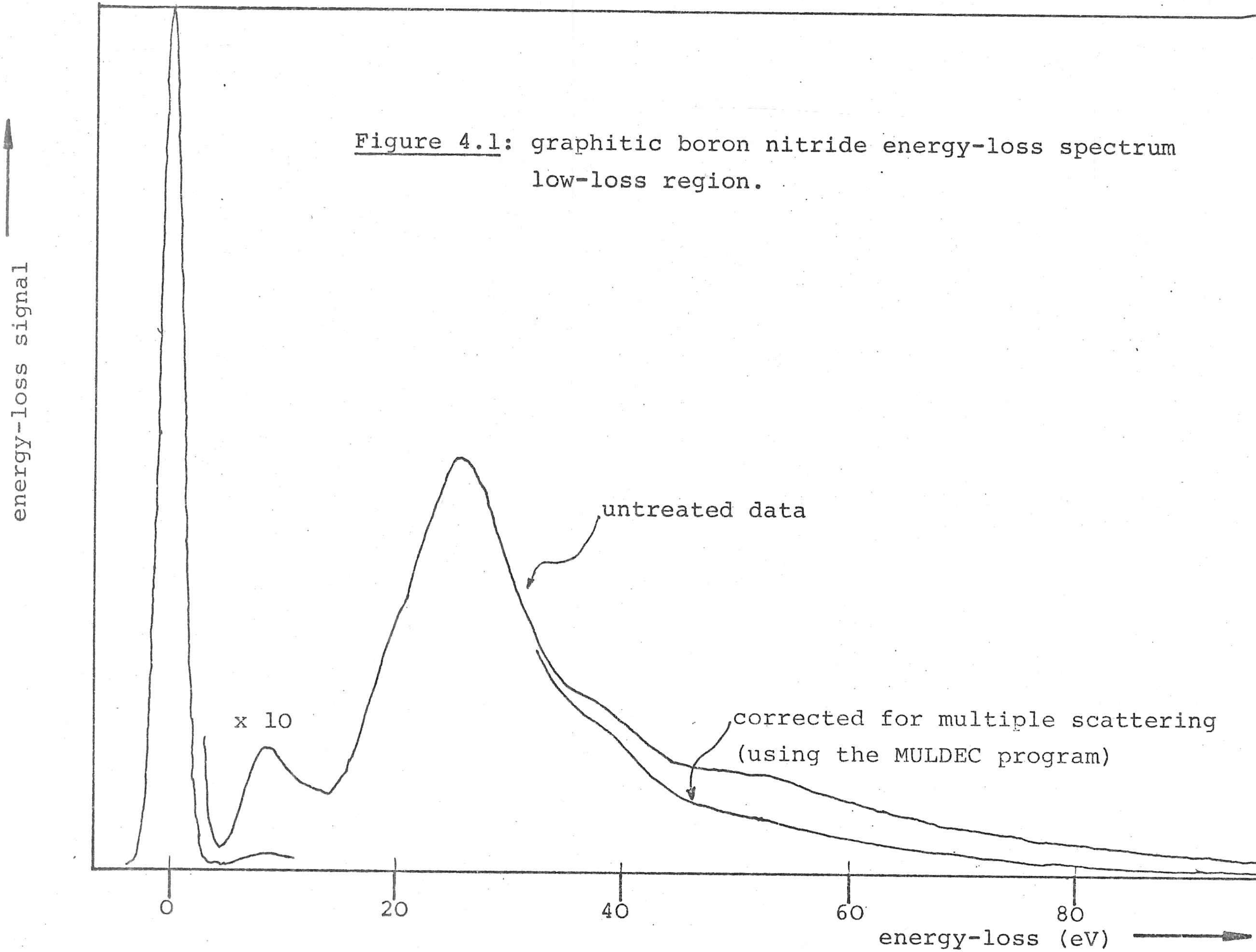

Figure 4.1: graphitic boron nitride energy-loss spectrum low-loss region.

to plasma oscillations of the π-band electrons (1 per atom) and the $\pi+\sigma$-band electrons (4 per atom) respectively. The reader is referred to the work on boron nitride by Leapman & Silcox (1978b) and to the work on graphite which also shows this double-plasmon (Taft & Phillipp 1964). This behaviour may be explained by a two-band model of boron nitride similar to the model for vanadium and niobium hydrides discussed in section 6.7.

3) The thickness of the foil, determined by measureing the ratio of plasmon to zero-loss areas, using the THICK program, is 100 Å. Correction for multiple scattering removes much of the scattered intensity above 50 eV, and most of the scattered intensity beyond 80 eV. The foil is thin enough for plasmon shift correction errors (see section 3.3.6.2) to be negligible compared with the experimental accuracies currently achieved.

The first energy-loss spectrum is shown in figure 4.2a alongside the results of the INTEGRATE program. The window chosen above the boron-K core-loss was 100 eV wide because the background extrapolation due to the boron-K core-loss at the nitrogen-K edge is not quite parallel to either the background slope before the boron-K edge or the slope of the separated nitrogen-K core-loss, when viewed on a log-log plot. So, because of the possible error in slope, it is best to choose a small window.

The separated nitrogen-K core-loss becomes very noisy beyond 850 eV, so a window extending to 840 eV was used for the nitrogen-K core-loss.

Using these values of the window widths, the following partial integrals were returned by the INTEGRATE program:

$I_B(100) = 2.02$ (arbitary units)
$I_N(435) = 1.01$ (to same scale)

The estimated window efficiencies were:

$\eta_B(100) = 0.752$
$\eta_N(435) = 0.889$.

The evaluation of equation 4.1, using the Gryzinski cross-sections for boron and nitrogen yields:

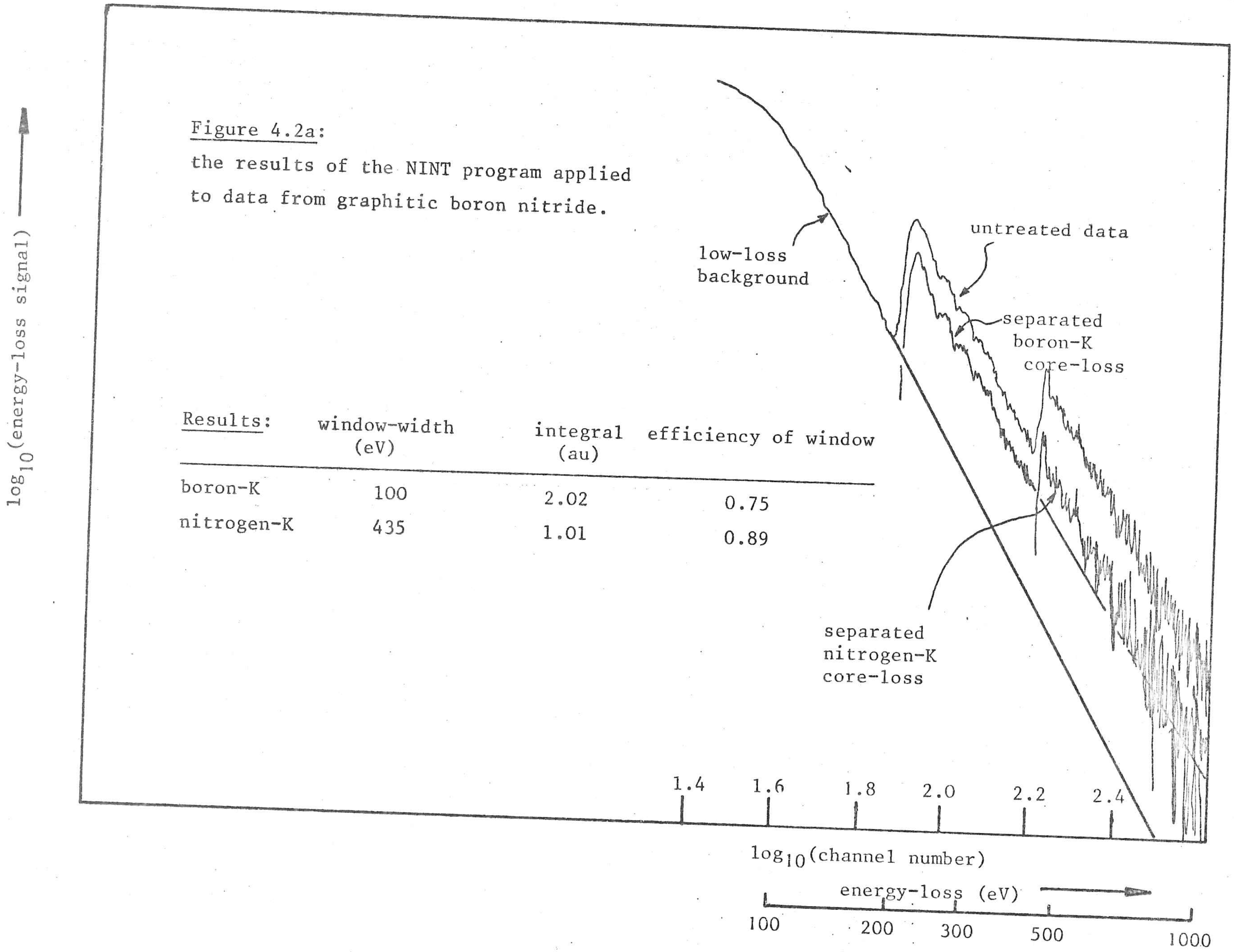

Figure 4.2a: the results of the NINT program applied to data from graphitic boron nitride.

Results:	window-width (eV)	integral (au)	efficiency of window
boron-K	100	2.02	0.75
nitrogen-K	435	1.01	0.89

$$\frac{n_B}{n_N} = 1.04.$$

The second energy-loss spectrum is shown in fig 4.2b. This spectrum was recorded for a longer time, so the statistics are much improved as compared with the previous spectrum. The background extrapolations seen on the log-log plot are more accurately parallel than in the previous spectrum. For this reason, the windows used were set to be as large as possible, yielding values of $\eta(\Delta)$ close to unity. The boron-K window was this 864 eV, and the nitrogen-K window was 651 eV.

The following partial integrals were obtained from the INTEGRATE program:

$I_B = 1.09$ (a.u.)
$I_N = 0.46$ "

The estimated window efficiencies were:

$\eta_B = 0.981$
$\eta_N = 0.876.$

Thus the resulting number ratio of atoms was:

$$\frac{n_B}{n_N} = 0.92.$$

The average for the two spectra yields:

$$\frac{n_B}{n_N} = 0.98\ (\pm\ 0.06).$$

Although a sample of two is too small to yield an accurate value of the standard error, the error term above (6 %) is in agreement with the expected experimental accuracy. The error term above cannot include the presence of systematic errors (for example, thickness effects or errors in the estimated cross-sections), it does, however, give a measure of the statistical accuracy of the result, which is the only measure of accuracy that can easily be determined.

The first energy-loss spectrum was analysed by the STEP program, yielding the results shown in fig 4.3a. The number ratio thus determined was:

Figure 4.2b:

The results of the NINT program applied to data from graphitic boron nitride.

Results:

	window-width	integral	efficiency
boron-K	864 (eV)	1.09 (au)	0.981
nitrogen-K	651	0.46	0.876

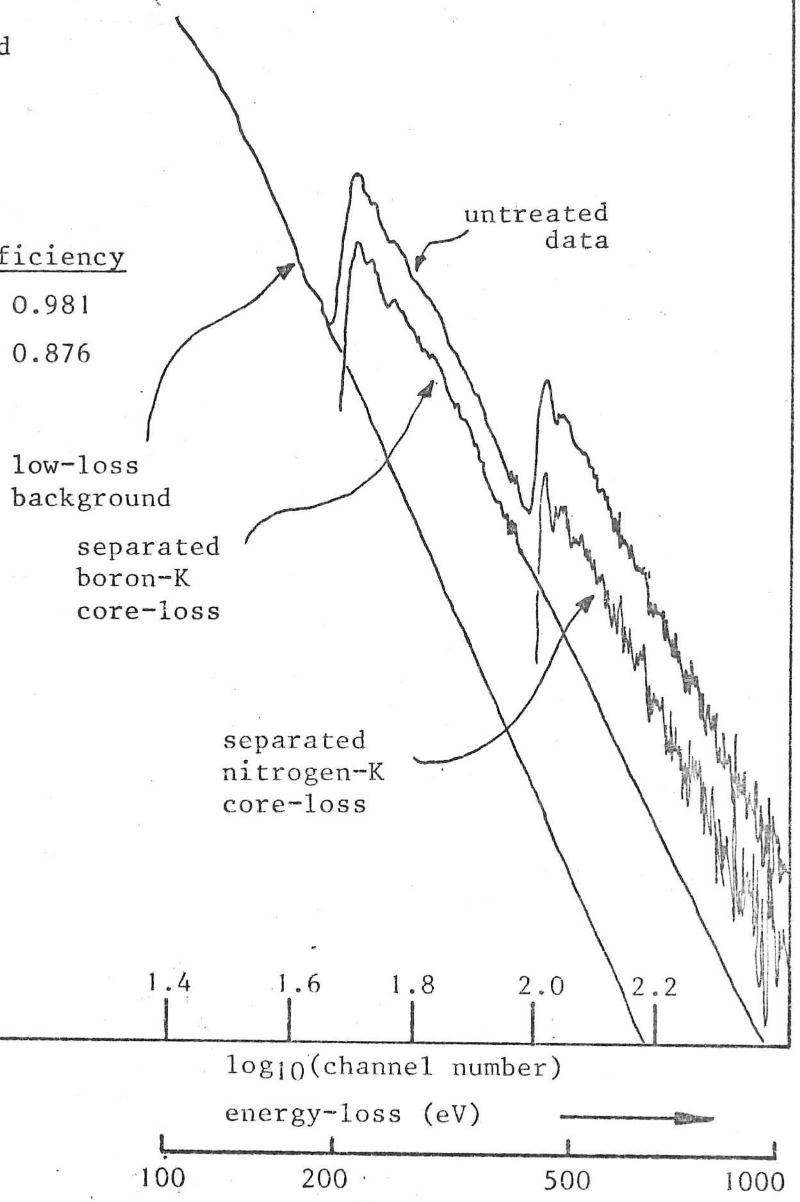

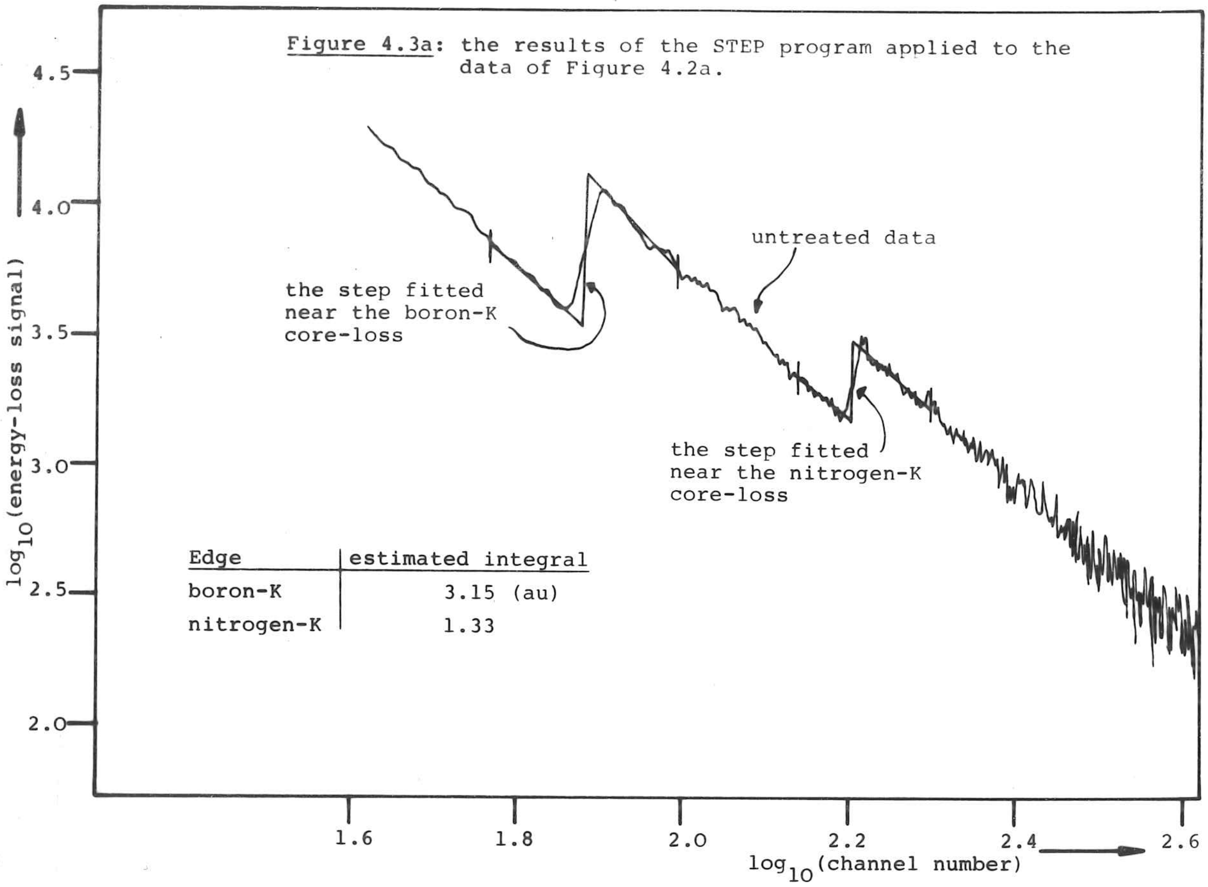

Figure 4.3a: the results of the STEP program applied to the data of Figure 4.2a.

Edge	estimated integral
boron-K	3.15 (au)
nitrogen-K	1.33

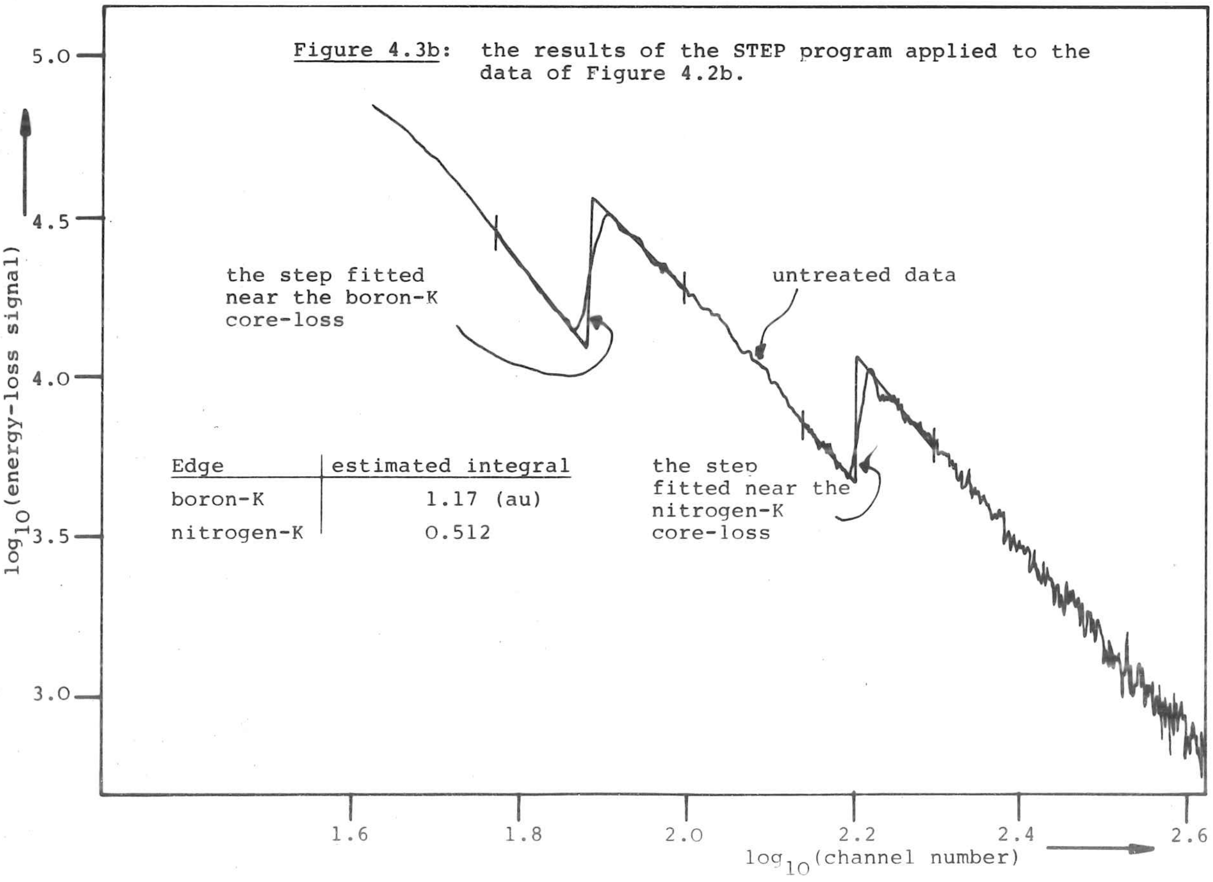

Figure 4.3b: the results of the STEP program applied to the data of Figure 4.2b.

Edge	estimated integral
boron-K	1.17 (au)
nitrogen-K	0.512

$$\frac{n_B}{n_N} = 0.97.$$

The second energy-loss spectrum was analysed in the same way yielding the results shown in figure 4.3b. The number ratio thus determined was 1.00.
These two results agree with the values obtained above to within the experimental accuracy.

It can be seen from figure 4.3 that the step fitted to the edges does not generally overestimate or underestimate the step height. If the edges had much bandstructure near the edge or were delayed due to the effect of centrifugal potential on high angular momentum state edges, then it is expected that the agreement between the two techniques of numerical analysis would not be as good as demonstrated here.

4.2 Aℓ - Mg - Be ALLOY

Aℓ - 5 atomic % Mg alloys suffer from rapid oxidation in damp atmospheres at elevated temperatures (400 to 600 °C) (Field 1980). It is found that the addition of small concentrations of beryllium in the range 100 to 1000 ppm dramatically reduces the oxidation rate of the metal surface (Field et al 1980, Whitaker & Heath 1953). Studies of electron thin regions of a specimen made by chemically etching a specimen foil from one side only reveal the presence of a complicated surface oxide. Selected-area electron diffraction reveals that the oxide is composed of four oxides: (Field et al 1980)

1) amorphous γ- alumina ($A\ell_2O_3$);
2) primary MgO crystallites (grown at the metal-oxide interface);
3) secondary MgO crystallites formed from the reduction of γ- $A\ell_2O_3$ by magnesium;
4) platelets of BeO at the oxide-metal interface.

The author was supplied with a specimen of Aℓ- 5 at. % Mg - 100at ppm Be by Dr. D Field (Imperial College Metallurge Dept - London). Conventional TEM studies of this foil confirmed the results of Field et al (1980), see figure 4.4.

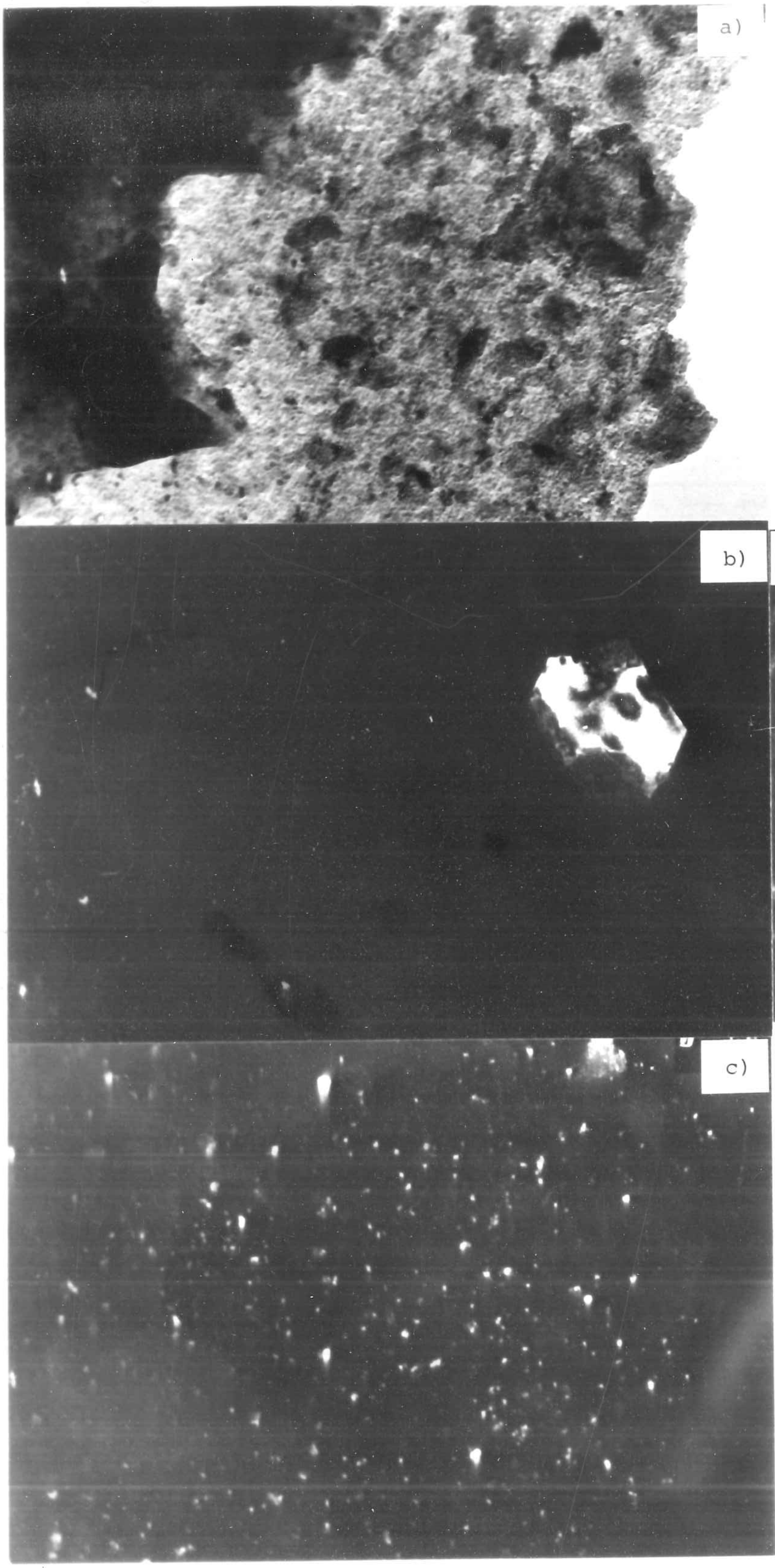

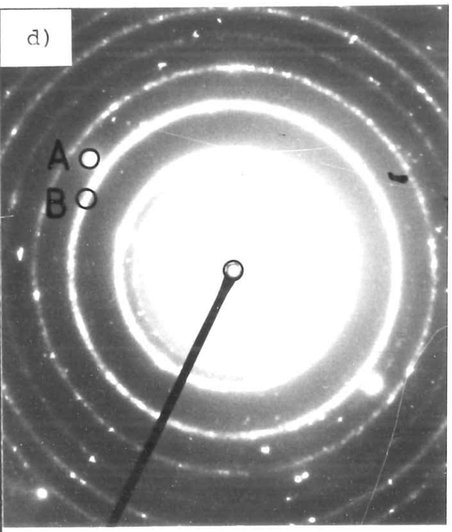

Figure 4.4: Aℓ-Mg-Be alloy

a) bright-field picture;

b) dark-field picture using BeO (110) reflection;

c) dark-field picture using MgO (220) reflection;

d) selected-area diffraction pattern from the oxide layer;

e) schematic drawing of a cross-section through the specimen near the edge.

1000 Å

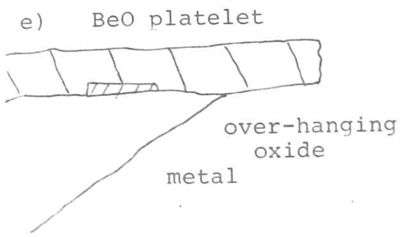

It is possible to identify the Be-O platelets from the electron diffration data. It was desired to confirm this identification using energy-loss spectroscopy and obtain a value for the thickness of the Be-O platelet.

Energy-loss spectra were recorded from the oxide film which overhung the metal edge (see fig 4.4e.), both of the Be-O platelet and of the surrounding oxide.
See figure 4.5 for the energy-loss spectrum of the Be-O platelet and the results of the INTEGRATE program applied to this spectrum.

A rather narrow window was chosen (100 eV) for the Be-K integration because:
1) the background, when viewed on a log-log plot, was curved below about 100 eV, hence it is not possible to obtain an accurate extrapolated background;
2) carbon contamination was present which restricts the window to less than 170 eV.

A wider window (540 eV) was used at the oxygen edge because the background before the edge could be determined more accurately than above.

The following partial integrals were obtained:

$I_{Be}(100) = 1.1$ (a.u.)
$I_O(540) = 0.207$ ".

The energy-window collection efficiencies were estimated to be:

$\eta_{Be}(100) = 0.909$
$\eta_O(540) = 0.904$.

In order to obtain the thickness of the specimen at this point, an energy-loss spectrum was recorded in the range 0 to 80 eV in analogue mode. The spectrum was recorded on a chart plotter and is reproduced in figure 4.6. The plasmon peak near 25 eV corresponds to a plasmon mean-free path (λ_p = MFP) of about 700 Å (from equation 2.36).
The ratio of plasmon area to zero-loss area, measured manually is:

$$\frac{I_{plasmon}}{I_{zero}} = 0.40 \quad (\pm 5\%).$$

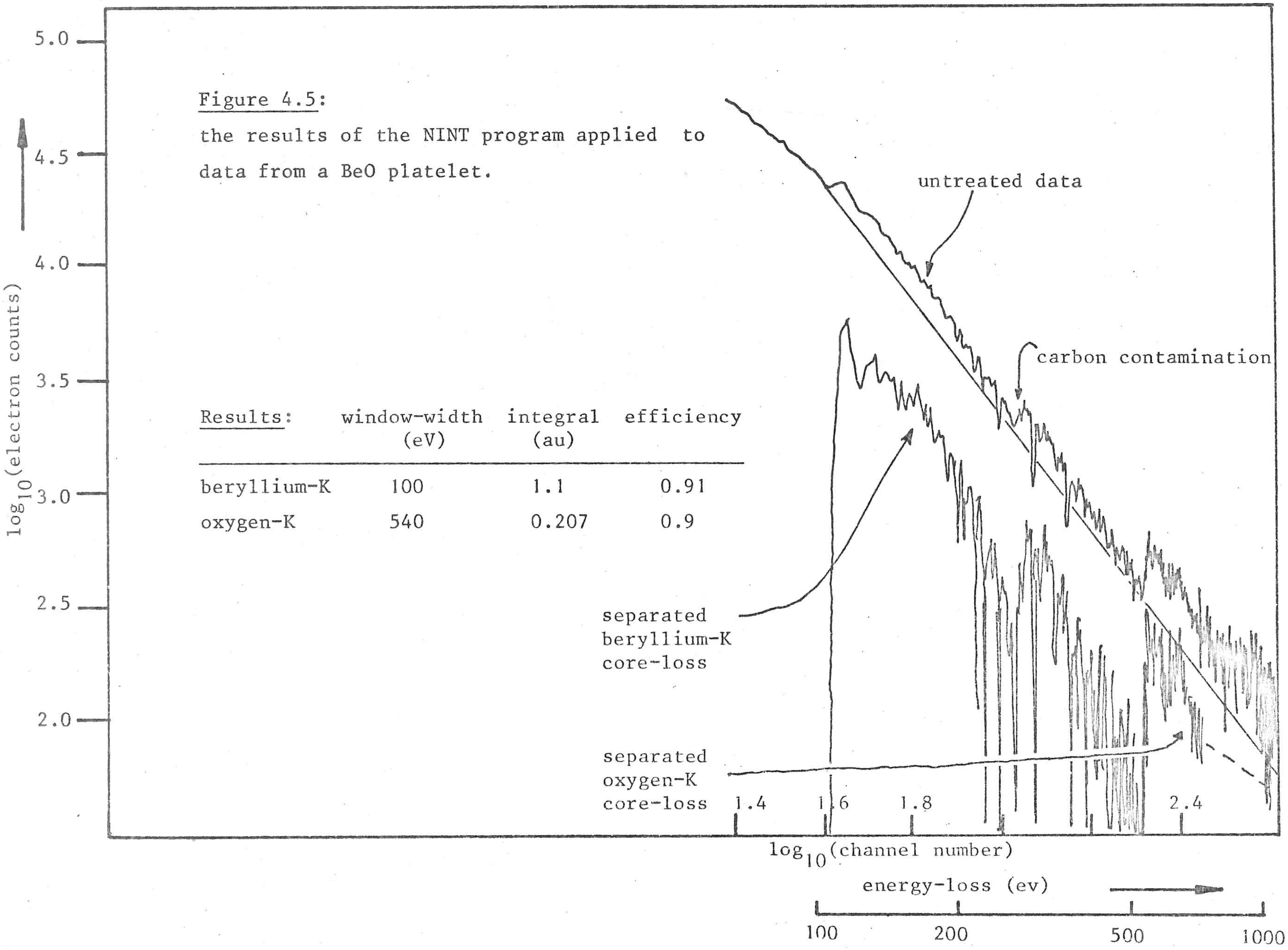

Figure 4.5: the results of the NINT program applied to data from a BeO platelet.

Results:	window-width (eV)	integral (au)	efficiency
beryllium-K	100	1.1	0.91
oxygen-K	540	0.207	0.9

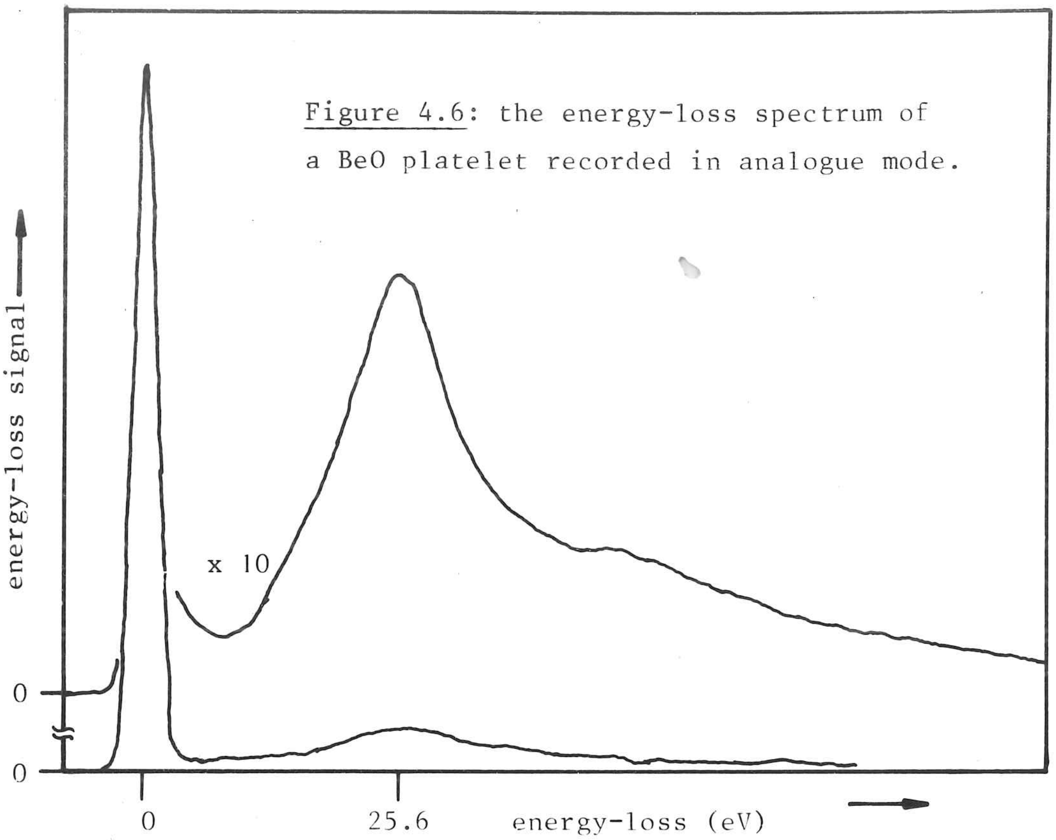

Figure 4.6: the energy-loss spectrum of a BeO platelet recorded in analogue mode.

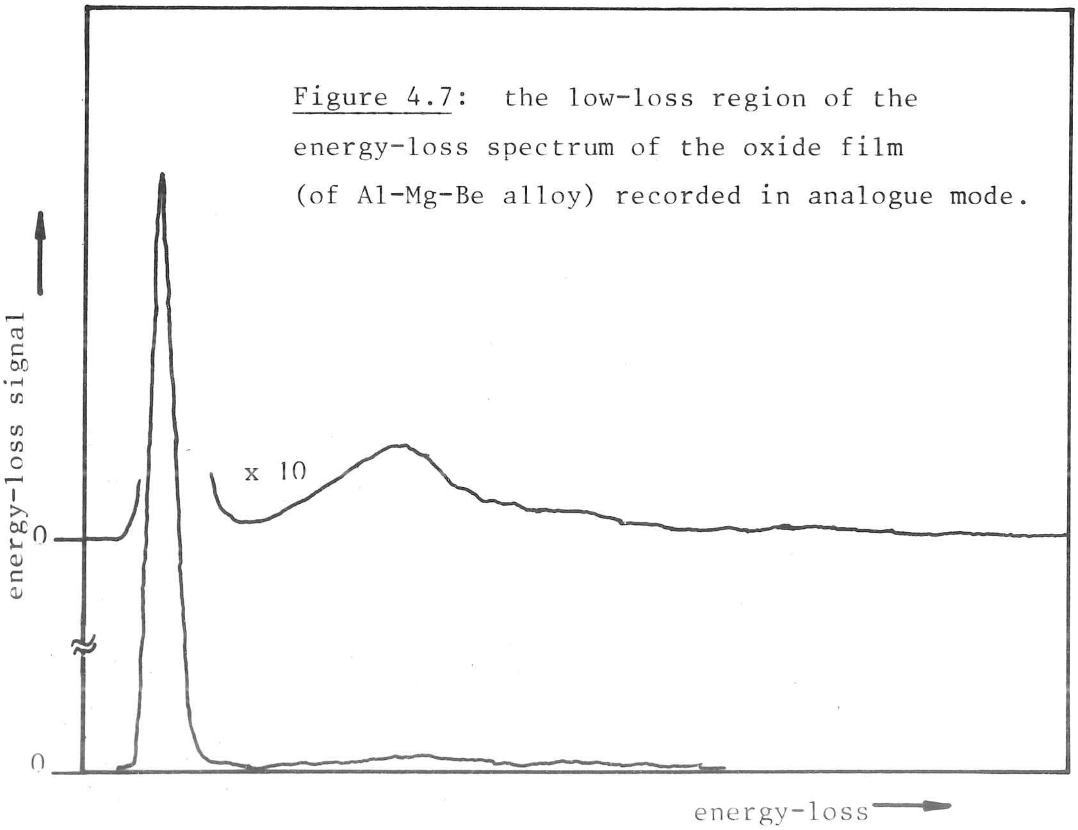

Figure 4.7: the low-loss region of the energy-loss spectrum of the oxide film (of Al-Mg-Be alloy) recorded in analogue mode.

Thus, the estimated specimen thickness is:

$$t_{support} + t_{BeO} = \lambda_p . \frac{I_{plasmon}}{I_{zero}} = 270\ (\pm 14\ \text{Å}).$$

An energy-loss spectrum was measured, in the same way, from the neighboring oxide support film, yielding the spectrum shown in figure 4.7. The estimated thickness of this film is ≃36 Å.

The total intensity under the oxygen-K core-loss peak will include intensity from inelastic events in the thin oxide layer, and the value for I_O^T estimated from $I_O(\Delta)$ and $\eta_O(\Delta)$ should be corrected for this effect. The oxide layer of 36 Å would correspond to approximately 44 Å of BeO (which is less dense), and so the total integrated signal for the oxygen-K core-loss should be reduced by the factor

$$(270 - 36)/270.$$

This rough-and-ready correction alters the value of n_{Be}/n_O by about 20 %; and this figure being not much larger than the experimental accuracies currently achieved by EELS, a more exact correction to I_O^T would not be worthwhile.

Approximate values for the total inelastic-scattering cross-sections were obtained by using the Gryzinski formula (equation 2.87), thus:

$$\sigma_O = 0.42\ .\ 10^{-24}\ m^2\ \text{electron}^{-1}\ \text{atom}^{-1}$$
$$\sigma_{Be} = 2.38\ .\ 10^{-24}\ \text{''}.$$

The corrected value of n_{Be}/n_O is given by:

$$\frac{n_{Be}}{n_O} = \frac{\sigma_O}{\sigma_{Be}} . \frac{I_{Be}(\Delta)}{\eta_{Be}(\Delta)} . \frac{\eta_{O(\Delta)}}{I_{O(\Delta)}} . \left(\frac{270}{270 - 36}\right) = 1.10$$

The curvature of the background at the Be-K edge would result in the program making an underestimate of the background in the region near 50 eV above the Be-K edge, so it is not surprising that the answer is slightly too large. The answer is, however, within the expected experimental accuracy of EELS. Thus quantitative EELS is able to confirm the composition of the platelet of Be-O and to yield a value for the thickness of the platelet as:

$$t_{BeO} = 240\ (\pm 14)\ \text{Å}.$$

Thus, the estimated specimen thickness is:

$$t_{support} + t_{BeO} = \lambda_p . \frac{I_{plasmon}}{I_{zero}} = 270\ (\pm 14\ \text{Å}).$$

An energy-loss spectrum was measured, in the same way, from the neighboring oxide support film, yielding the spectrum shown in figure 4.7. The estimated thickness of this film is ≃36 Å.

The total intensity under the oxygen-K core-loss peak will include intensity from inelastic events in the thin oxide layer, and the value for I_0^T estimated from $I_0(\Delta)$ and $\eta_0(\Delta)$ should be corrected for this effect. The oxide layer of 36 Å would correspond to approximately 44 Å of BeO (which is less dense), and so the total integrated signal for the oxygen-K core-loss should be reduced by the factor

$$(270 - 36)/270.$$

This rough-and-ready correction alters the value of n_{Be}/n_O by about 20 %; and this figure being not much larger than the experimental accuracies currently achieved by EELS, a more exact correction to I_0^T would not be worthwhile.

Approximate values for the total inelastic-scattering cross-sections were obtained by using the Gryzinski formula (equation 2.87), thus:

$$\sigma_O = 0.42 . 10^{-24}\ m^2\ \text{electron}^{-1}\ \text{atom}^{-1}$$
$$\sigma_{Be} = 2.38 . 10^{-24}\ \text{"}.$$

The corrected value of n_{Be}/n_O is given by:

$$\frac{n_{Be}}{n_O} = \frac{\sigma_O}{\sigma_{Be}} . \frac{I_{Be}(\Delta)}{\eta_{Be}(\Delta)} . \frac{\eta_{O(\Delta)}}{I_{O(\Delta)}} . \left(\frac{270}{270 - 36}\right) = 1.10$$

The curvature of the background at the Be-K edge would result in the program making an underestimate of the background in the region near 50 eV above the Be-K edge, so it is not surprising that the answer is slightly too large. The answer is, however, within the expected experimental accuracy of EELS. Thus quantitative EELS is able to confirm the composition of the platelet of Be-O and to yield a value for the thickness of the platelet as:

$$t_{BeO} = 240\ (\pm 14)\ \text{Å}.$$

4.3 THIN "BORON" FILMS

It was proposed to determine the structure of amorphous boron films using the technique of EXELFS (see chapter 5). The author was very kindly supplied with several thin foils by Dorignac (1979) of the kind used as low-noise supports for high-resolution electron microscopy. The foils were supposed to be pure boron about 15 Å thick.

Electron energy-loss spectra of these films were obtained using a focussed electron probe of semi-angle of convergence 8.5 milli-radians and an energy-resolution of 2 eV. The energy-loss spectrum of the foil between 80 and 500 eV is shown in figure 4.8, together with the results of the STEP program. The first point to note is that the energy-loss spectrum (ELS) of figure 4.8 shows that there is considerably more carbon present than boron.

In order to ensure that the carbon signal on this ELS is due to carbon in the specimen and not carbon contamination produced by the action of the electron probe on the specimen surface, the specimen was observed in dark-field imaging mode (using the annular detector) before and after the collection of the spectra. It was found that no contamination spots were visible if the beam was moved around the specimen, and the general area of interest (a few micro-metres) was "flooded" with a defocussed beam prior to data collection.
The signal from the dark-field detector could be observed whilst simultaneously collecting energy-loss data. No increase of this signal (as would be cause by the build-up of contamination) was observed for the energy-loss spectra presented here. An increase in dark-field signal of 5 % would be noticed whilst collecting energy-loss data, and would leave a clearly-visible contamination spot. It is thought that the contribution to the energy-loss spectrum due to the presence of carbon contamination is less than 5 %.

The results obtained from the STEP program were:

I_B^T = 0.92 (arbitary units)
I_C^T = 8.68 (on same scale as above).

The Gryziński formula for the inelastic scattering cross-section gives:

Figure 4.8: the results of the STEP program applied to energy-loss data from a "boron" thin film specimen.

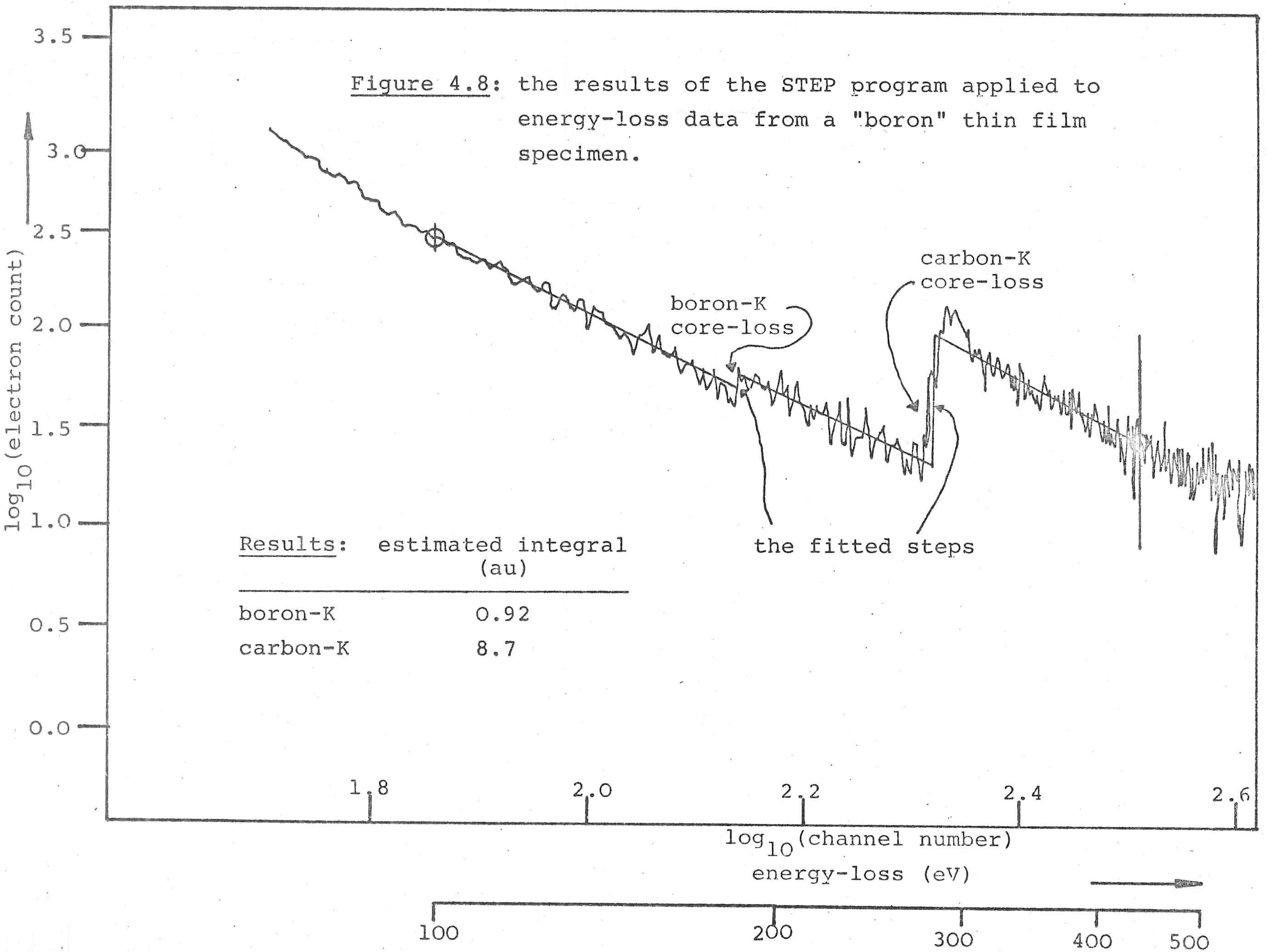

Results:	estimated integral (au)
boron-K	0.92
carbon-K	8.7

$$\sigma_C = 0.84 \cdot 10^{-24} \text{ m}^2 \text{ electron}^{-1} \text{ atom}^{-1}$$
$$\sigma_B = 1.33 \cdot 10^{-24} \quad \text{"}$$

Thus, equation 3.65 gives that:

$$\frac{n_B}{n_C} = \frac{\sigma_C}{\sigma_B} \cdot \frac{I_B^T}{I_C^T} = 0.07$$

Because the step at the boron edge is of a similar height compared with the noise in the spectrum at that point, it is expected that the value of I_B^T is only correct to within 50 %. The poor statistical nature of the spectrum derives from the extreme thinness of the foil. the spectrum shown in figure 4.8 was collected over a period of 1 hour.

The low-loss region was recorded using an analogue scan (on a chart recorder) because the count-rate in the zero-loss peak was too high for the computer system to be used. More importantly, the ratio of zero-loss count rate to plasmon count-rate was so large that, in order to collect an un-distorted zero-loss peak, the plasmon peak would be distorted by digitisation error caused by a low count rate (< few counts per bin period).

The energy-loss spectrum of the low-loss region is shown in figure 4.9. The areas of the zero and plasmon-loss peaks (I_z and I_p) were measured manually. The thickness thus determined is

$$t = \lambda_p \cdot \frac{I_p}{I_z} = 60 \text{ Å}$$

where: $\lambda_p \simeq 770$ Å for a 22 eV plasmon as given by equation 2.36. The estimated accuracy is 20 %.

Thus, assuming that the densities of boron and carbon are not very different, it is possible to express the number ratio result (above) in terms of equivalent thickness. The equivalent thickness of carbon present is: $t_C = 55$ (±11) Å,

and the equivalent thickness of boron present is:

$$t_B = 4 \ (\pm 2) \text{ Å} .$$

4.3.1 The energy-loss results from thicker regions

The specimen used above was supported on aholey carbon film. The spectra shown above were recorded from portions of thin film that lay

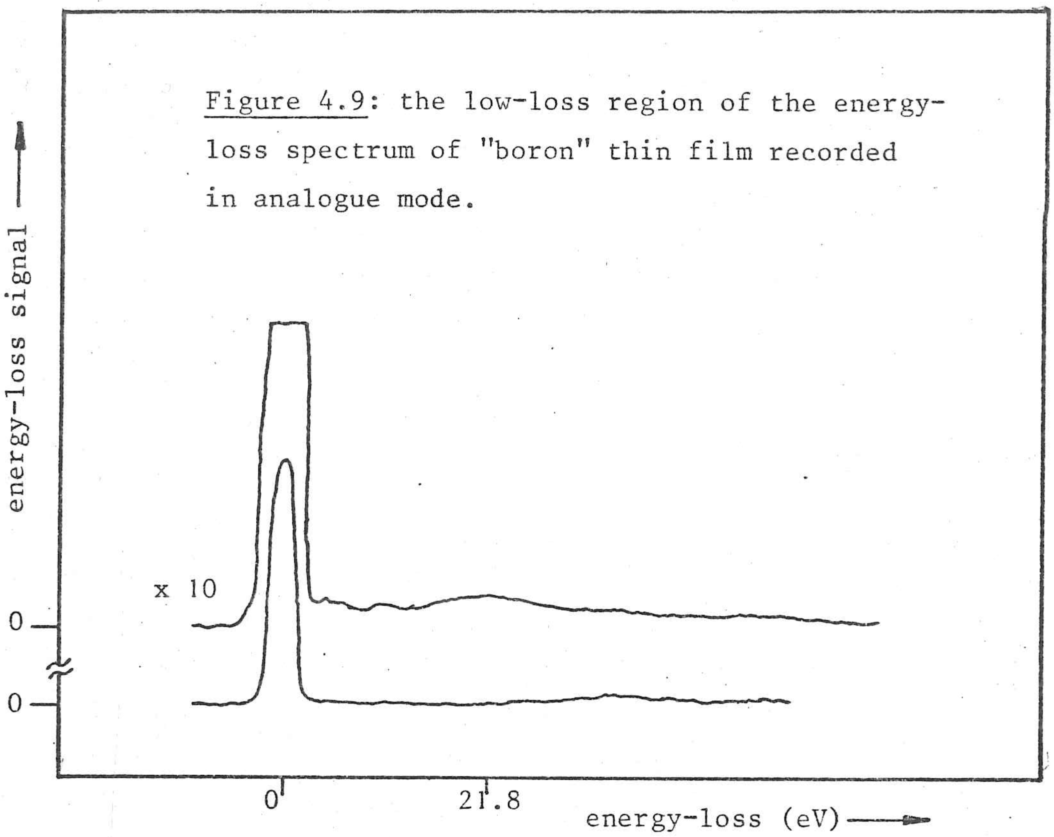

Figure 4.9: the low-loss region of the energy-loss spectrum of "boron" thin film recorded in analogue mode.

over holes in the carbon substrate. As an additional test of the technique, spectra were recorded from portions of the film that lay over the support film. These spectra are shown in figure 4.10. The STEP program was applied to the data, giving the results in fig 4.10b. A similar step to that chosen by the STEP program would have been chosen by the practised eye. In this spectrum, the step is buried in the noise, and the limit of resolution of the STEP program has been reached. The same analysis as in the previous section gives the results:

$t_C = 170\ (\pm 20)$ Å
$t_B = 4\ (\pm\ 3)$ Å.

The assignment of an error term to the result for boron is somewhat arbitrary. A more satisfactory error term could be evaluated by repeating the experiment of the section for several points on the foil and repeating the numerical analysis.

This section shows that a step may be smaller than the noise in its immediate vicinity and it is still possible to detect the step. This is possible because the fit of the power-law is rather insensitive to noise in the data.

4.3.2 Summary of results from "boron" films

The results of the previous two sections show that the thin films supplied by Dorignac were not primarily boron, but were mainly carbon. The equivalent thickness of the boron was the same in both cases at $t_B = 4$ (±2 and 3 respectively) Å.

4.4 SILICON CARBIDE

One of the "discoveries" made with the aid of high spatial resolution EELS is that specimens are very often not what the maker of those specimens thought them to be. Section 4.3 shows that the thin films supplied by Dorignac (1979) and supposed to be mainly boron were, in fact, mostly carbon.

In this section, it is shown that a specimen ofpure silicon carbide (type: Refel "A" - Page (1977)) was mostly silicon in the electron-thin portions of the specimen.

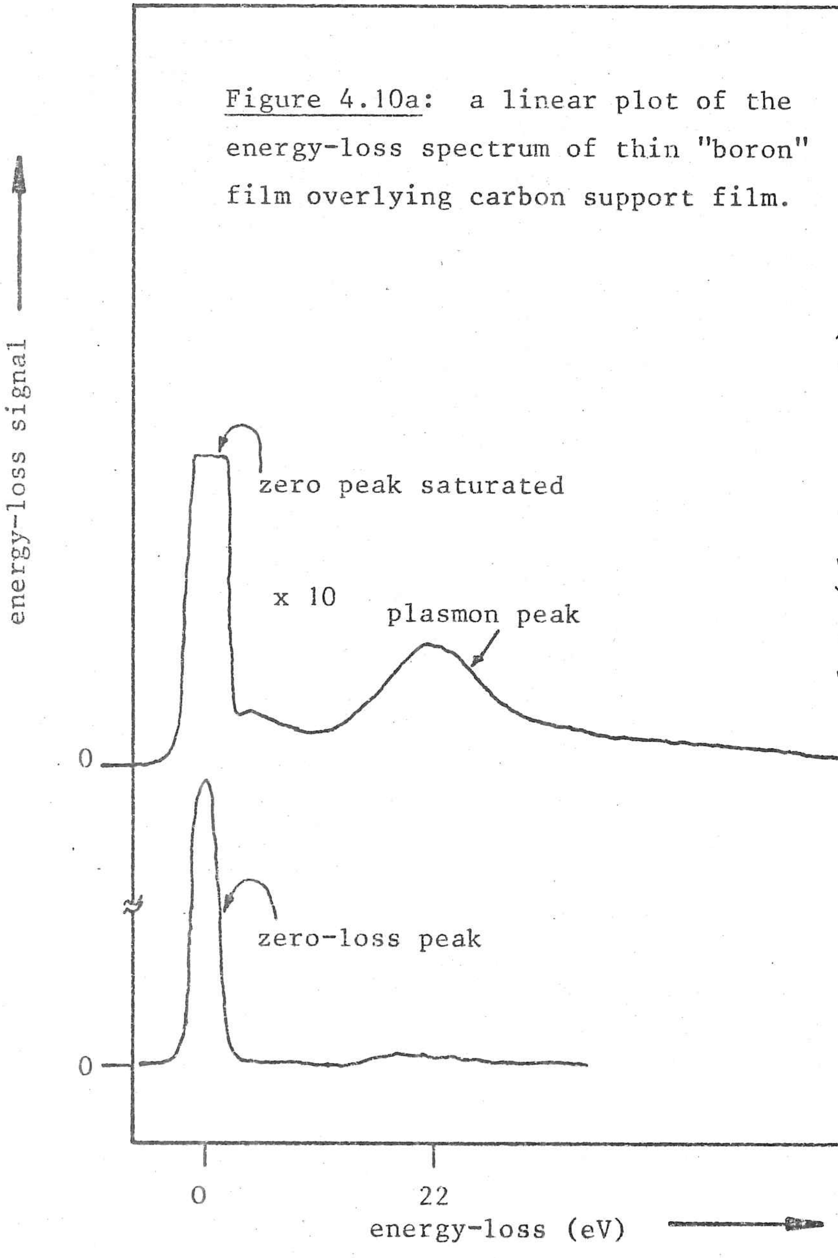

Figure 4.10a: a linear plot of the energy-loss spectrum of thin "boron" film overlying carbon support film.

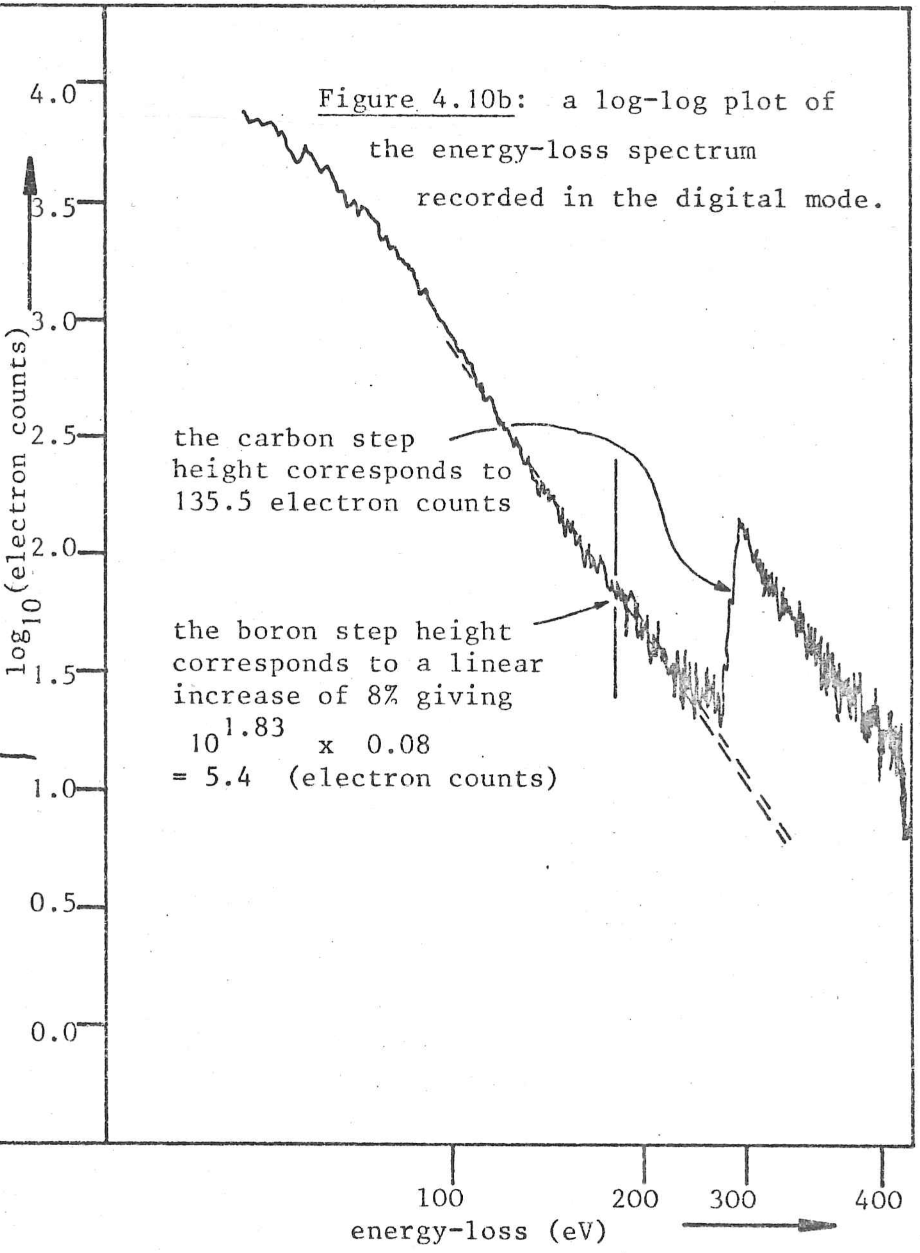

Figure 4.10b: a log-log plot of the energy-loss spectrum recorded in the digital mode.

This form of silicon carbide is made from pure silicon and carbon powders by the application of pressure at high temperatures. The silicon and carbon are thought to inter-diffuse, and the resulting carbide is known to be locally non-stochiometric (Page 1977).
A specimen was made for electron microscopy by the following method:

1) a disc of silicon carbide is cut from a hot pressed rod using a diamond saw.
2) A 3mm disc is cut from this disc using an ultrasonic drill.
3) The resulting disc is mechanically lapped to about 200 μm thickness using diamond abrasive paste and a lapping wheel.
4) The disc is then ion- beam thinned so that a central hole is formed.

A specimen was very kindly supplied by Dr. N Jepps (Cambridge University - Metallurgy and Materials Science Department, England).

All the energy-loss spectra recorded from electron thin regions of the specimen (up to 1000 Å thick) looked very much alike (apart from the expected differences due to multiple-scattering varying with thickness). A representative energy-loss spectrum from a portion of the specimen about 500 Å thick is shown in figure 4.11.

There is a prominent peak near 100 eV arising from excitation of the silicon L_{2-3} core electrons. The edge is broadened by the effects of centrifugal potential (see section 2.2) and multiple scattering. Were the specimen to contain significant amounts of carbon, nitrogen or oxygen, edges should be visible at 285, 399 and 532 eV respectively. The contributions to the energy-loss spectrum that would arise from a 50 atomic % concentration of C, N or O, as given by the Gryzinski formula for the inelastic scattering cross-section , have been marked on figure 4.11.

The noise content at these edge positions relative to the expected step height is 25%, 35%, 50%. A step of the same height as the noise content would still be clearly visible (see section 4.3.1). It is estimated from consideration of figure 4.11 that concentrations of carbon, nitrogen or oxygen of 5,5 and 10 atomic % would be visible on the log-log plot, and would be detected by the STEP program (which tends to perform similarly well as the human eye).

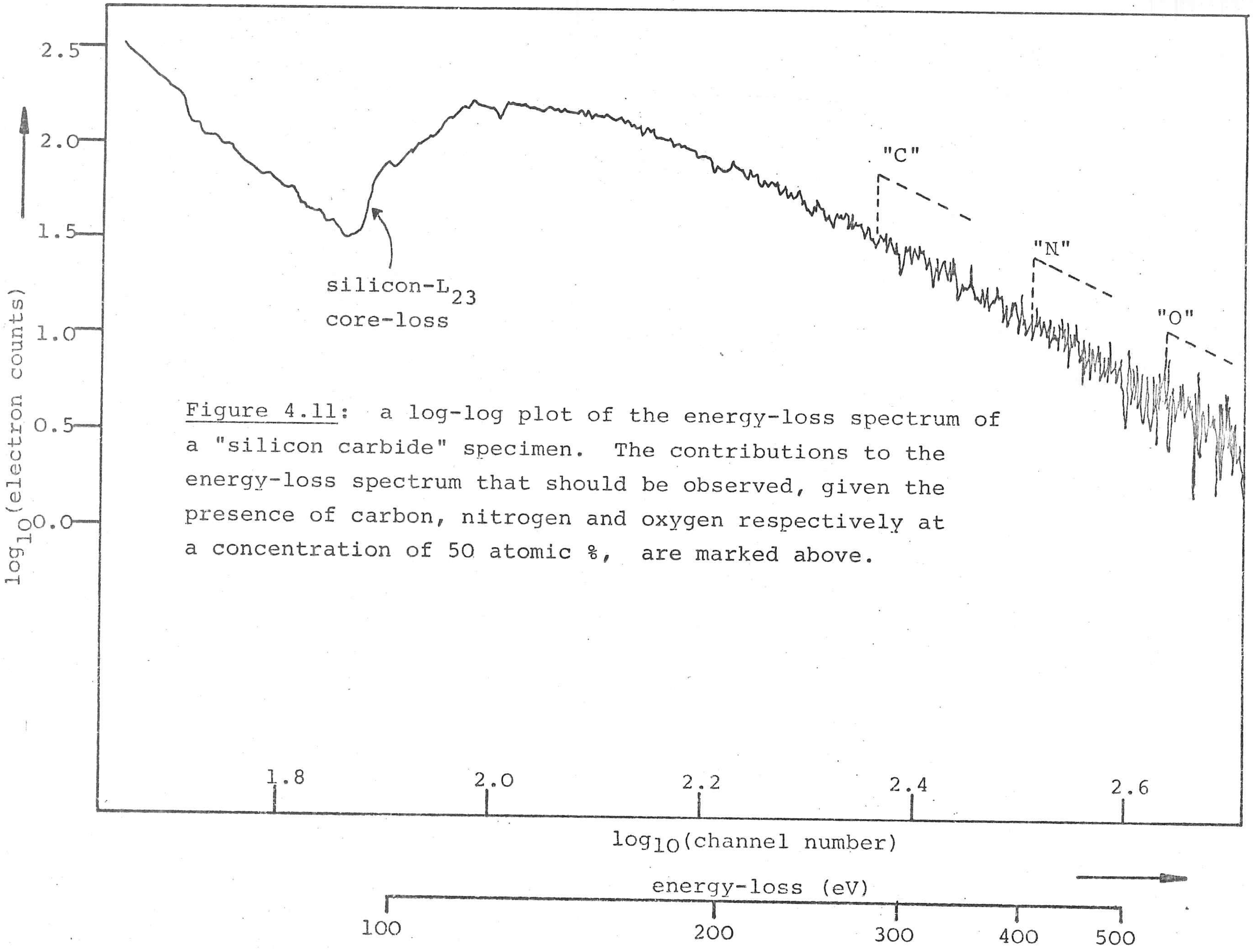

Figure 4.11: a log-log plot of the energy-loss spectrum of a "silicon carbide" specimen. The contributions to the energy-loss spectrum that should be observed, given the presence of carbon, nitrogen and oxygen respectively at a concentration of 50 atomic %, are marked above.

It can therefore be stated that the concentrations of carbon, nitrogen and oxygen in the specimen in the electron thin regions examined are less than 5,5, and 10 atomic % respectively.

These uncertainties could be reduced by increasing the data-collection time and thus decreasing the height of the noise seen on the log-log plot.

Chapter 5 - The extended energy-loss fine structure of boron nitride

- 5.1 Specimen preparation and conventional electron microscopy
- 5.2 A resumé of EXELFS theory
- 5.3 Electron energy-loss results
  - 5.3.1 Numerical techniques
    - 5.3.1.1 The numerical correction of thickness effects
    - 5.3.1.2 A simplified numerical processing scheme
    - 5.3.1.3 Tests of the numerical procedures
  - 5.3.2 The numerical analysis of boron nitride EXELFS data
  - 5.3.3 Self-consistent boron nitride results
  - 5.3.4 Comparison of the energy-loss results with the predictions from the known crystal structure
  - 5.3.5 The synthesised RDF using calculated phase-shifts and scattering amplitudes
- 5.4 Nitrogen-K EXLEFS
- 5.5 Bandstructure and specimen orientation effects

Chapter 5 - The extended energy-loss fine structure of boron nitride

5.1 SPECIMEN PREPARATION AND CONVENTIONAL ELECTRON MICROSCOPY

A specimen of boron nitride was prepared by scratching a hole in a 3 mm disc, 0.25 mm thick, cut from a rod of polycrystalline boron nitride.

Boron nitride has at least three different crystalline forms (Wycoff 1960). The room-temperature form has a graphite-like (hexagonal layered) structure in which the atoms lie in sheets which are hexagonally packed. Bonding between the sheets is due to van der Waals forces.

Conventional transmission electron microscopy (CTEM) reveals the existence of thin platelets about 2000 Å across near the edge of the hole in the specimen (see figure 5.1), and a selected area diffraction pattern from an area covering many crystallites is shown in figure 5.1 indexed according to the hexagonal structure.

Boron nitride is an excellent specimen with which to test the accuracy of extended energy-loss fine structure (EXELFS) because:

1) the structure of hexagonal boron nitride is well-known and easily verified by electron diffraction;

2) boron and nitrogen both have K-shell core-losses at energies well within the convenient working range of the HB5 microscope.

5.2 A RESUMÉ OF EXELFS THEORY

The theory of EXELFS has been discussed in section 2.2.6. The result of simple EXELFS theory is that the energy-loss spectrum due to a single atom is modified when in a solid by the presence of neighboring atoms. This modification may be expressed as a modulation:

EXPERIMENTAL-SPECTRUM = SINGLE-ATOM-SPECTRUM × (1 + $\chi(E)$).

where: $\chi(E)$ represents a modulation of the single-atom spectrum, given under the plane-wave approximation as:

$$\chi(k) \simeq \frac{A(k)}{k} . \sum_j \frac{N_j}{R_j^2} \exp(-R_j / \lambda(k) . \exp(-\sigma_j^2 k^2/2) . \times \sin(2kR_j + \phi(k)) \qquad - \quad 5.1$$

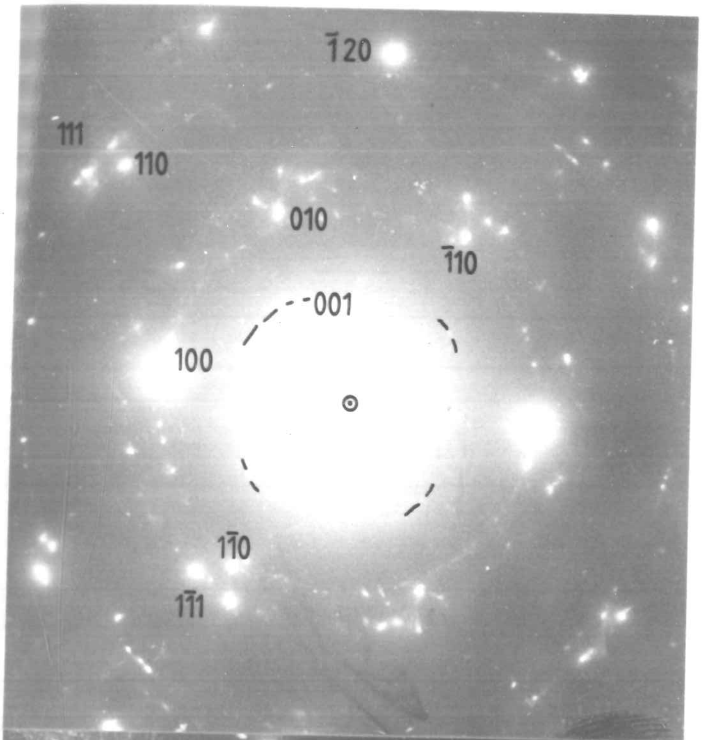

Figure 5.1a: selected-area diffraction pattern of graphitic boron nitride. The area used contained several crystallites. The reflections are labelled with reference to the hexagonal structure.

The rings are:

001	at	3.33 Å
100,$1\bar{1}0$		2.169
101		1.817
110,$\bar{1}20$		1.252
111		1.172
⋮		⋮

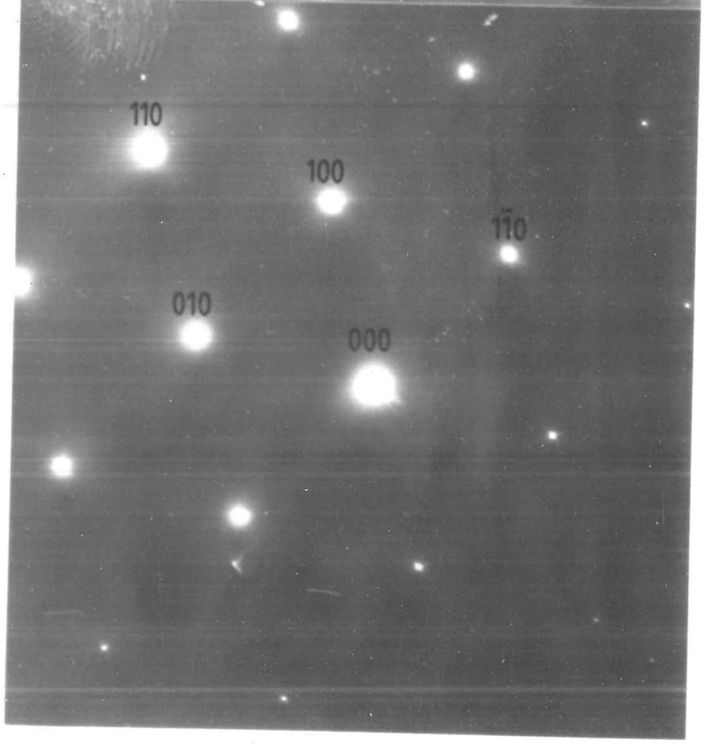

Figure 5.1b: selected-area diffraction pattern from a single-crystal area of graphitic boron nitride in the (001) orientation.

Figure 5.1c: bright-field micrograph of graphitic boron nitride showing large platelets containing large (several hundred Å) uniform-thickness areas.

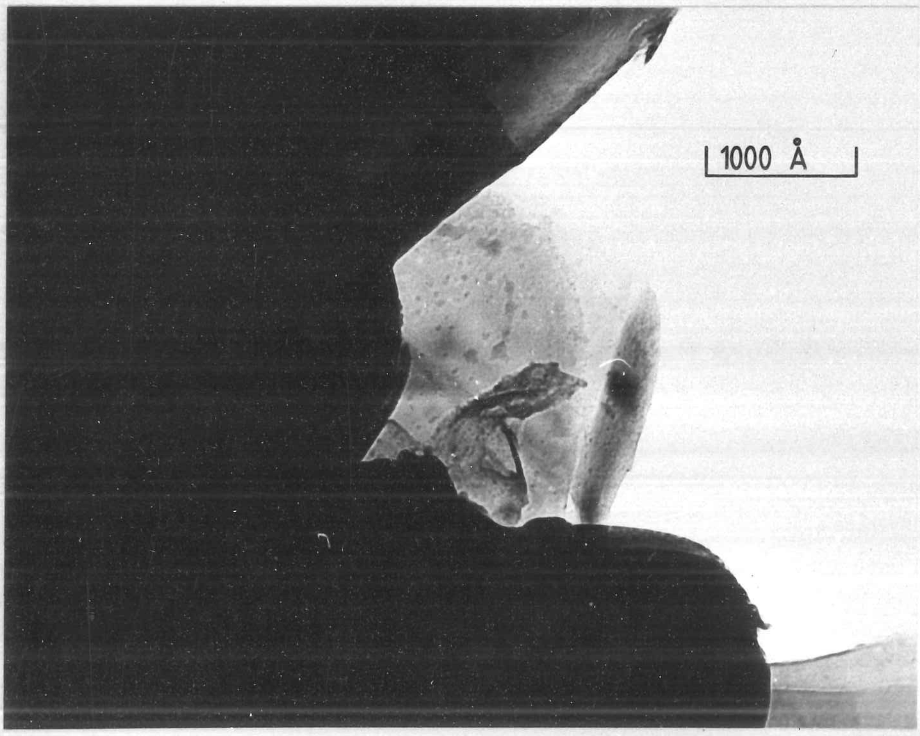

Figure 5.1d: bright-field micrograph of graphitic boron nitride corresponding to the lower right corner of Fig. 5.1c. The edge of the flake may be as thin as 50 Å (see text).

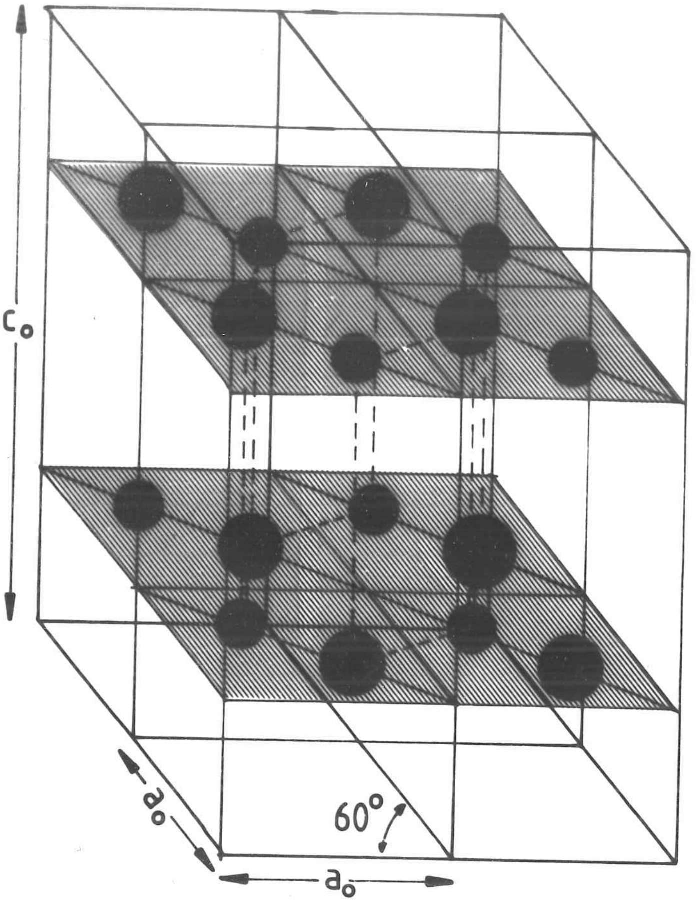

Figure 5.2:
the crystal structure
of hexagonal (graphitic)
boron nitride.

● nitrogen

● boron

a_o = 2.504 Å

c_o = 6.66 Å

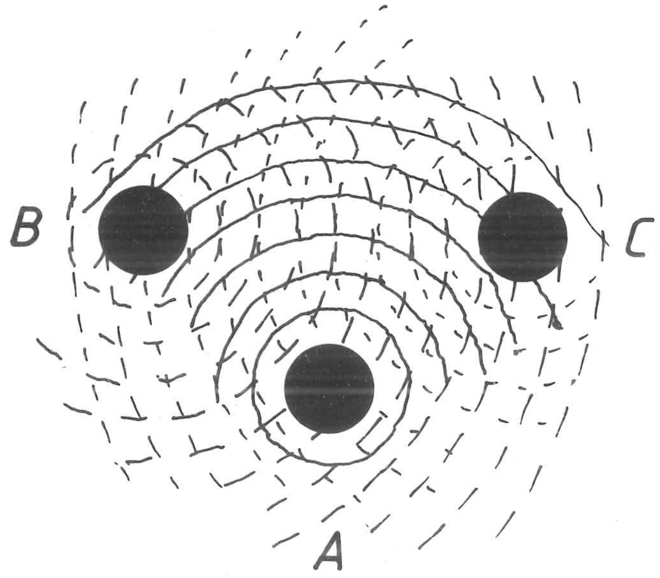

Figure 5.3: a simple physical understanding of EXELFS. See text.

where: k is the wave-vector of the ejected secondary electron;
$A(k)$ is the atomic backscattering amplitude;
N_j is the number of atoms in the shell j at radius R_j;
$\lambda(k)$ is the mean free path (MFP) of the secondary electron;
σ_j is a term due to thermal motion and structural disorder;
$\phi(k)$ is the total atomic phase-shift.

This result may be given a physical interpretation: consider the origin atom, marked "A" in figure 5.3, emitting a secondary electron. The out-going wave-front is partially back-scattered (and shifted in phase) by neighboring atoms "B" and "C" and interferes with the out-going wave at the origin atom. This modifies the final state $|f>$ and thus the probability of ejection of the secondary electron which depends on the matrix element $|<f|\exp(i\underline{q}.\underline{r})|i>|$.
The inverse dependence of $\chi(k)$ on distance is intuitively reasonable considering the angular extent of the backscattering atom seen from the origin atom to determine the probability of backscattering.
The effect of thermal and structural disorder is to destroy the coherence between the back-scattered waves from atoms in the same shell, thus depressing the depth of modulation.

The only species-specific dependence is contained in the atomic back-scattering $A(k)$ and the total phase shift $\phi(k)$.
Structural information is present only in the sum over atomic shells j.
If the sum over j is replaced with an integration over radial distance, R, then all structural information is present in the function

$$n(r) = \sum_j \frac{N_j}{R_j^2}.\delta(r - R_j) \qquad - \quad 5.2$$

This is loosely termed the radial-distribution function (RDF) and may be extracted from the modulations $\chi(k)$ using the techniques of sections 2.2.6 and 3.3.5.

5.3 ELECTRON ENERGY-LOSS RESULTS

The energy-loss spectrum is represented in the computer as a series of numbers, each giving the number of electrons detected within a certain range of energy-losses: i.e., the energy-loss range is divided into a number (usually several hundred) of channels (or bins).

In order to obtain accurate information from EXELFS, the number of electrons in each channel should be made as large as possible, thus minimising statistical noise. For example: to obtain 1% statistics (noise to signal ratio) in a given channel, at least 10^4 electrons should be detected in that channel. The number of electrons detected follows a Poisson distribution (Papoulis 1965). Because the EXELFS is a small modulation ($|\chi(k)| < 5\%$) on the smooth atomic energy-loss spectrum, the effect of noise on the numerically-extracted EXELFS is correspondingly enhanced. Thus, care must be exercised in order to obtain results with sufficiently good statistics.

The energy-resolution of the spectrometer may be adjusted by means of the slits separation and collector aperture acceptance angle. The worse the energy-resolution, the greater will be the electron current detected by the photomultipler tube; therefore the worst energy-resolution consistent with little observed degradation in the depth of the modulations is employed.

5.3.1 Numerical techniques

The reader is referred to appendix A for a detailed description of the operation of the computer programs.

Figure 5.4 shows a log-log plot of the energy-loss spectrum from a thin flake of boron nitride in the energy-loss range 150 to 450 eV. It will be shown later that the thickness was about 80 Å, the flake is certainly thin enough to ignore the effects of multiple scattering.

The boron nitride core-loss region (i.e. 150 to 450 eV) energy-loss spectrum is processed as follows:

1) correction for finite aperture size is made using the APCOR program;

2) the background before the boron-k core-loss is removed using the NRAMP program;

3) the edge spectrum is deconvoluted with an aperture-corrected low-loss spectrum;

4) the modulations $\chi(E)$ are extracted using the NRAMP program again;

5) the modulations $\chi(E)$ are transformed to $\chi(k)$ and fourier transformed.

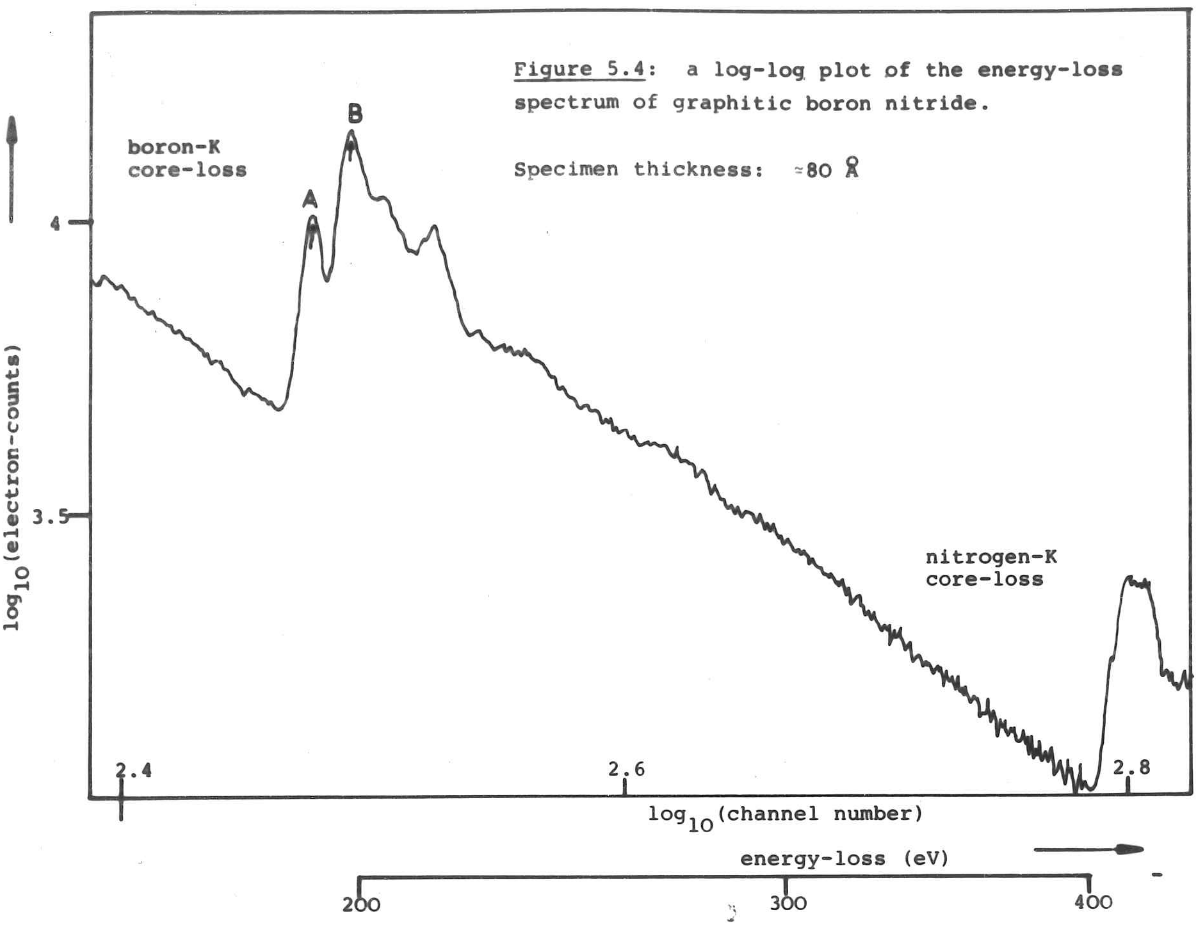

Figure 5.4: a log-log plot of the energy-loss spectrum of graphitic boron nitride.

Specimen thickness: ≈80 Å

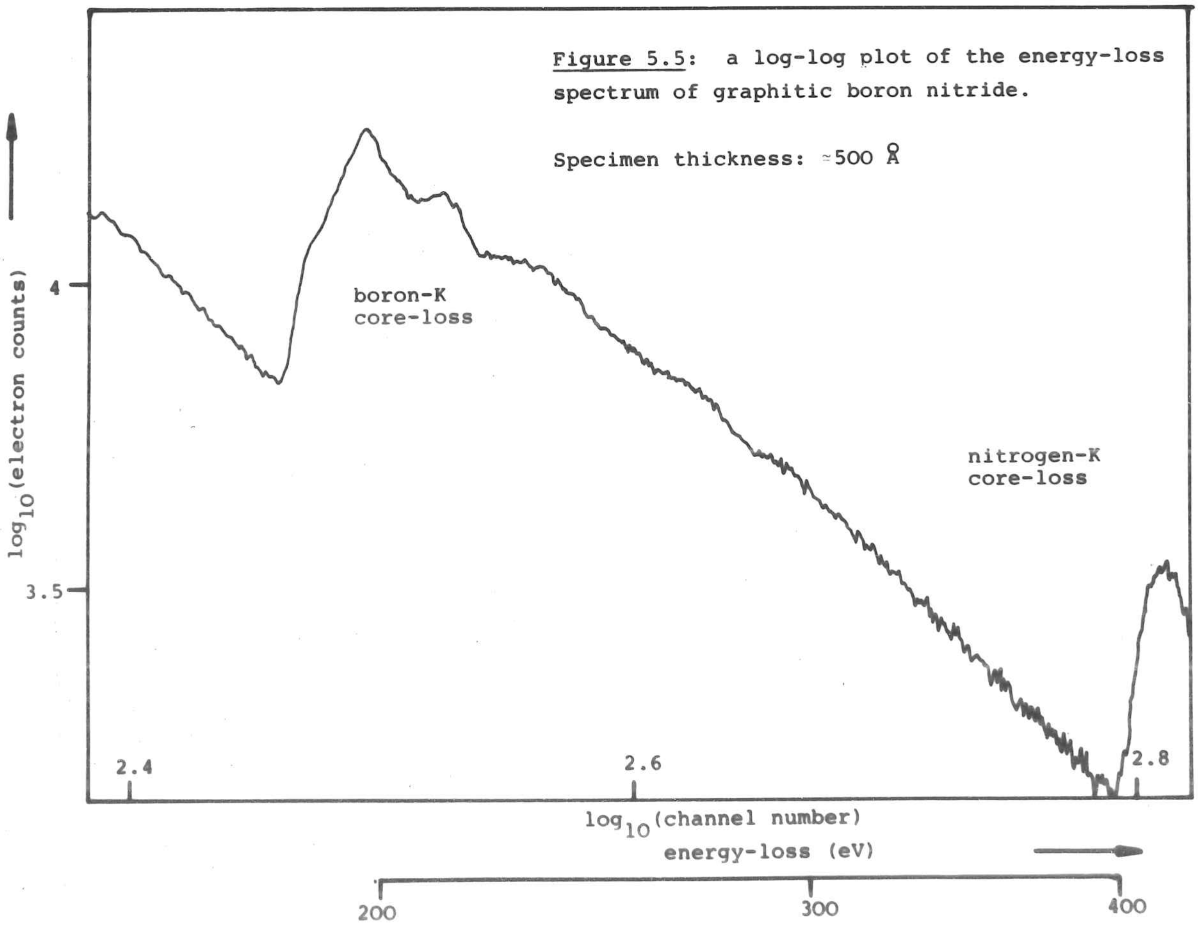

Figure 5.5: a log-log plot of the energy-loss spectrum of graphitic boron nitride.

Specimen thickness: ≈500 Å

The modulus of the fourier transform, which is an approximation of the radial distribution function (RDF) is evaluated and displayed graphically. Also, at this stage, any windowing that has to be introduced into the modulations is performed. The operations of this step are all carried out by the TRANS program.

Two variables need to be determined during the analysis of the data:
1) the position of the energy-loss (E_e) which is just sufficient to promote a core electron to an un-bound state. The wave-vector of the secondary electron is then given by

$$k = \frac{2m}{\hbar} \cdot (e(E - E_e))^{\frac{1}{2}} \qquad - \qquad 5.3$$

where: E is the energy-loss of the incident electron.
The theoretical value of E_e depends on the average inner potential experienced by the secondary electron and may be calculated from a suitable model of the specimen. Alternatively, E_e may be considered to be a variable which is adjusted to bring the peaks in the imaginary part of the fourier transform of $\chi(k)$ into line, given accurate correction of the phase-shift and back-scattering terms. This approach can only work if the approximations to the phase shift and back-scattering amplitude are sufficiently good, and if the statistics of the data are rather better than currently achieved by EELS. For an example of the latter approach, the reader is referred to a paper by Lee & Beni (1977) which describes the analysis of X-ray absorption data from Germanium. Their results show that E_e for germanium-K should be placed approximately 5 eV below the energy corresponding to transitions to the vacuum level. They also demonstrate that error in the position of E_e will introduce an effective k^{-1} term into the phase-shift and thus slightly displace the peaks in the RDF from their correct position. This point is tested below (in section 5.3.1.3).
2) The modulations $\chi(k)$ need to be windowed in such a way that spurious side-lobes are not introduced into the RDF. The lower energy-window should be adjusted to exclude structure in the data due to bandstructure (i.e. - structure which is not properly explained by the approximate EXELFS formulation). For long-wavelength secondary electrons, the effects of a curved wave-front (i.e. a spherical out-going wave) and an anisotropic inner potential and

density of states are not important. Also, the assumption that the back-scattering amplitude A(k) may be approximated by Rutherford scattering (i.e. $A(k) \propto 1/k^2$) fails to hold true at low wave-vector, k, and any error in the phase-shift $\phi(k)$ due to uncertainty in the position of E_e is worse at low values of k. As will be discussed later, band-structure effects are considered not to extend beyond 30 eV above the core-loss edge. The use of a low-energy window of this value also simplifies the discussion of multiple inelastic scattering (see section 5.3.1.1), and makes the RDF relatively insensitive to errors in the value of E_e.

5.3.1.1 The numerical correction of thickness effects

The thicker the specimen (in the range 0 - 1000 Å), the greater will be the electron count-rate, but the collected spectrum will contain a contribution from incident electrons which have undergone multiple inelastic scattering which also increases with thickness.
Figure 5.4 shows the energy-loss spectrum (ELS) of a thin specimen of graphitic boron nitride. Collection time for this spectrum was 1 hour. The energy-loss resolution was degraded from 1.5 eV to 4 eV (FWHM) and the electron probe moved to a thicker portion of the specimen. The low-loss region of the ELS was recorded (0 to 100 eV), and then a core-loss spectrum was recorded (150 to 450 eV). These last two spectra were corrected for finite aperture size (using the APCOR program). The count-rate in both spectra was kept below 7 kHz, thus limiting dead-time correction to less than 3 % (see section 3.3.1).

As a check of the self-consistency of the low-loss spectrum, the low-loss data were multiply deconvoluted (using the MULDEC program), giving the results of figure 5.6. It can be seen that multiple deconvolution is not greatly in error as the bulk of the second plasmon peak has been removed correctly (although a little structure remains that is due to multiple-scattering). Were the ratio of zero-loss peak intensity to plasmon peak intensity to be greatly in error, the correction for the second plasmon would be seen to be in error. The expected sign of the error caused by count-rate dead-time would be an overestimate of double-scattering producing a corrected spectrum which went negative between 50 and 100 eV. The success of

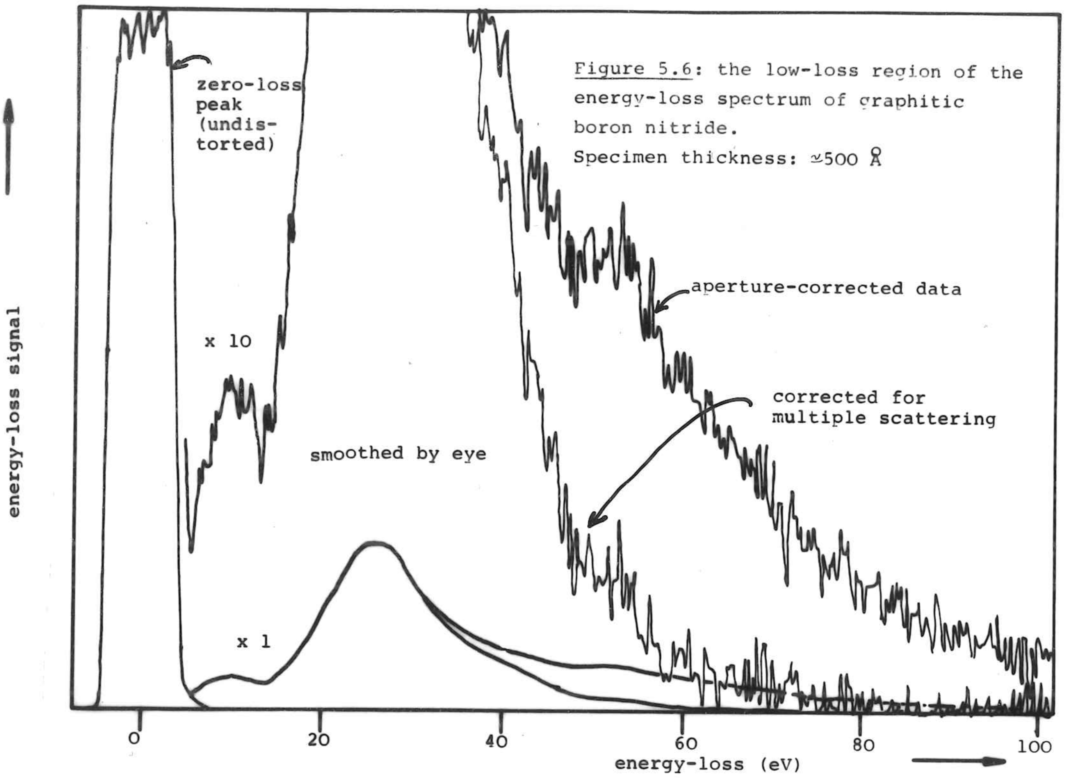

Figure 5.6: the low-loss region of the energy-loss spectrum of graphitic boron nitride.
Specimen thickness: ≃500 Å

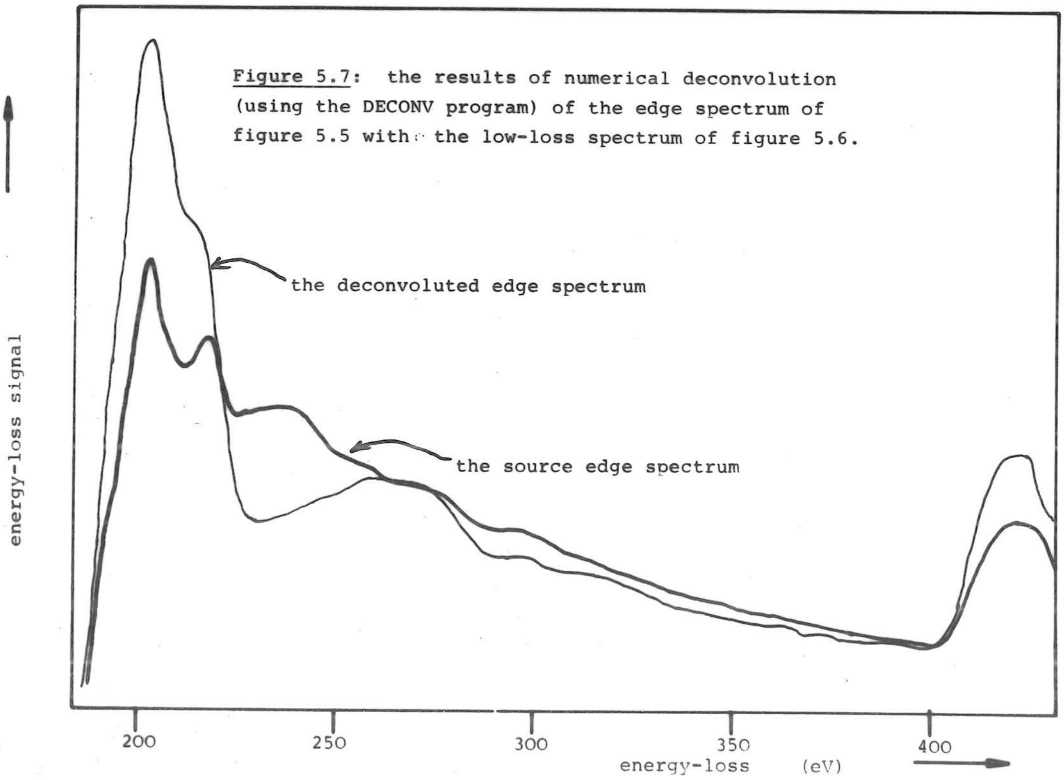

Figure 5.7: the results of numerical deconvolution (using the DECONV program) of the edge spectrum of figure 5.5 with the low-loss spectrum of figure 5.6.

multiple deconvolution implies that the low loss data are not greatly distorted by count-rate errors.

The spectrum of the core-loss region was corrected by background removal (using the RAMP program)and deconvoluted with the low-loss spectrum. The results of the deconvolution are shown in figure 5.7. It can be seen, by comparison with the spectrum of a thin specimen (figure 5.4), that the deconvolution has over-estimated the amount of double-scattering present quite seriously. Two possible causes of this error are:

1) The double-scattering angular convolution correction. With the probe convergence geometry (α = 8 mR), conventional deconvolution is expected to underestimate the amount of double-scattering present by a factor of 1.00 ± 0.02 (see section 3.3.3.4). The size of the correction is too small to be noticable and is in the wrong sense.

2) The low-loss region does not adequately represent the specimen in the area from which the core-loss spectrum was recorded. The thinnest foils can be seen to etch slowly under the electron beam, and it may be that the energy-loss spectrum of the boron-K core-loss which was recorded over many minutes corresponds to a thinner foil than the region from which the low-loss spectrum was recorded. It may simply be that, although recorded from the immediate vicinity, there was sufficient variation in specimen thickness to make the thickness corresponding to the low-loss region different from that corresponding to the edge region.

The dramatic failure of deconvolution in this particular case sounds a warning note: the RDF is sensitive to structure after the edge. Numerical deconvolution introduces or modifies structure after the edge. Unless both low-loss and core-loss regions are captured simultaneously (and therefore both corresponding to the same foil thickness), numerical deconvolution of an edge spectrum with a low-loss spectrum in order to correct EXELFS structure cannot be performed with any confidence in the significance of the results. It is unfortunate that it is not possible to record both low-loss and edge spectra simultaneously on the data capture system used at the time of writing because of severe count-rate limitations and because of the limited dynamic range of the computer system. It is expected that the commissioning of a new LINK SYSTEMS 860 combined X-ray and EELS data-collection system will provide a great improvement in the maximum count-rate and dynamic range of the energy-loss spectrum.

Because of the experience gained from the work of this section, all energy-loss spectra presented hereinafter were collected from regions of the specimen which were less than 100 Å thick. Due to specimen drift and etching, it was necessary to use areas of the specimen about 500 Å across during the collection of the core-loss data, and move the probe about the specimen whilst collecting energy-loss data. This may easily be accomplished as the specimen cleaves naturally, and many large, thin platelets could be found.

The choice of a low-energy window at an energy 25 eV above the edge also lessens the dependence of the RDF on thickness, the major effect of multiple-scattering being not the introduction of false structure into $\chi(E)$, but the degradation of the amplitude of $\chi(E)$ by an estimated 10% at approximately 100 Å foil thickness. This occurs because double inelastic scattering introduces extra essentially featureless intensity (of value $\simeq$ thickness/λ_{plasmon} $\times$ edge signal) which contributes to the smooth edge signal, but does not modify the absolute depth of the fine structure on the edge.

Therefore the following simplified numerical processing scheme was employed for these thin foils (see below).

5.3.1.2 A simplified numerical processing scheme

1) The core-loss region energy-loss data are corrected for finite aperture size (using the APCOR program).

2) The background is stripped and the modulations $\chi(E)$ are extracted (both using the RAMP program).

3) The modulations $\chi(E)$ can then be transformed to $\chi(k)$, windowed (as described below in detail) and fourier transformed. The modulus of the fourier transform is displayed graphically (using the TRANS program).

5.3.1.3 Tests of the numerical procedures

The processing scheme, given above, was tested using synthesised spectra. A program (called GEN) was written which:

1) generated a zero-loss peak of specified width;

2) generated a plasmon-loss peak of specified width and energy, corresponding to a specified thickness of material;

3) generated an idealised core-loss edge (given by a sharp edge and a power-law decay) for a specified core-loss voltage, number of electrons in the edge and corresponding to a specified thickness of material;

4) generated $\chi(E)$ given by the theory of section 5.2 for a set of specified R_j and N_j, the phase-shift being given either by a set of parameters, or a tabulation of calculated model phase-shifts and backscattering-amplitudes (see section 5.3.5).

5) The structure after the edge was generated from the results of steps 3) and 4), and the plasmon-peak and zero-loss peaks were added from the results of steps 2) and 1).

6) The resulting spectrum was multiply-scattered using the theory of section 3.3.3.

7) The resulting spectrum was scaled by a specified amount, and random noise added (with Poisson statistics) to simulate electron arrival statistics.

In step 4), the EXELFS were normalised to an arbitrary maximum depth of 5%. This is in rough accord with experimental observations.

The synthesised spectrum is processed numerically in exactly the same was as energy-loss data in order to obtain the RDF. The peaks in the RDF thus extracted may be compared with the parameter set R_j and N_j, which should determine the RDF, and any differences may be attributed to the effect of the numerical procedures employed.

The first test spectrum was generated with 1 "atom" at 1.5 Å from the origin atom and 2 atoms at 4.0 Å. The window function used in the course of numerical processing was the product of three terms:

1) a top-hat function of variable low-energy edge and with the

edges smoothed (by a cosine/sine function) so that they rise over a range of wave-vector of 0.5 $Å^{-1}$;

2) a gaussian function centred at $k = 0$, of width (FWHM) 16 $Å^{-1}$;

3) a k^{-1} funtion which attenuates the effect of noise at large k.

The term A(k)/k in equation 5.1 may be approximated by Rutherford scattering, thus giving k^{-3}. Therefore the modulations $\chi(k)$ should be scaled by k^3 prior to fourier transformation. In practice, a scale of k^2 is used which is effectively the correct approximation to the A(k)/k term multiplied by a k^{-1} function. The k^{-1} function therefore appears as part of the windowing procedure.

The result of this processing, in which the k^{-1} window term has been omitted is given in figure 5.8a. The two peaks can be seen to centred at their correct positions. Additional structure is present which may be ascribed to the effect of the window function. The result of processing, including the k^{-1} window term, is given in figure 5.8b. It can be seen that the peaks are still centred at the correct radial distances, although the detail in the noise background has altered.

The synthesised spectrum was processed using window terms 1) and 3) only, thus omitting the gaussian cut-off: see figure 5.8c. The multiplication of the modulations by a gaussian is equivalent to a convolution of the fourier transform by a gaussian. The omission of this term results in a slight increase in resolution (i.e. the peaks are slightly narrower than fig 5.8b) at the expense of more-pronounced noise peaks. It is now becomes clear that the peaks at 0.25 and 0.7 Å are due to window termination effects.

The synthesised spectrum was processed using window terms 1) and 3), as before, but the window term 1) was modified so that the edges were sharp (i.e. the function takes only the values of zero and unity). The resulting RDF is shown in figure 5.8d. It can be seen that the side-lobes have become more pronounced.

The synthesised spectrum was processed using window terms 1) and 2), except that the window term 1) included a low-energy window 25 eV

Figure 5.8a: the modulus of the fourier transform of $\chi(k)$ (the RDF) obtained from a generated energy-loss spectrum. See text.

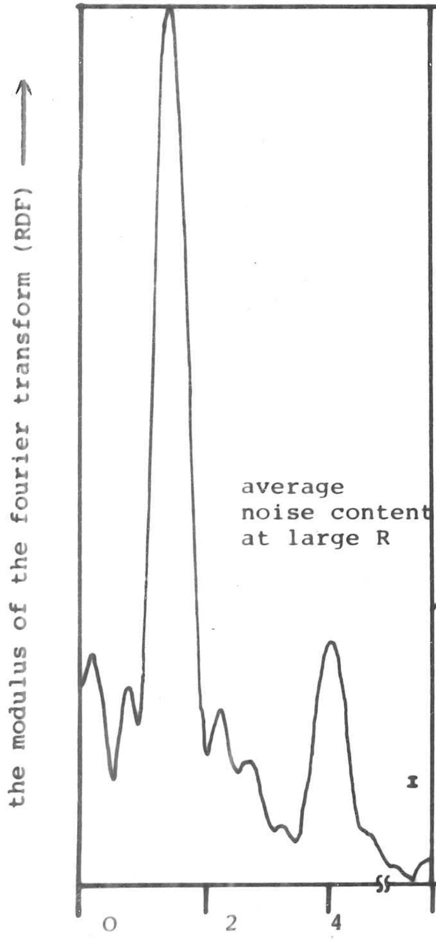

Figure 5.8b: $\chi(k)$ has been multiplied by k^3 rather than k^2.

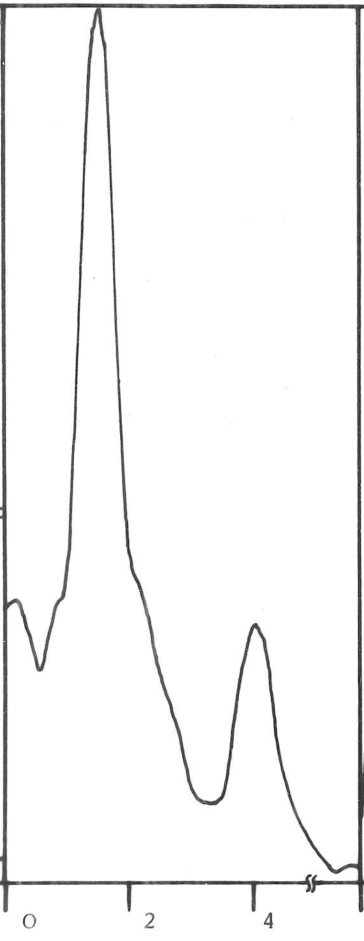

Figure 5.8c: $\chi(k)$ has not been multiplied by a gaussian.

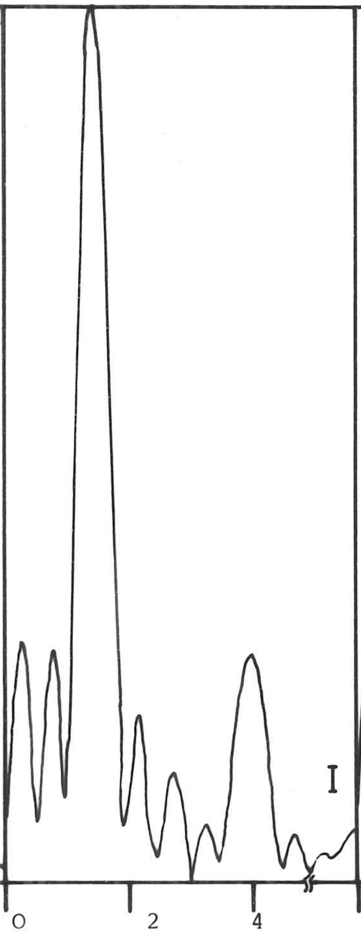

Figure 5.8d: $\chi(k)$ has not been multiplied by a gaussian and the window function has sharp edges.

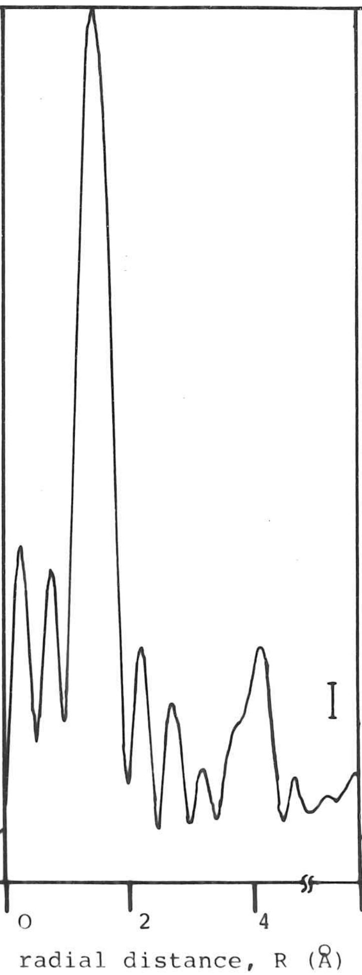

Figure 5.8e: as fig. 5.8a except a smooth left window has been introduced at 25 eV above the edge.

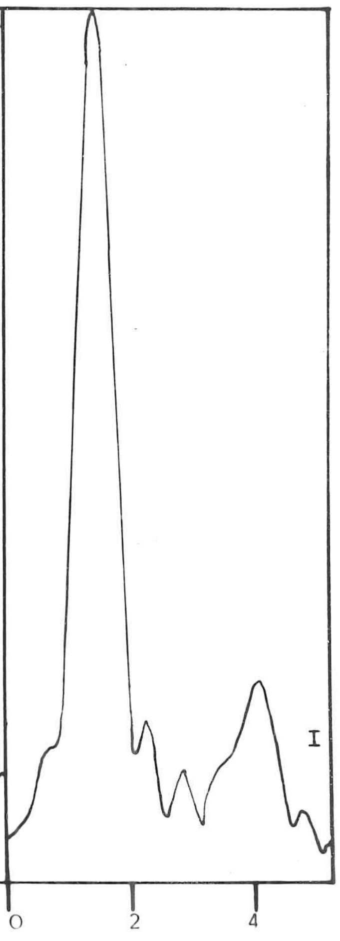

above the edge energy, giving the RDF of figure 5.8e. The effect of introducing a low-energy window may be determined by comparing this figure with fig 5.8a. It can be seen that the centres of gravity of the two main peaks are still at the correct position, but the effect of noise have become more important because the very clean data excluded by the introduction of a 25 eV low-energy window may no longer contribute to the RDF. The noise on this RDF is not due entirely to termination errors in the window function, but is also due to statistical noise in the synthesised data, otherwise the peak at 4 Å would not be distorted in shape.

In order to test the effect of an error in E_e (the position of $k = 0$ on the energy-loss spectrum), the modulations $\chi(E)$ were shifted along the energy axis. A shift of -5 eV (i.e. E_e chosen to be 5 eV below the correct edge voltage) produced the RDF shown in fig 5.8f. It can be seen that the peak near 1.5 Å has been shifted to the right (increasing R) by about 0.1 Å, whilst the peak near 4 Å has been shifted by a much greater amount 0.25 Å. The addition of a low-energy window 25 eV above the edge does little to reduce the shift (see fig 5.8g).
A shift of +5 eV produced the RDF shown in figure 5.8h. The peak near 1.5 Å is relatively undisturbed, although a shoulder has been introduced on the low-R side of this peak. The peak near 4 Å has been shifted to the left by about 0.2 Å and, again, a window 25 eV above the edge does little to reduce this shift (see figure 5.8i).

These tests show that the following window function may be applied to the modulations $\chi(k)$ without fear that it will significantly distort the interpretation of the RDF. The window function is the product of three terms:
1) a smooth window function with a low-energy bound approximately 25 eV above the edge, the edges rise and fall smoothly over a range of wave-vector of 0.5 $Å^{-1}$;
2) a gaussian function centred at $k = 0$ of width (FWHM) about 16 $Å^{-1}$;
3) an effective k^{-1} scaling produced by approximating $A(k)/k$ by k^{-2} rather than k^{-3} (as would be given by Rutherford scattering).

The fourier transform of the window function is shown in figure 5.9. It can be seen that the resolution (half width at half maximum) given by the use of this window

Figure 5.8f:
E_o is chosen to be 5 eV below the edge position.

Figure 5.8g:
as fig. 5.8f except the left window is 25 eV above E_o.

Figure 5.8h:
E_o is chosen to be 5 eV above the edge position.

Figure 5.8i:
as fig. 5.8h except the left window is 25 eV above E_o

Figure 5.9:
the RDF of the final window function used.

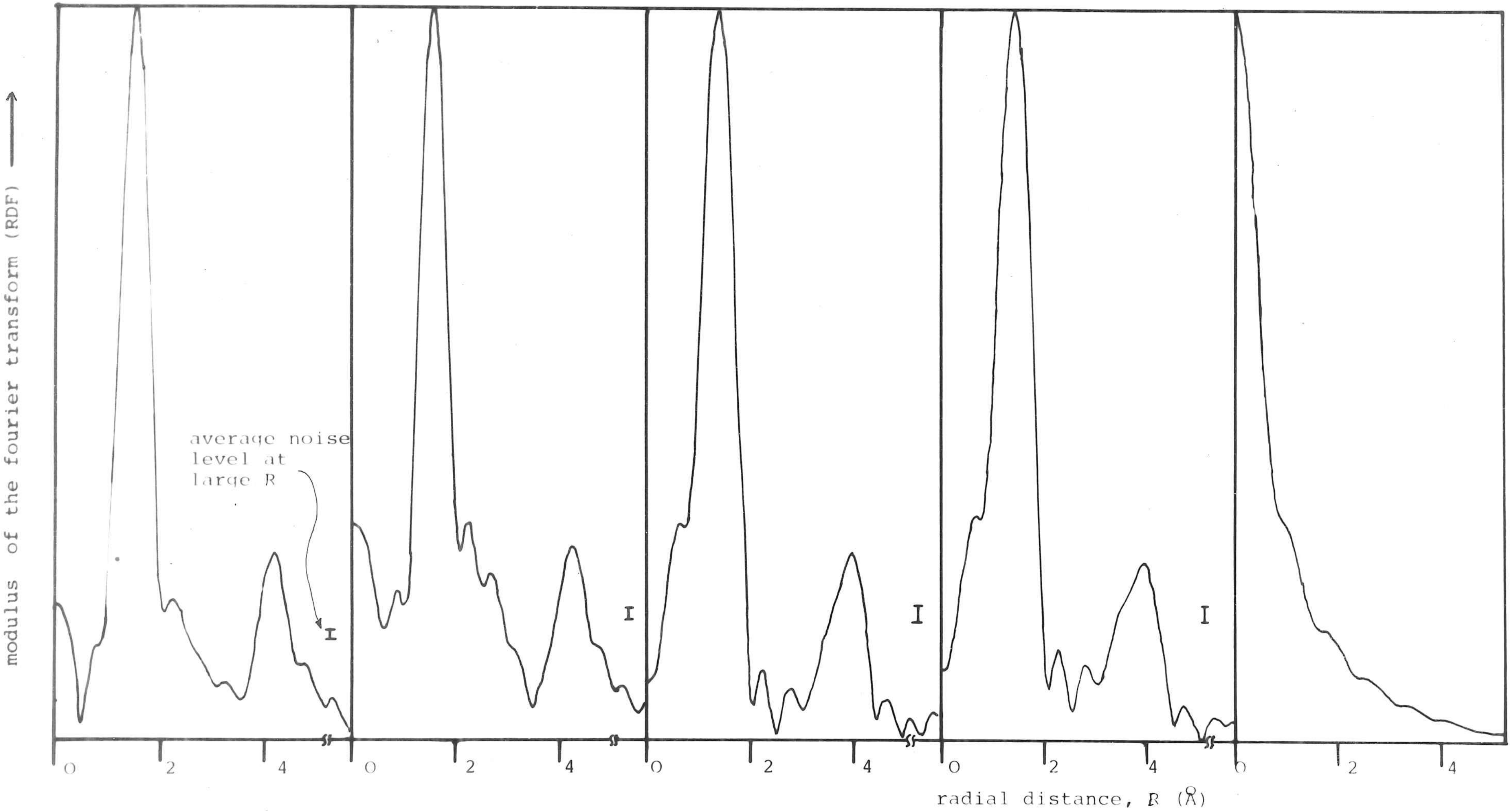

is about 0.6 Å. This is not a very useful measure, however, as there is considerably more intensity at large values of the radius than would be obtained by approximating the peak shape by a gaussian.

The reader is once again referred to figure 5.8b which shows the combined effects of the windowing and other numerical procedures on the synthesised spectrum.

5.3.2 The numerical analysis of boron nitride EXELFS data

The numerical procedure, established in section 5.3.1.3 to yield an undistorted RDF with resolution about 0.6 Å, was applied to energy-loss data from a thin (100Å) boron nitride specimen.

In order to strengthen further confidence in the results of the numerical processing scheme, the window parameters were adjusted in a series of tests.

The RDF produced using the normal window function (as defined above) but with a low-energy window at the edge position (chosen to be peak "A" of figure 5.4) is shown in figure 5.10a. There are three features above the level of noise:

1) a large peak at 1.1 Å;
2) a smaller, slightly broader peak at 3.2 Å;
3) a broad peak at about 4.8 Å which contains at least two peaks separated by about 1 Å.

A low-energy window was introduced at 25 eV above the edge, giving the RDF of figure 5.10b. The precise details of shape of the peaks 1) to 3) above have changed: this is to be expected because the dubious data near the edge have been excluded. However, the peaks are not altered in horizontal position. The narrower range of wavenumber for which data is avilable means that the resolution in radius should be slightly worsened. The measured width (FWHM) of the peak at 3.2 Å has increased slightly from 1.1 to 1.2 Å, thus providing a confirmation of this degradation.

The position of E_e, so far taken to be peak "A" of figure 5.4 was altered to correspond to the peak marked "B", in order to test the

Figure 5.10a:
the modulus of the fourier transform of $\chi(k)$ (the RDF) from energy-loss data from graphitic boron nitride.

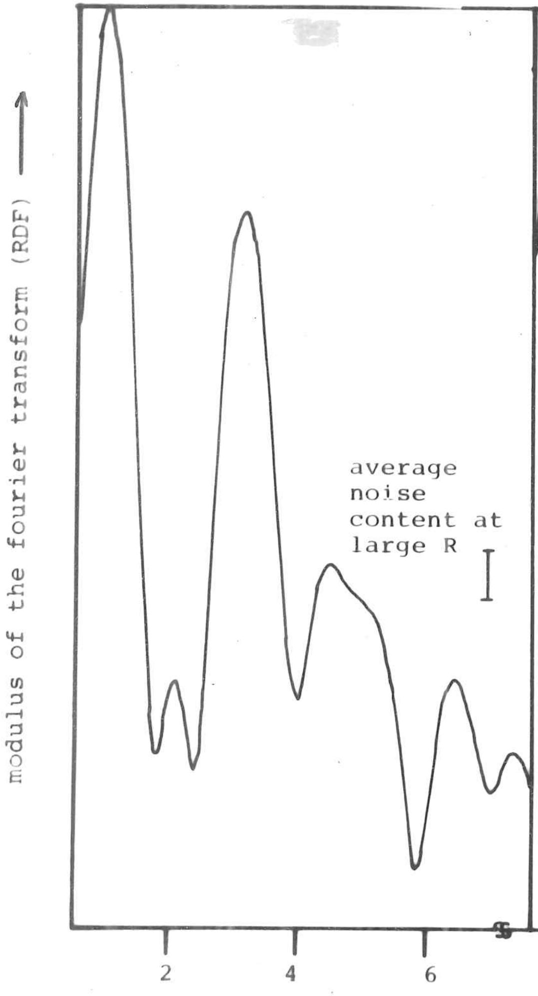

Figure 5.10b:
as figure 5.10a except the left window is 25 eV above the edge.

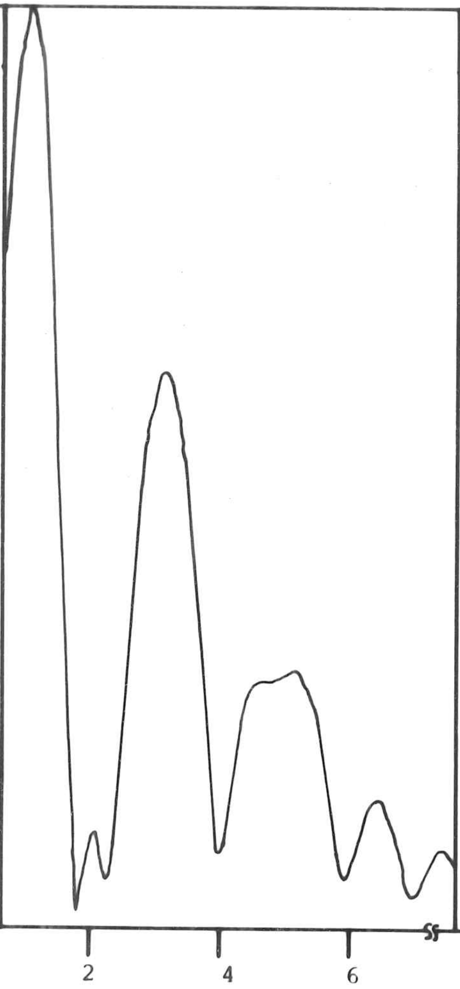

Figure 5.10c:
as figure 5.10a except the edge voltage (E_0) is increased by 12 eV.

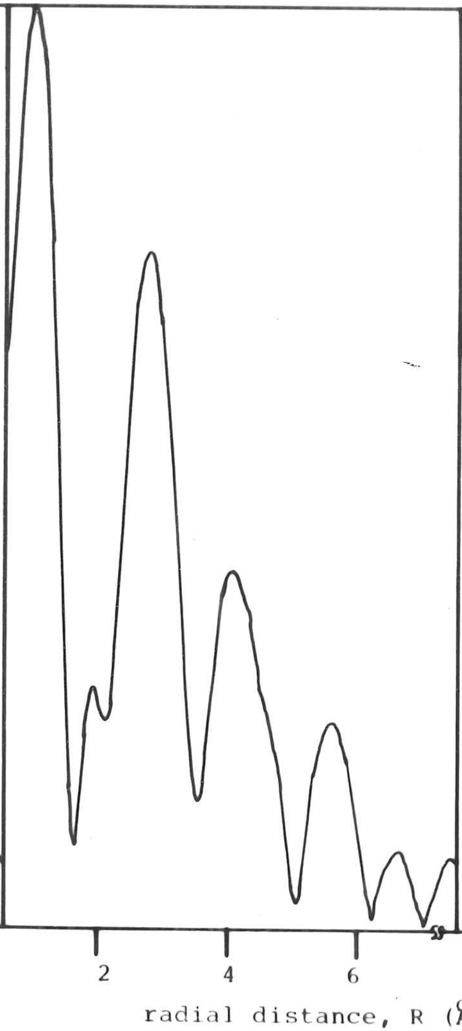

Figure 5.10d:
as figure 5.10c except the left window is 25 eV above the edge.

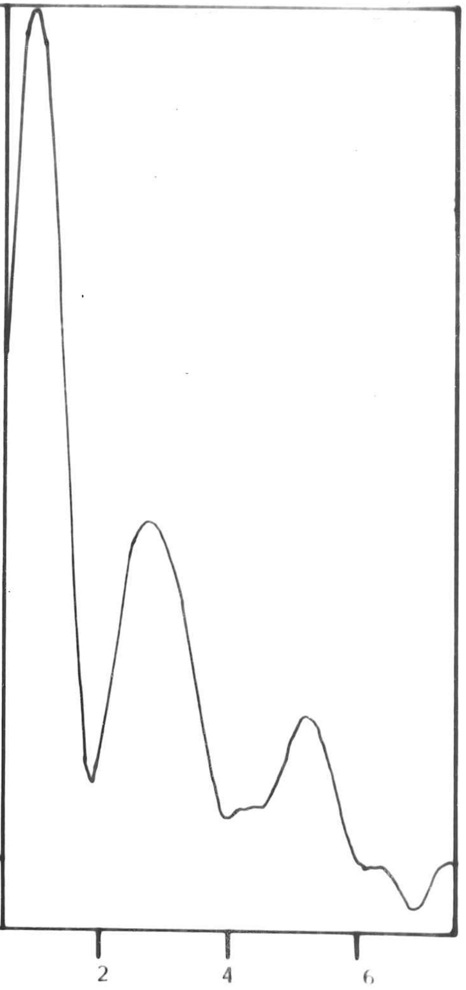

effect of an error in the chosen position of E_e. The resulting RDF is shown in fig 5.10c. The low-energy windown was chosen to be 0 eV above the edge in this case. It can be seen that the three major peaks are all shifted to the left by 0.15,0.3 and 0.4 Å respectively. The introduction of a 25 eV window can be seen to decrease the shifts in the position of the two first peaks to 0.1 and 0.2 Å respectively. It is rather difficult to compare positions above 4 Å because of the differences in shape of the peaks.
Visual comparison of figures 5.10a,b,c,d would suggest that the RDF of figure 5.10d is closer to the RDF's of fugures 5.10a,b than is figure 5.10c, although this is a somewhat subjective decision. Therefore, the addition of a low-energy window 25 eV above E_e reduces the effect of an error in chosen edge position (E_e).

In order to test the effect of the k^{-1} scaling present in the window used so far, the modulations were processed normally, except the effective k^{-1} scaling was not included. The resulting RDF is shown in figure 5.10e. It was to be expected that there would be an increase in the general level of noise, and this is confirmed by visual comparison of figures 5.10b and 5.10e. There is no observed shift in the positions of the major peaks, although the relative intensities of the three major peaks have altered slightly.

The effect of the gaussian window function was investigated by processing the data as the last test, but omitting the gaussian window function. The resulting RDF is shown in figure 5.10f. It can be seen that the ultimate noise level (the noise level at high radius) has increased, and is probably responsible for the modification in shape of the broad peak near 5 Å. The positions of the other two peaks are unaltered.

The effect of window edge smoothness was investigated by processing the data as in the previous test except using a window function with sharp edges. The resulting RDF is shown in figure 5.10g. It can be seen that the noise has increased. The noise contains a periodic component thus showing that termination errors are an important contributory source of noise in this RDF.

Figure 5.10e:
as figure 5.10b except $A(k)/k$ is approximated by $1/k^3$.

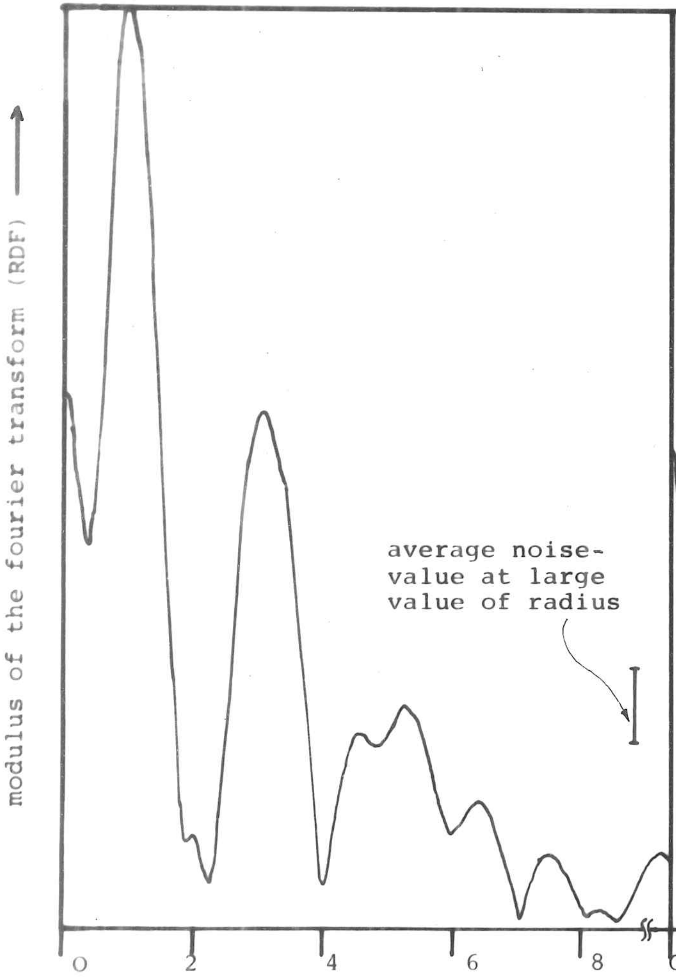

Figure 5.10f:
as figure 5.10e except the modulations ($\chi(k)$) are not multiplied by a gaussian.

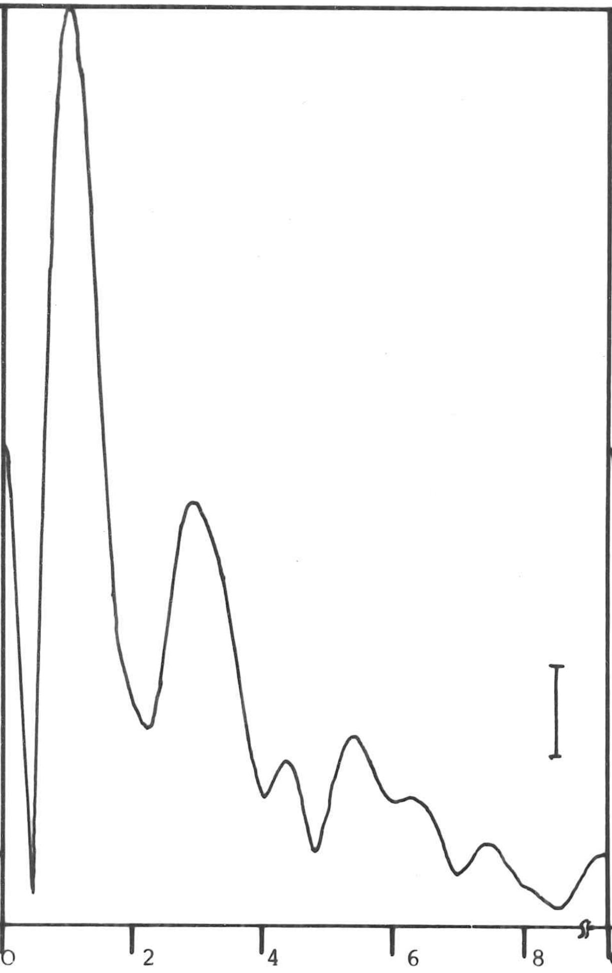

Figure 5.10g:
as figure 5.10f except the window function has sharp edges.

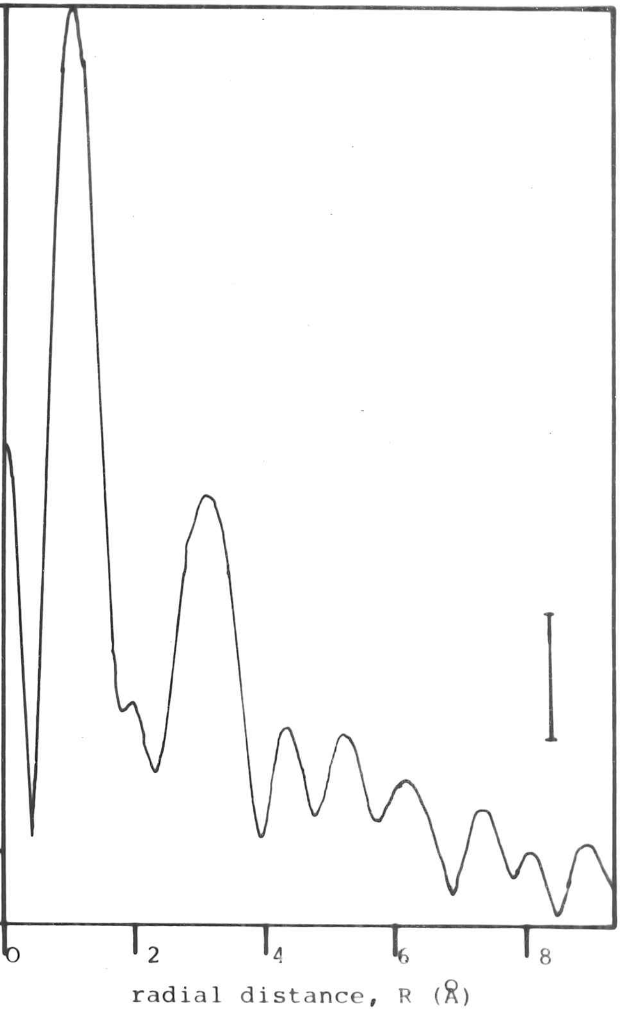

These tests prove that the numerical procedures adopted above minimise the effects of noise in the data and error in the chosen position of E_e on the resulting RDF.

5.3.3 Self-consistent boron nitride results

As a test of the self-consistency of the energy-loss results, two spectra were recorded from different regions of the specimen on different days. Experimental conditions were the same for both spectra: the geometry of the electron probe and spectrometer were the same, and the specimen orientation was similar (to within a few degrees) as demonstrated by the relative intensities of the first two peaks on the boron-K core-loss edge (Leapman & Silcox 1978). The spectra are presented in figure 5.11a as a linear plot and in figure 5.11b as a log-log plot. The two spectra took about 1 hour each to record.

The modulations $\chi(E)$ were extracted (using the RAMP program), and the results are presented in figure 5.12. It can be seen that the two curves are very similar, differing significantly only at about 220 eV. The modulations were transformed to $\chi(k)$ and windowed using the window of section 5.3.1.3 with a low-energy window at about 220 eV. The resulting RDF's are shown in figure 5.12b.
It is not surprising, given the similarity of the modulations (fig 5.12a), that the RDF's of both spectra are in good agreement.

The results can be summarised thus:
there are three major peaks which are in good agreement
1) the nearest-neighbor peak at 0.9 to 1.0 Å;
2) the peak at 3.2 to 3.3 Å;
3) the peak at 4.8 to 5.0 Å.

The width of the second peak is taken as a measure of the resolution of the RDF and gives a value of 1.1 Å (FWHM) on both curves.
The peak near 5 Å on the second curve is seen to consist of two peaks about 0.8 Å apart. No such splitting is observed in the other RDF. The intensities of the peaks above 6 Å are seen to be in poor agreement. The amplitude of the RDF at this point is not much

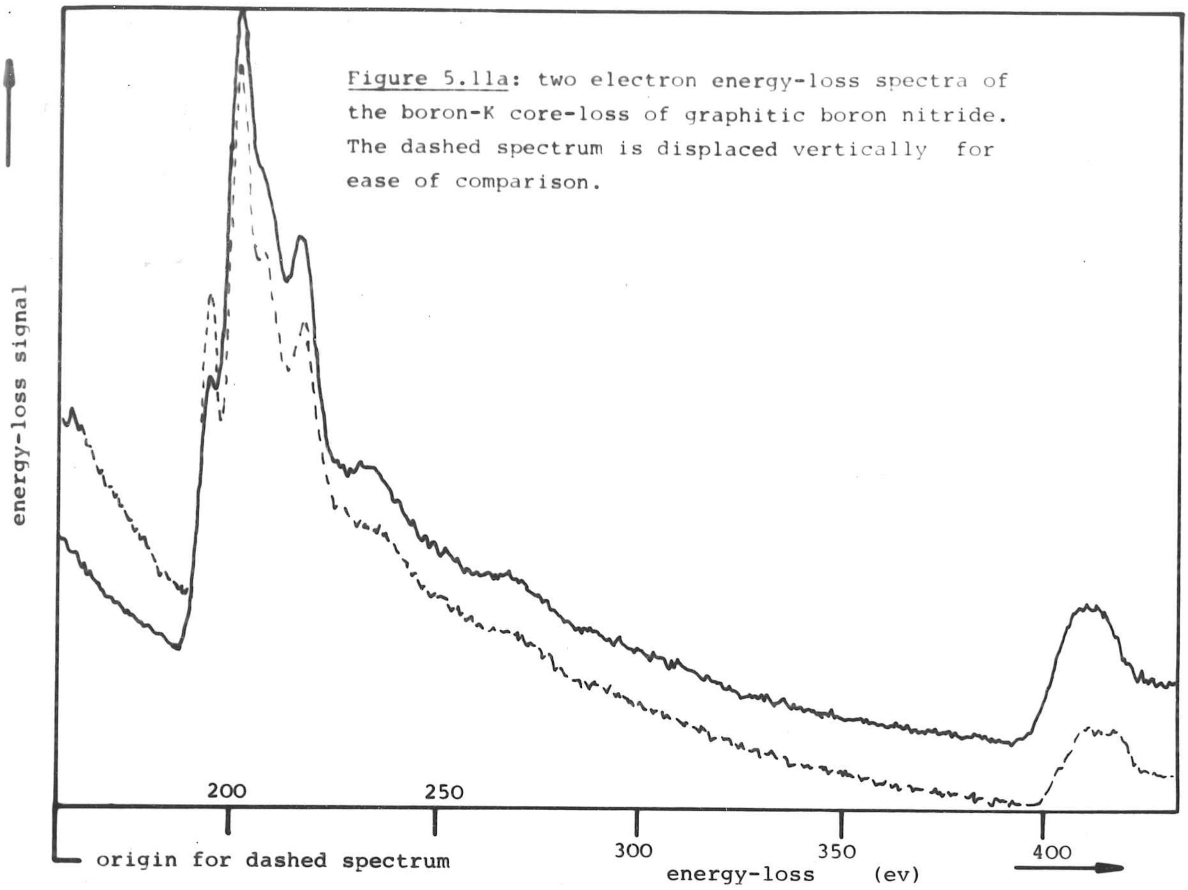

Figure 5.11a: two electron energy-loss spectra of the boron-K core-loss of graphitic boron nitride. The dashed spectrum is displaced vertically for ease of comparison.

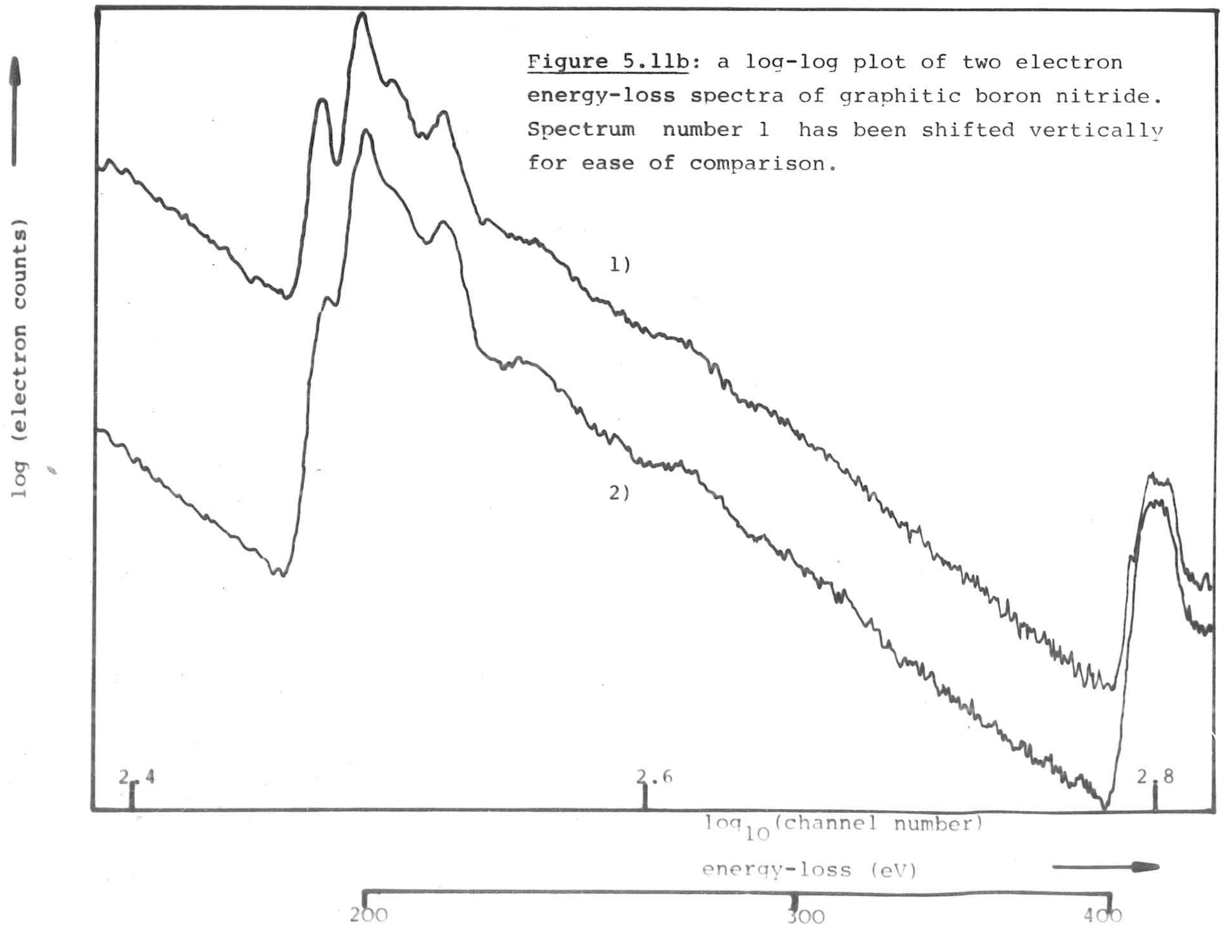

Figure 5.11b: a log-log plot of two electron energy-loss spectra of graphitic boron nitride. Spectrum number 1 has been shifted vertically for ease of comparison.

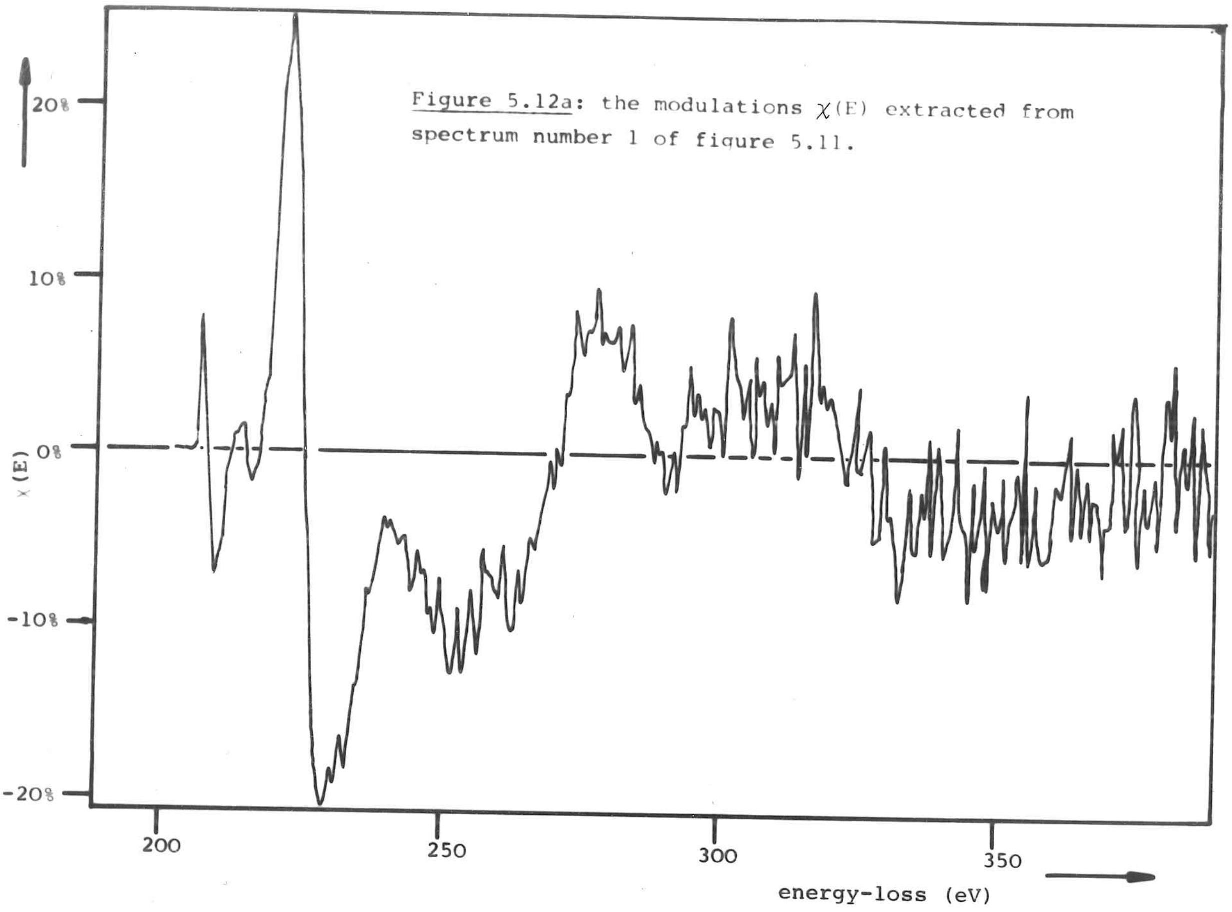

Figure 5.12a: the modulations $\chi(E)$ extracted from spectrum number 1 of figure 5.11.

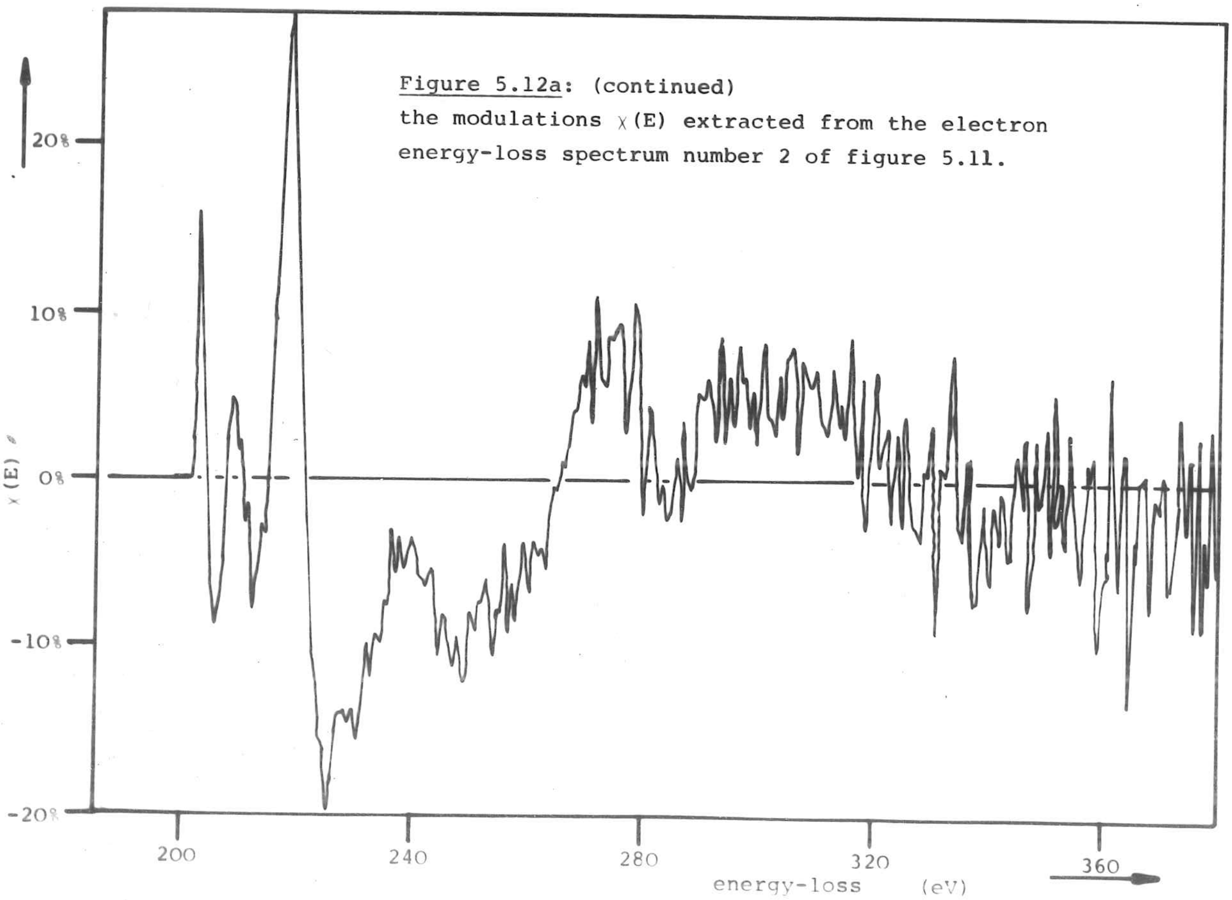

Figure 5.12a: (continued)
the modulations $\chi(E)$ extracted from the electron energy-loss spectrum number 2 of figure 5.11.

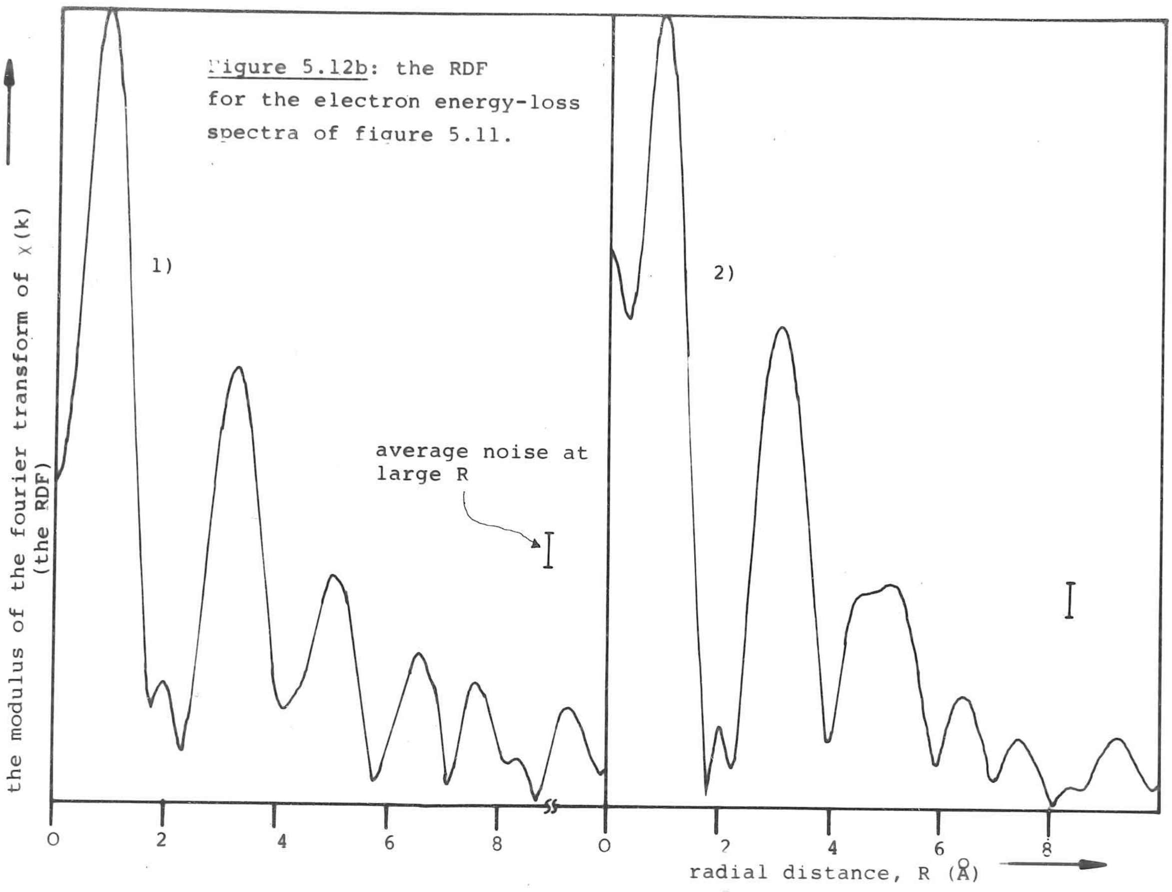

Figure 5.12b: the RDF for the electron energy-loss spectra of figure 5.11.

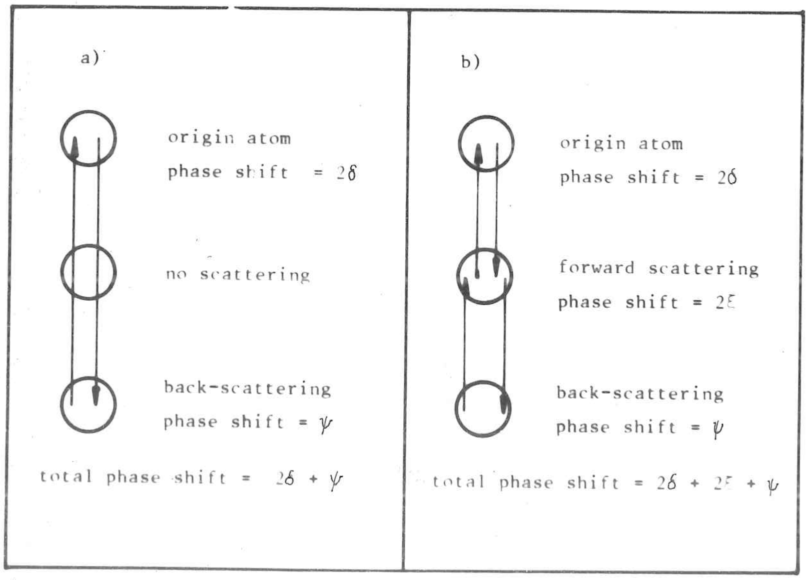

Figure 5.13: scattering diagrams for the fourth-nearest-neighbor path in copper: a) the direct path; b) the multiply-scattered path.

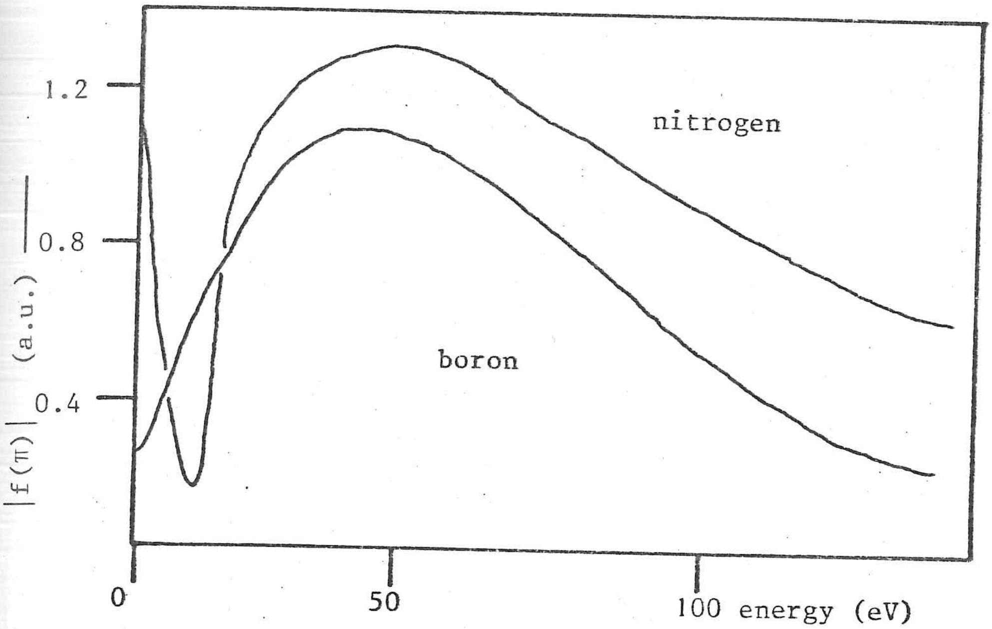

Figure 5.14a: the back-scattering amplitude |f(π)| for boron and nitrogen calculated by Gurman (1980).

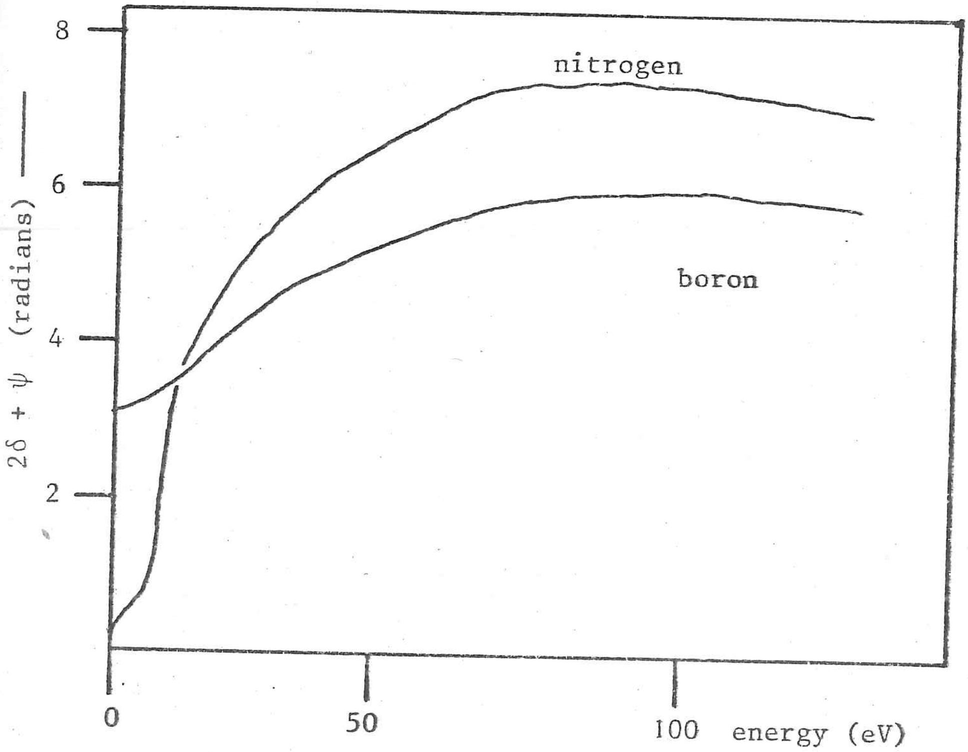

Figure 5.14b: the total phase-shift 2δ + ψ for boron and nitrogen calculated by Gurman (1980).

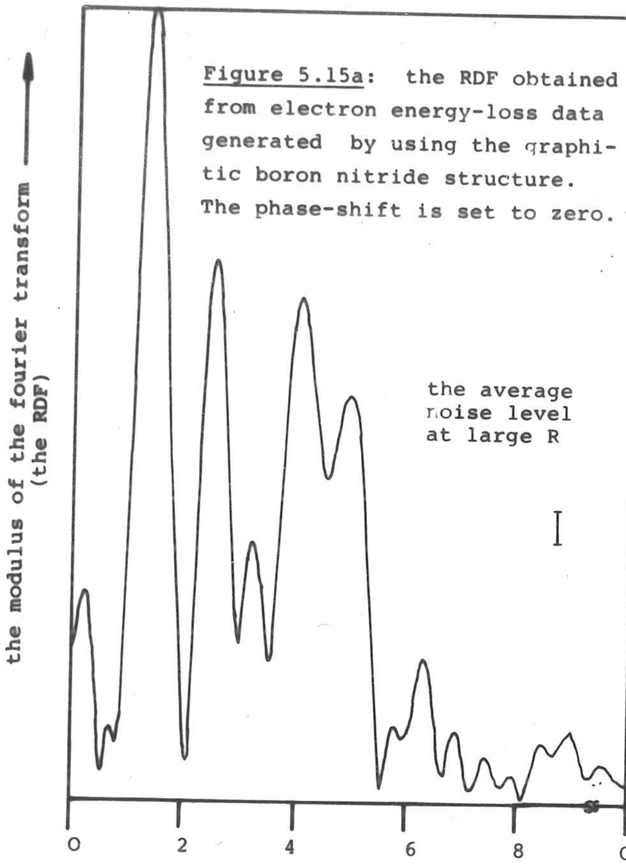

Figure 5.15a: the RDF obtained from electron energy-loss data generated by using the graphitic boron nitride structure. The phase-shift is set to zero.

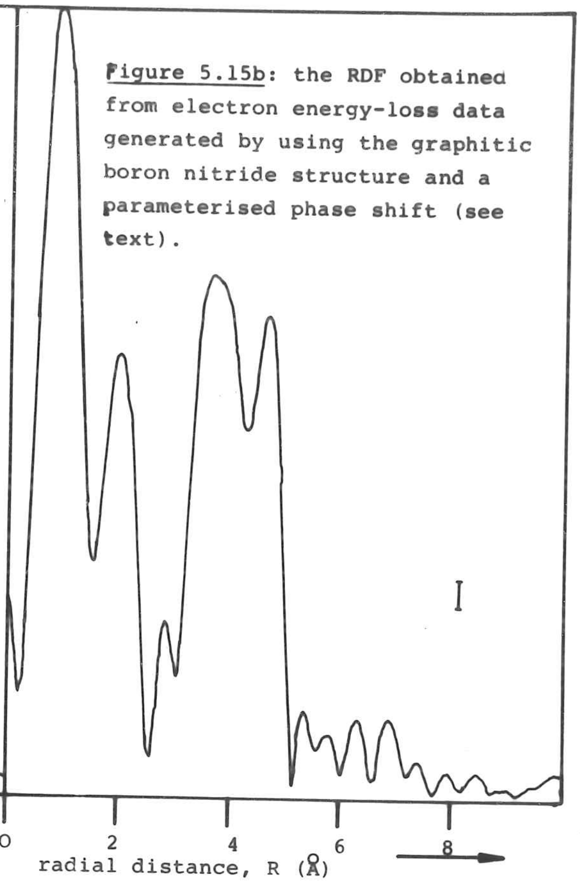

Figure 5.15b: the RDF obtained from electron energy-loss data generated by using the graphitic boron nitride structure and a parameterised phase shift (see text).

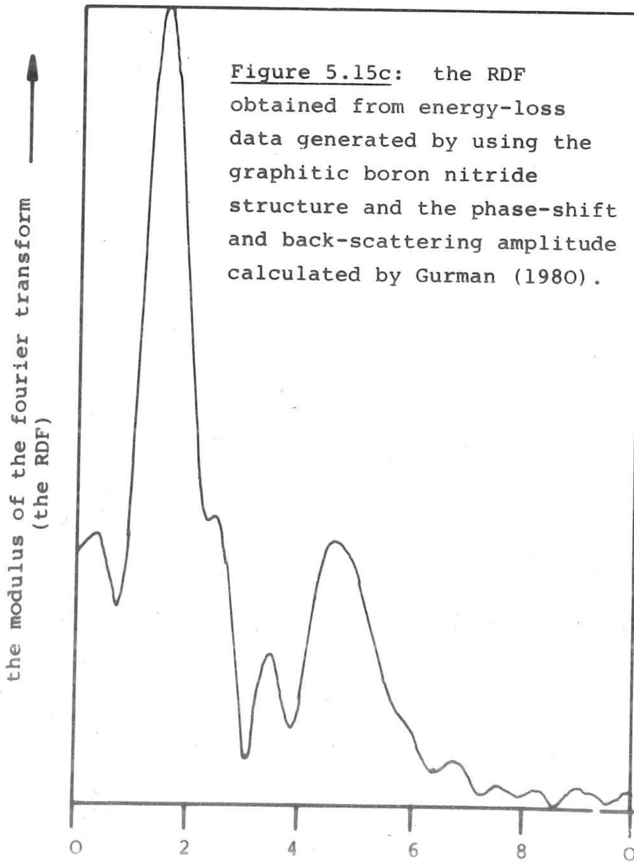

Figure 5.15c: the RDF obtained from energy-loss data generated by using the graphitic boron nitride structure and the phase-shift and back-scattering amplitude calculated by Gurman (1980).

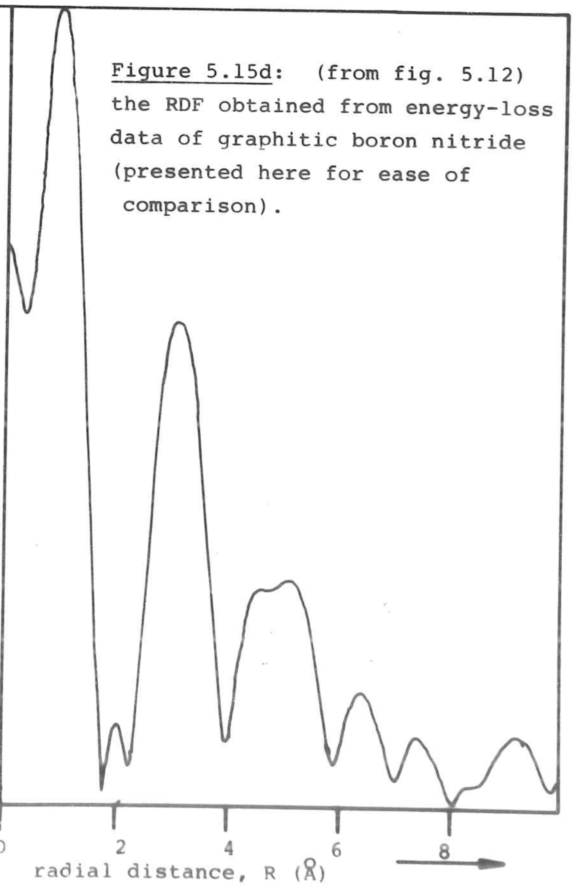

Figure 5.15d: (from fig. 5.12) the RDF obtained from energy-loss data of graphitic boron nitride (presented here for ease of comparison).

greater than the intensity of the noise at large radial distance, so these peaks will be susceptible to modification by random noise in the data.

Beyond 10 Å (not shown on fig. 5.12b), there is no visible correlation between the two RDF's, and all amplitude in the RDF beyond 10 Å is taken to be due to random noise in the data.

It can be seen from these results that confidence may be placed in the measured positions of the first two major peaks in the RDF. The measured position of the third major peak cannot be specified with a tolerance less than 0.4 Å.

5.3.4 Comparison of the energy-loss results with the predictions from the known crystal structure

In order to compare the RDF's obtained from energy-loss results with the known crystal structure, energy-loss spectra were synthesised (using the GEN program) for a given crystal structure and then analysed in the same way as the energy-loss data from boron nitride. Various phase-shift factors were used in the synthesis of the EXELFS as described below. The n$^{\underline{th}}$ nearest-neighbor separations, calculated from the crystal structure of figure 5.2 and used in the synthesis of the EXELFS are given in table 5.1.

Table 5.1: boron-boron and boron-nitrogen distances for graphitic boron nitride.

boron-boron	radius R_j (Å)	coordination N_j	N_j/R_j^2
	2.504	6	0.957
	3.631	6 *	0.455
	4.338	6	0.319
	4.411	6 *	0.308
	5.065	12 *	0.468
	5.08	6	0.233
boron-nitrogen			
	1.446	3	1.435
	2.892	3	0.359
	3.331	2 *	0.180
	3.815	6	0.412
	4.167	12 *	0.691
	5.213	6	0.221
	5.469	12 *	0.401
	5.784	3	0.090

* inter-planar coordination

The first synthesised spectra contained no phase-shift terms. A(k) was approximated by Rutherford scattering ($A(k) \propto k^{-2}$). The resulting RDF can be seen in figure 5.15a. Comparison of the energy-loss RDF (figure 5.12b) and the synthesised RDF shows:

1) the first major peak in the synthesised RDF is present in the RDF of the experimental spectra, but shifted towards lower radius by about 0.5 Å. The magnitude of this shift is in agreement with experimental results from carbon EXELFS (Batson 1979).

2) The second major peak in the synthesised RDF at 2.5 Å should be observed on the experimental RDF at about 2 Å. It can be seen from figure 5.12b that there is no such peak (above the level of noise and termination errors) present in the energy-loss results.

3) The second major peak in the experimental RDF at 3.3 Å should correspond to a peak at 3.8 Å in the synthesised RDF. The rising edge of a strong peak is observed at this radius in the synthesised RDF.

To summarise: by comparing the synthesised and experimental RDF's, the first peak is in the expected position, but none of the other peaks agree. Particularly worrying is the complete absence of the second major peak of the synthesised RDF in the experimental RDF.

An attempt to resolve these differences was made by including a non-linear parameterised phase-shift $\phi(k)$ in the GEN program used in the synthesis of test spectra. The phase-shift is given by:

$$\phi(k) = a + bk + ck^2 + d/k^3 \qquad - \quad 5.4$$

where:
$a = -2$ (radians),
$b = -1.25$ (radians Å),
$c = 0.036$ (radians Å^2),
$d = 30.$ (radians Å^{-3}).

The form of the phase-shift was obtained from Lee _et al_ (1974) and values for the parameters were obtained by extrapolation from their values (which are tabulated for elements heavier than carbon). The RDF thus obtained is shown in figure 5.15b. It can be seen that the major effect of the phase-shift is a linear shift in the positions of the peaks measured from figures 5.15b and 5.15a, due to the prominence of the linear term in $\phi(k)$. There is some change in the shapes of the peaks, but the underlying structure noted in the previous RDF is still present.

Comparison of the experimental RDF and figure 5.15b shows that the nearest-neighbor peak is now in the correct position. As before, the peak in the synthesised RDF near 2 Å (corresponding to the second-nearest neighbor separation) is conspicuously absent from the experimental RDF. The shape of the peaks near 4 Å, although slightly different from the previously synthesised RDF is still in poor agreement with the observed RDF.

To summarise: the inclusion of a parameterised phase-shift has not improved the correspondence between the experimental RDF and synthesised RDF, apart from the linear shift.

The discrepancy between these two spectra cannot be explained by the presence of noise or the effects of the numerical techniques used. The crystal structure has been verified by electron diffraction. It is concluded, therefore, that there is some effect present in the experimental data that is not adequately described by the expression for $\chi(k)$ (equation 5.1) together with the values for the phase-shift and back-scattering amplitude so far employed.

There are two effects to explain:

1) the absence of any peak in the experimental RDF near 2 Å;
2) the shift of the peak(s) near 4 Å in the synthesised RDF to 3.3 Å in the experimental RDF.

The nearest-neighbor and second nearest-neighbor vectors both correspond to directions in the hexagonal planes, and it is not possible that geometric effects (such as specimen orientation) could be responsible for the first effect. The absence of a peak has been observed in the results from the extended X-ray absorption fine structure (EXAFS) of copper (Lee & Pendry 1975, Ashley & Doniach 1975), where the 4th nearest-neighbor peak is completely absent. This may be explained by multiple elastic scattering of the ejected secondary electron producing back-scattered amplitude at the origin atom from three processes: (see figure 5.13)

1) secondary electrons that are backscattered by the fourth-nearest neighbor atom only;
2) secondary electrons that are forward-scattered by the nearest

neighbor, back-scattered by the 4th. nearest neighbor (of the origin atom) and then forward scattered by the nearest-neighbor atom;

3) secondary electrons that are back-scattered by the 4th. nearest neighbor atom and forward-scattered once by the nearest neighbor atom.

Processes 1) and 2) are illustrated in figure 5.13.

These three processes all have the same value of the distance travelled by the secondary electron, but have differing values for the secondary electron phase-shift. The phase-shift consists of three terms:

1) the phase shift experienced by the secondary electron as it leaves and enters the origin atom, δ;

2) the phase-shift experienced if the secondary electron is forward scattered by the nearest neighbor, ξ ;

3) the phase-shift experienced by the secondary electron upon being back-scattered by the 4th. nearest neighbor atom, ψ.

The origin atom phase-shift is not the same as the backscattering phase-shift because the origin atom can relax as the secondary electron is emitted, thus changing the observed atomic potential and thus the phase-shift.

These processes do not exhaust all the possibilities of scattering of the secondary electron over the same total path length, but they are sufficient to show that there may be two or more scattering paths of the same path length and differing total phase shift. These back-scattered amplitudes interfere at the origin atom and may give rise to enhanced amplitude at the origin atom (constructive interference), or the may interfere destructively, thus depressing the amplitude of the back-scattered secondary electron corresponding to a path-length of twice the origin-atom to 4th. nearest neighbor separation.

The effect that is observed is the complete removal of the 4th. nearest neighbor peak in copper.

It is not possible to explain the absence of the 2nd. nearest neighbor peak in boron nitride in the same way. Such an explanation would require the presence of two scattering paths of nearly equal length and this would therefore have to involve the nearest neighbor atom. The multiple-scattering path length for the 2nd nearest via the nearest neighbor corresponds to a separation of 2.89 Å, whereas the single-scattering path-length corresponds to the second nearest neighbor to origin-atom separation of 2.5 Å. The multiple scattering path would involve "forward" scattering through an angle of 60^{o}. The form of the scattering amplitude as a function of deviation angle θ is strongly peaked at $\theta = 0$, and weakly peaked at $\theta = 180^{o}$, corresponding to back-scattering. The value for the scattering amplitude at $\theta = 60^{o}$ is likely to be very small (Buxton 1980), so the contribution from the multiple-scattering path given above is likely to be very small.

The second-nearest neighbor path (boron-boron) cannot be impeded by the nearest neighbor (the nitrogen atom), which is too small to interfere with the secondary electron at even modest kinetic energies (25 eV) (Buxton 1980, Brown 1980).

5.3.5 The synthesised RDF using calculated phase-shifts and scattering amplitudes

There are two possible explanations of the discrepancy between the experimental RDF and the RDF synthesised, so far, from the crystal structure which have yet to be discussed:

1) A(k) is not adequately represented by the Rutherford scattering approximation and the parameterisation of the phase-shift is not sufficiently accurate.

2) The assumptions underlying the simple EXELFS formulation (section 2.2.6) do not hold true.

In order to test the first of these, the author contacted Dr, S.J. Gurman (University of Leicester Physics Department, England) who had written computer programs to calculate an approximation of the back-scattering amplitude and phase-shift. He very kindly provided the data shown in figure 5.14 (Gurman 1980), viz:

1) the phase-shift (δ) due to a relaxed, singly-ionised origin atom for both boron and nitrogen;

2) the back-scattering amplitude (A(k)) for atomic boron and nitrogen;

3) the back-scattering phase-shift (ψ) for atomic boron and nitrogen.

The total phase shift for boron-boron EXELFS is then given by:

$$\phi_{BB} = 2\delta_B + \psi_B \qquad - \quad 5.5$$

and the total phase shift for boron-nitrogen EXELFS is given by:

$$\phi_{BN} = 2\delta_B + \psi_N. \qquad - \quad 5.6$$

The following points should be noted:

1) The form of A(k) approaches k^{-2} at high k, but at energies less than 100 eV, deviates from Rutherford scattering. A(k) for both boron and nitrogen shows a maximum near 45 eV. A(k) for nitrogen shows a pronounced dip at 10 eV.

2) The total phase-shifts ϕ_{BB} and ϕ_{BN} are increasing over the range of k used. The phase shift ϕ_{BN} shows a rapid change of π at the position of the dip in A(k) for nitrogen. This is resonance scattering at about 10 eV.

3) The effect of a low-energy window at 25 eV secondary electron energy should remove the effect of any structure in A(k) and ϕ(k) below the value of wave-vector corresponding to 25 eV secondary electron energy. Thus, from 25 eV upwards, the scattering amplitude and phase shift behave similarly for both boron and nitrogen.

The curves for A(k) and ϕ(k) were tabulated and entered into the Gen program. Values of A(k) and ϕ(k) were determined from the tabulated values by linear interpolation. Thus the results of these calculations could be used to synthesis energy-loss spectra and thence obtain a synthesised RDF to compare with the experimental RDF.

The synthesised energy-loss spectrum, generated using the calculated values of A(k) and ϕ(k) was treated in exactly the same way as the energy-loss data. There should, therefore, be direct comparison between the experimental RDF and the synthesised RDF. These two RDF's are presented together in figures 5.15c and d.

From a comparision of the newly-synthesised RDF and the RDF corresponding to a synthesised spectrum containing no phase-shift terms (figures 5.15c and 5.15a), it can be seen that:

1) the resolution of the new RDF has been degraded from 0.8 to 1.1 Å;

2) the new RDF peaks near 1.5, 2.5, 3.5 and 4.8 Å all reflect structure seen in the old synthesised RDF, but:
3) the new RDF second nearest neighbor peak near 2.5 Å is of decreased amplitude and has merged with the nearest-neighbor peak, although it is still clearly discernible, and;
4) the new RDF peak near 4.8 Å results from the merging of two peaks near 4 and 5 Å in the old synthesised RDF.

The structure of the synthesised spectrum with no phase-shift can be seen in the newly-synthesised spectrum, although details of peak amplitudes have changed.

A comparison of the new RDF and the experimental RDF shows that:
1) the nearest neighbor peak in the new RDF is at too high a value of the radial distance, R, by about 0.5 Å;
2) there is no observed shoulder on the nearest neighbor peak of the experimental RDF, even though the two RDF's have very similar resolutions;
3) the peak in the experimental RDF near 3 Å does not correspond to any major structure in the synthesised RDF;
4) the peak in the experimental RDF near 5 Å corresponds reasonably well with the position of the peak in the new RDF. This agreement becomes rather poor if the new RDF is shifted horizontally to bring the nearest-neighbor peaks into alignment.

Thus the two points noted from the comparison of section 5.3.4 still hold true:
1) the second-nearest neighbor peak is absent from the experimental spectrum, although observed clearly in the synthesised spectrum;
2) there is no explanation for the peak in the experimental spectrum near 3 Å.

The observed error in the position of the nearest neighbor peak in the synthesised RDF casts doubt on the accuracy of the model calculations for A(k) and $\phi(k)$. The model calculations were performed using an approximate atomic potential (a Tietz potential - Gurman 1980). More seriously, as boron nitride is a III-V compound, charge is transferred from nitrogen to boron, so the phase-shift, δ, should be calculated for a neutral boron atom, and the back-scattering phase-shift, ψ, should be calculated for N^+ and B^- ions. The model calculations were performed assuming no charge transfer (i.e.: δ calculated for B^+ and ψ calculated for N and B atoms).

A second explanation for the poor agreement between the experimental RDF and the synthesised RDF may lie in the assumptions made in deriving the simple EXLEFS formula (equation 5.1). The most important assumption made is that the outgoing secondary electron may be represented as a plane wave at the back-scattering centre. The validity of this assumption is subject to double at low secondary electron energies (less than 100 eV) (Lee & Pendry 1975, Buxton 1980). More-exact calculations of $\chi(k)$ have been performed which do not make this assumption (Gurman 1979).

The EXELFS of boron nitride is a sensitive test of the simple EXELFS theory, and it has been shown that the use of a simple parameterised phase-shift and Rutherford scattering for A(k) is inadequate if it is desired to synthesise the observed RDF from the known crystal structure. Model calculations of $\chi(k)$ should be made not making a plane-wave approximation and using calculated values of $\phi(k)$ and A(k).

5.4 NITROGEN-K EXELFS

It is very difficult to obtain nitrogen-K EXELFS of good statistical quality because the count-rate at the nitrogen-K core-loss is approx. one eighth of the count-rate at the boron-K core-loss, and it is difficult to obtain spectra integrated over a period in excess of one hour because of specimen drift, etching, microscope alignment and operator fatigue.

As one of the powerful features of EXELFS is the ability to sample neighbors around different chemical species, it is worthwhile examining the nitrogen-K EXELFS in order to obtain a further test of the technique. A log-log plot of the energy-loss data from a thin boron nitride flake is shown in figure 5.16. The spectrum was

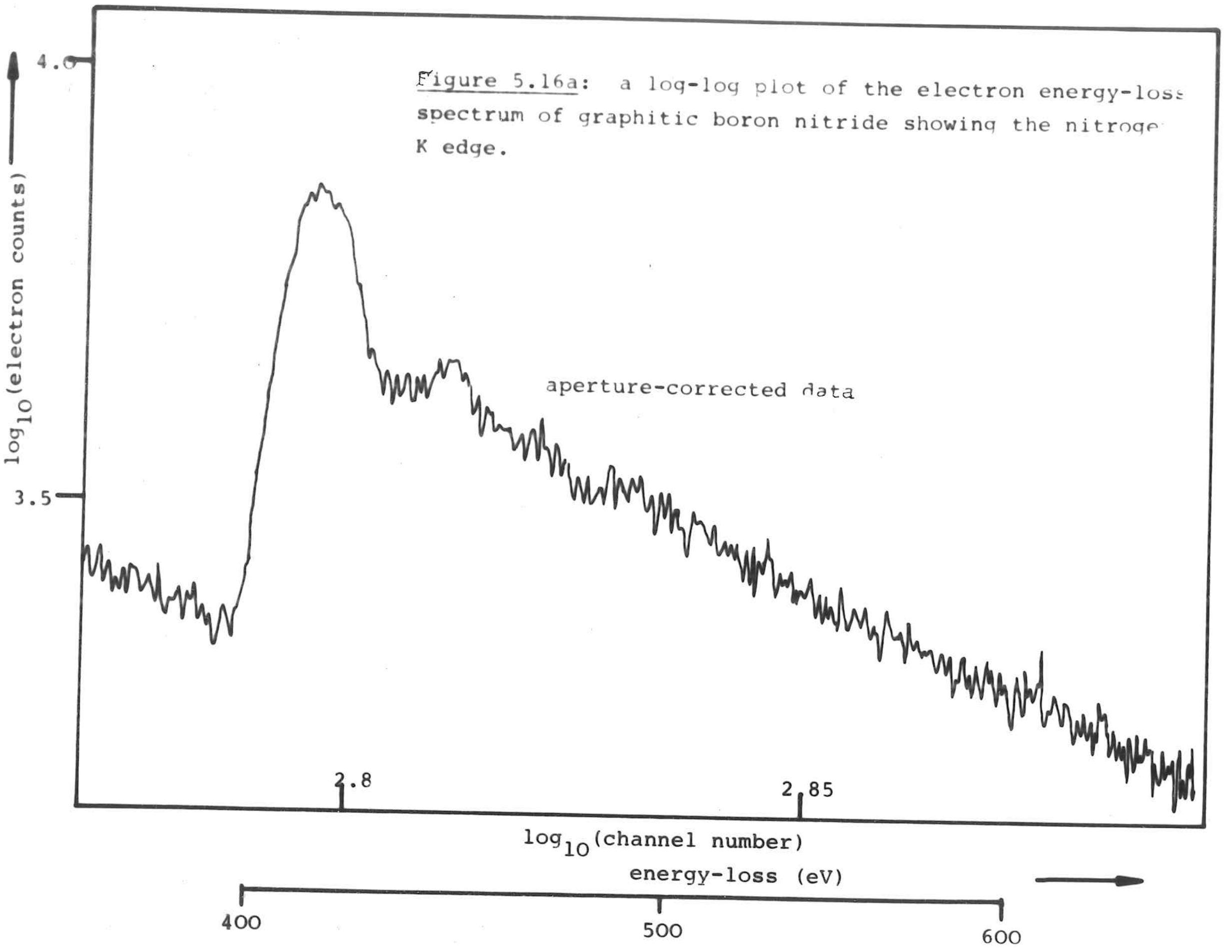
Figure 5.16a: a log-log plot of the electron energy-loss spectrum of graphitic boron nitride showing the nitroge K edge.

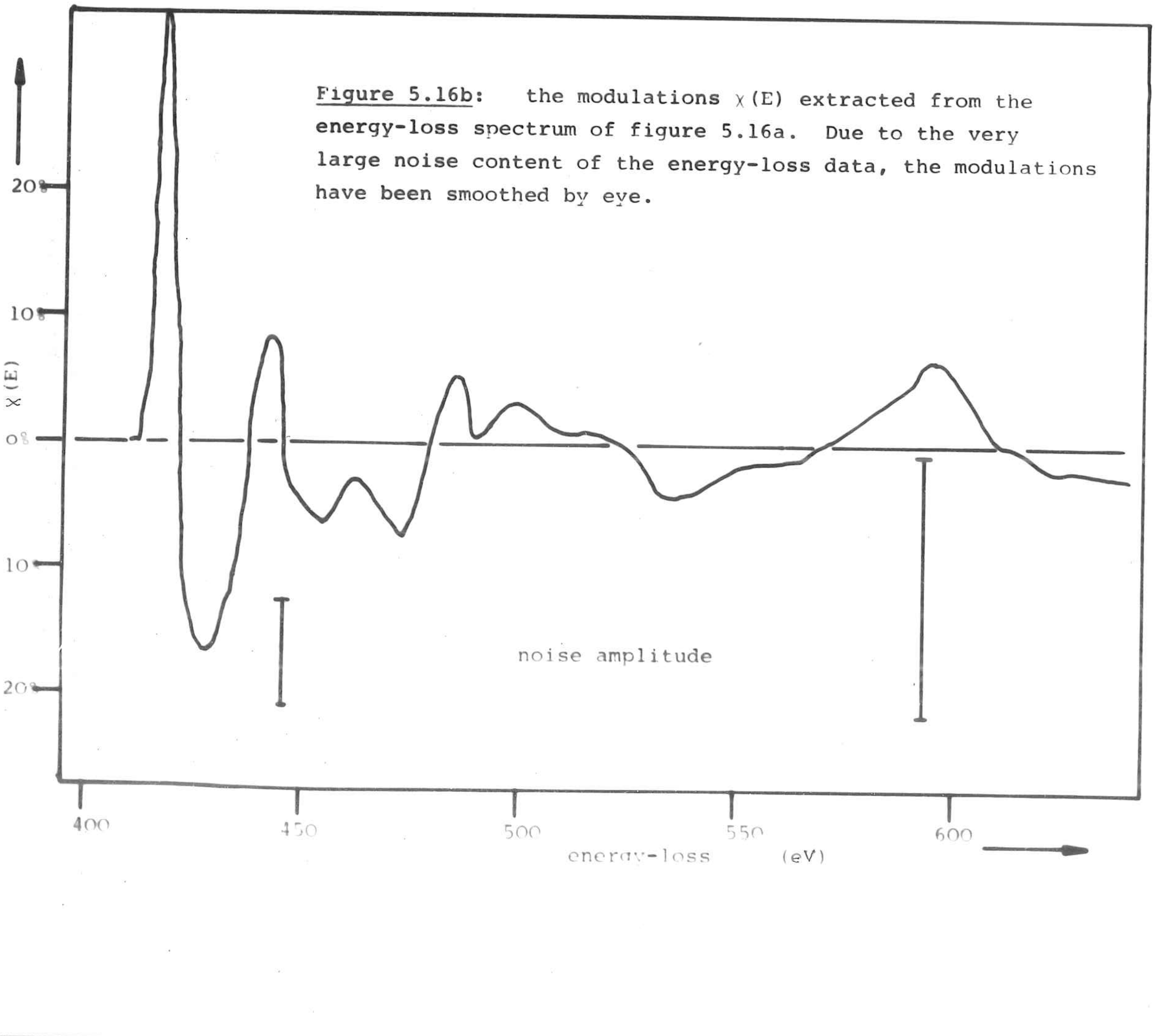
Figure 5.16b: the modulations $\chi(E)$ extracted from the energy-loss spectrum of figure 5.16a. Due to the very large noise content of the energy-loss data, the modulations have been smoothed by eye.

processed as before, except that a low-energy window 40 eV above the nitrogen-K edge was used (this corresponds to a zero in the modulations $\chi(E)$ and ensures minimum noise content due to the low-energy window edge). The modulations $\chi(E)$, before being windowed in any way, are shown in fig 5.16b. Because of the very large noise content in $\chi(E)$, the curve drawn in fig 5.16b represents the modulations after having been smoothed by eye; the bars represent the average (RMS) noise content on the original (unsmoothed) modulations.

The unsmoothed modulations were converted to $\chi(k)$, windowed and then converted to the RDF (using the TRANS program). The RDF is shown in figure 5.17. The following points should be noted:

1) the first four major peaks correspond remarkable well with the RDF synthesised using no phase shift.

2) The very high noise content (at $R > 10$ Å), which is comparable in amplitude to all the major peaks except the nearest-neighbor peak, implies that the structure observed between 2 and 6 Å has little significance. The nearest-neighbor peak at 1.5 Å is significantly above the noise, but its position may be effected by the presence of noise. The presence of the peaks between 2 and 6 Å above the level of the noise shows that there is a contribution to $\chi(E)$ from further than nearest-neighbor atoms, but little credence can be placed in the observed positions of these peaks.

The only peak of any real significance is the nearest-neighbor peak at 1.5 Å. The physical nearest neighbor separation is 1.45 Å. It is concluded, therefore that either:

1) the noise content has shifted the apparent position of the peak by about 0.5 Å compared with the RDF from the boron-K core-loss, or

2) the total phase-shift $\phi_{NB}(k)$ differs from the boron-nitrogen phase-shift $\phi_{BN}(k)$.

It is unlikely that the peak could be shifted by as much as 0.5 Å. The addition of a noise peak, of average noise amplitude, close enough to the true peak position that it does not show up as a shoulder, is unlikely to shift the observed position of the first major peak by more than 0.2 Å (it is not possible to be certain

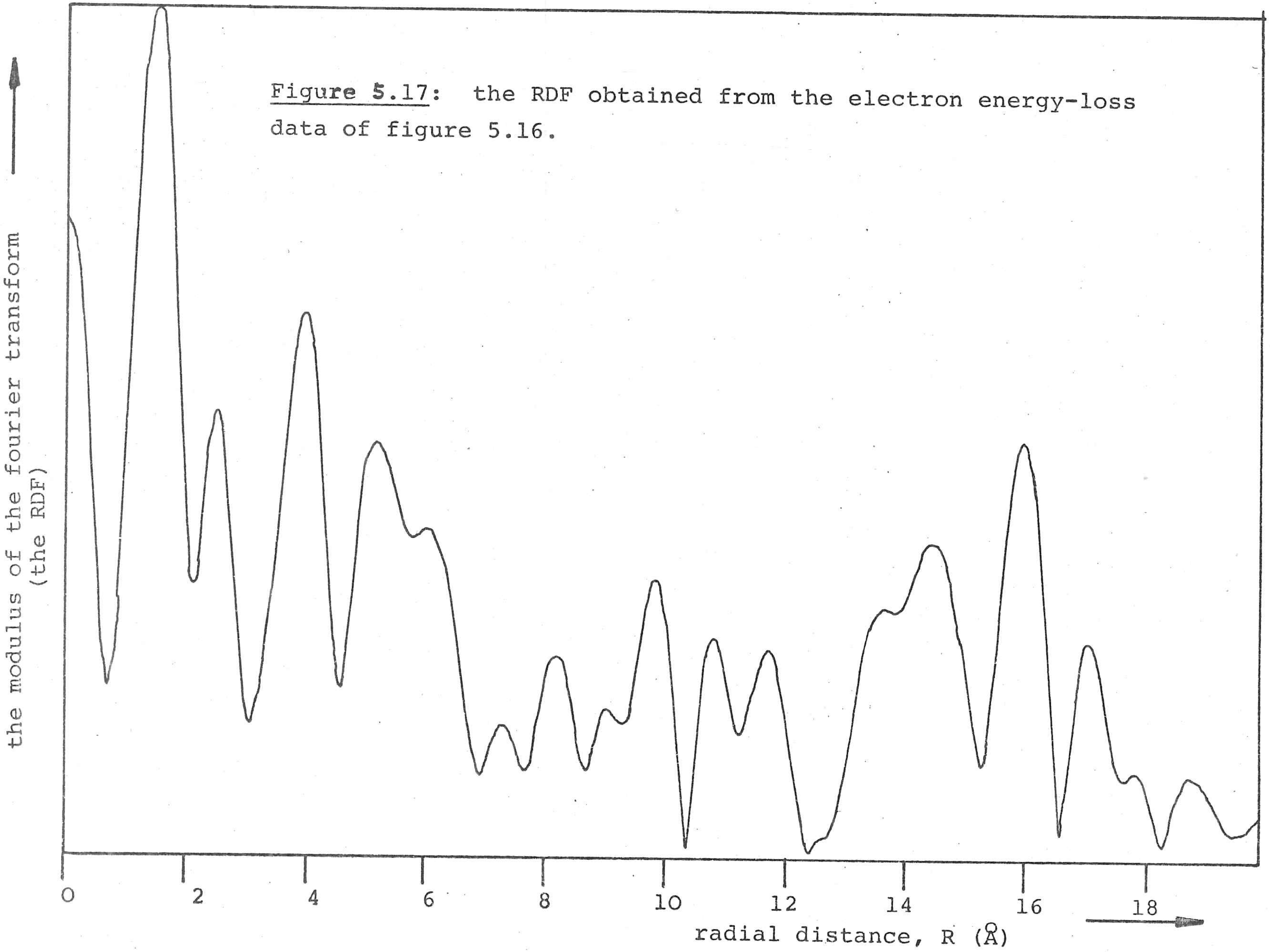

Figure 5.17: the RDF obtained from the electron energy-loss data of figure 5.16.

because of the random nature of the noise content).
It may concluded, therefore, that the total nitrogen-boron phase-shift $\phi_{NB}(k)$ introduces a rather smaller shift in the observed position of the nearest neighbor peak in the RDF than for a boron origin atom and a nitrogen backscatterer. This means that ϕ_{NB} is a comparatively weak function of k.

The two phase-shifts ϕ_{NB} and ϕ_{BN} are not expected to be the same because the conditions experienced by the secondary electron are not the same in both cases. In the first case, the electron is emitted by a N^{++} ion and back-scattered from a B^{-} ion. In the second case, the origin atom is a B atom, and the back-scattering ion is N^{+}.

5.5 BANDSTRUCTURE AND SPECIMEN ORIENTATION EFFECTS

The effect of tilting the specimen is to alter the relative direction of the secondary electron's motion with respect to the crystallographic axes of the specimen. This direction is also given by the incident electron probe geometry and the collector aperture geometry. When the energy lost by the incident electron is just above the binding energy of the electron, the incident electron is forward scattered through small angles $0(\theta_E)$ where:

$$\theta_E = \frac{\Delta E}{2E_o} \quad \text{(see figure 5.18).}$$

where: ΔE is the energy lost by the incident electron and
E_o is the primary energy of the incident electron.

The scattering angle is not fixed at the "hard sphere" scattering angle:

$$\theta_c = \sqrt{\Delta E/E_o}$$

which is found in classical kinematics, because of the orbital momentum of the core electron. This cannot be known precisely, so at a given energy-loss, there is a distribution of scattered intensity with angle, peaked near $\theta = 0$.

As the energy-loss increases, the relative importance of the orbital momentum of the core electron decreases and the scattered intensity peaks at the hard-sphere angle θ_c, the effect of orbital momentum being to broaden the scattered intensity into a peak centered at the

Figure 5.18:

For $\Delta E \simeq E_{binding}$

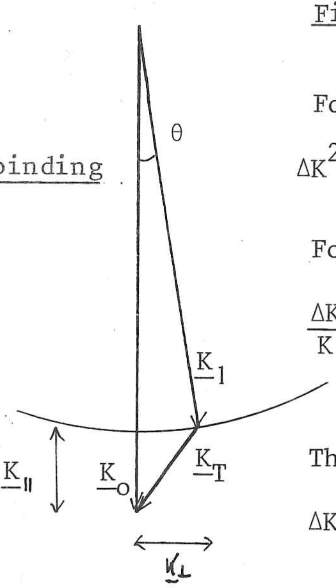

For small angles:

$$\Delta K^2_{min} = K_o^2 - K_1^2 \propto \Delta E$$ (conservation of energy)

For small changes:

$$\frac{\Delta K}{K} = \frac{\Delta E}{E}\cdot\frac{1}{2}$$

Therefore:

$$\Delta K_\parallel \simeq \frac{\Delta E}{2E_o}\cdot K = \theta_E\cdot K$$

For $\Delta E >> E_{binding}$

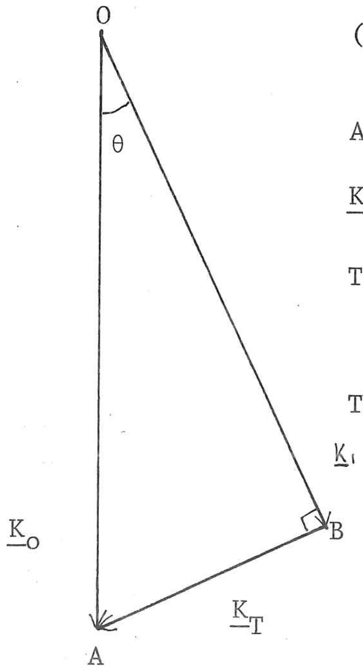

$$K_o^2 - K_1^2 = K_T^2 \propto \Delta E$$

(conservation of energy)

And:

$$\underline{K}_o - \underline{K}_1 = \underline{K}_T$$

Therefore OAB is right-angled

Therefore, for small θ,

$$\theta \simeq \frac{K_T}{K_o} = \sqrt{E/E_o}$$

hard-sphere scattering angle, but of finite width. These points are discussed in detail by Inokuti (1971).

Bandstructure effect are observed at secondary electron kinetic energies less than 30 eV; and thus the primary electron is forward scattered. A deviation in the primary electron angle of θ_E corresponds to a direction of momentum transfer in the specimen lying at 45 ^{o} to the optic axis of the microscope.
By adjusting the collector aperture to admit electrons which have been scatteredthrough an angle close to θ_E, an energy-loss spectrum can be formed corresponding to a known direction of momentum transfer, for energy-losses near the edge. It would then be possible to tilt the specimen and observe the band-structure effects as a function of momentum transfer direction within the specimen.

Such a series of experiments has been performed by Leapman & Silcox (1978) on boron nitride. Their results demonstrate that the peaks marked "A" and "B" in figure 5.4 may be interpreted as the elevation of the core electron to the π^* and σ^* anti-bonding orbitals. These arise from the graphitic structure of boron nitride, the π^* anti-bonding orbital being an appropriate sum of empty atomic $2p_z$ orbitals, parallel to the c-axis; and the σ^* state being a hybridization of $2sp_xp_y$ atomic orbitals, directed along the nearest-neighbor bond in the layer plane. An intuitive understanding expects the π^* orbital to be of lower energy than the σ^* orbital, there being a lower electronic density detween the layers than in the layer planes.

In order to observe the effect of specimen orientation on the energy-loss spectrum of boron nitride, the following experiment was performed:

1) an energy-loss spectrum was obtained using
   electron-probe semi-angle of convergence = 8.5 mR,
   spectrometer acceptance semi-angle = 1 mR,
   specimen orientation: c-axis parallel to the optic axis.
   The resulting energy-loss spectrum is shown in figure 5.19a.
2) an energy-loss spectrum was obtained using
   electron-probe semi-angle of convergence = 2 mR,

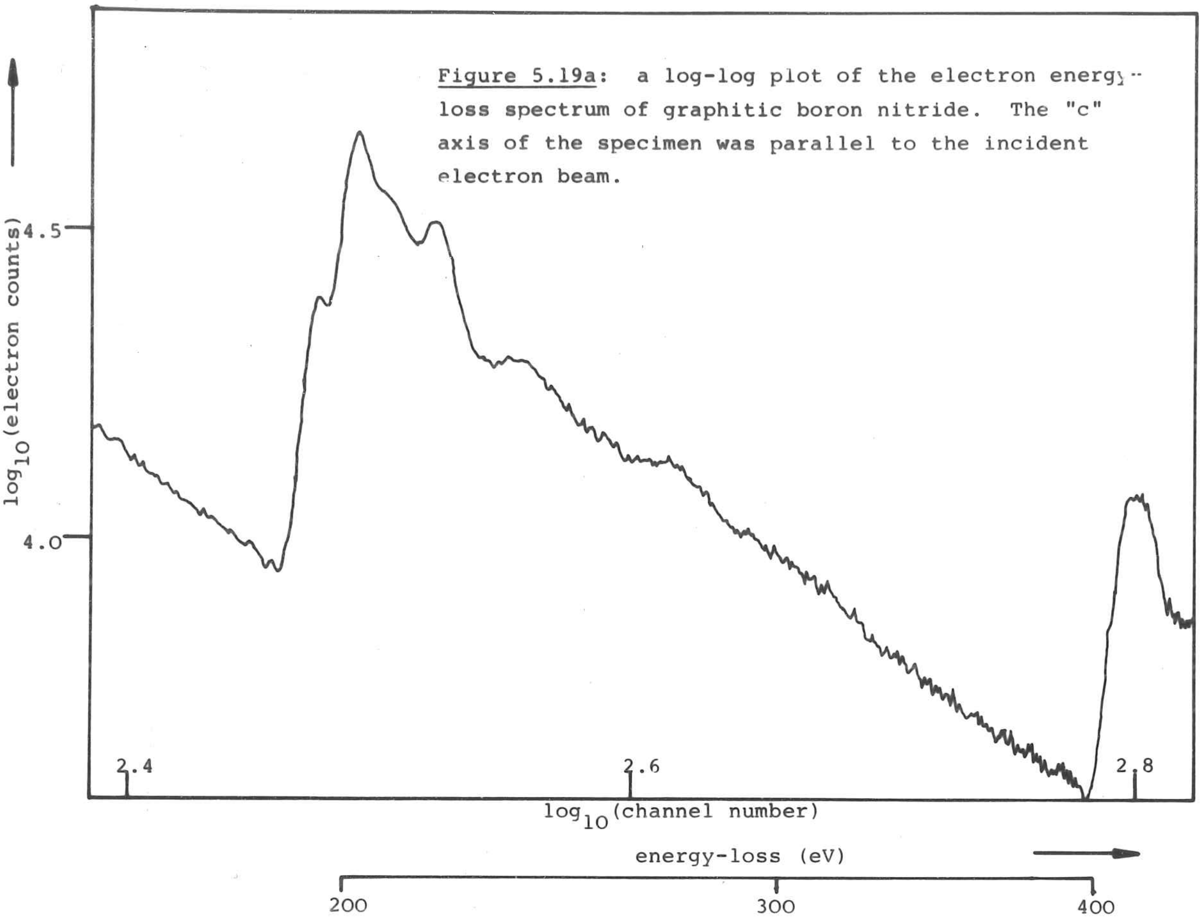

Figure 5.19a: a log-log plot of the electron energy-loss spectrum of graphitic boron nitride. The "c" axis of the specimen was parallel to the incident electron beam.

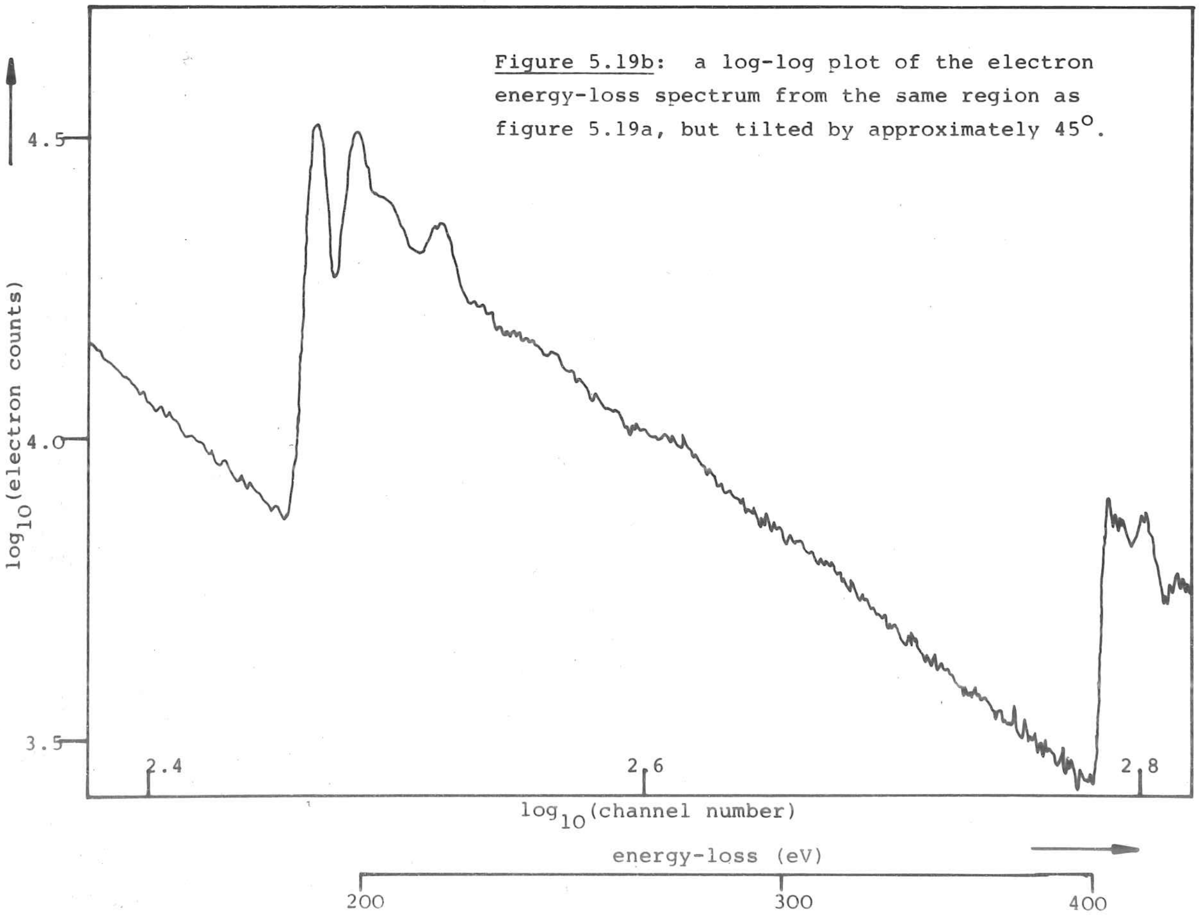

Figure 5.19b: a log-log plot of the electron energy-loss spectrum from the same region as figure 5.19a, but tilted by approximately 45°.

acceptance angle = 1 mR,

specimen orientation: c-axis about 45° to the optic axis; yielding the energy-loss spectrum of figure 5.19b.

The first experiment accepts electrons scattered through angles 0 to 8.5 mR. As θ_E is much less than 8.5 mR, ($\theta_E \simeq 1$ mR) most of the electrons correspond to momentum transfers nearly perpendicular to the optic axis, i.e. the specimen c-axis. In the second case, a smaller probe convergence was used, resulting in an "average" direction of momentum transfer approximately 45° to the optic axis. As the specimen is now tilted by about 45°, some electrons will be detected which correspond to a direction of momentum transfer close to the c-axis, hence the increased relative intensity of the π^* peak.

The structure at the nitrogen-K core-loss is seen to reflect the structure at the boron-K core-loss. The effect of band-structure is to modify the density of states as a function of secondary electron energy. The energy-loss signal is proportional to the product of the density of states and a matrix element between the initial bound (core) state and the final (unbound) state. It is not surprising, therefore, that the shape of the core-loss near the nitrogen-K edge is similar to the shape near the boron-K edge, although seen at decreased energy resolution due to instrumental effects.

The angular distribution of secondary electrons within the specimen will vary in a complex way with probe geometry and secondary electron energy. It is not clear what effect this will have on EXELFS. One way to minimise this effect is to use a large probe convergence angle which will then produce an angular distribution of electrons in the foil that is not sharply peaked, but samples all directions approximately isotropically.

The energy-loss results of the two experiments above were processed numerically in order to obtain the RDF's shown in figure 5.20. A low-energy window at 25 eV above the edge was used to exclude any

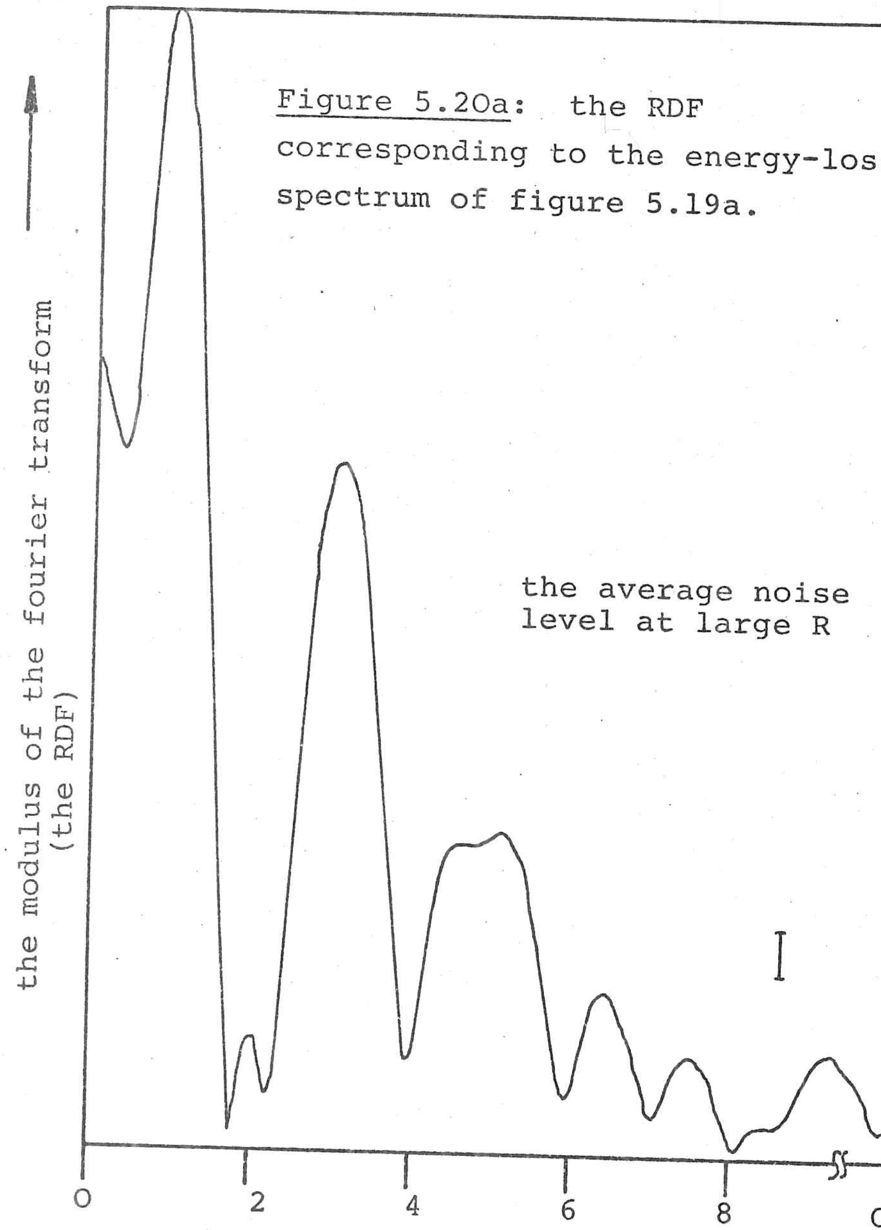

Figure 5.20a: the RDF corresponding to the energy-loss spectrum of figure 5.19a.

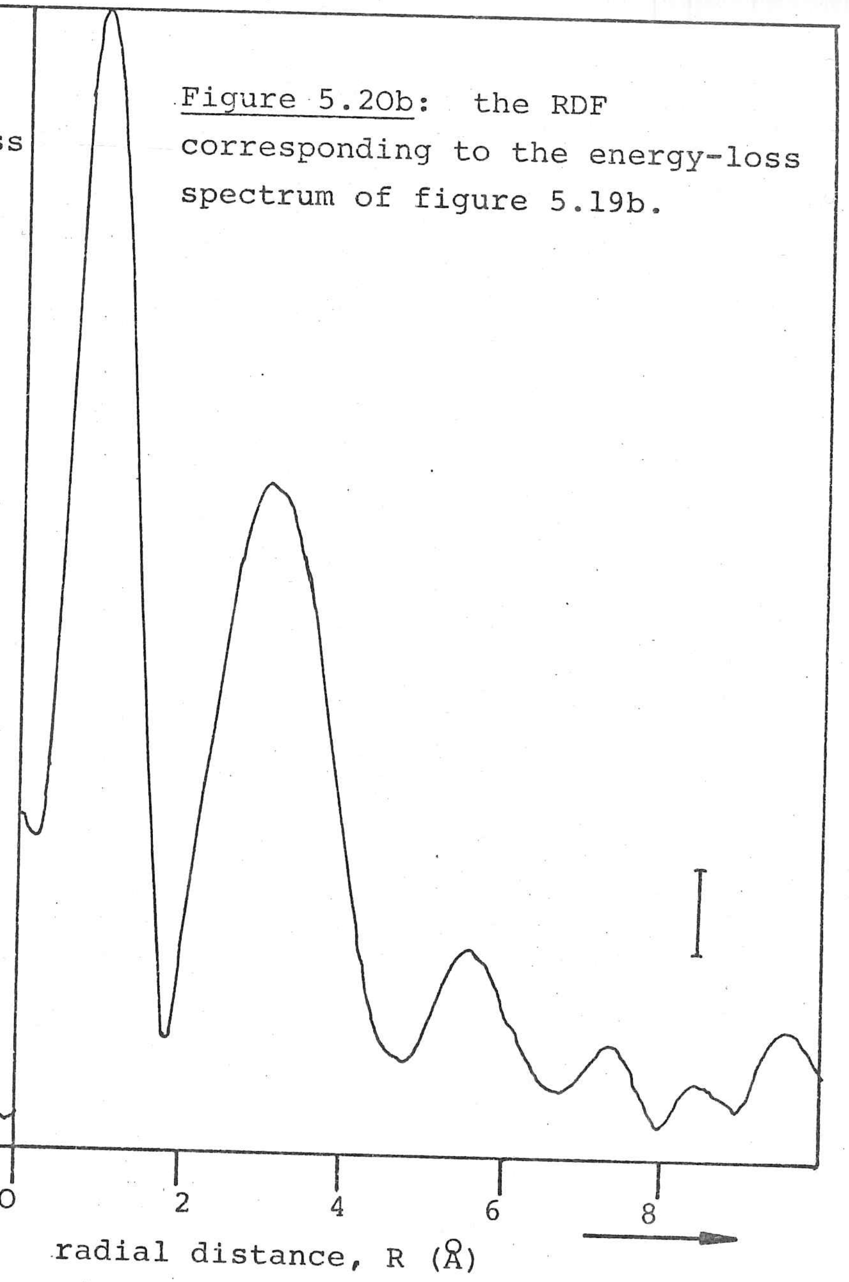

Figure 5.20b: the RDF corresponding to the energy-loss spectrum of figure 5.19b.

bandstructure. The two energy-loss spectra look very similar beyond the low-energy window, and is is not surprising, therefore, that the two RDF's look similar. The following points may be derived from figure 5.20:

1) the position and width of the nearest neighbor peak at 1 Å is identical in both RDF's;

2) the second peaks are centred at very nearly the same value of radius. The width of the second peak in the second experiment is rather greater than in the first experiment and greater than the numerical resolution as measured from the width of the nearest-neighbor peak. This indicates either that the peak has been modified by the presence of noise (which is unlikely in such a strong peak), or more than one closely-separated peak is present in the RDF.

3) The third peak in figure 5.20b has shifted towards greater radius by 0.6 Å and is much smaller than the third peak of figure 5.20a. The noise content of the second spectrum is greater than that of the first, and the third peak of the second RDF is comparable to the level of the noise content in that RDF. It is entirely possible, therefore, that the observed shift in the position of this peak is an artefact due to the presence of noise.

One possible explanation for the increased intensity observed near 3.3 Å in the second RDF (figure 5.20b) may be that the secondary electron angular distribution has an appreciable value in the direction of the c-axis (as demonstrated in the case of band-structure effects), and the peaks in the RDF due to inter-planar distances at half the c-axis repeat and above should appear on the RDF.

It may be concluded that pronounced orientation dependence of the band-structure just above the edge does not seriously affect the EXELFS structure.

Chapter 6 - The energy-loss spectroscopy of niobium and vanadium hydride

Chapter 6 - The energy-loss spectroscopy of Niobium and Vanadium hydride.

6.1 INTRODUCTION

EELS is a technique that is best suited to the detection of light elements (Egerton 1978). The lightest element and one of considerable importance in both theory and practise is hydrogen. The practical interest includes the study of the effect of hydrogen as a cause of embrittlement in many metals and alloys. One important use of transition-metal hydrides is as a hydrogen storage element in hydrogen-fuelled engines. The hydrogen content of amorphous silicon films is known to affect their electrical properties very strongly. The hydrogen content of the recently-developed hard carbon films is thoughtto have an important effect on their electrical and physical properties (Turner 1980).

The hydrogen 1s atomic orbital has a binding energy of 13.6 eV. There is considerable debate as to the way that the hydrogen enters a metallic lattice. The hydrogen electron may either be kept by the hydrogen nucleus (a proton) or given up to the conduction band of the host lattice. In the former case, the hydrogen 1s energy-loss edge would be affected by the presence of the conduction electrons which have time to relax about the field caused by the hydrogen 1s electron. This is equivalent to a dielectric constant. The hydrogenic K-loss would be shifted to lower energies, but would still appear as an edge (i.e. a sharp onset and a power-law decay).

If the hydrogen looses its electron to the conduction band of the host metal, it is expected that the fermi level of the metal would rise, and this may result in a change in the physical structure of the metal in order to minimise the total electronic energy. As is shown later, the addition of hydrogen does provoke a phase change for both niobium and vanadium from b.c.c. to f.c.t. (face-centred tetragonal) accompanied by a change in unit cell volume and much increased brittleness.

Niobium was chosen as a suitable matrix metal because:

1) Niobium is known to take up a large amount of hydrogen;

2) There is a considerable body of work on the niobium-hydrogen system that has been published, phase diagrams are available (Schober 1973, 1975a);

3) Conventional T.E.M. has shown that it is possible to observe superlattice reflections in the electron diffraction pattern, thus indicating that the hydrogen is retained by very thin foils. The microstructural morphology of the phase transitions has been well-characterised (Schober 1975a,b).

4) A tested technique existed for the addition of hydrogen to metallic niobium electrolytically. The details of this technique were very kindly disclosed by Dr. Harris - University of Birmingham Department of Metallurgy. (See fig. 6.1).

Vanadium was also chosen because:

1) vanadium is also well characterised (Wanagel et al 1972);

2) specimens could be prepared using the same experimental techniques as in the case of niobium.

6.2 SPECIMEN PREPARATION

1) 3 mm discs of niobium and vanadium were spark-eroded from high-purity single-crystal rod and poly-crystalline sheet respectively.

2) The discs were electrolytically jet-etched to produce a small hole in the centre (using the conditions specified in fig 6.1). During this operation, the specimen absorbs hydrogen (Schober 1975b).

3) In order to produce hydrogen-free specimens, the thinned discs were heated to 800 ^{o}C for at least 1 hour in a vacuum (less than 10^{-5} torr). This process removes the dissolved hydrogen (Schober 1973).

4) The specimens were hydrogen-charged by making the discs the cathode of an electrolytic cell, using the same etchant as above. A supply current of 1 - 3 amps passing for between 1 and 3 minutes was used to charge the foils.

Steps 1) to 4) in the above process are summarised in fig 6.1. The specimens produced by this technique had a bright metallic finish after step 2) which changed to a dull metallic finish after step 4). The discs were visibly warped and many showed cracks. It was possible to powder a charged disc between thumb and fore-finger, so the specimens had to be treated very gently. The specimen is embrittled because of the change in physical structure of the metal,

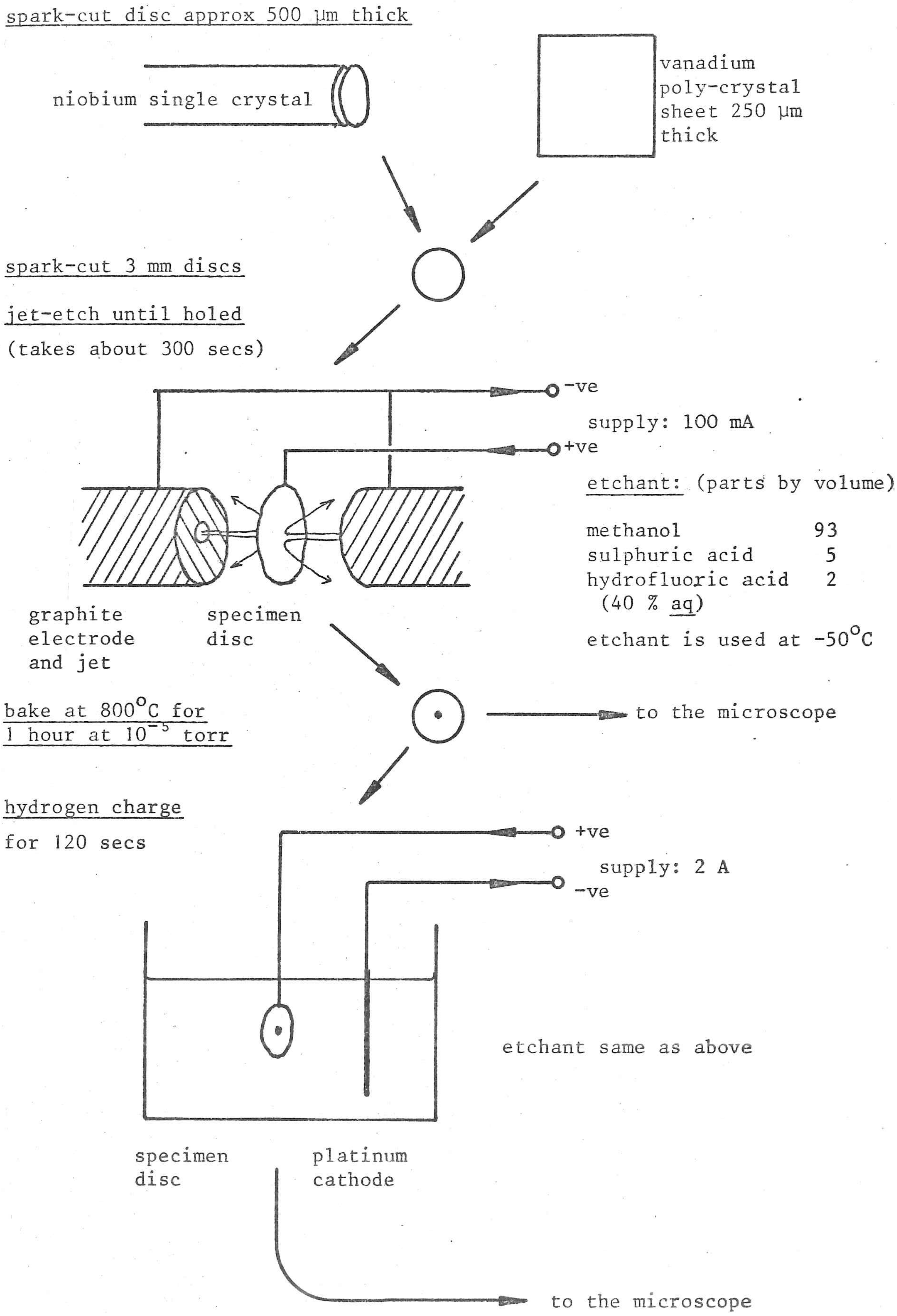

Figure 6.1: vanadium and niobium specimen preparation.

which involves an increase in unit cell volume (of approx 12%) which introduces strain between hydride crystallites of differing orientation as the lattice expansion is anisotropic.
The strain involved may cause the specimen to warp or crack.

6.3 DATA COLLECTION TECHNIQUES

The hydride specimen could not be baked in vacuo before examination in the S.T.E.M. because this would probably drive out most of the dissolved hydrogen. It would certainly invalidate comparison with conventional T.E.M. studies made on a freshly-prepared specimen. Because the specimens were unbaked, care had to be taken to ensure that the specimen did not contaminate during data collection.

The hydrogen-free foils could be baked in the microscope airlock prior to their use, and contamination was much less of a problem.

The LINK SYSTEMS computer collection facility, as described in chapter 3, was used to obtain the spectra. Details of the data-collection hardware and subsequent numerical processing techniques are given in section 3.2.3.1 and details of how to use the numerical procedures are given in appendix A.

Unless specified otherwise, spectra were recorded using the following experimental conditions:

1) incident electron energy, $E_o = 80$ keV;
2) probe semi-angle of convergence, $\alpha = 8.5$ mR;
3) collector aperture semi-angle, subtended at the specimen, $\beta < 0.5$ mR;
4) spectrometer energy resolution, $\Delta \simeq 1.5 - 2.5$ eV.

Electron energy-loss spectra were recorded from thin (< 500 Å) regions of each of the four specimens: vanadium, niobium and their β - hydrides.
The presence of hydrogen was seen to effect the low-loss region of the energy-loss spectra of the metals, so instrumental conditions were generally optimised for good energy-resolution, requiring the use of small collector apertures and therefore giving a low electron count-rate.

6.4 NIOBIUM AND VANADIUM HYDRIDE DIFFUSION TIMES

The hydrogen-charged foils have a limited life-time before the hydrogen diffuses out in vacuo. The hydrogen should diffuse a distance s in time t given by the diffusion law

$$t = s^2 / D \qquad - \quad 6.1$$

where D is the diffusion coefficient.

Values of D in the literature vary depending on the hydrogen concentration, but, for a typical hydrogen concentration of 70 atomic % (in the case of niobium), D is given as 10^{-9} (m^2/s) at 300 K (Bauer at al 1976).

Taking s to be half a typical foil thickness, s = 200 Å, then application of equation 6.1 yields a diffusion time of

$t = 0.4\ \mu s$.

A similar calculation for the thickest portion of the specimen yields t = 22 seconds.

With such small diffusion times, in comparison with the time taken to perform an experiment, the hydrogen should largely have disappeared by the time a spectrum was recorded, and it should not have been possible to observe the effects of hydrogen on the energy-loss spectra at all.

Shen et al, (1978) have shown that a surface barrier must exist in a similar system (Pd hydride). A latency time of several hours has been observed by some workers (Schober et al 1973).

Thus, the presence of a surface barrier means that the hydrogen can escape only very slowly. It was confirmed that superlattice reflections were visible from the hydrides after several hours in vacuo.

6.5 CONVENTIONAL T.E.M. STUDIES OF THE HYDRIDE STRUCTURE

Conventional T.E.M. investigations of these specimens were performed in order to confirm the presence of the β-hydride phase in the hydrogen-charged specimens.

Figure 6.2a shows a bright-field micrograph of niobium hydride. It can be seen that laminar crystallites are formed from the single-crystal metal matrix. These crystallites are twins related by the f.c.t. (face-centred tetragonal) hydride structure (see below). A selected-area diffraction pattern (fig 6.2b) shows the presence of doublet rings, in agreement with a tetragonal struc-

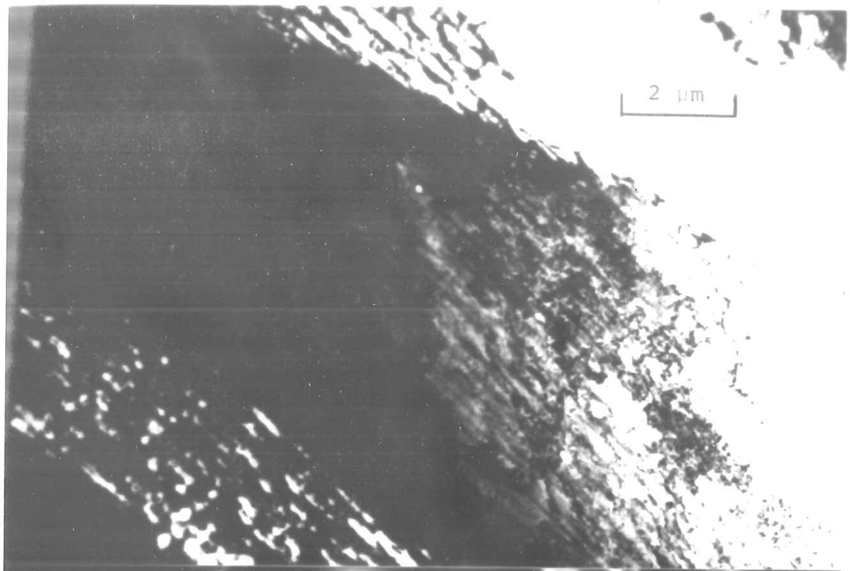

Figure 6.2a: bright-field micrograph of niobium hydride showing laminar structure.

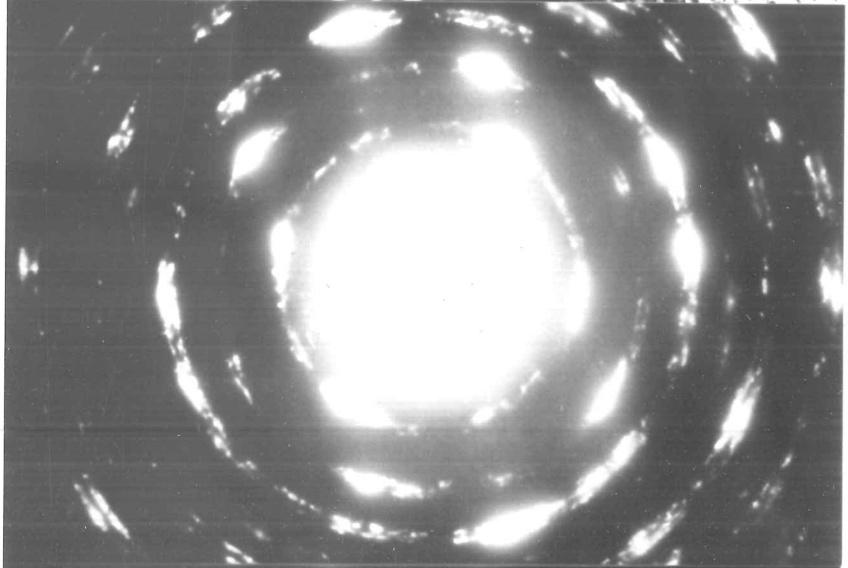

Figure 6.2b: selected-area diffraction pattern from the region above. The b.c.c. metal ring pattern has been modified by the addition of hydrogen. The rings are split, showing that the tetragonal β-phase is present.

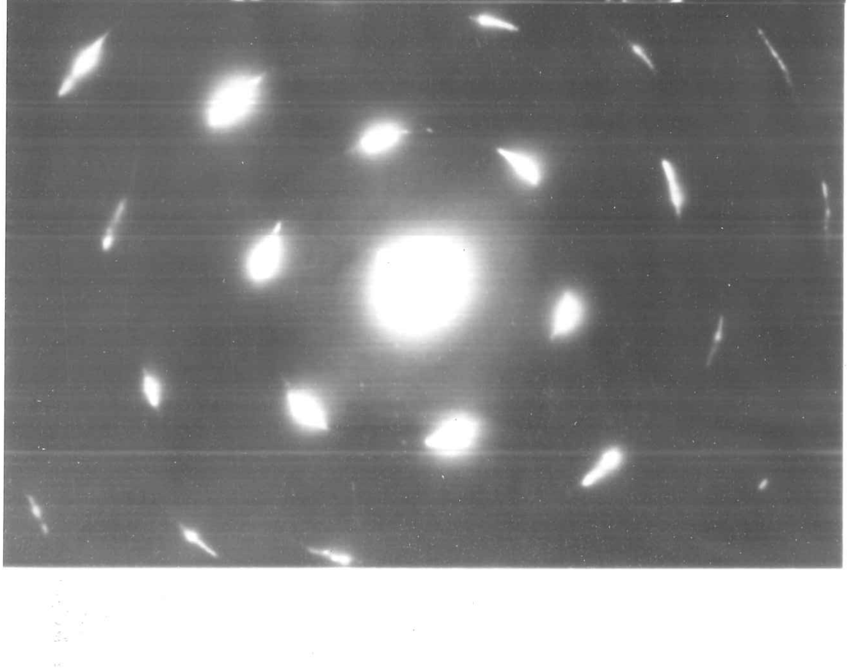

Figure 6.2c: selected-area diffraction pattern from a similar portion of the specimen after having been baked to remove any hydrogen present.

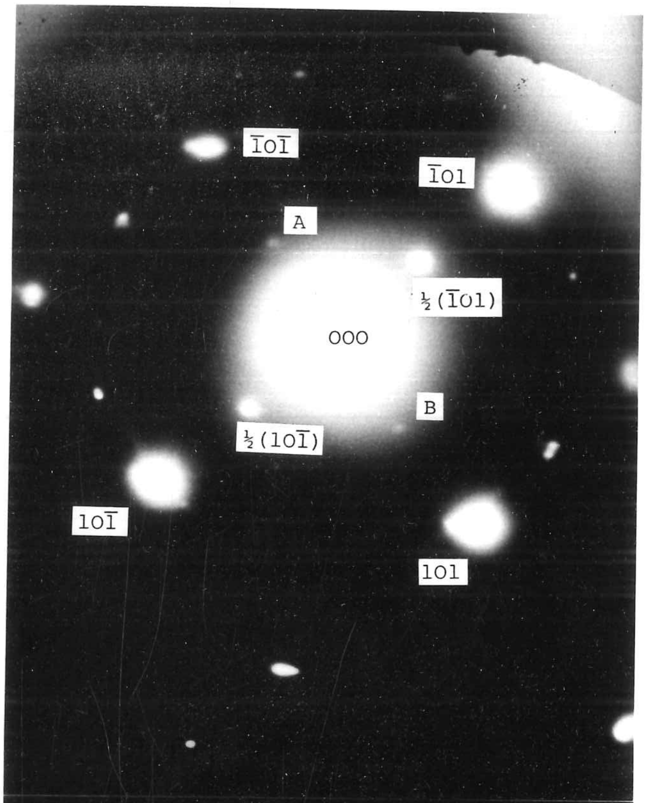

Figure 6.2d: selected-area diffraction patterm of β-vanadium hydride. The faint ring passing through the $(10\bar{1})$ reflections is due to a carbon film aperture used. The spots at $\pm\frac{1}{2}(10\bar{1})$ are superlattice reflections due to the presence of hydrogen.
The corresponding spots marked "A" and "B" are much weaker superlattice reflections that probably arise from the presence of microtwins between areas of ordered hydride.
The diffraction pattern is indexed using the body-centered tetragonal unit cell of Wanagel et al (1972).

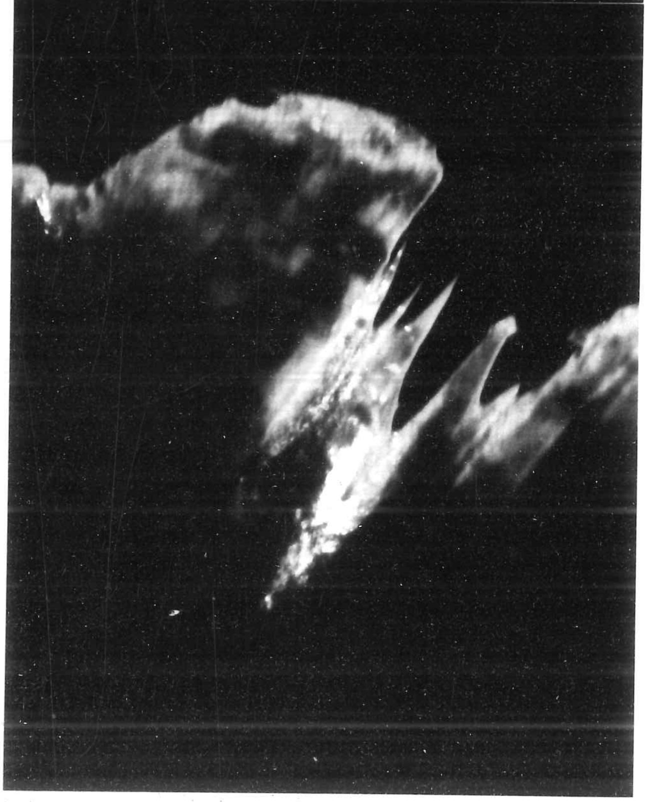

Figure 6.2e: dark-field micrograph corresponding to the above diffraction pattern taken using the $\frac{1}{2}(\bar{1}01)$ superlattice reflection. The specimen contains both α (solid solution) and β (ordered hydride) phases. The β-hydride has etched preferentially.
Magnification: approx. 15000.

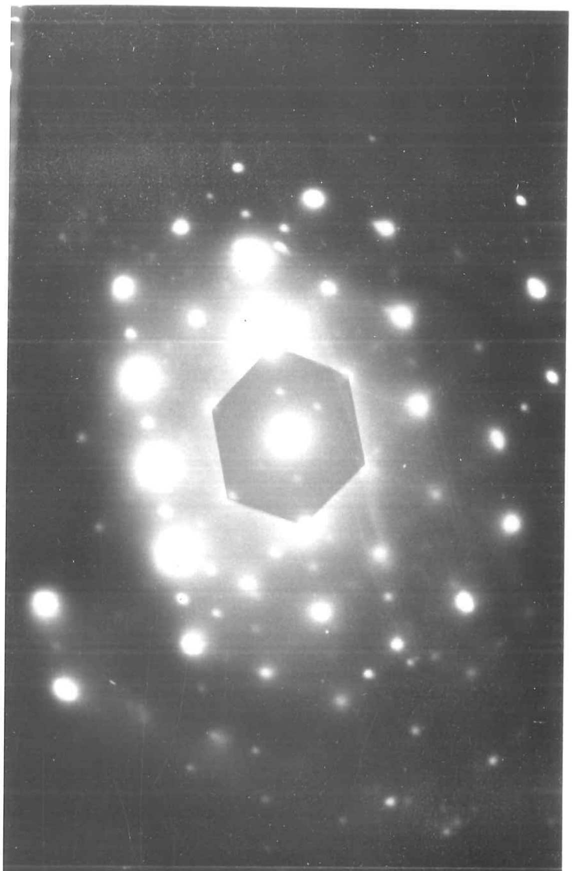

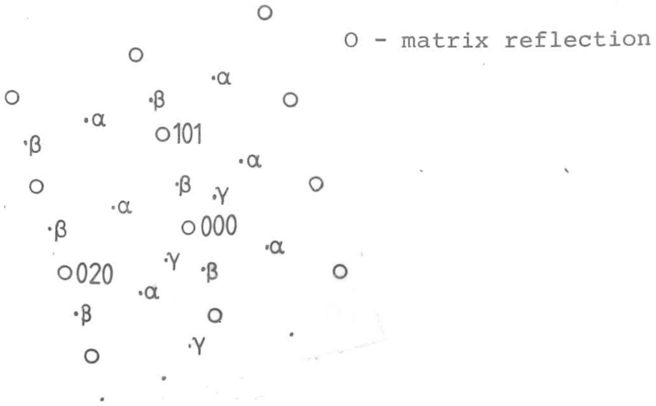

Figure 6.2f: selected-area diffraction pattern from β-vanadium hydride. The matrix reflections are labelled according to the hydride b.c.t structure. The superlattice reflections labelled α are correct for this orientation. The superlattice reflections β and γ may be explained by the presence of microtwins.

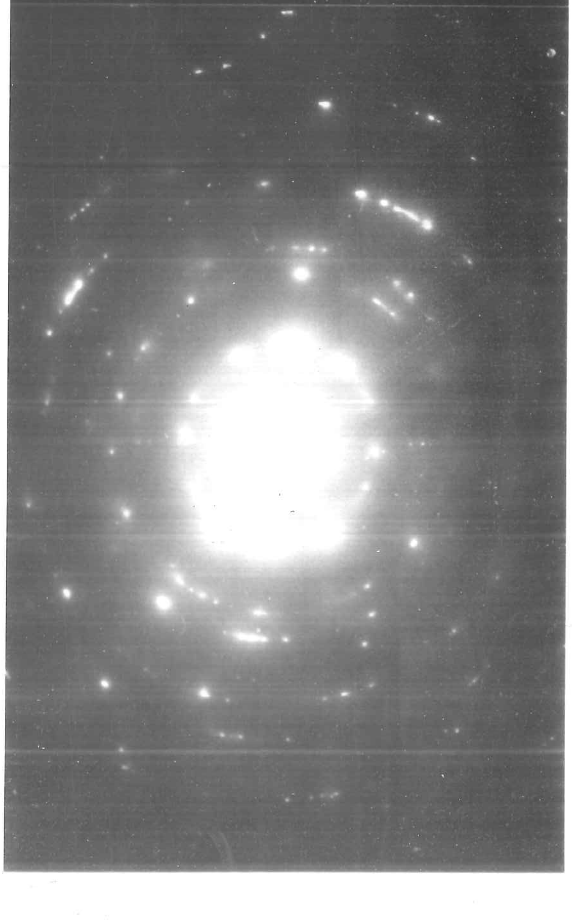

Figure 6.2g: a selected-area diffraction pattern of vanadium which has been baked to remove any hydrogen present. The absence of any splitting of the rings indicates the absence of the β-hydride phase.

ture. This is sufficient evidence to indicate the presence of a hydride phase, and measurement of the ring diameters confirms the presence of the β-hydride phase.

The specimens were then baked to remove the dissolved hydrogen. Selected area diffraction of the baked specimen (fig 6.2c) reveals that there is no splitting of the rings, the structure has reverted to the b.c.c. niobium structure. Work by Schober (1975a,b) shows that β-phase niobium-hydride has a face-centred tetragonal structure which is reproduced in fig 6.3.

A similar sequence of experiments was performed on vanadium hydride. Figure 6.2d shows a selected area diffraction pattern from a vanadium hydride specimen. The spots are indexed according to the body-centred tetragonal structure of Wanagel et al(1972) which is shown in fig 6.3c. The thin ring passing just inside the $(10\bar{1})$ reflections arises from the use of a carbon film aperture, and provides a convenient calibration. The spots at $\pm\frac{1}{2}(10\bar{1})$ are attibuted to hydrogen superlattice reflections. The spots marked "A" and "B" cannot be identified with the structure of fig 6.3c, in the same orientation, but may be explained by the presence of a twin in the field defined by the selected area aperture. When viewed at high magnification, it is possible to observe fine laminar boundaries inside crystallites, and these may be micro-twins on a scale of 100Å.

A dark-field micrograph taken using the $\frac{1}{2}(\bar{1}01)$ superlattice reflection shows the hydride to have been present in the form of laminae which have been preferentially etched.

Repeated selected-area diffraction patterns (for example, see fig 6.2f) show the presence of superlattice reflections and microtwins.

The vanadium hydride specimen was removed and baked to remove the dissolved hydrogen. Selected-area diffraction patterns taken from the baked specimen show a ring-pattern that may be indexed according to to b.c.c. vanadium structure (see fig 6.2g). No splitting of the rings was observed, and no superlattice reflections were observed from single-crystal portions of the specimen.

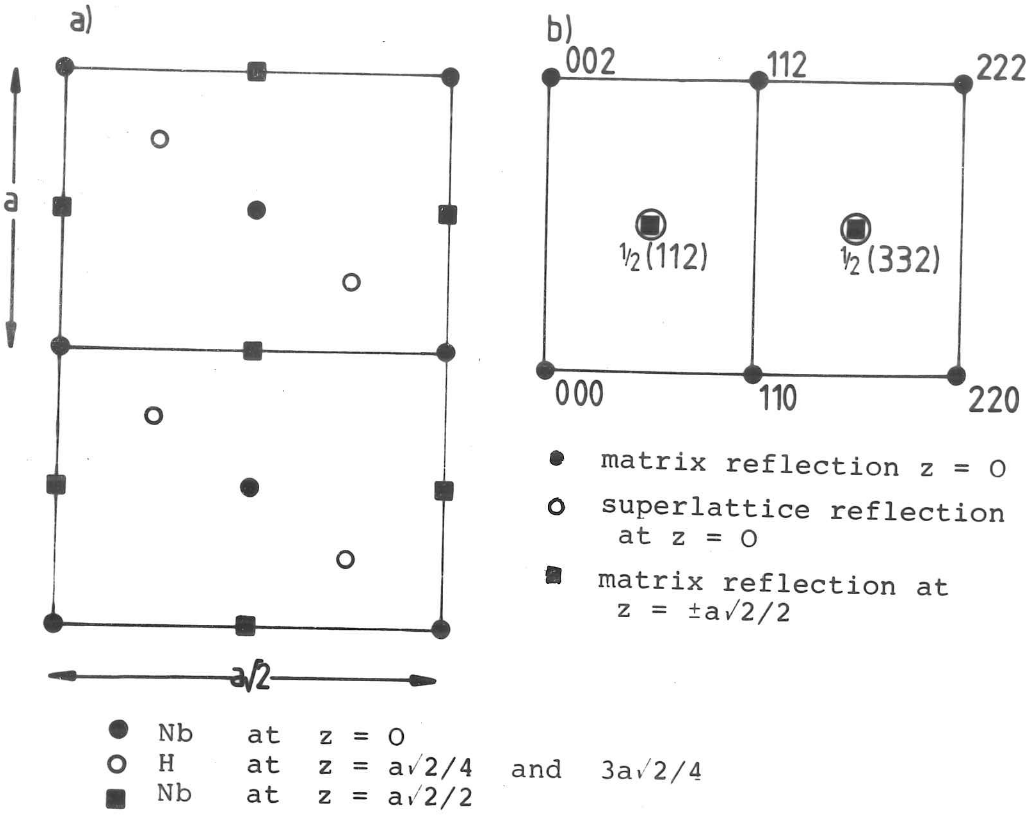

Figure 6.3: orthorhobic β-phase niobium hydride. a) the positions of the hydrogen in the "bcc" lattice in real space; b) the reciprocal lattice. (From Schober (1975))

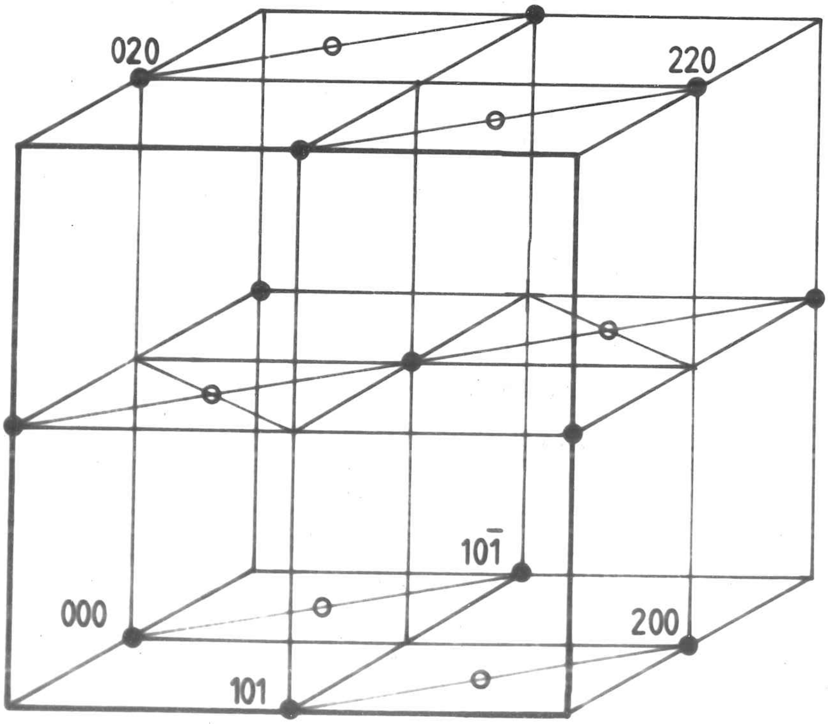

Figure 6.3c: the reciprocal lattice of β-vanadium hydride indexed with reference to the body-centered tetragonal structure. ● - matrix reflections; ○ - superlattice reflections. (From Wanagel *et al* (1972))

Thus it was possible to demonstrate that the specimen preparation techniques, given in detail above, were able to produce hydrogen-free specimens and β-hydride specimens of both niobium and vanadium.

6.6 ENERGY-LOSS RESULTS

Many energy-loss spectra of niobium and the hydride were collected. The two spectra shown in fig 6.4a are typical of these spectra, and show the following features:

1) a broad peak at about 40 eV;

2) a sharper peak at about 22 eV due to a bulk plasmon;

3) a shoulder on the 22 eV peak of variable position(the energy-loss varied between different positions on the same specimen);

4) a peak at about 6 eV observed only in the case of hydride specimens.

A detailed discussion of the peaks 1), 2) and 4) is given later. It was thought that the variable peak may be due to the presence of an oxide layer of variable composition and thickness. In order to test this, energy-loss spectra were recorded from Nb_2O_5 (prepared from a suspension of powdered Nb_2O_5 in alcohol evaporated on a holey-carbon film), and a spectrum is presented in fig 6.4a. It can be seen that there is a prominent double-plasmon, and that the lower peak of this corresponds to the position of the shoulder seen on the leading edge of the plasmon peak of the niobium spectra. The variable peak is thus attributed to the presence of a surface oxide film.

The peak near 6 eV in the hydride is similar in appearance to the peak observed in the energy-loss spectra of some carbon films. (Taft et al 1965). It was noticed that the energy-loss spectrum of a thick contamination spot produced by leaving a focussed probe stationary on the surface for some minutes and the energy-loss spectrum of the hydride are similar (see fig 6.4b). The bulk plasmon of the contamination was at a slightly greater energy (about 25 eV) than the hydride plasmon (about 23 eV). The hydride peak near 6 eV is duplicated in the contaminated spectrum, although it has shifted slightly towards lower energy.

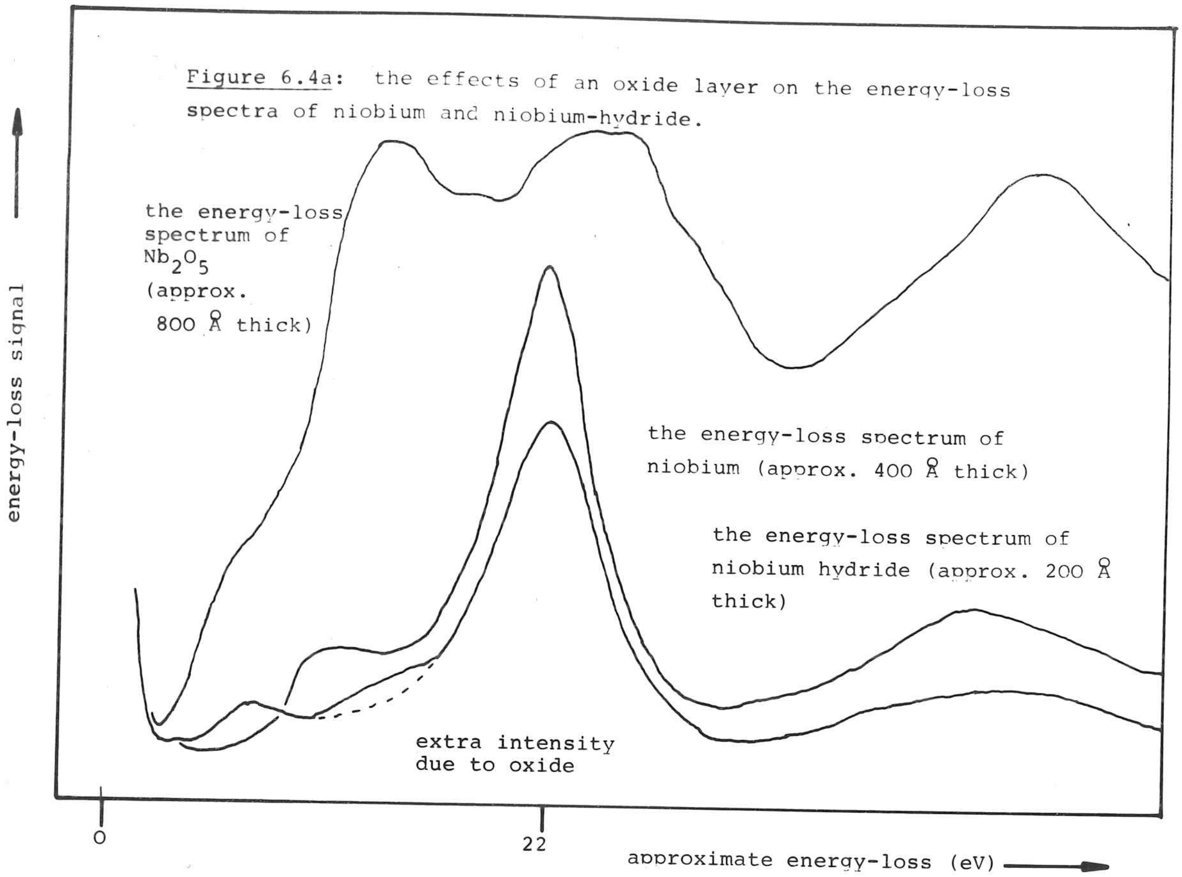

Figure 6.4a: the effects of an oxide layer on the energy-loss spectra of niobium and niobium-hydride.

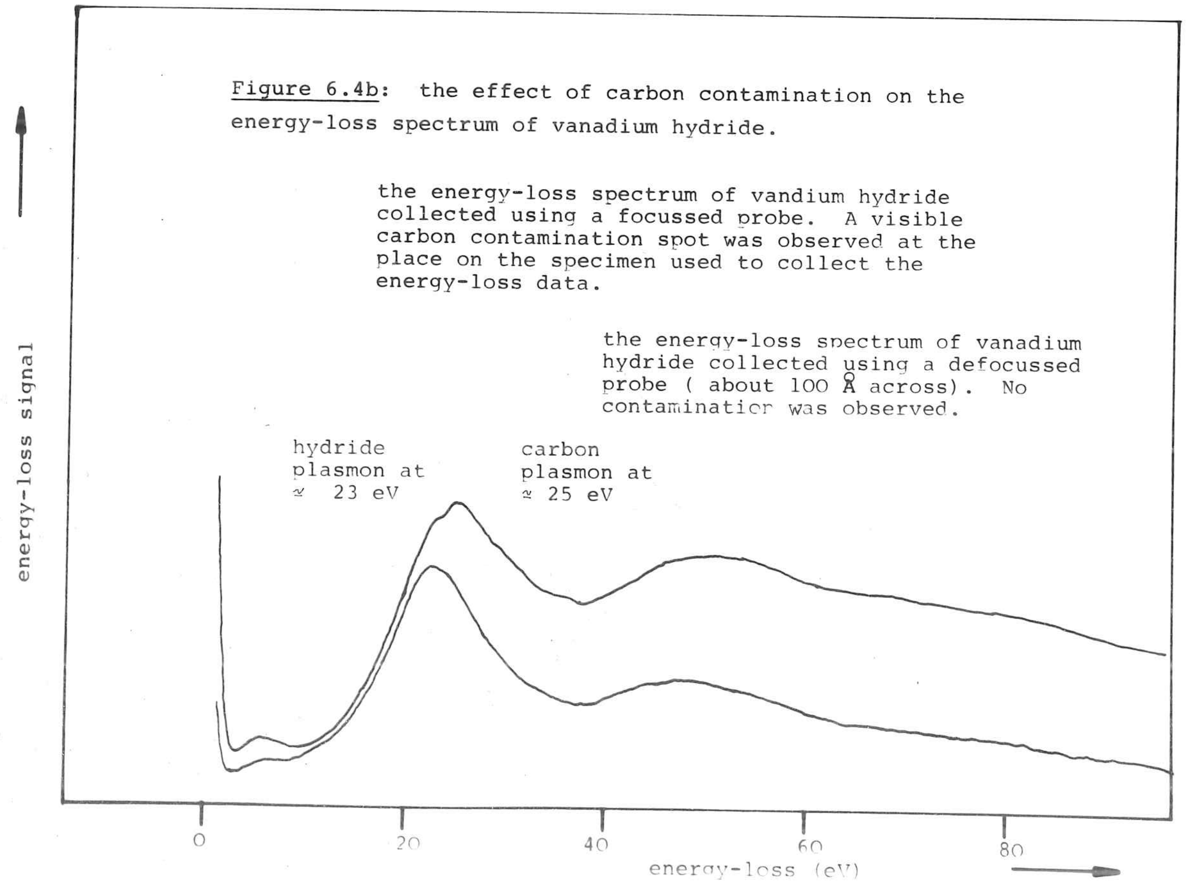

Figure 6.4b: the effect of carbon contamination on the energy-loss spectrum of vanadium hydride.

As mentioned earlier, care was taken in subsequent spectra to ensure that the specimen was not visibly contaminated by carbon. In practice, a contamination layer of approx. 5 % of the thickness of the specimen would be observed as an increase in the annular detector signal during energy-loss data collection, and would be observed as a spot in the dark-field image of the specimen.

Energy-loss spectra recorded from vanadium and vanadium hydride are shown in figures 6.5 and 6.6 respectively, and spectra of Nb and Nb-hydride are shown in figure 6.11. A detailed discussion of the results is given below.

6.7 INTERPRETATION OF THE ENERGY-LOSS SPECTRA: THE TWOBAND MODEL

The presence of hydrogen in the specimen correlates with the presence of an extra peak in the spectrum at approx 5-6 eV. The hydride spectra appear to be similar to the results for graphite showing a peak near 7 eV (Taft & Philipp 1965, Boyce and Embling 1980). The theory developed by Liang & Cundy (1969, see also Bell & Liang 1976) to explain these peaks is based on a two-band model: i.e., this model assumes that the effect of hydrogen on the matrix metal is to introduce an energy-gap into the valence band. This energy-gap arises from the change in physical structure of the metal which itself is caused by the minimisation of the valence-band electronic energy. The addition of hydrogen is not viewed as adding an impurity band of localised states.

Following the method of Liang & Cundy, the dielectric function may be written as

$$\varepsilon(\omega) = 1 - \frac{Ne^2}{\varepsilon_o m}\sum_{\ell\ell'} \frac{f_{\ell\ell'}(\omega,k)}{\omega^2 - \omega_{\ell\ell'}^2 + i\omega/\tau} \qquad - \quad 6.2$$

Where: N is the number of atoms per unit volume;

$f_{\ell\ell'}(\omega,k)$ is the oscillator strength for transitions from state (ℓ,k) to state (ℓ',k) where ℓ and ℓ' denote filled and empty status respectively, involving an energy change $h\omega_{\ell\ell}{}' = h(\omega_{\ell}{}' - \omega_{\ell})$.

τ is the relaxation time averaged over all electron-scattering processes, assumed to be long (i.e. $\omega\tau >> 1$). All transitions are vertical (i.e. $\Delta k = 0$).

The oscillator strength satisfies the f-sum rule

$$\sum_{p\ell}\sum f_{p\ell}(\omega,k) = n_\ell \qquad - \quad 6.3$$

where: n_ℓ is the number of electrons contributing to band ℓ and the sum over p is taken over all bands.

Liang & Cundy make a single-oscillator approximation by introducing an average inter-band gap $\overline{\omega}_{\ell'\ell}$. Thus equation 6.2 is reduced to

$$\varepsilon(\omega) = 1 - \sum_{\ell'\ell} \frac{\omega^2_{p\ell}}{\omega^2 - \overline{\omega}^2_{\ell'\ell} + i\omega/\tau} \qquad - \quad 6.4$$

where: $\omega_{p\ell} = (Ne^2 n_\ell/\varepsilon_o m)^{\frac{1}{2}}$.

In a narrow band-gap material, where all filled bands other than the top valence band are well removed from the conduction band, such that $\omega_{cv} < \omega_p << \omega_{c\ell}$, the energy for plasma resonances is nearly that of a free-electron gas.

In a material where there are two valence bands (v_1 and v_2) near the conduction band, plasma resonances can be found arising from:

1) valence electrons from both bands, giving a plasma frequency

$$\omega^2_{p_2} = \frac{Ne^2}{\varepsilon_o m}(n_{v_1} + n_{v_2}) \qquad - \quad 6.6$$

provided that $\omega_{p_2} > \overline{\omega}_{cv_1}$ and $\omega_{p_2} > \overline{\omega}_{cv_2}$

2) valence electrons from the highest valence band only (v_2).

The second plasmon can exist only if there is a clear separation between the two valence bands, such that, in the frequency region

$$\overline{\omega}_{cv_1} < \omega < \overline{\omega}_{cv_2},$$

Im(ε) is small and Re(ε) may be approximated as

$$\varepsilon_1(\omega) = (1 + \delta\varepsilon_{v_1}) + \frac{Ne^2}{\varepsilon_o m}.n^*_{v_2} \qquad - \quad 6.7$$

where: $$\delta\varepsilon_{v_1} = \frac{Ne^2}{\varepsilon_o m}.\frac{1}{\omega^2_{cv_1}}.\sum_k f_{cv_1} \qquad - \quad 6.8$$

represents the contribution to the dielectric function from the transitions from the lower valence band to the conduction band; i.e. the lower valence band can relax and partially screen the low-frequency plasmon.
The second term in equation 6.7 represents an enhancement of the number of electrons in the upper valence band due to transitions from the lower valence band. The second term is usually small and may sometimes be determined as zero from considerations of orbital symmetry.

The value of the lower plasmon frequency ω_{p_2}, given by $\varepsilon_1(\omega_{p1}) = 0$ is

$$\omega_{p1}^2 = \frac{(\omega_{pv1}^*)^2}{1 + \delta\varepsilon_{v1}} \qquad - \quad 6.9$$

where:

$$(\omega_{pv1}^*)^2 = \frac{Ne^2}{\varepsilon_o m}\left(n_{v1} + \sum_k f_{v1v2}\right) \qquad - \quad 6.10$$

Thus, the observed frequency of the low-energy resonance may be strongly modified by the presence of the deeper valence band, especially if they are separated by only a small energy.

The dielectric function may thus by expressed as a function of six parameters:

$$\varepsilon(\omega) = 1 - \frac{\omega_{pv1}^2}{\omega^2 - \omega_{cv1}^2 + i\omega/\tau_{v1}} - \frac{\omega_{pv_2}^2}{\omega^2 - \omega_{cv_2}^2 + i\omega/\tau_{v2}} \qquad - \quad 6.11$$

where:

$$\omega_{pv_1}^2 = \frac{Ne^2}{\varepsilon_o m}(n_{v1}) \qquad - \quad 6.12$$

$$\omega_{pv_2}^2 = \frac{Ne^2}{\varepsilon_o m}(n_{v2}). \qquad - \quad 6.13$$

In the case of niobium and vanadium hydrides, it is not known beforehand how many electrons are contained in each valence band. In order to obtain values of the six parameters in equation 6.11, the parameters are varied, and the energy-loss spectrum synthesised from equation 6.11 is compared with energy-loss data. The parameters are varied in order to obtain the best fit to the energy-loss data.

6.7.1 The synthesis of a spectrum using the two-band model

The program GEN (see appendix A for operational details) was used to perform the following operations:

1) the dielectric function, $\varepsilon(\omega)$, given by equation 6.11, was calculated using values for the six parameters entered at the terminal;

2) the energy-loss function $\mathrm{Im}(-1/\varepsilon)$ was obtained from $\varepsilon(\omega)$;

3) the energy-loss function was scaled for a given specimen thickness;

4) the single-scattering spectrum, thus obtained, was multiply-scattered to synthesise a spectrum from a specimen of finite thickness;

5) the spectrum was convolved with a gaussian zero-loss peak to simulate the effect of a finite experimental energy resolution.

The spectrum thus synthesised was plotted together with an experimental spectrum (using the COMPARE program), scaled both horizontally and vertically so that the energy-scales and plasmon peak heights corresponded.

The six parameters were varied by hand, so that the best match occurred between synthesised and experimental spectra. Errors in the estimated values of the parameters were determined by adjusting each parameter in turn until the correspondence between the synthesised and experimental spectra was noticeably impaired.

6.7.2 The physical interpretation of the results of the two-band fit

In all this mathematical discussion, it is easy to loose sight of the physical interpretation of the two-band model.

Provided that the gap between the two valence bands is wide enough for the uppermost band to have a separate plasmon, but not so deep that it cannot contribute to a joint plasmon, two plasmons will be observed. The first of these will be screened by the relaxation of the lower valence band electrons which behave as a polarisable core. The higher-energy plasmon reults from the excitation of electrons from both valence bands to the conduction band and is screened by the core polarisability due to deeper bands. In the two-band model, the deep-lying bands are assumed to have little effect. A core polarisability term could be included in equation 6.11

and described by three parameters, thus improving the fit between the experimental and synthesised spectra. There is, however, a law of diminishing returns, and one could introduce as many bands as were neccessary to obtain an arbitrarily-good fit to the data, but this would require much programming effort and computer time and would direct the attention away from the physical interpretation of the model towards the numerical techniques employed.

6.8 DISCUSSION OF THE ENERGY-LOSS RESULTS FOR VANADIUM

See figure 6.5 for the energy-loss spectrum of vanadium which have been processed to remove multiple scattering. The following features are observed:

1) a zero-loss peak of width 1.5 eV (FWHM);

2) a plasma excitation peak at 24.5 eV. The free-electron plasma frequency given by section 2.1.2.1 is

$$\omega_p^2 = \frac{ne^2}{\varepsilon_o m\Omega} \qquad - \quad 6.14$$

where: n is the effective number of valence electrons per atom, contributing to the plasma oscillation, and

Ω is the atomic volume.

For vanadium: $\Omega = 1.39 \,.\, 10^{-29}\ m^3$ (from X-ray data), the measured plasmon energy is 24.5 eV, thus the calculated value of n is n = 6 electrons / atom.

The electronic configuration of atomic vanadium is $1s^2 2s^2 2p^6 3s^2 3p^6 3d^3 4s^2$ (assuming overlap between the 3d and 4s electrons), suggesting that the number of electrons free to contribute to the plasma oscillation is 5 per atom.

This figure would be modified by the presence of coupling between the 3p and the 3d and 4s electrons, tending to raise n, and the polarisability of the 1s-3p core states, tending to lower n.

The measured value of n will differ from the atomic values in the metal because of bandstructure effects which modify the effective mass of the valence electrons (Reather 1965).

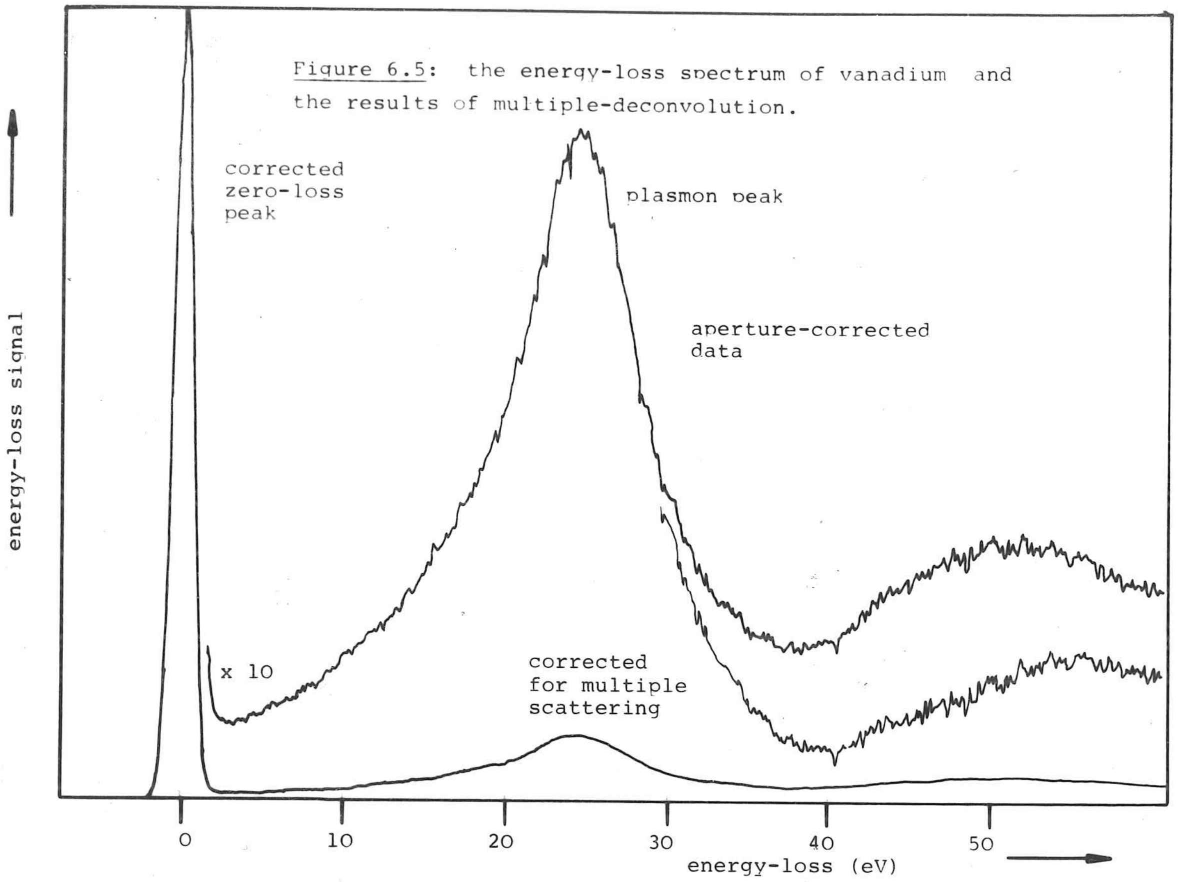

Figure 6.5: the energy-loss spectrum of vanadium and the results of multiple-deconvolution.

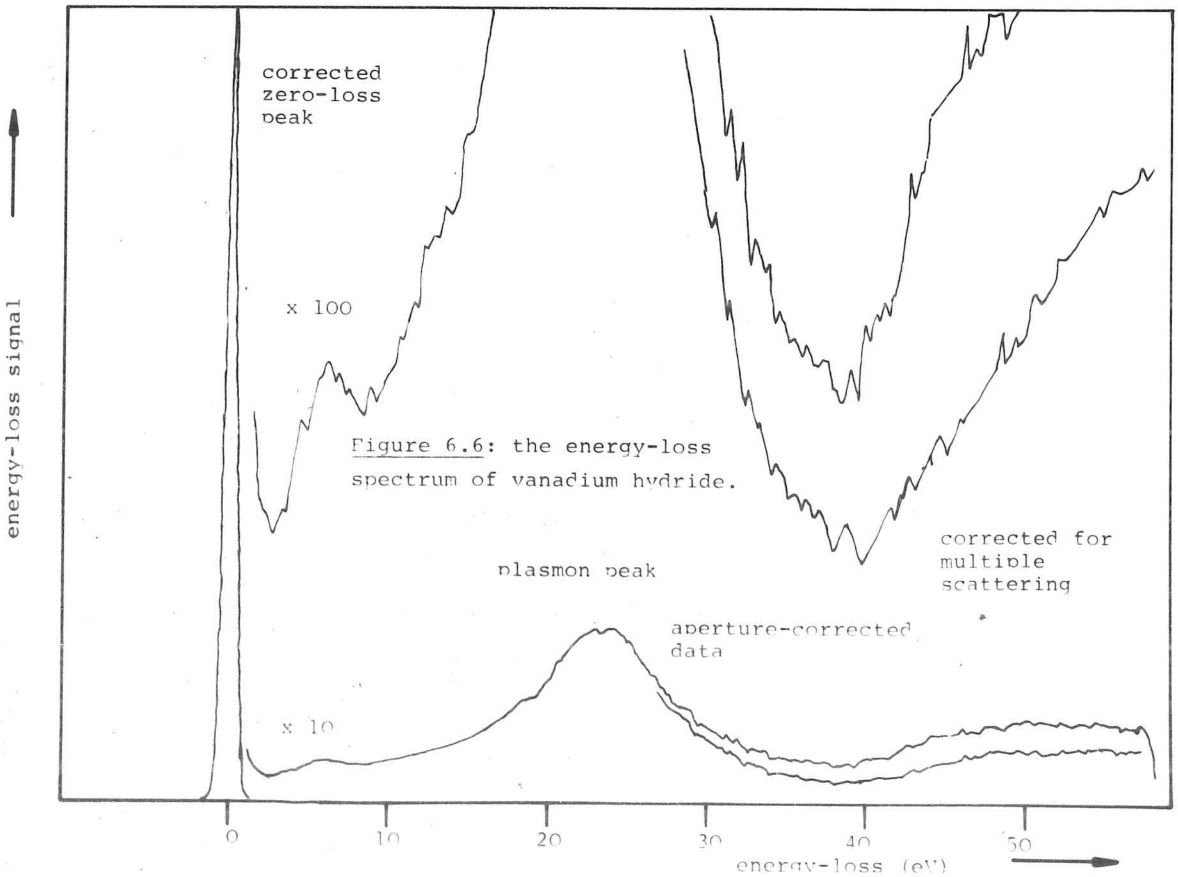

Figure 6.6: the energy-loss spectrum of vanadium hydride.

3) A broad peak is observed near 52 eV composed of a doubly-scattered plasmon (i.e. an incident electron excites two plasmons and loses an average of twice the average plasmon energy - in this case, twice 24.5 eV) and the vanadium M_{2-3} single-electron excitation corresponding to excitation of the atomic 3d electrons to the fermi level. The effect of multiple scattering may be removed by multiple deconvolution (using the MULDEC program). The deconvolved spectrum is shown in fig 6.5. Much of the scattered intensity between 35 and 60 eV has been removed, the remainder shows that the M_{2-3} core loss starts near 39 eV and rises slowly to a peak near 55 eV.

The atomic binding energy of vanadium M_{2-3} given by Bearden & Burr (1967) is 38 eV. It is difficult to obtain an exact edge position measurement from energy-loss data because the M_{2-3} core-loss, being a transition from an $\ell = 1$ angular momentum state, demonstrates the delay caused by the centrifugal potential (Inokuti 1971). At these low energies, the shape and position of the edge may be modified by a chemical shift (i.e. the chemical environment effects the fermi-level and average inner potential (Salem et al 1978)).

See figure 6.6 for the energy-loss spectrum of vanadium hydride, which shows the following features:

1) a zero-loss peak;

2) an extra peak at approximately 7 eV;

3) a volume plasma excitation at 23.8 (±0.2) eV;

4) a broad peak near 50 eV. The discussion of this peak is not modified by the presence of hydrogen. The only effect that may be observed is a shift in the edge position due to a shift in the fermi-level due to the addition of extra electrons from the hydrogen. Because the edge is slowly-rising, it is not easy to measure the position of the edge accurately. The edges on both spectra appear to occur at 40 (±1) eV.

The volume plasma excitation energy is shifted downward in energy by ≈0.7 eV. The b.c.c. lattice of vanadium undergoes a transformation to the b.c.t. (or monoclinic - Wanagel (1972)) structure upon addition of hydrogen and experiences a 12% increase in unit cell volume. Equation 6.14 may be evaluated, taking into

3) A broad peak is observed near 52 eV composed of a doubly-scattered plasmon (i.e. an incident electron excites two plasmons and loses an average of twice the average plasmon energy - in this case, twice 24.5 eV) and the vanadium M_{2-3} single-electron excitation corresponding to excitation of the atomic 3d electrons to the fermi level. The effect of multiple scattering may be removed by multiple deconvolution (using the MULDEC program). The deconvolved spectrum is shown in fig 6.5. Much of the scattered intensity between 35 and 60 eV has been removed, the remainder shows that the M_{2-3} core loss starts near 39 eV and rises slowly to a peak near 55 eV.

The atomic binding energy of vanadium M_{2-3} given by Bearden & Burr (1967) is 38 eV. It is difficult to obtain an exact edge position measurement from energy-loss data because the M_{2-3} core-loss, being a transition from an $\ell = 1$ angular momentum state, demonstrates the delay caused by the centrifugal potential (Inokuti 1971). At these low energies, the shape and position of the edge may be modified by a chemical shift (i.e. the chemical environment effects the fermi-level and average inner potential (Salem et al 1978)).

See figure 6.6 for the energy-loss spectrum of vanadium hydride, which shows the following features:

1) a zero-loss peak;
2) an extra peak at approximately 7 eV;
3) a volume plasma excitation at 23.8 (±0.2) eV;
4) a broad peak near 50 eV. The discussion of this peak is not modified by the presence of hydrogen. The only effect that may be observed is a shift in the edge position due to a shift in the fermi-level due to the addition of extra electrons from the hydrogen. Because the edge is slowly-rising, it is not easy to measure the position of the edge accurately. The edges on both spectra appear to occur at 40 (±1) eV.

The volume plasma excitation energy is shifted downward in energy by ≃0.7 eV. The b.c.c. lattice of vanadium undergoes a transformation to the b.c.t. (or monoclinic - Wanagel (1972)) structure upon addition of hydrogen and experiences a 12% increase in unit cell volume. Equation 6.14 may be evaluated, taking into account this volume increase to give a value of n = 6.4 electrons / vanadium atom. The β-hydride composition at room temperature lies in the range $VH_{0.45}$ to $VH_{0.7}$ (Wanagel 1972). Thus, it is expected that the number of electrons, per vanadium atom, able to take part in a volume plasma oscillation will show an increase of 0.45 to 0.7 electrons / vanadium atom.

The measured value of the increase in s is 0.4 electrons / vanadium atom, which is in reasonable agreement with the expected value, bearing in mind the simplicity of the free-electron plasma model used.

The extra peak, seen in the hydride spectrum near 7 eV, appears only in the vanadium-hydride spectra, and its appearance must therefore by caused by the presence of hydrogen in the host lattice.

The spectrum of the hydride has been processed numerically (using the DENSITY program) to obtain the dielectric function $\varepsilon(\omega)$ from the energy-loss function $\mathrm{Im}(-1/\varepsilon)$ using the technique of Kramers-Kronig analysis (see sections 2.1.3.5 and 3.3.4). The results are shown in figure 6.7.

The conditions for volume plasma oscillation , at frequency ω , are (Reather 1965, Liang & Bell 1976):

1) $\mathrm{Re}(\varepsilon(\omega)) = 0$ and of positive slope;
2) $\mathrm{Im}(\varepsilon)$ has negative slope.

It can be seen from fig 6.7 that there are two values of energy-loss in the spectrum at which these two conditions are satisfied. The energy-losses at the two plasmon energies are 6 eV and 20 eV. Thus, the two peaks in the energy-loss spectrum near these two values can be attributed to plasma oscillations and not to individual particle oscillations.

Using the two-band model (see above), it should be possible to adjust the parameters ω_{pv_1}, ω_{cv_1}, τ_{v1}, ω_{pv_2}, ω_{cv_2}, τ_{v2} to obtain correspondence between the experimental spectrum and the two-band model spectrum, provided that the effect of hydrogen on the metal is adequately described by the two-band model.

The parameter-fitting procedure outlined in section 6.7.1 was

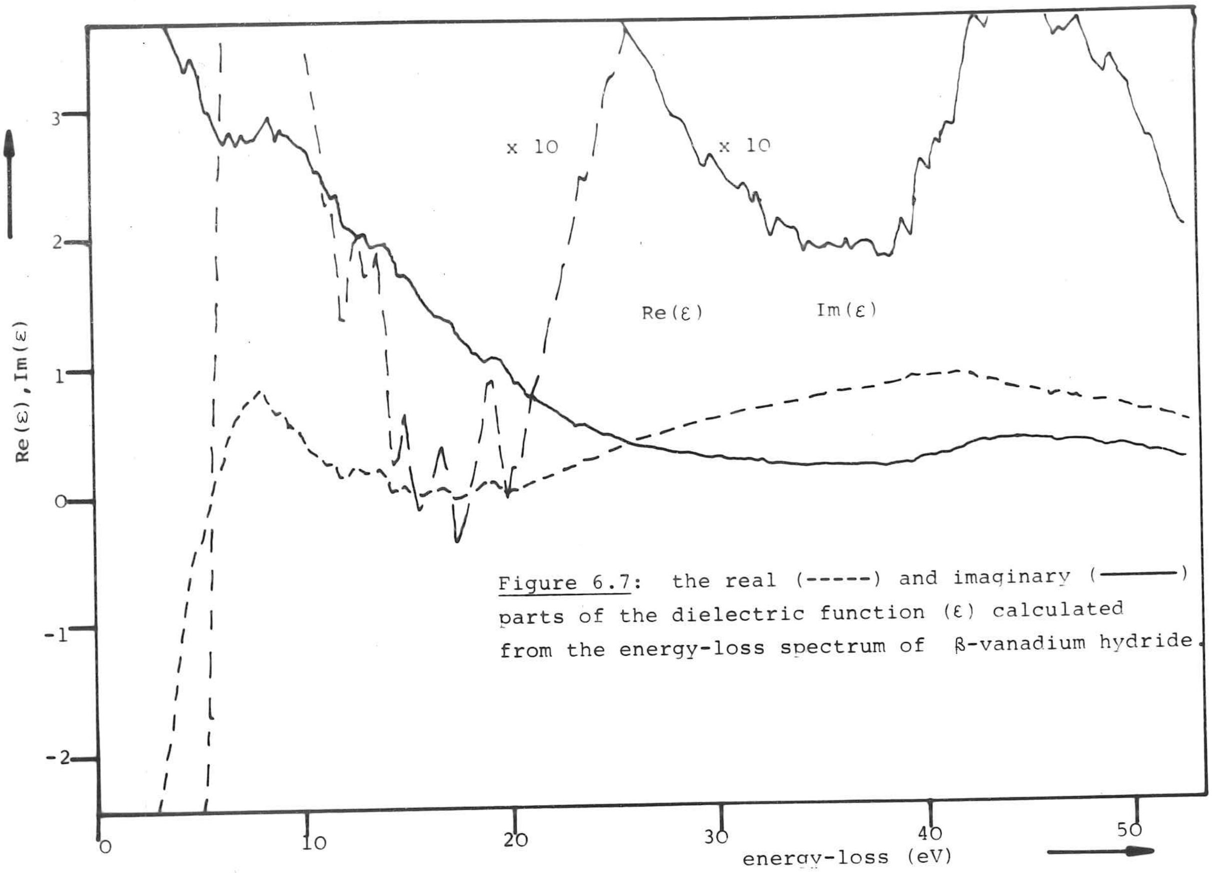

Figure 6.7: the real (-----) and imaginary (———) parts of the dielectric function (ε) calculated from the energy-loss spectrum of ß-vanadium hydride.

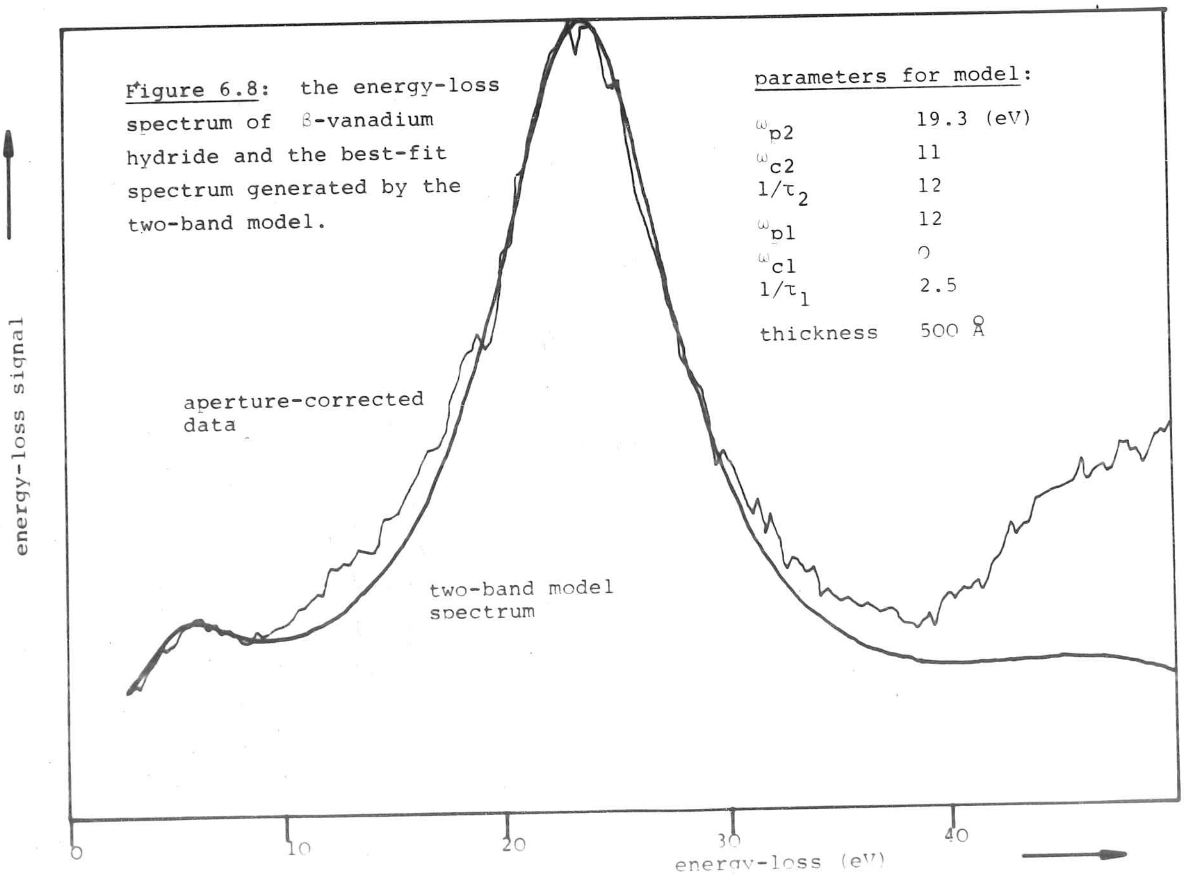

Figure 6.8: the energy-loss spectrum of β-vanadium hydride and the best-fit spectrum generated by the two-band model.

parameters for model:

ω_{p2}	19.3 (eV)
ω_{c2}	11
$1/\tau_2$	12
ω_{p1}	12
ω_{c1}	0
$1/\tau_1$	2.5
thickness	500 Å

The parameter-fitting procedure outlined in section 6.7.1 was applied to the vanadium-hydride spectrum. The synthesised spectrum assumes a foil thickness of approx 500 Å (as determined from the hydride spectrum). The comparison of synthesised and experimental spectra is shown in fig 6.8. The accuracy of the parameters determined as giving the best fit was found by varying each parameter in turn until there was a noticeable worsening of the agreement between the two spectra. The final values of the parameters are:

$\omega_{p2} = 19.3\ (\pm 0.5)$ eV
$\omega_{cv2} = 11\ (\pm 0.5)$ eV
$1/\tau_{v2} = 12\ (\pm 0.5)$ eV
$\omega_{p1} = 12\ (\pm 0.5)$ eV
$\omega_{cv1} = 0\ (+1.0)$ eV
$1/\tau_{v1} = 2.5\ (\pm 0.5)$ eV

It can be seen that the agreement is particularly good at the two plasmon peaks. The experimental spectrum shows extra intensity near 15 eV and 35 eV. The former may be explained by the presence of a surface oxide, which has a volume plasmon near 15 eV, or the presence of a surface plasmon. The latter may be due to the presence of an oxide which would have a delayed oxygen L_1 core-loss after 24 eV (Bearden and Burr 1967), or the thickness of the synthesised spectrum may underestimate that of the experimental spectrum. The vanadium M_{2-3} core-loss, from 40 eV upwards is not present in the synthesised data and explains the marked discrepancy from 40 eV upwards.

The application of equations 6.12,13 reveals that the upper band plasmon frequency (12 eV) corresponds to 1.6 electrons per atom. The lower band plasmon frequency (19.3 eV) corresponds to 4.2 electrons per atom. Thus, a simple two-band model for β vanadium-hydride may be constructed, and is shown in figure 6.9.

The following points should be noted:

1) This model gives ω_{c1} = 0 eV. Values of ω_{cp1} up to 1.0 eV caused little difference in the shape of the synthesised spectrum, so there might be a slight gap at the fermi level. The hydride is,

however, metallic in appearance, so this gap would have to be < 1 eV. The hydride is a good electrical conductor at room temperature, which indicates the absense of a significant gap (> few meV) at the fermi surface.

2) The relaxation times are different for the two bands.

3) the total number of electrons per vanadium atom is 1.6 + 4.2 which gives 5.8. The value expected from the hydride composition should lie in the range 5.45 to 5.7, employing the arguments set out above. Thus the figure of 5.8 electrons per vanadium atom is in closer agreement to the expected value than the value given by the simple plasmon model. The improvement is, however, slight.

4) The two-band model assumes that bands of finite width can be represented by an average position. Bell & Liang (1976) show that the position of a band may be determined from a weighted average of the positions of sub-bands within that band, and that the average band-gap can still be represented by a single frequency ω_T which is given by:

$$\omega_T^2 = \left(\frac{1}{n} \quad n_1\omega_{T_1}{}^2 + n_2\omega_{T_2}{}^2 + \ldots\right) \qquad - \quad 6.15$$

where: ω_{T_i} are the individual band gaps,

n_i are the numbers of electrons in the sub-bands and

$n = \sum_i n_i$ is the total number of electrons in the band.

Thus, although the low-energy band need not be very narrow, it may be regarded, for the purposes of obtaining the fit between the experimental and synthesised spectra, as narrow and thus described by its average position given by equation 6.15.

There is a lack of detailed theoretical calculation on vanadium hydride against which to test the experimentally-determined two-band model. The only calculations that the author is aware of are reproduced in fig 6.10. These are calculations of the density of states for b.c.c. vanadium and b.c.c. $VH_{1.0}$ (in which structure each vanadium atom is accompanied by a hydrogen atom at (0,0,a/2)).

Figure 6.9: a simple band-model for β-vanadium hydride.

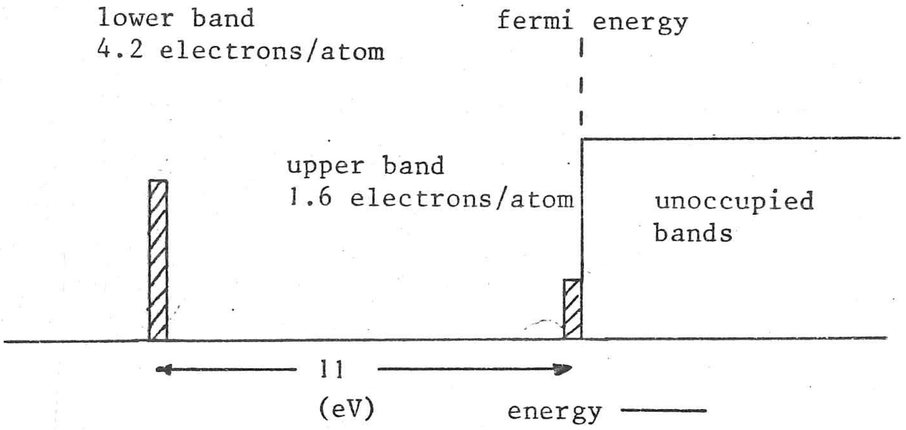

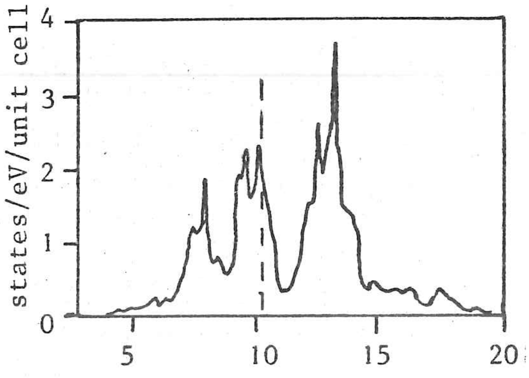

Figure 6.10a: the density of states for body-centered cubic vanadium.

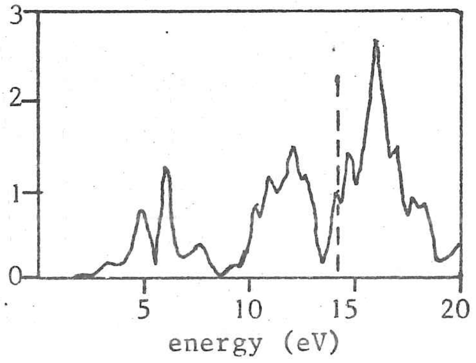

Figure 6.10b: the density of states for VH (from Switendick 1978).

It can be seen from fig 6.10 that one of the effects of hydrogen on the density of states is to separate the two main peaks (near 7 and 9 eV) below the fermi-level, which are broadly merged in the case of vanadium so that they are about 6 eV apart. The low-energy band is now about 8eV below the fermi level. The number of states in the upper and lower bands, measured manually from fig 6.10b are 3.7 and 2.05 electrons per vanadium atom respectively, giving a total of 5.75 states per vanadium atom.

Thus there is broad agreement between the band model given by a fit of the two-band model to the energy-loss data of vanadium hydride and the theoretical calculation for $VH_{1.0}$. The two agree that there is a large band-gap introduced by the presence of hydrogen, but disagree in the precise value of the band gap (by about 3 eV) and, more seriously, in the number of states in each band. They agree on the total number of electrons in both bands.

In order to proceed furthur, detailed calculations of the band-structure of β vanadium-hydride in the known composition range should be performed using the known β vanadium-hydride crystal structure.

6.9 THE ENERGY-LOSS RESULTS FOR NIOBIUM AND NIOBIUM HYDRIDE

The energy-loss spectra of niobium and vanadium and their two β-hydrides show remarkable similarity in the low-loss region of the energy-loss spectrum. Much of the discussion of section 6.8 for vanadium and vanadium hydride applies also to niobium and niobium hydride, so this section concentrates on the numerical analysis of the niobium and niobium hydride spectra without repeating the discussion of section 6.8.

The energy-loss spectrum of niobium, shown in fig 6.11a, shows the following features:

1) a zero-loss peak of width 2.5eV (FWHM);

2) a plasma excitation peak at 23.2 (±0.2) eV. The free-electron model for the plasma frequency gives a value for n, the number of electrons per niobium atom contributing to the plasmon of

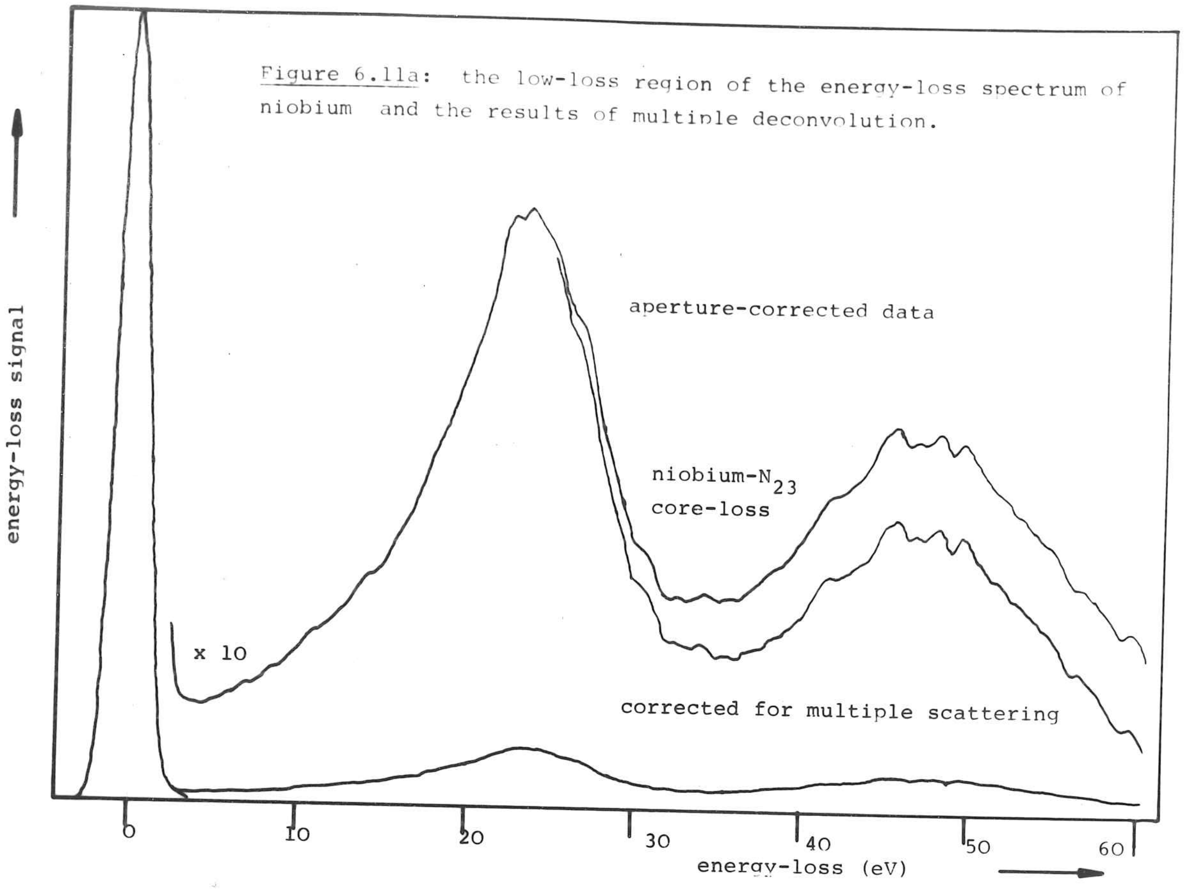

Figure 6.11a: the low-loss region of the energy-loss spectrum of niobium and the results of multiple deconvolution.

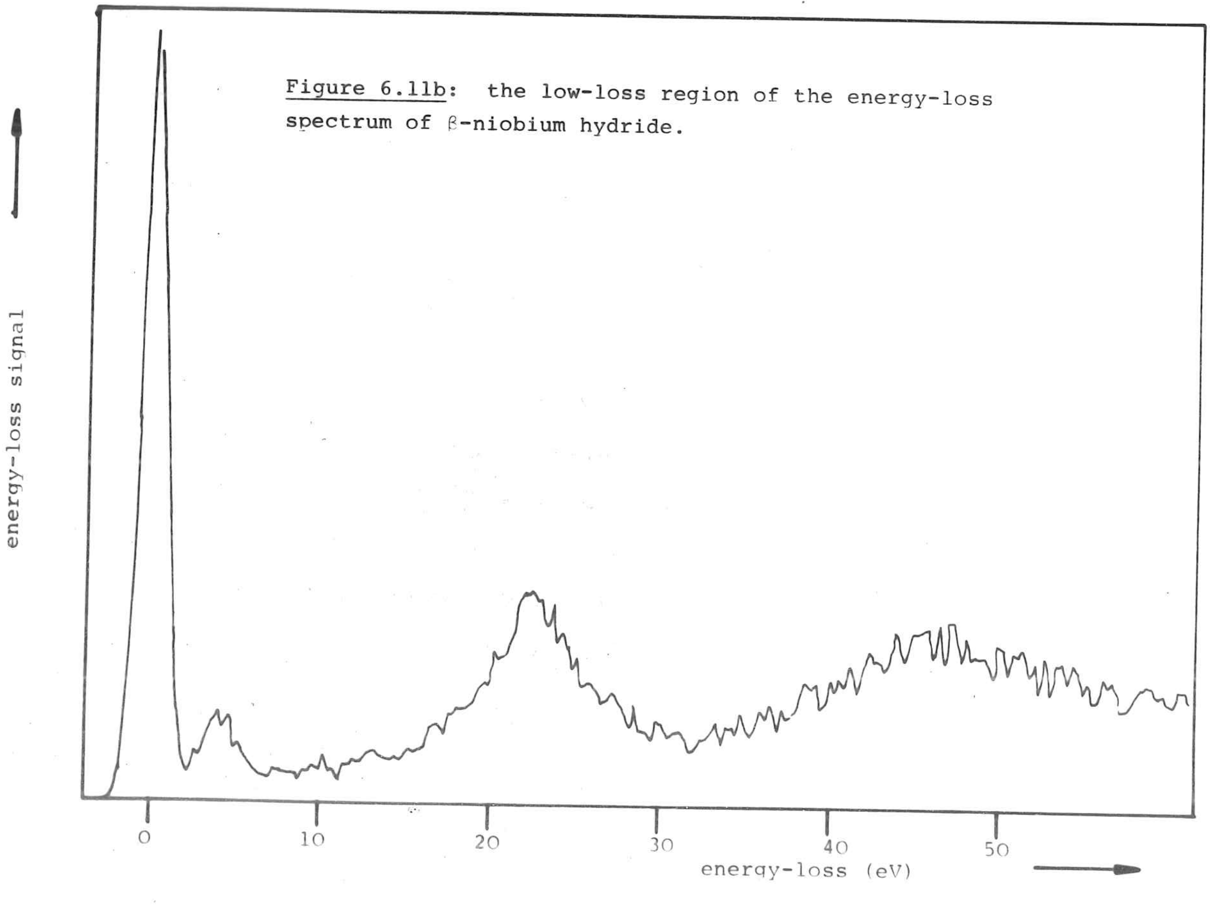

Figure 6.11b: the low-loss region of the energy-loss spectrum of β-niobium hydride.

$n = 7.06$.

The electronic configuration of niobium is:

$1s^2 2s^2 2p^6 3s^2 3p^6 3d^{10} 4s^2 4p^6 4d^4 5s^1$

which gives a value for the expected number of electrons free to contribute to the plasmon, $n = 5$.

3) A broad peak near 47 eV comprised of a double plasmon excitation and the niobium N_{2-3} single electron excitation. The results of the multiple deconvolution procedure applied to this spectrum (using the MULDEC program) are shown in fig 6.11a. Some of the intensity in this region is due to double plasmon excitation, but most is due to the niobium core-loss. The edge can be seen to start near 34 eV, which is the atomic N_{2-3} binding energy.

The energy-loss spectrum of β niobium hydride is shown in fig 6.11b. The following features can be seen:

1) a zero-loss peak;
2) an extra peak near 4.2 eV;
3) a plasma excitation peaked at 22.3 eV;
4) a broad peak near 47 eV starting near 34 eV. The discussion of this peak is not modified by the presence of hydrogen.

The volume plasma excitation is shifted downwards by about 0.9 eV. The b.c.c. niobium lattice changes to the b.c.t. β niobium hydride in the composition range $NbH_{0.7}$ to $NbH_{1.05}$ at room temperature (Schober _at al_ 1973, Schober 1975b) upon the addition of hydrogen and undergoes a unit cell volume expansion of ≃12%.
The number of electrons contributing to the volume plasmon at 22.3 eV, given by equation 6.14 is now

$n = 7.3$ electrons / niobium atom.

This shows an increase of 0.24 electrons per niobium atom upon the addition of hydrogen, whereas the composition range of the β - hydride would indicate an increase of between 0.7 and 1.05 electrons per niobium atom. The agreement between simple plasmon theory and practise is not as good, in this case, as in the case of vanadium and vanadium hydride.

The extra peak at 4.2 eV is correlated with the presence of hydrogen in the foil.

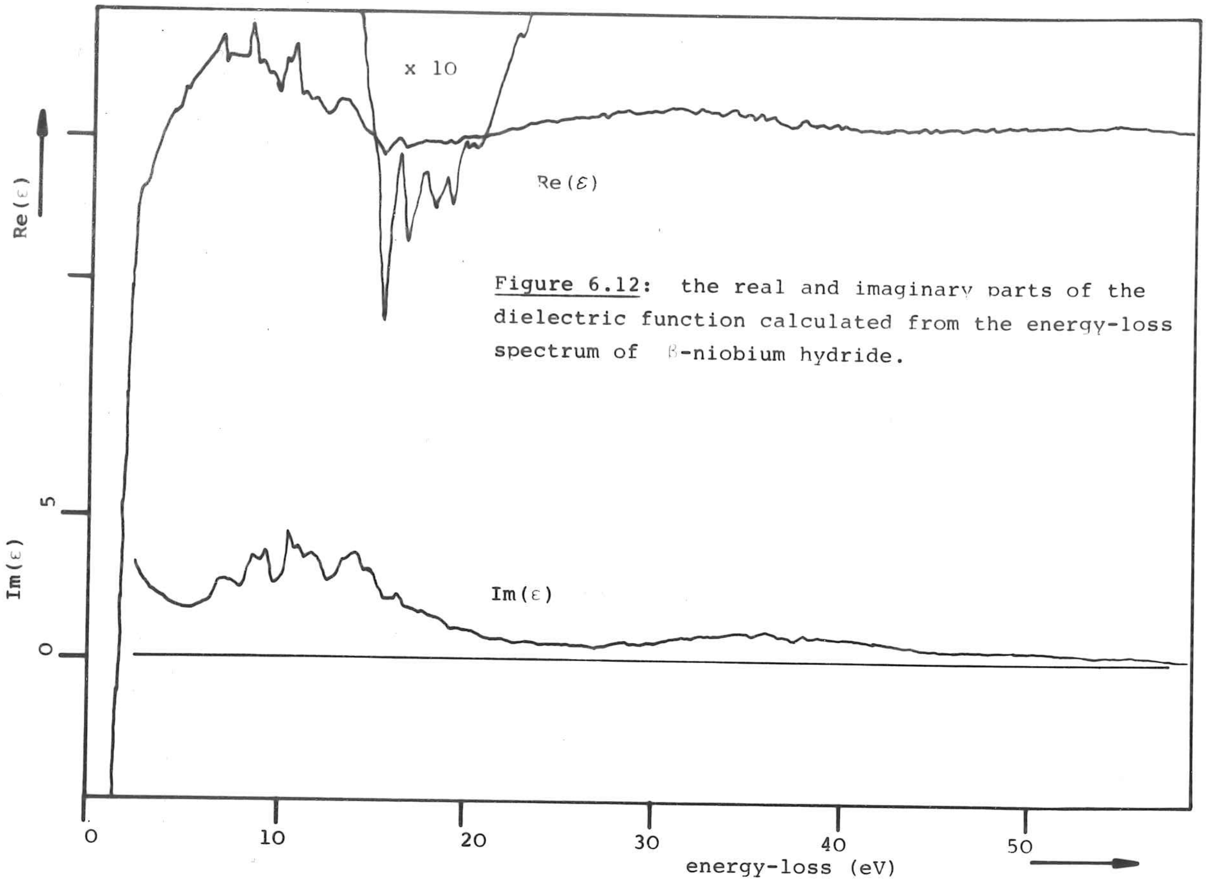

Figure 6.12: the real and imaginary parts of the dielectric function calculated from the energy-loss spectrum of β-niobium hydride.

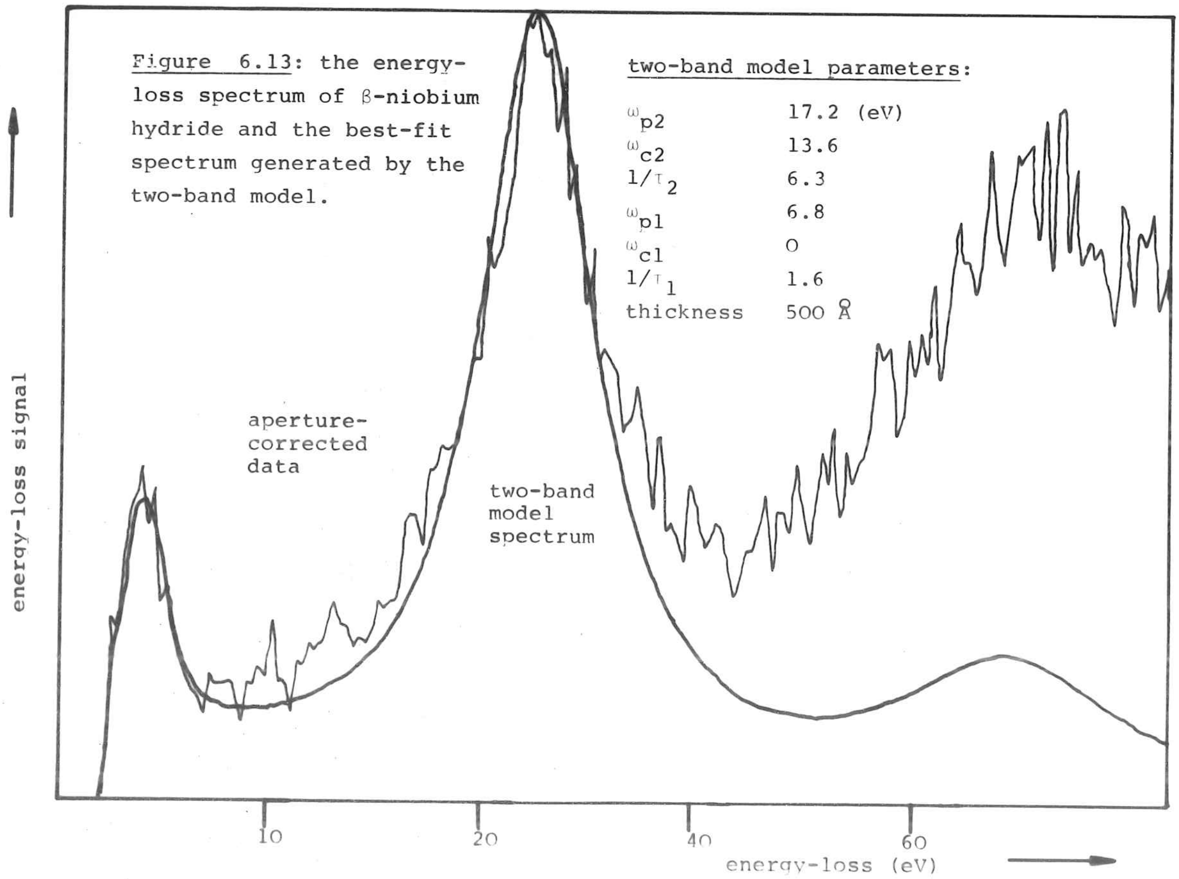

Figure 6.13: the energy-loss spectrum of β-niobium hydride and the best-fit spectrum generated by the two-band model.

two-band model parameters:

ω_{p2}	17.2 (eV)
ω_{c2}	13.6
$1/\tau_2$	6.3
ω_{p1}	6.8
ω_{c1}	0
$1/\tau_1$	1.6
thickness	500 Å

The dielectric function $\varepsilon(\omega)$ was calculated from these energy-loss results (using the DENSITY program) and the results are given in fig 6.12. The conditions for plasma resonance (i.e. $\varepsilon_1(\omega) = 0$,(incr.) and $\varepsilon_2(\omega)$ is decreasing) are both satisfied near 4 and 21 eV, thus the two peaks int the energy-loss spectrum near these two energy-losses may be attributed to plasmon excitations.

The two-band model was used to synthesise energy-loss spectra corresponding to a specimen thickness of 500 Å, and the two-band model parameters were adjusted to obtain the best fit between experiment and the synthesised spectrum, as described in section 6.7. The two spectra are presented together for ease of comparison in fig 6.13. The discussion of the differences between the two spectra is the same as for the case of vanadium (see section 6.7). The model spectrum agrees with the experimental spectrum very well at the two plasmon peaks.

The values of the two-band model parameters given by the best fit are:

ω_{p2} = 17.2 (±0.5) eV
ω_{c2} = 13.6 (±0.5) eV
$1/\tau_2$ = 6.3 (±0.5) eV
ω_{p1} = 6.8 (±0.5) eV
ω_{c1} = 0.0 (+1.0) eV
$1/\tau_1$ = 1.6 (±0.25)eV

The uppermost band (v_1) corresponds to 0.7 electrons per niobium atom, and the lower band corresponds to 4.3 electrons / Nb-atom, determined using equations 6.12 and 6.13. The total is 5.0 electrons per niobium atom. Thus, as in the case of vanadium, a simple density of states diagram may be drawn (fig 6.14).

There is no calculation of Niobium hydride density of states known to the author. The similarity between the physical and chemical properties of niobium and vanadium and their hydrides would suggest that a density of states calculation for niobium hydride would show the same introduction of a band-gap as in the case of $VH_{1.0}$

Figure 6.14: a simple band-model for β-niobium hydride.

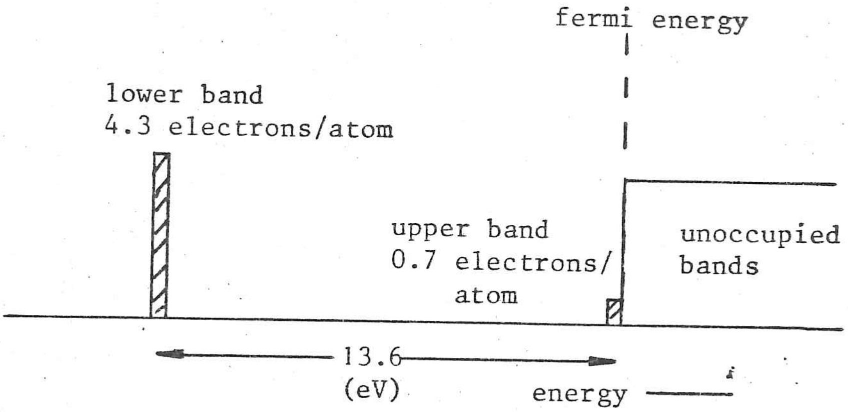

given above.

It has been shown that energy-loss spectra of the β-hydrides of niobium and vanadium can be described adequately by the two-band model, which is physically reasonable, subject to the approximations made in assuming just two valence bands and no core polarisability.

Appendix A - Energy-loss programs at Cambridge

APPENDIX A - Energy-Loss Programs at Cambridge

This appendix describes the commands available at Cambridge which implement the theory of Chapters 2 and 3.

A1.1 FILES

Energy-Loss spectra are entered into the package of programs for analysing Energy-Loss data (hereafter called the "system") as a table of numbers giving the contents of the individual channels comprising the spectrum. This data is first processed using the NDATA command to a format that is acceptable to the other fortran-written programs. Various checks are made and corrections to the zero-loss peak for count-rate error and to the whole spectrum for aperture collection efficiency are performed if desired. The data is now called a spectrum and is referred to by a spectrum name.

Spectra are stored on disc-file in a partitioned dataset which is called a spectrum-file and is called by a spectrum-file-name. A spectrum with name, for example, CARBON and spectrum-file-name .SPEC is stored in the disc files .SPEC:CARBON and .SPEC:PCARBON. The former contains the channel contents and the latter contains parameters which descibe the energy scale, the number of channels and also keep a record of operations performed on the original data.

The details may seems somewhat tedious, but the user does not have to be aware of this file-structure unless he wants to edit the data manually (for example to change the energy scale). The use of the above technique is that a spectrum is referred to by a single name (e.g. "CARBON") and is contained in a spectum-file which may, for example, contain a day's results. The spectrum-file-name need only by quoted once in any one console session.

The fileowner MP99 contains the energy-loss programs.
MP99.A contains short command sequencies,
MP99.B contains the main command sequencies,
MP99.C contains the fortran program source,
MP99.L contains compiled command macro libraries,
MP99.LIB contains the compiled fortran programs.

The system fileowner INFO contains specifications of Cambridge commands. The reader is referred to the User's Reference Manual (published by the Computing Service) for a complete description of the local operating environment.

A1.2 COMMANDS AND LIBRARIES

The energy-loss package is made available to a console session by typing:

```
C MP99.A:INIT
```

which then initialises the system, making available the command libraries.
The action of a command such as "PLOT CARBON" is to scan the command libraries declared above for a definition of the expansion of the command called "PLOT". The macro expansion will default values for parameters that have not been given in the command line, producing something like:

```
  C MP99.B:RUNLIB PROG=PLOTN COMM=PLOT OPT=01 MEM=CARBON.
```

Exactly the same results may be obtained by typing this command line directly, but the use of a macro library allows mnemonic commands to be defined and saves typing!

The command sequencies are written in a language called PHOENIX. Their responsibility is to prepare data and the environment that is necessary for the fortran programs. They also provide a measure of error detection (for example in the use of non-existing data) and correction. They are the interface between the user and the fortran programs.

A .3 OFFLINE AND ONLINE EXECUTION

The system is designed to be used online, although the capability exists to run many of the programs offline (by including "RUN=OFFLINE" in the command line - see section A1.6.2).
The programs run online produce results directly on the terminal. Those that run offline enter a queue and their execution may be delayed during busy times of the day. The execution time of offline jobs depends on the number of jobs in the queue and on the user's project status (see User's Reference Manual under "scheduling").

A .4 GRAPHICAL OUTPUT

All of the fortran programs produce graphical output. This may be "drawn" on a graphics terminal or/and sent to the plotter at the West Cambridge outstation. The graphical output of a program is stored on a disc file and may be viewed on a graphics terminal under the control of the command sequence when online. An offline job produces the same disc file for graphical output, but may be forced to produce direct plotter output by using the "DIRECT" command; for example:

```
  DIRECT
 PLOT CARBON RUN=OFFLINE
 PLOT IRON
 PLOT CHROME RUN=OFFLINE
 UNDIRECT
 PLOT STEEL RUN=OFFLINE
```

will submit jobs to plot spectra CARBON,CHROME and STEEL offline. The output for CARBON and CHROME will be sent directly to the plotter. The spectrum IRON is plotted interactively and may be viewed on the terminal or sent to the plotter. The graphical output of the spectrum STEEL may be viewed on the terminal after the job has run by typing "VP STEEL" and/or sent to the plotter by typing "P STEEL". These commands are explained in section A1.7.3.

A .5 THE RUNLIB COMMAND SEQUENCE

RUNLIB is the command sequence that is invoked by most of the fortran program commands.

A .5.1 Input files

a) The input spectrum is found either in disc files sf:name and sf:Pname, where "sf" is the spectrum-file-name and "name" is the spectrum-name or, if a source spectrum name is not quoted, in the disc files &DATA and &PARS.

b) An executable load-module may be provided in the disc files &module-name:MAIN or .LOAD.module-name:MAIN depending on the state of the KEEP switch (see the KEEP command). If the load-module is not provided, it will be generated by the command sequence and kept for subsequent calls to the same fortran program.

c) Some programs which requires a large number of parameters to be entered request that an "input file" be typed at the terminal. The command sequence shows how the numbers should be typed and reminds the user of the file termination marker (a /* beginning in column one). Jobs that require "input" files cannot be run offline.

d) The command sequence tests various parameters, and may require others to be set up in response to a prompt. A table of possible prompts and valid responses is given in Fig. A1.1.

A .5.2 Output files

a) Graphical output is sent to the disc file .PLOT.name (where "name" is the name of the source spectrum) or .PLOT.TEMP in the case of temporary source spectra. This file is usually deleted at the end of the command sequence unless specifically requested to be kept in response to a prompt (see Fig A1.1).

b) Some results are sent direct to the terminal (or line-printer if running offline). These are always duplicated on the graphical output.

c) The command sequence always leaves an executable load-module for the current module-name so that the next time a command with the same module-name is quoted, the command sequence will not have to link-edit an executable load-module, saving some time at the terminal.

d) If the program creates a spectrum as output (e.g. RAMP but not PLOT) and if the command line entered contained a destination name (e.g. RAMP S1 TO S2), the spectrum of that name is created in the spectrum-file and the index (in spectrum-file-name:INDEX) is updated. If spectrum output is produced, but no destination spectrum is named, spectrum output goes to the temporary spectrum dataset (disc files &DATA and &PARS) and a message indicating this is displayed on the console. The index is not updated, but a record of the last spectrum name that produced the data in the temporary spectrum file is kept, and, if the temporary spectrum is then used as a source spectrum, the last source spectrum name which was used to create the temporary spectrum file is quoted (in parenthesis) on graphical output. This enables the user to remain aware of the original source spectrum, even after several processes have modified it via the temporary spectrum file.

Figure A1.1 RUNLIB command sequence prompts

	CONDITION	PROMPT	VALID RESPONSES	ACTION
1)	the program requires INPUT data and an INPUT file already exists	OLD INPUT DATA ?	Y(ES) anything else	No new input file is entered. The program requests an INPUT file to be entered.
2)	no spectrum-file is set and source spectrum is not the temporary spectrum	SPECTRUM FILENAME ?	a valid spectrum filename	sets up spectrum-file-name for rest of the session
3)	source spectrum is the temporary spectrum	PLOT NAME ?	any name (e.g. CARBON)	plot dataset is set to .PLOT.name
4)	the program is running online	VIEW ?	Y(ES) B P 2	draws graphical output on terminal; as above, but only red & green pens; submits job to send to the plotter; both P and B.
5)	answer to 4) was P or 2	TITLE ?	a title line for the plotter job (< 17 chars)	appears on plotter output
6)	same as 5)	KEEP ?	Y(ES) any other	no action plot dataset deleted after being plotted
7)	answer to 4) was not P or 2 and job not offline	KEEP PLOT DATASET ?	Y(ES) any other	no action plot dataset is deleted immeadiately

A1.6 FORTRAN PROGRAM COMMAND SUMMARY

A1.6.1 Command syntax

1) Upper-case letters are typed as shown.
2) Lower-case words should be replaced with an appropriate value:

name: a word starting with a letters containing only alphanumerics;
integer: an integer (e.g. 1435);
nn: a two-digit integer (e.g. 21, 20, 03, 99);
real: a real number (e.g. 12, 12.1, .01);
dsname: a valid dataset name (e.g. .INPUT, .MY.SPEC).

3) A vertical list of words enclosed in braces $\{\ \}$ means that one of the words shown must be chosen: e.g. $\left\{\begin{array}{l}\text{MOD}\\ \text{EDGE}\\ \text{ALL}\end{array}\right\}$.

4) An item enclosed in square brackets [ ] is optional: e.g. [RUN=OFFLINE] .

5) A module-name (if given) is the member-name of the fortran main program in both MP99.LIB and MP99.C. If the module-name is not given, it is the same as the command name.

6) a single-digit post-fix is used to distinguish between multiple occurrences of the same type: e.g. in RAMP name1 TO=name2, name1 and name2 are both names (as defined in 2) above) which may be the same or different.

A1.6.2 Default values

1) Parts of the command that are optional and are not typed as part of a particular command line are given their default values.

2) The default for a missing spectrum name is the temporary spectrum dataset.

3) If a module-name is not given, it is the same as the command-name.

4) All the following fortran program commands (except those which require an INPUT file) may be forced to execute offline by appending the phrase "RUN=OFFLINE" to the command line. The default action is to execute online.

A1.6.3 Fortran program command list

■ APCOR [[FROM=]name1] [[TO=]name2] $\left\{\begin{array}{l}\text{ANGLE}\\ \text{ALPHA}\end{array}\right\}$=real1

Input:

1) "name1" - an energy-loss spectrum to be aperture corrected

2) "real1" - the probe semi-angle of convergence (or the collector semi-angle if larger).

Output:

1) plot dataset - a log-linear plot of the input and output spectra.

2) "name2" - the input energy-loss spectrum divided by the aperture efficiency function.

```
■ COMPARE   [[FROM=]name1]          {WITH} = name2
                                    {AND }
```

Input:

two energy-loss spectra "name1" and "name2" which need not have the same energy scale or vertical scale.

Output:

Plot dataset - a linear plot of both "name1" and "name2" on their correct energy scales and scaled vertically so that the peak heights match.

Module-name: PCOMP

```
■ {DECONV}      [[FROM=]name1]      {WITH} = name2    [[TO=]name3]  [RES=real1]
  {DEC   }                          {AND }
```

Input:

1) "name1" - an energy-loss spectrum of an edge with the background removed (using RAMP EDGE);
2) "name2" - an energy-loss spectrum of the low-loss region which need not have the same energy scale but should have a correct zero-loss peak and be corrected for aperture collection efficiency (using the APCOR) program;
3) "real1" - the width (FWHM) of the reconvoluting gaussian (defaults to 2.0 volts).

Action:

DECONV deconvolutes an edge-loss spectrum with a low-loss spectrum and then reconvolutes the resulting deconvolute with a gaussian to decrease the visible noise.

Output:

1) "name3" - the output spectrum;
2) plot dataset - a linear plot of the low-loss region on page 1 and linear plots of the edge spectrum "name1" and the output spectrum "name3" on page 2.

Module-name: NDEC

```
■ DENSITY   [[FROM=] name1]
```

Input:

"name1" - an energy-loss spectrum with an accurate zero-loss peak which has been corrected for aperture size and multiple scattering effects (using APCOR and MULDEC).

Action:

DENSITY evaluates Im($-1/\varepsilon$), the energy-loss function, from the input spectrum "name1". The absolute value is obtained by adjusting the scale such that Re($1/\varepsilon$) is zero at zero frequency. The two density functions n_{eff} and n (see section 3.3.4.1) are evaluated. The dielectric function $\varepsilon(\omega)= \varepsilon_1 + i\varepsilon_2$ is obtained by a Kramers-Kronig transformation. (see section 3.3.4).

Output:

plot dataset - a plot of the energy-loss function on page 1, a plot of the density functions on page 2 and a plot of the dielectric function on page 3 (or pages 3 and 4).

■ $\left\{\begin{matrix}\text{GENERATE}\\ \text{GEN}\end{matrix}\right\}$ [[TO=]name1]

Action:

GENERATE deos not use the command sequence RUNLIB, but has its own command sequence in MP99.B:GEN. GENERATE is used to generate energy-loss spectra using one of three models:

1) a twoband model (see section 6.71);
2) an n-band model (given by equation 2.59);
3) a hydrogenic edge with optional exelfs.

The generated single-scattering spectrum is then multiply-scattered, convolved with a gaussian zero-loss peak and noise is added if desired. The command sequence GEN prompts for many values to be set up (such as zero-loss width, energy scale, plasmon position etc...), the required response should be obvious from the prompt.
If an edge spectrum is being generated, the command sequence will ask for an input file which describes the exelfs to be added to the edge. A parameterised phase shift may be used by responding appropriately to the prompts.

Output:

1) "name1" - an energy-loss spectrum generated by the appropriate model which contains a zero-loss peak.

2) Plot dataset - a log-linear plot of the single-scattering spectrum on page 1, a linear plot of the dielectric function if the n-band model was used (on page 2) and a log-linear plot of the output spectrum on the next page.

Module-name: GEN

■ $\left\{\begin{matrix}\text{INTEGRATE}\\ \text{INT}\end{matrix}\right\}$ [[FROM=]name1] [PLASMON=real1,real2]

Input:

1) "name1" - an energy-loss spectrum containing at least one edge;
2) "real1" - the plasmon voltage
3) "real2" - the plasmon peak width (FWHM).
4) INTEGRATE asks for an input dataset to be entered, one line per edge, with the format:

lower-window-energy,upper-window-energy,safe-area-width,edge-energy

where:

lower-window-energy (defaults to lowest energy in the spectrum) and upper-window-energy (defaults to highest energy in the spectrum) define a window about an edge;
and the safe-area-width defines an area centered on the edge position that is not used in background fitting (the default value is 20 volts and should be increased for slowly-rising edges) and edge-energy defines the position of the edge.
If the edge energy is zero, then the program searches for an edge in the window defined above and then uses this value to position the safe-area.

Action:

For each edge, the window definition is read. If the edge voltage quoted is zero, automatic edge location is performed. The background is approximated by a power-law which is least-squares fitted in the window in front of the edge. The fitted background is then subtracted from the whole spectrum. A power-law is fitted to the remainder in the window after the edge and the power-law coefficient r (in $A.E^{-r}$) is saved for use later. When all the edges have been thus treated, the integral of the contribution due to each edge alone is evaluated over four window widths, and an estimate of the collection

efficiency of each window is made using the value of r for each edge determined above. The integrated signal inside each window and the window efficiency are displayed.
For the first edge only, if "real1" is non-zero, the background is evaluated using a Drude model for a free-electron-gas with plasmon energy "real1" (eV) and width (FWHM) "real2" (eV) and a least-squares fit in the window in front of the first edge.

Output:

plot dataset - each separate edge contribution is plotted on the same log-log plot. The positions of the extrema of each energy window used are marked with an arrow. The values of the window bounds, the integral inside the window and an estimate of the window efficiency are displayed for each edge as a table on page 2.

Module-name: NINT

■ $\left\{\begin{matrix}\text{MULDEC}\\ \text{DEC4}\end{matrix}\right\}$ [[FROM=]name1] [[TO=]name2] [SAFE=real1] [OPT=nn]

Input:

1) "name1" - an energy-loss spectrum including a zero-loss peak, which has been corrected for count-rate errors (if necessary) using ZERO and corrected for a finite aperture size using APCOR.
2) "real1" - the energy (above zero volts on the energy-scale) below which all signal is assumed to be due to the zero-loss peak. The default is 1.0 volts. This should be increased if the zero-loss peak is noisy and is not correctly removed.
3) "nn" - the number of orders of multiple-scattering removed. The residual multiple-scattering is of order (nn + 1). The default value is 5.

Action:

MULDEC performs a multiple deconvolution of the low-loss region "name1". The technique of section 3. is applied.

Output:

1) "name2" - the multiply-deconvolved input spectrum (i.e. an

approximation of the single-scattering spectrum.

2) plot dataset - the zero-loss peaks, original spectrum and deconvolved spectrum are plotted on a linear plot.

Module-name: DEC4

■ NDATA   [[TO=]name1]   [FROM=dsname]

Input:

1) "dsname" - a sequential dataset containing raw energy-loss data with the format:

```
title                      ( < 20 characters)
escan,offset               (two real values in free-format)
134578 128957 298990  189850  ...   (a table of integers giving
                 .                    successive channel
                 .                    contents in free-format)
                 .
 ... 18956 08746 00236 00000 00000
```

where:

title is a title that appears on plotter output and remains associated with the spectrum "name1"; escan is the energy scan in volts/channel for escan < 20. If escan > 20, escan is the value of the scan width (in volts) given on the HB5 analyser control front panel. A correct value of the scan width is determined from a table. Offset is the offset in volts of the zero-loss peak position from the middle of the energy scan towards the left (i.e. lower energy-losses).

2) The command sequence prompts to see whether the offset value is measured from the analyser panel (in which case a correction is applied) or from the drift-tube voltage. This is only done once at the start of a session, and remains in force for the rest of the console session.

3) The command sequence prompts for values of the zero peak height to plasmon peak height ratio and probe semi-angle of convergence. If non-zero values are given in response to the prompt, the NDATA program will apply the relevant correction.

Action:

The program reads the title, escan and offset. If escan is greater than 20 volts, the correct table value of the energy scan width is found from a table. The channel count number is used to find the nearest table value of channel counts which is correct for the HB5 timebase control. This number is only used to provide a value for the energy scan in volts per channel if a table value of the energy scan has been used.

If the zero-loss peak should be on the spectrum, it is searched for and used to define the zero of the energy scale. The low-loss peak may then be corrected for count-rate errors by supplying the value of the ratio of zero-loss to plasmon-loss peak heights, measured from an analogue scan, in response to a prompt. The spectrum may be corrected for finite aperture size by supplying an aperture semi-angle in response to a prompt.

The program searches the data for corruptions introduced in the transfer of data from the LINK computer to the IBM 370 computer (a corruption can be detected by comparings its value with that predicted by its neighbors) and attempts to repair these by linear interpolation and a warning message is issued. Adjacent corruptions are not repaired and another warning message is issued.

Output:

1) "name1" - an energy-loss spectrum;
2) plot dataset - a linear plot of the unprocessed data and the output data.

■ PATCH [[FROM=]name1] [[TO=]name2]

Input:

1) "name1" - an energy-loss spectrum containing a major edge (which it is intended to analyse later for exelfs) which has a minor edge following the major edge (which would make the extraction of exelfs data impossible);
2) an INPUT dataset describing one or more minor edges with the same format as used in NDATA (q.v.) with the exception that the edge voltage must be given explicitly (i.e. no automatic minor edge location).

Action:

For each minor edge in the INPUT dataset, PATCH fits a power law inside the windows before and after the minor edge position. The data to the right of the minor edge position are all divided by a constant that brings the two fitted power-laws into line at the minor edge position. The region in the "safe-area" is replaced by a power-law. The effect is thus to remove an edge from the input spectrum. An error message is issued if the minor edge is too large (i.e. the constant divisor is greater than 1.5).

Output:

1) "name2" - the patched energy-loss spectrum;

2) plot dataset - log-log plots of the spectrum both before and after being patched.

■ PLOT [[FROM=]name1]
■ PLOTL
■ PLOTLL
■ PLOTL

Input:

"name1" - an energy-loss spectrum.

Output: (to plot dataset)

for PLOT: a linear-linear plot of the input data
for PLOTL: a log-linear "
for PLOTLL: a log-log "
for PLOTA: all of the above three plots on successive pages.
Module-name: PLOTN

■ RAMP [[FROM=]name1] [[TO=]name2] $\left[\left\{ \begin{array}{l} \text{EDGE} \\ \text{SIMPLE} \\ \text{MOD} \\ \text{EXTRACT} \\ \text{ALL} \\ \text{BOTH} \end{array} \right\} \right]$

Input:

1) "name1" - an energy-loss spectrum containing at least one edge;

2) an INPUT file describing one edge with the same format as in NDATA (q.v.);

3) one of the list EDGE,SIMPLE,MOD,EXTRACT,BOTH or ALL may be typed in the command line.

Action:

1) With EDGE or SIMPLE typed, the program fits a power-law before the edge and subtracts this from the data. The spectrum is then left-shifted so that the edge occurs at the left of the spectrum. The edge position is either quoted in the INPUT dataset, or, if its value is not given, automatic edge location is performed.

2) With MOD or EXTRACT typed, "name1" is expected to be an edge with the background removed. The modulations $\chi(E)$ are extracted from the edge by the method of section 3.

3) With ALL, BOTH or no options typed, both of the above steps are performed.

Output:

1) "name2" - an energy-loss spectrum of an edge or the modulations $\chi(E)$ as relevant.

Module-name: NRAMP

■ **SAMPLE** [[FROM=]name1] [[TO=]name2] RATIO=real

Input:

1) "name1" - an arbitary spectrum;

2) "real1" - a real value (> 1) describing the ratio of the number of data points in the input spectrum to that of the output spectrum.

Action:

SAMPLE reduces the number of data points in a spectrum. This is useful if the spectrum consists of many data points (> 500) as it reduces the computing time required to perform subsequent operations on the spectrum (important for the programs TRANS and DENSITY).

Output:

1) "name2" - the input spectrum sampled at a reduced number of points;

2) plot dataset - a linear plot of both the input and output spectra.

■ SMOOTH [[FROM=]name1] [[TO=]name2] [OPTR=real1]

Input:

1) "name1" - an arbitary spectrum
2) "real1" - the standard deviation (in channels) of the gaussian used to convolve "name1".

Action:

SMOOTH performs a convolution of the input spectrum with a gaussian of standard deviation "real1" channels. It is used to reduce the noise in the input spectrum at the expense of resolution.

Output:

plot dataset - a linear plot of the input and output spectra.

■ STEP [[FROM=]name1]

Input:

1) "name1" - an energy- loss spectrum containing at least one edge;
2) an INPUT dataset with the same format as that of INTEGRATE (q.v.) describing the edge(s) to be analysed.

Action:

STEP fits a power-law to the spectrum in the two windows below and above each edge. These power-law approximations are then used to evaluate the contribution to the input spectrum from each edge, yielding an estimate of the total (integrated) signal due to that edge alone. Step height analysis is only accurate for sharp (hydrogenic) edges and tends to overestimate the signal for delayed (high angular momentum) edges. STEP is used to obtain rough answers when the edge is very weak, the input spectrum is very noisy or the background is highly curved.

Output:

1) plot dataset - a log-log plot of the input spectrum together with the power-law approximations inside the windows used for each edge. Window extrema are arrowed.

2) The values of the window bounds, edge voltage, power-law slope r (before and after the edge) and estimated integral intensity are written, for each edge, to the terminal and the plot dataset.

■ THICK [[FROM=]name1] [SAFE=real1]

Input:

1) "name1" - an energy-loss spectrum with correct zero peak and which has been aperture corrected (if necessary) using APCOR.

2) "real1" - the energy (in eV) below which all the signal in the input spectrum is assumed to be due to the zero-loss peak. The default value (1.0 volts) will always work for spectra that have been zero-corrected (using ZERO). This value may have to be increased if the zero peak is very noisy (an unusual occurrence).

Action:

The THICK program evaluates the signal due to the zero-loss peak and the first plasmon loss. The plasmon mean free path is calculated (using equation 2.   ) and the estimated thickness of the foil is evaluated. Note that the plasmon area is usually overestimated because of single-particle excitations, so the estimated thickness is usually too great (≃ 10% error).

Output:

1) plot dataset - a linear plot of the zero-loss peak, plasmon-loss peak and the remainder of the input spectrum;

2) The values of the peak height ratio and area ratio of the zero-loss and plasmon-loss peaks, the plasmon mean-free-path and the estimated thickness are written to the plot dataset.

■ $\left\{\begin{matrix}\text{TRANS}\\\text{TRANSF}\end{matrix}\right\}$ [[FROM=]name1] [OPTR=real1,real2,real3,real4]

Input:

1) "name1" - the modulations $\chi(E)$ produced by the RAMP program.

2) "real1" - a left window position, in electron-volts above the edge position. The right window position is the highest energy on the input spectrum. Input data outside this window are ignored.

The default value is 0. volts.

3) "real2" - the value of the power of the wave-vector (k) which is used to approximate for the A(k)/k term in equation . The modulations $\chi(k)$ are multiplied by $|k|^n$. The default value (n=2) effectively underestimates n, producing an effective scaling of 1/k in the final $\chi(k)$. This is done to help attenuate the effect of noise in the modulations at high k. (see section

4) "real3" - if this value is non-zero, the modulations $\chi(k)$ are not multiplied by a gaussian. The default is zero. The absence of the gaussian multiplier will increase both resolution and noise in the resulting modulus of the fourier transform of $\chi(k)$ (the "rdf").

5) "real4" - the number of channels over which both the extreme left and right windows are switched on. This is an edge-smoothness parameter. The default value is 80 channels (out of a total of 800 channels). Lower values of "real4" will increase both the resolution in the "rdf" and the sharpness of the spurious side-lobes due to window termination effects.

Note that "real1" is the only value usually quoted, then the rest of the line is omitted. For example: TRANS CARBON OPTR=25.

Action:

The program TRANS transforms $\chi(E)$ to $\chi(k)$, windowed at the lower window "real1", the window being of edge smoothness "real4" channels. $\chi(k)$ is then multiplied by a gaussian and by $|k|^n$ where n = "real2". The fourier transform of $\chi(k)$ and the modulus of the fourier transform are evaluated.

Output:

plot dataset - a linear plot of the final $\chi(k)$ used on page 1 and a linear plot of the modulus of the fourier transform of $\chi(k)$ on page 2.

Module-name: TRANS

■ $\left\{\begin{array}{l}\text{ZERO}\\ \text{ZC}\end{array}\right\}$ [[FROM=]name1] [[TO=]name2] RATIO=real1

Input:

1) "name1" - an energy-loss spectrum including a zero-loss peak which has not been corrected for aperture efficiency effects.
2) "real1" - a real number giving the ratio of zero-loss peak height to the plasmon-loss peak height as measured from an analogue scan.

Action:

The zero-loss peak is extracted, the wings of the zero-loss peak with height less than the plasmon peak height are taken to be undistorted. A gaussian of height given by "real1" times the plasmon peak height is fitted to these wings and replaces the original zero-loss peak.

Note: 1) this technique requires that the plasmon peak be undistorted (i.e. count-rate corrections are negligable at the plasmon peak); 2) for the ratio of areas to remain correct, the correct zero peak should be approximately gaussian in shape between the "wings" (as defined above). If the shape of the true zero-loss peak is "square" (i.e. the slits are opened too wide), the area of the fitted peak will be an underestimate.

Output:

1) plot dataset - a linear plot of the data showing both the old and the new zero peaks;
2) "name2" - an energy-loss spectrum with a corrected zero-loss peak.

Module-name: ZC

A1.7 UTILITY PROGRAM COMMANDS

The above commands process energy-loss data, producing graphical output. The following commands are connected with data file manipulation, load-module manipulation, graphical output, editing source files and using magnetic tape.

A1.7.1 Data manipulation and display commands

- $\left\{\begin{array}{l}\text{CMPRS}\\ \text{CMPS}\end{array}\right\}$

  Action:

  CMPRS compresses the spectrum file, eliminating any "dead-space" present (and therefore yielding the minimum-possible disc storage requirement). CMPRS should only become necessary if spectra are over-written on a permanent spectrum-file (i.e. written to more than once).

- DATA $\left[\ \left\{\begin{array}{l}\text{name1}\\ \text{TO=name2}\end{array}\right\}\ \right]$

  Action:

  With "name1" quoted: DATA files spectrum "name1" to the temporary spectrum dataset. With "TO=name2" quoted: DATA files the temporary spectrum dataset to the spectrum "name2".

  If the spectrum-file is not set up, DATA types out the names of the current permanent spectrum-files in the user's filespace and then prompts for a spectrum-file-name to be given.

- DS name1

  Action:

  DS (delete spectrum) deletes the spectrum "name1" and then compresses the spectrum-file.

- EDS name1

  Action:

  EDS (edit spectrum) invokes the text editor ZED (for details see INFO.SPEC.ZED) to edit the member "name1". For example, to change the position of the zero on the energy scale of spectrum FRED, the following might be typed:

```
EDS PFRED               (edit the parameters of FRED)
M2                      (move to line 2)
E/10/12/                (exchange 10 for 12)
W                       (windup - finish edit)
```

- ■ EXS

Action:

EXS (examine spectrum-file) examines the spectrum-file and gives information on the disc space taken up (see INFO.SPEC.EXAMINE).

- ■ INDEX

Action:

INDEX types the index of the current spectrum-file (see PRTINDEX).

- ■ NOTE

Action:

NOTE is used to add notes to the index of the current spectrum-file. The user types in a message, terminated with /* (beginning in column 1), which is then added to the top of the index.

- ■ $\left\{\begin{array}{l}\text{PRTINDEX}\\ \text{PI}\end{array}\right\}$

Action:

PRTINDEX (Print index) submits a job to print the index of the current spectrum-file on the line-printer at the West-Cambridge outstation.

A1.7.2 Load-module manipulation commands

- ■ DL name

Action:

DL (delete load-module) deletes the load-module associated with module-name "name".

- ■ KEEP/UNKEEP name

Action:

KEEP will first check to see if the load-modules are kept on a temporary disc file or a permanent (catalogued) disc file. In the former case, a parameter is set which remains in force for the rest of the console session (unless unset by typing UNKEEP) which directs subsequent load-modules to be kept on permanent disc files.
If a name was quoted, the load-module "name" (assumed to be on a temporary file) is catalogued and becomes a permanent file.
The KEEP switch is also set by the LINK command (see below).

■ LINK name

Action:

LINK submits a job to link-edit the module "name". Note that "name" is a module-name and not a command name. The KEEP switch is set.

A1.7.3 Graphics control commands

The fortran programs all produce graphical output. The plot dataset is called after the source spectrum ("name1") and is kept in the file .PLOT.name1.

■ DP name

Action:

DP (delete plot) deletes the plot dataset associated with spectrum "name".

■ P name

Action:

P (send to Plotter) submits a job to file the plot dataset associated with spectrum "name" to the plotter. The command sequence prompts for a title (which appears at the head and foot of the plotter output) to be supplied and asks whether the plot dataset is to be kept after having been plotted. Unless the reply to the last prompt is Y(ES), the plot dataset is deleted at the end of the job.

■ VB name

Action:

VB (view brief) invokes the VIEW command (see INFO.SPEC.VIEW for details) to produce graphical output on a graphics terminal. The plot dataset associated with spectrum "name" is VIEWed. Only lines that would appear red or green on the plotter are drawn.

■ VP name

Action:

VP (view plot) behaves as above except all lines are drawn.

A1.7.4 Fortran program manipulation commands

- COMP name

  Action:

  COMP (compile) compiles the module called "name". If an executable load-module exists with this module-name, that load-module is deleted. COMP must be used after editing fortran source files.

- EDC name

  Action:

  EDC (edit MP99.C) invokes the text editor ZED (see INFO.SPEC.ZED) to edit a fortran source module called "name". "Name" is a member of the partitioned dataset (see User's Reference Manual) MP99.C which contains all the fortran source. "name" should be re-compiled using COMP.

A1.7.5 Magnetic tape commands

- TAPEDUMP dsname

  Action:

  TAPEDUMP submits a job to file "dsname" to a magnetic tape (which must have been initialised for TLS). The tape identifier is prompted for, as is a remark string (less than 24 characters in length) which appears on the tape directory. "dsname" is then deleted.

- TAPEX

  Action:

  TAPEX (magnetic tape examine) prompts for a search string and a magnetic tape identifier. A copy of the tape directory is searched for the string and all lines containing that string are displayed at the console.

- TLS

  Action:

  TLS (tape library system) requests the user to enter an INPUT dataset of valid TLS commands (see INFO.SPEC.TLS). TLS is used to transfer files to and from magnetic tape. The tape identifier is prompted for.

A1.7.6 Miscellaneous commands

■ CHAIN/UNCHAIN

Action:

CHAIN ensures that no further offline jobs can run concurrently. This saves the chance of error caused by jobs trying to modify the same data at the expense of slower real-time execution (jobs run sequentially). The effect of CHAIN may be reversed by typing UNCHAIN.

■ DIRECT/UNDIRECT

Action:

The DIRECT command ensures that subsequent offline graphical output is sent direct to the plotter. UNDIRECT has the reverse effect.

■ MACROCMP [n]

Action:

MACROCMP (phoenix macro compiler) compiles the phoenix macro source module (in MP99.A:MACRO[n] where n = 2 or 3) and then reloads the relevant macro library.

The source may be edited by typing EDA MACRO n (see INFO.SPEC.MACRO for details of the phoenix macro language and INFO.SPEC.ZED for details of the text editor).

■ LOAD/UNLOAD

Action:

These commands load and unload the phoenix macro libraries used by the energy-loss system. All the commands in this summary require the macro libraries to be loaded. (This is done automatically by the command sequence MP99.A:INIT).

■ LOGOFF

Action:

To end a session, type LOGOFF. The command sequence will the ask if:

1) the user's filespace should be tidied-up (this means the deletion of plot datasets and load-modules);

2) MP99 files are to be printed on the west Cambridge outstation lineprinter (this produces 6000 lines of output, so answer "Y" with caution !);

3) MP99 files are to be compressed. It is essential that MP99 files be compressed if any programs have been altered and recompiled.

- SMALL

  Action:

  SMALL submits a job to perform step 3) above

- DUMP

  Action:

  DUMP submits a job to perform step 2) above.

A1.8 EXAMPLES

1) To process energy-loss spectra of BN (boron nitride) to obtain the boron : nitrogen ratio, the following might be typed:

```
        NDATA BN  (creates the spectrum BN)
        INTEGRATE BN  input dataset: 150.,380.,20.,190.
                                     300.,0.,30.,0.
                     (automatic edge location on Nitrogen, but not Boron)
or:
        STEP BN         with the same input dataset.
```

2) To obtain boron exelfs:

```
        NDATA BN
        RAMP BN TO RBN EDGE  input dataset: 150.,380.,20.,190.
        (enter low-loss spectrum from paper tape)
        NDATA BNLLOSS   (creates the spectrum BNLLOSS)
        DECONV RBN WITH BNLLOSS
        RAMP MOD  (to extract exelfs)  with same input dataset
        TRANS OPTR=25.  (transform and get "rdf").
```

3) To obtain the dielectric funtion:

```
(enter BN low-loss spectrum from paper-tape)
NDATA BNLLOSS   (correct for zero peak and aperture if necessary)
MULDEC BNLLOSS  (remove multiple scattering)
DENSITY
```

APPENDIX B - The design of a dedicated data-collection device for energy-loss spectroscopy

It is readily seen that the maximum count rate that may be used before dead-time correction become important is woefully low. This is because each pre-scaled number of events generates an interrupt which takes ≃50 μS to be serviced. During the execution of the service routine the computer is insensitive to any furthur interrupts.

A far better data-collection scheme is to count electron events in a fast digital counter which is outside the computer, but may be stopped,started, cleared or read by the computer. Electron events are counted for a period of time, the counter is stopped and the contents of the counter is read by the computer. The counter is then cleared and restarted. The computer adds the count to the corresponding energy bin.

Using fast logic (emitter coupled logic - ECL), it is possible to count at rates up to 100 MHz: an improvement in maximum count rate of approximately 10,000 times!

The advent, in the past three years, of cheap microprocessor-based computer systems means that a complete energy-loss spectroscopy data-collection system can be built for under £800 (1979 prices). Such a system was suggested as a Part II project by the author and run under the supervision of Mr. N. Bett (Cavendish Laboratory Electronics section).

The success of a project of this nature rests almost entirely on the quality and enthusiasm of the student engaged to build it.

The completed system has the following features: It can:

1) count electrons arriving at rates up to 100 MHz;
2) display the accumulated spectrum on an oscilloscope;
3) produce plots of the data on an X-Y plotter;
4) communicate data via a serial link to the University computer (an IBM 370/165);
5) provide an analogue spectrometer current signal to control the energy scan.

References

Ashley C.A. & Doniach S.	Phys. Rev. B 11 1279
Batson P.E. (1978a)	private communication
∿(1978b)	"Analytical electron microscopy", specialist worksop, Cornell Univ., New York
∿& Chapman J.N., Craven A.J., Ferrier R.P. (1978)	"9th international congress on electron microscopy" - Toronto 1
∿& Craven A.J. (1979)	Phys. Rev. Let. 42 893
Bauer H.C., Völkl J., Tretkowski J., Alefield G. (1976)	Z. Physik B 29 17
Bearden J.A. & Burr A.F. (1967)	Rev. Mod. Phys. 39 127
Bell M.G. & Liang W.Y. (1976)	Adv. Phys. 25 53
Bethe H. (1930)	Ann. Phys. 5 325
Bohm D. & Pines D. (1951)	Phys. Rev. 82 625
∿(1952)	Phys. Rev. 85 338
∿(1953)	Phys. Rev. 92 609
Boyce J.F. & Embling H.V. (1980)	J. Phys. D 13 471
Buxton B. (1980)	private communication
Chapman J.N., Batson P.E., Waddell E.M., Ferrier R.P. (1978)	"9th international congress on electron microscopy" - Toronto 1
Citrin P.H., Eisenberger P., Kincaid B.M. (1976)	Phys. Rev. Let. 36 1346
Colliex L.,Gasgnier M., Trebbia P.(1976)	J. Physique 37 397
Cook R.F. (1971)	Phil. Mag. 24 1347
Cooper M.J. (1977)	Phys. Bulletin October 1977 463
Crewe A.V., Isaacson M., Johnson D. (1971)	Rev. Sci. Inst. 42 411
Cundy S.L. (1967)	Ph.D. thesis, University of Cambridge
Daniels J., Festenberg C.V., Raether H., Zeppenfeld K. (1970)	Springer tracts in modern physics 54 77
Dorignac D. (1979)	Ultramicroscopy 4 85

Egerton R.F. (1978)	Ultramicroscopy 3 243
∿(1979)	Ultramicroscopy 4 169
∿ & Whelan M.J. (1974)	"8th international congress on electron microscopy" - Canberra 1 384
Fano U. (1956)	Phys. Rev. 103 1202
∿ & Cooper J.W. (1968)	Rev. Mod. Phys. 40 441
Fiddy M.A. & Greenaway A.H. (1978)	Nature 276 421
Field D. (1980)	private communication
∿, Butler E.P., Scamans G.M. (1979)	Inst. Phys. Conf. Ser. No. 52 401
Ferrell R.A. (1956)	Phys. Rev. 101 554
Gryziński M. (1965)	Phys. Rev. 138 A 336
Gull S.F., Daniell G.J. (1978)	Nature 272 686
Gurman S. (1979)	"notes on Beni, Lee & Platman (Phys. Rev. B 13 5170)" - private comm.
∿(1980)	private communication
Hillier J. & Baker R.F. (1944)	J. Appl. Phys. 15 663
Hirsch P.B., Howie A., Nicholson R.B., Pashley D.W., Whelan M.J. (1977)	"The electron microscopy of thin crystals" - Krieger, New York (2nd Ed.)
Inokuti M. (1971)	Rev. Mod. Phys. 43 297
Isaacson M. & Utland M. (1978)	Optik 50 213
Leapman R.D. & Rez P., Mayers D.F. (1978)	"9th int. cong. on elec. microscopy" - Toronto 1 526
Leapman R.D. & Silcox J. (1978)	Phys. Rev. Let. 42 1361
Lee P.A., Boon-Keng Too, Simons A.L. (1976)	"EXAFS: a new parameterisation of phase shifts" - Bell labs, Murray Hill, New Jersey
Lee P.A. & Pendry J.B. (1975)	Phys. Rev. B 11 2795
Lee P.A. & Beni G. (1977)	Phys. Rev. B 15 2862
Liang W.Y. & Cundy S.L. (1969)	Phil. Mag. 19 1031

Maher D., Egerton R.F., Mochel P. (1978) "The functional form of energy-differential cross-section for C" - Bell Labs, Murray Hill, New Jersey

Marton L. & Leder L.B. (1954) Phys. Rev. 94 203

Menzies R.G., Bricknell R.H., Craven A.J. (1980) Phil. Mag. A 41 493

Metherell A.J.F. (1965) Ph.D. thesis - University of Cambridge

Nozieres P. & Pines D. (1958a) Phys. Rev. 109 741

∿(1958b) Phys. Rev. 109 762

∿(1958c) Phys. Rev. 109 1062

∿(1959) Phys. Rev. 113 1254

Page T. (1977) private communication

Pennycook S.J. (1978) Ph.D. thesis, University of Cambridge

∿(1980) private communication

Pennycook S.J., Craven A.J., Brown L.M. (1977) Inst. Phys. Conf. Ser. No. 36 69

Pines D. (1956) Rev. Mod. Phys. 28 184

∿ & Bohm D. (1952) Phys. Rev. 85 338

Platzmann P.M. & Wolff P.A. (1973) "Waves & Interactions in solid plasmas" - Academic, New York

Powell C.J. (1976) Rev. Mod. Phys. 48 33

Raether H. (1965) Springer tracts in modern physics 38 84

Rau A.R.P. & Fano U. (1967) Phys. Rev. 162 68

Reed S.J.B. (1975) "Electron microprobe analysis" Cambridge University Press - London

Riley K.F. (1974) "Mathematical methods for the physical sciences" C.U.P.

Ritchie R.H. (1957) Phys. Rev. 106 874

Rudberg E. (1930) Proc. Roy. Soc. 127A 111

Salem S.I., Chang C.N., Lee P.L., Severson V. (1978)	J. Phys. C 11 4085
Schober T.(1975a)	Phys. Stat. Sol. A 30 107
∿(1975b)	Phys. Stat. Sol. A 29 395
∿, Pick M.A., Wenzl H.V. (1973)	Phys. Stat. Sol. A 18 175
Schen L.Y.L., Chen H.S., Dynes R.C., Garno J.P. (1978)	J. Phys. Chem. Sol. 39 33
Stern E.A. (1974)	Phys. Rev. B 10 3027
∿ & Ferrell R. (1960)	Phys. Rev. 120 130
Taft E.A. & Philipp H.R. (1965)	Phys. Rev. A 138 197
Treacy M.M.J. (1980)	Ph.D. thesis, University of Cambridge
Turner P. (1980)	private communication
Wanagel J., Sass S.L., Batterman B.W. (1972)	Phys. Stat. Sol. A 10 49
Wehenkel C. & Gauthé B. (1974a)	Solid State Com. 15 558
∿(1974b)	Phys. Let. 47 A 253
Wertheim G.K. (1975)	J. Elec. Spec. & Rel. Phen. 6 239
Whitaker M. & Heath A.R. (1953)	J. Inst. Metals 82 107
Wyckoff R.W.G. (1960)	"Crystal structure" Vol 1 (2nd Ed.) - Interscience - London
Switendick A.C. (1978)	"Hydrogen in metals" Vol 1 101 ("Topics in app. phys." 28) Springer-Verlag New York